ATMOSPHERIC RIVERS AND EXTREME PRECIPITATION OVER INDIA

Ph.D. Thesis

By

ROSA VELLOSA LYNGWA

DISCIPLINE OF CIVIL ENGINEERING

INDIAN INSTITUTE OF TECHNOLOGY INDORE

OCTOBER 2023

ATMOSPHERIC RIVERS AND EXTREME PRECIPITATION OVER INDIA

A THESIS

Submitted in partial fulfillment of the requirements for the award of the degree
of
DOCTOR OF PHILOSOPHY

by
ROSA VELLOSA LYNGWA

DISCIPLINE OF CIVIL ENGINEERING
INDIAN INSTITUTE OF TECHNOLOGY INDORE
OCTOBER 2023

INDIAN INSTITUTE OF TECHNOLOGY INDORE

I hereby certify that the work which is being presented in the thesis entitled **Atmospheric Rivers and Extreme Precipitation over India** in the partial fulfillment of the requirements for the award of the degree of **Doctor of Philosophy** and submitted in the **Department/School of Civil Engineering, Indian Institute of Technology Indore**, is an authentic record of my own work carried out during the time period from July 2019 to October 2023 under the supervision of Dr. Mohd. Farooq Azam, Associate Professor, Department of Civil Engineering, Indian Institute of Technology Indore, Simrol-453552, Madhya Pradesh, India, and Dr. Munir Ahmad Nayak, Assistant Professor, Department of Civil Engineering, National Institute of Technology Srinagar, Srinagar-190006, Hazratbal, Jammu and Kashmir, India.

The matter presented in this thesis has not been submitted by me for the award of any other degree of this or any other institute.

signature of the student
(Rosa Vellosa Lyngwa)

This is to certify that the above statement made by the candidate is correct to the best of my/our knowledge.

Mohd. Farooq Azam

Signature of Thesis Supervisor
(Dr. Munir Ahmad Nayak)
(Main Supervisor)

Signature of Thesis Supervisor
(Dr. Mohd. Farooq Azam)

Rosa Vellosa Lyngwa has successfully given his/her Ph.D. Oral Examination held on

Mohd. Farooq Azam

Signature of Thesis Supervisor
(Dr. Munir Ahmad Nayak)
(Main Supervisor)

Signature of Thesis Supervisor
(Dr. Mohd. Farooq Azam)

ACKNOWLEDGEMENTS

In all humility, I am eternally grateful to the LORD Jesus, who has always blessed me. Despite my moments of doubt and fear, He remains my constant source of strength and courage.

My gratefulness goes to my thesis advisors: Dr. Munir Ahmad Nayak and Dr. Mohd. Farooq Azam.

I am thankful to Dr. Munir Ahmad Nayak, who is the reason I am an Atmospheric River (AR) researcher. Despite my initial struggles with ARs, your guidance, and critical supervision have helped me commit to the work and complete my thesis. I sincerely appreciate your dedication and continuous efforts to improve my research skills which have greatly helped me grow in this area.

I am deeply grateful to Dr. Mohd. Farooq Azam for welcoming me into his Glacio-Hydro-Climate Lab (GHC Lab) after Dr. Munir joined NIT Srinagar. Your guidance and discussions on Himalayan projects have been invaluable in enriching my research. Your constant support and encouragement were crucial in completing this thesis. Thank you for fostering a friendly and motivating atmosphere throughout my Ph.D. journey.

You both are truly inspiring and I wish you a beautiful life ahead. I extend my heartfelt wishes to your families.

I sincerely thank my dear friends Gideon, Yoshini, and Smriti for their valuable discussions, support, and encouragement in both my research work and personal life. I also thank Waqar for his meticulous review, suggestions, and support which significantly improved the clarity of my work. I extend my gratitude to my friends/lab members at IIT Indore and NIT Srinagar for always lending a helping hand especially, Parul, Nisha, Megha, Arif, Mehvish, Junaid, Saika, Sageer, Manoj, Himanshu, Sachin, and Humaira.

I sincerely thank my PSPC members, Dr. Guru Prakash, and Dr. Lalit Borana, for their thoughtful comments and suggestions during the annual evaluations and overall Ph.D. journey, which have continued to resonate with me. My appreciation also goes to Dr. Abhishek Rajput, HOD, and the Civil Engineering Department staff members, Mrs. Rinki Kukrejra, Mr. Amit Jadhav, Mr. Ajay Malviya, Mr. Avdhesh for their assistance with administrative matters. I express my gratitude to IIT Indore for providing me a workplace, resources, and a supportive community that contributed to my professional and personal growth.

I deeply thank my parents (J. Shullai and S. Lyngwa), sisters (Samanda, Manca, and Deita), and my uncle (O. T. Lyngwa) for their continuous encouragement and belief in my abilities to pursue a Ph.D. even from afar. Their support has helped me overcome challenges and persevere in my Ph.D.

Finally, I thank the Science and Engineering Research Board (SERB) for providing financial support for my PhD tenure under the projects (i) Early Career Research Award (ECR/2017/002782) and (ii) Core Research Grant (CRG/2020/00487).

DEDICATION

To my dear family

Abstract

Atmospheric rivers (ARs) are qualitatively described as long, narrow, and transient corridors of strong horizontal moisture transport in the lower troposphere. They are the strongest moisture fluxes in the mid-latitude atmosphere. Upon landfall at coastal or inland regions, ARs exert a diverse range of impacts spanning from beneficial to catastrophic. However, South Asia, particularly India, has seen limited exploration of ARs. This thesis aims to address that gap by investigating ARs and their connection to extreme events in these regions, through three key objectives.

First and foremost is to examine the potential role of ARs in the recent second-largest flood in Kerala, South India, on August 2018. This study involves the identification of ARs before and during the flood, examine the factors intensifying precipitation, and pinpoint locations of surplus moisture uptake. There was an intense and long-duration AR during the second week of August, and its perpendicular impact on the Western Ghats amplified AR-moisture depletion. The polar jet trough dipped towards India and strengthened the region's monsoon trough. High-and-low pressure anomalies over India directed moisture mainly from the north-central and eastern Indian Ocean into the region.

In northern India, ARs striking the south-facing Himalayan arc and impacting the Indus Basin (IB) and Ganga Basin (GB) are investigated. The study focuses on the characteristics of ARs, precipitation impacts, atmospheric stability, precipitation-driving mechanisms, and moisture sources of extreme AR events. The ARs are frequent (mostly of low-intensity) during winter in extratropical regions of Himalaya, and during summer (high intensity) in tropical portions. The extreme AR events led to extreme precipitation in and around the ARs. Moisture convergence sustains intense ARs, influencing precipitation intensity, while mechanisms driving high precipitation within ARs are controlled by orographic processes near mountains (air is weakly unstable) and frontal processes (unstable warm air ascend) along its central axis. Excess moisture for high precipitation came from both tropical and extratropical sources, with the highest contributions traced to the tropical ones.

The quantitative contributions of ARs to the Himalayan hydrology of IB and GB, on precipitation, extremes, and floods are investigated. ARs contribute over a quarter of the annual rainfall in these basins, with the highest impact during winters, notably in IB. Over half of the average winter precipitation (rainfall and snowfall) occurs during AR events, with ARs largely explaining the winter precipitation variability in mountains. A large fraction of annual maxima of perceivable magnitude along the foothills in winter and spring are AR-influenced. In relation to large floods, ARs are particularly associated with floods near the mountains and plains of West Bengal.

LIST OF PUBLICATIONS

Publications from PhD thesis work:

a. Publications in refereed journals.

1. Lyngwa, R. V., Nayak, M. A. & M. F. Azam., 2023. Large fraction of winter precipitation variability in two major Himalayan basins explained by Atmospheric Rivers. *Journal of Climate*, pp.1-30, DOI: https://doi.org/10.1175/JCLI-D-22-0599.1 (IF: 5.38)
2. Lyngwa, R. V. & Nayak, M. A., 2021. Atmospheric river linked to extreme rainfall events over Kerala in August 2018. *Atmospheric Research, 253*, p.105488, DOI: 10.1016/j.atmosres.2021.105488 (IF: 5.96)

b. **Articles in submitted/preparation (Journals)**

3. Lyngwa, R. V. Nayak, M. A., & M. F. Azam. Himalayan Atmospheric Rivers: Thermodynamics of extreme Atmospheric rivers and their precipitation mechanisms in two major Himalayan basins

c. Refereed conferences.

1. Lyngwa, R. V, Nayak, M. A. & M. F. Azam., 2022. Distinctive Characteristics of Atmospheric Rivers and Active Monsoon in India, *Asia Oceania Geosciences Society 19th Annual Meeting* (1st – 5th August)
2. Lyngwa, R. V. & Nayak, M. A., 2021. Quantitative study of atmospheric rivers in the Indian subcontinent *European Geosciences Union General Assembly* (19th – 30th April 2021)
3. Lyngwa, R. V. & Nayak, M. A., 2020. The Contribution of Arabian Sea to the Mumbai flood of July 2005, *Roorkee Water Conclave* (26th – 28th February)
4. Lyngwa, R. V. & Nayak, M. A., 2019. Impacts of integrated water vapor anomalies on extreme precipitation events, *8th APHW International Conference on Emerging Technologies in Urban Water Management* (22nd – 23rd November)

Other Publications during PhD:

Hassan, W. U., Nayak, M. A. & Lyngwa, R. V., 2021. Recent changes in heatwaves and maximum temperatures over a complex terrain in the Himalayas. *Science of Total the Total Environment*, *794*, p.148706, DOI: 10.1016/j.scitotenv.2021.148706 (IF: 10.75)

TABLE OF CONTENTS

LIST OF FIGURES

Main Text Figures

Supplementary Figures

LIST OF TABLES

Main Manuscript

Supplementary tables

NOMENCLATURE

Symbols	Terms	Equations	Units
IWV	Integrated water vapor	$IWV = g^{-1}\int_{1000hPa}^{300hpa} qdp$	mm or cm
IVT	Integrated water vapor transport	$IVT = \frac{1}{g}\sqrt{\left(\left(\int_{psur}^{ptop} qudp\right)^2 + \left(\int_{psur}^{ptop} qvdp\right)^2\right)}$	$(kg.m^{-1}.s^{-1})$
$\boldsymbol{R^2}$	Coefficient of Determination	$r^2 = \left(\frac{n(\sum xy) - (\sum x)(y)}{\sqrt{[n\sum x^2 - (\sum x)^2][n\sum y^2 - (\sum y)^2]}}\right)^2$	
$\boldsymbol{-\nabla\overrightarrow{IVT}}$	Moisture Flux Convergence	$= -\frac{1}{g}\int_{1000\ hPa}^{300hPa} \nabla.(\bar{V}q)dP$	$mm.day^{-1}$
$\boldsymbol{e}$	Vapor pressure	$= 6.112 \times exp\left[\frac{17.67 \times T_d}{(T_d + 243.5)}\right]$	hPa
$\boldsymbol{f_{n,t}}$	Fractional contribution of uptake amount $(\Delta q_{n,t})$ to moisture q_n in the parcel	$= \frac{\Delta q_{n,t}}{q_n} \times 100$	%
$\boldsymbol{f_{m,t}}$	Fractional contribution of previous moisture uptakes $(\Delta q_{m,t})$ to moisture (q_n) ahead	$= \frac{\Delta q_{m,t}}{q_n} \times 100, m > n$	%

ACRONYMS

20 CRV2	Twentieth Century Reanalysis Version 2 Project
ACET	Aerosol Characterization Experiment Balloon Trajectories
ASTER	Advanced Spaceborne Thermal Emission and Reflection Radiometer
ARL	Air Resources Laboratory
AR (s)	Atmospheric River(s)
ARTMIP	Atmospheric Rivers Tracking Method Intercomparison Project
ANATEX	Across North America Tracer Experiment
CH	Central Himalaya
CAPTEX	Cross-APpalachian Tracer EXperiment
Cat	Category
CV	Coefficient of variation
CWC	Central Water Commission
DEM	Digital Elevation Model
DJF	December-January-February
ECMWF	European Centre for Medium-Range Weather Forecasts
ENSO	El Niño-Southern Oscillation
ERA5	European Centre for Medium-Range Forecasts reanalysis version 5
ERA-Interim	ECMWF Re-Analysis Interim
ETEX	European Tracer Experiment
FFC-GOP	Federal Flood Commission Government of India
GB	Ganga Basin
GDAS	Global Data Assimilation System
GDEM2	Global Digital Elevation Model
GMTED2010	Global Multi-Resolution Terrain Elevation Data 2010
GPCC	Global Precipitation Climatology Centre
GPM IMERG	Global Precipitation Measurement Integrated Multi-Satellite Retrievals
GOES	Geostationary Operational Environmental Satellite
GoM	Glossary of Meteorology
HK	Hindu-Kush

HKKH	Hindu-Kush-Karakoram-Himalaya
HMA	High Mountain Asia
HYSPLIT	Hybrid Single-Particle Lagrangian Integrated Trajectory model
IB	Indus Basin
IMD	India Meteorological Department
ISM	Indian Summer Monsoon
ITCZ	Inter Tropical Convergence Zone
IWV	Integrated Water Vapor
IVT	Integrated Water Vapor Transport
JJA	June-July-August
JRA-55	Japanese 55-year Reanalysis
KA	Karakoram
LLJ (s)	Low-Level Jet (s)
MAM	March-April-May
MERRA	Modern-Era Retrospective analysis for Research and Applications
MJO	Madden Julian Oscillation
MSL	Mean Sea Level
NASA	National Aeronautics and Space Administration
NCEP-DOE	National Centers for Environmental Prediction-Department of Energy
NCEP-NCAR	National Centers for Environmental Prediction-National Center for Atmospheric Research
NOAA	National Oceanic
NOAA-20C	NOAA-CIRES Twentieth Century Reanalysis v2
READY	Real-Time Environmental Applications and Display
RSMC	Regional Specialized Meteorological Centre
SH	Specific Humidity
SRTM	Shuttle Radar Topographical Mission
SSM/I	Special sensor microwave/Imager
SSMIS	Special Sensor Microwave Imager/Sounder
SON	September-October-November
tARget	Tracking Atmospheric Rivers globally

THDC	Tehri Hydro Development Corporation
TME (s)	Tropical Moisture Export (s)
USGS	United States Geological Survey
USA	United States of America
UTC	Universal Time Coordinated
UTM	Universal Transverse Mercator
WCB (s)	Warm Conveyor Belt (s)
WD	Western Disturbances
WH	Western Himalaya
WFDE5	WATCH (Water and Global Change) Forcing Data ERA5
WFDEI	WATCH (Water and Global Change) Forcing Data ERA-Interim
WRIS	Water Resource Information System

Chapter 1

Introduction

1.1. Brief historical perspective of Atmospheric Rivers

The most notable features in atmospheric water vapor flux maps and satellite radiation reflectivity imageries are filamentary forms that stretch over long distances, often many times their width, and exhibit poleward movement (Newell *et al.*, 1992). Before the 1990s, these features were considered part of the warm conveyor belts (WCBs) or linked to extratropical cyclones (Browning, 1990; Newell and Zhu, 1994). However, with the aid of satellite images, scientists discerned them as organized formations situated several thousand kilometers away from cyclones or cyclonic precipitating systems (Newell and Zhu, 1994). They were noted as having briefer residence time (transient) than typical cyclonic systems (Newell *et al.*, 1992; Newell and Zhu, 1994) but may still be closely associated with large-scale atmospheric systems. In 1992, they were termed "Tropospheric Rivers", emphasizing their propagation in the lower troposphere, and their high volumetric flow rates akin to the fluxes in the Amazon River (Newell *et al.*, 1992). Two years later, they were renamed "Atmospheric Rivers" (ARs) (Zhu and Newell, 1994) because they are the strongest fluxes in the atmosphere with filamentary form (Zhu and Newell, 1998). Zhu and Newell, (1998) computed integrated water vapor flux (IVT) on each grid ($2.5° \times 2.5°$, (Zhu and Newell, 1994)), and introduced IVT threshold (large deviations from zonal means) for a given latitude to segregate ARs from other transport systems globally, and provided the first 2D visual understanding of these features (See Figure 2 of Zhu and Newell, (1998)).

Several dropsonde experiments conducted between 1997 and1998 confirmed the presence of strong low-level moisture in filamentary forms near Low-Level Jets (LLJs), both ahead of and along cold fronts (Ralph, Neiman and Wick, 2004; Ralph, Neiman and Rotunno, 2005). In the 2000s, satellite imageries of atmospheric water vapor (or IWV, integrated water vapor) were extensively available, and investigation on ARs started in the west coast of USA. Special Sensor Microwave Imager (SSM/I) provided IWV that enabled discernable identification of ARs in the eastern North Pacific (west coast of USA), and derivation of some preliminary key features of ARs (through visual inspection): IWV ≥ 2 cm, spatial length exceeding 2,000 km, and width range between 300 – 500 km (Ralph, Neiman and Wick, 2004). These studies also revealed that in ARs, 75% of the horizontal moisture flux occurs within 2.5 km of altitude, with moist neutral conditions extending up to 3 km altitude.

Since Ralph, Neiman and Wick, (2004), ARs studies emerged in the western USA and Europe, primarily concerning their extreme hydrological impacts. These studies adopted the basic characteristics of ARs such as low-level, strong horizontal moisture flux in long and narrow regions, to detect them, but their quantitative definitions varied. For instance, regarding the minimum length requirement for ARs, studies have used different criteria to address their specific objectives: ≥ 950 km (Lavers and Villarini, 2013b), ≥ 1,500 km (Kamae *et al.*, 2017; Thapa, Endreny and Ferguson, 2018), ≥ 2,000 km (Guan and Waliser, 2015), among others. In general, a minimum length of 2,000 km is preferred (Fish, Wilson and Ralph, 2019; Pan and Lu, 2019). The concept of ARs sparked debates among scientists about their distinctiveness from preexisting concepts like WCBs, Tropical Moisture Exports (TMEs) (Bao *et al.*, 2006; Knippertz and Wernli, 2010; Sodemann and Stohl, 2013), and the analogy of the term "rivers" to "terrestrial rivers". However, after years of discussions, and through two key workshops (Dettinger, Ralph and Lavers, 2015; Ralph *et al.*, 2018) it was established that ARs, WCBs, and TMEs are distinct but interrelated features. In 2018, a formal definition of AR was introduced in the Glossary of Meteorology (GoM) to provide clarity in the scientific literature (https://glossary.ametsoc.org/wiki/Atmospheric_river). An AR is then described as elongated and transient corridors of strong horizontal moisture transport in the lower troposphere, that is typically associated with LLJs ahead of an extratropical cyclone's cold front. Moisture in ARs originates from tropical-subtropical or extratropical sources. When ARs encounter mountains or are lifted by fronts, they often result in heavy precipitation. Notably, ARs constitute the largest freshwater "rivers" on Earth, conveying more than double the volume of water compared to the Amazon River (Ralph *et al.*, 2018). This definition helped establish AR perspective and enhanced their global recognition within the meteorological, hydrological, and glaciological community, leading to rapid advancement in AR science.

1.2. Global presence of ARs and their diverse impacts

1.2.1. Non-extratropical ARs

The AR definition in GoM describes ARs qualitatively, based on experiments and studies conducted in the western USA and Europe (mid-latitude regions). It highlighted that ARs are "typically" associated with the cold front's LLJs of extra-tropical cyclones; however, Zhang et al. (2019) found that around 82% of ARs are paired with extra-tropical cyclones in the North Pacific. It also hints at the possible independent existence of ARs, and relevance in non-extratropical context. Due to the lack of regional investigations around the world, this has led to ARs being considered as primarily an extra-tropical phenomenon.

In IVT maps of selected years in Zhu and Newell, (1998), few filamentary features with inclined poleward direction were noticed in the tropical-subtropical latitudinal bands. However, regional studies over these latitudes only emerged post-2000. These studies revealed distinctive characteristics of tropical-subtropical ARs: subtropical ARs' strength is dominated by large moisture content, while extratropical ARs' strength is dominated by strong winds (Zhou *et al.*, 2022). In extra-tropics, ARs peak in autumn and winter (Lavers *et al.*, 2012; Nayak and Villarini, 2017; Doiteau *et al.*, 2021), due to increased storm activity enhanced by intense thermal gradients, whereas in tropics-subtropics ARs are more frequent in summer due to strong monsoonal flows (Kamae *et al.*, 2021; Mahto *et al.*, 2023). During the East Asian Summer Monsoon, AR frequency (the ratio of 6-hourly instances where AR conditions are met to the total time between June-September during 1979-2018) varies monthly between June to September: peaking in June-July, weakening in July-August, and declining in August-September. This variation corresponds with the strengthening and northward shift of the western North Pacific High, the Asian Monsoon, and migrating extra-tropical cyclones (Pan and Lu, 2020; Park, Son and Kim, 2021). Australia experiences fewer ARs annually on its tropical coasts (4-8 days/year) due to infrequent occurrence of tropical-origin ARs, compared to its extratropical coast (16 days/year) with frequent ARs of extratropical origins (Guan and Waliser, 2015).

Ahead of the extra-tropics, ARs extend into the Artic and Antarctic regions, and caused record-breaking temperatures, surface melting, or deposit extreme snowfall (Maclennan *et al.*, 2023; Zhang *et al.*, 2023). While such ARs are less frequent and have short durations (Maclennan *et al.*, 2023), a two or three-day AR event produced positive mass anomalies and contributed about 22% of the total surface mass balance over the East Antarctic ice sheet (Gorodetskaya *et al.*, 2014). In these regions, ARs have lower tropospheric IWV (< 2cm) than those in the extra-tropics (≥ 2cm), however, the moisture content is much higher compared to the latitudinal IWV mean. The findings indicate that ARs may play as much of an important role in tropical-subtropical and polar regions' climate as in extra-tropics, though the characteristics of ARs impacting the regions may vary.

Extratropical ARs transport moisture from the tropics and extra-tropics to the poles. Some ARs travel long distances, sustained by moisture inputs from local regions, convergence from neighboring sources, or contributions from distant sources (Payne *et al.*, 2020). ARs that persist for very long durations (> 72 hours, persistent ARs) typically originate in the subtropical western North Pacific and travel eastward with growing intensities (Zhou and Kim, 2019) and hit the west coast (Payne and Magnusdottir, 2016), or Alaska (Zhou, Kim and Guan, 2018). While, ARs that briefly exist (< 24 hours) originate mostly in eastern subtropics or are confined within tropical (or polar) regions, and are less intense. Persistent ARs are often supported by successive occurrences of extratropical cyclones (Sodemann and Stohl, 2013). The above findings affirm that ARs play a crucial role in the transport of moisture, heat, and energy from the tropics and extra-tropics to the poles (Hu and Dominguez, 2019).

1.2.2. Impacts beyond midlatitude regions: extreme precipitation and floods linked to ARs

Prior to the ARs definition in GoM, extensive research delved into understanding their impacts that helped realized their influence and appreciated their presence. ARs emerge as the most efficient horizontal moisture transport in mid-latitudes (Zhu and Newell, 1998; Lavers and Villarini, 2015b). In the western USA and Europe, ARs contribute over 60% of the annual precipitation, their presence increases flooding by 80%, and hydrological drought incidences by 90% (Paltan *et al.*, 2017). On average (1978-2017), ARs result in a $1.1 billion loss in flood damages in 11 states of the western USA (Corringham *et al.*, 2019).

AR impacts are generated when the moist-neutral stability (Ralph, Neiman and Rotunno, 2005) in ARs is disturbed by external forces, such as interaction with high mountains, ascending over warm conveyor belts, or cold-frontal motion ahead of warm air. The impacts of ARs are shaped by their magnitudes and duration, and depending on whether they make landfall on plains or rugged terrain, they can result in a diverse range of impacts. Across western USA and Europe, ARs bring a wide range of impacts both at coastal and deep inland regions, ranging from heavy rainfall, extreme snowfall, floods, extreme winds, storm surges (Ralph *et al.*, 2006; Guan *et al.*, 2010; Ralph and Dettinger, 2012; Khouakhi and Villarini, 2016; Waliser and Guan, 2017), etc., to important regional water resources, climatological contributions, alleviating droughts, boost snowpack, sustain floodplains, and support ecosystem health (Dettinger *et al.*, 2011; Florsheim and Dettinger, 2015; Albano, Dettinger and Soulard, 2017; Hu and Nolin, 2019). Motivated by the wide range of AR impacts, regional studies around the world have emerged to establish such links between extreme hydro-meteorological events and ARs, and advance in understanding extremes and AR science. Precipitation events causing substantial losses in South Asia were examined recently and were found due to the presence of ARs (Ramos *et al.*, 2018; Lakshmi and Satyanarayana, 2019; Kamae *et al.*, 2021). For example, during extreme storms, ARs increased the discharge of the Moulouya River in Morocco up to 40% (Paltan *et al.*, 2017). ARs' landfall on the Andes, amplify precipitation intensity to levels surpassing those seen along North America's west coast (Viale *et al.*, 2018). In polar regions, ARs induced lower tropospheric warming by transporting warm moist air from the extra-tropics at a large-scale (Komatsu *et al.*, 2018), which led to ice melt and reduced the recovery rate of sea ice in Bren-kara Seas and central Artic (Zhang *et al.*, 2023). Similarly, ARs convey warm moist air to Greenland during AR events, and in a rare case in the summer of 2012, it caused the entire ice sheet surface to melt (Neff *et al.*, 2014). ARs are less frequent in Artic, but when they occur, the influx of warm and moist extra-tropical air significantly diminishes sea ice along marginal ice zones (Liang et al. 2023). The melting action of ARs over ice in the Antarctic forms pools of water that accelerate the disintegration of sea ice (Bozkurt *et al.*, 2018). Thus, major extreme events in other parts of the globe are linked to ARs.

1.3. Presence and influence of ARs in India

1.3.1. Frequency of AR landfalls

The frequency of ARs is a key focus in research, typically measured as the number of AR instances in a given time season or year. It can be computed at each grid or for specific latitude/longitude bands. Frequency can also refer to the number of AR events (a group of consecutive AR timesteps) impacting a region over a selected time period. Previous studies have shown that ARs make landfall in various regions worldwide, but with different frequencies. For example, in South Asia, the frequency varies between 8 – 16 AR days/year. Different AR definitions have led to different approaches in AR identification across studies, and have produced varying AR frequencies across the globe. However, there is a general agreement among the algorithms on AR frequency distribution in extratropics, compared to other latitudes that showed discrepancies.

Historically and till today, heavy precipitation in northern India, particularly on the southern slopes of Central Himalaya (CH) and Eastern Himalaya (EH), has been chiefly attributed to the number of cyclone landfalls. However, with the recognition of ARs' significance and frequency (~16 AR days/year) on the west coast peninsula of India, Bangladesh, and Myanmar (Guan and Waliser, 2015), regional investigations into AR frequency and impacts in inland South Asian regions began in 2018. It was found that ARs were frequent in May and October, often coinciding with peak occurrences of tropical cyclones in these regions. Hence, heavy precipitation in South Asia may also be due to ARs. ARs that travel beyond coastal regions of India are blocked by the Himalaya and extrude heavy precipitation through orographic effects (Yang *et al.*, 2018). ARs are shown to have penetrated western Nepal (a region in CH) more frequently in September post-ISM, contributing over 35% (70%) to annual (non-monsoon) maxima of daily precipitation (Thapa, Endreny and Ferguson, 2018).

AR landfall varies seasonally across the Indian peninsula with higher frequency in summer on the west coast, and in winter on the east coast (Gimeno *et al.*, 2016; Lakshmi and Satyanarayana, 2020). This pattern is influenced by large-scale processes that shaped moisture currents, for instance, the positive phase (phase 6) of the Boreal Summer Intraseasonal Oscillation increased ARs over the subcontinent due to heightened cyclonic activity (Guo *et al.*, 2021). Recent studies showed that ARs are most prevalent in summer, with the highest frequency in July, followed by August, June, and September (Mahto *et al.*, 2023). These findings corroborate the impactful presence of ARs in India.

1.3.2. AR characteristics and associated extreme precipitation and floods

As ARs have recently gained recognition in South Asia, especially in India, studies now shift focus to their regional impacts. In December 2015, Chennai experienced severe flood due to torrential rainfall (77–496 mm) from a 2-day persistent ARs (Lakshmi and Satyanarayana, 2019), resulting in an estimated loss of ~ $3 billion (Rana, 2015). Kerala also experienced a devastating flood caused by excess rainfall (3 times the normal) during a 4-day AR event, which resulted in ~ $3.7 billion loss in damage (News Asia, 2018). This flood was aggravated by the perpendicular orientation of the AR to the Western Ghats (Lyngwa and Nayak, 2021). In February 2013, intense snowfall in northern India and Nepal, along with flash floods in Pakistan, was linked to ARs (Thapa, Endreny and Ferguson, 2018), though detailed and rigorous AR analysis was lacking for this event. Despite the limited and scattered studies in India, they have provided valuable insights. Over the Bay of Bengal, more than 50% of the ARs have led to extreme rainfall events (90th percentile of daily precipitation above 1 mm), with 70% of ARs lasting over 12 hours, and 50% lived up to 18 hours, but the 6-hours difference produced a minor impact on precipitation intensity (Yang *et al.*, 2018). In Nepal, the average AR duration (total sequential timesteps in AR events) for 1979-2013 was 40-hours ($\pm$30-hours), with average AR precipitation exceeding 2.7 mm/day. Additionally, 78% of daily precipitation above 33mm occurred during ARs (Thapa, Endreny and Ferguson, 2018). In southern India, ARs in summer generally have higher average IVT ($> 580\ kg.m^{-1}.s^{-1}$) than in winter ($\sim 300\ kg.m^{-1}.s^{-1}$) (Lakshmi and Satyanarayana, 2020). Similarly, in the Himalaya less than 6% of ARs have an average IVT of $250\ kg.m^{-1}.s^{-1}$ in winter, spring, and autumn, and more than 14% have over $300\ kg.m^{-1}.s^{-1}$ in summer (Nash *et al.*, 2021). Thus, it can be understood that in central and southern India ARs are frequent in summer, and their strong intensities (>$500\ kg.m^{-1}.s^{-1}$) combined with favorable topography (Western Ghata and inland mountains) are likely to bring heavy precipitation. Conversely, ARs in other seasons have lower IVT, but can still be an important source of regional water availability. ARs contribute 18 – 24% (28% in the Western Ghats, and central India's mountain range) to India's extreme precipitation (exceeding 95th percentile daily rainfall), and are linked to 72% of floods between 1985-2020, including the top ten largest floods (Mahto *et al.*, 2023).

ARs' impacts are scaled by two key characteristics: peak IVT intensity and event duration over a region. Peak intensity drives peak rain rates, while duration affects total event precipitation (Ralph *et al.*, 2013; Lamjiri *et al.*, 2017). High topography intensifies AR impacts. Grouping ARs aids practical understanding of their physical impacts and holds significance from a water resources perspective. Thus, studying AR characteristics is important to understand their patterns of regional impacts.

1.4. ARs in Himalayan region and their potential regional impacts

The Himalayan ranges (including Karakoram (KA) and Hindu-Kush (HK) ranges) — are known as the Third Pole— has the largest non-polar snow and ice cover on Earth, feeding the headwaters of three major rivers forming large basins draining through India: Indus, Ganga, and Brahmaputra Rivers and impacting a billion-plus people (Azam *et al.*, 2021). The complex topography and elevation of the Himalaya created distinct climatic regimes (subtropical/tropical) unlike the warm tropical climates (Bookhagen and Burbank, 2006). The mountains impede moist winds and extract moisture as rain in lower altitudes and as snowfall in higher altitudes (Lang and Barros, 2004).

Little is known about the presence and impact of ARs on the Himalaya-Karakoram-Hindu Kush region. Prior studies revealed that ARs originate from tropical waters near India or as far as the Atlantic Ocean and hit the HK, resulting in extreme weather events such as heavy rainfall, snowfall, floods, landslides, etc. However, global studies have reported a low annual AR frequency in these regions, possibly due to high cutoff thresholds used for the Himalayan climate. For instance, a global AR detection algorithm considered IVT climatology in various regions, including Artic and Antarctic, but lacked such consideration for the Himalayan region, due to limited studies in the region (Guan and Waliser, 2015; Paltan *et al.*, 2017). This oversight not only hinders accurate assessment of AR impacts in the region but also risks underestimating the role of ARs in the region.

Comprehensive investigations on AR frequency and extreme precipitation in the Himalaya began in 2018, and focused on EH and part of CH (Yang *et al.*, 2018), while Thapa et al. (2018) targeted ARs in Nepal. These studies considered the strong seasonal decrease in IVT magnitude, across the Himalayan foothills to Tibet highlands to define the threshold's lower limit. This helped identify extreme moisture transports relative to regional climatology. However, the study by Nash et al. (2021) may have overlooked ARs in winter, spring, and autumn that affect these regions, due to a high threshold limit for AR identification. Nonetheless, these studies showed ARs' extensive reach from the coastal regions to the Himalayan ranges. Strong ARs often extend their influence beyond the point of contact or even penetrate higher latitudes to Tibet (as seen in Thapa, Endreny and Ferguson, (2018)).

The presence of ARs over the Himalayan region can induce a range of hydro-meteorological impacts influencing precipitation and temperature patterns, and in turn, affect snow and ice dynamics. These impacts include extreme snowfall or melt events, as seen for New Zealand mountain glaciers (Little *et al.*, 2019), or the warm moist air incursions experienced by the Brewster Glacier in Southern Alps, New Zealand, which resulted in the glacial mass loss of 117.8 mm w.e., with melt energy estimated to be 455.5 $W.m^{-2}$ (Kropač *et al.*, 2021), or melting can be enhanced by increased surface air temperature above freezing during ARs, resulted from more rainfall than snowfall (Skinner *et al.*, 2023), or by strong winds accompanying AR inducing downslope winds and intensify foehn conditions (low relative humidity and warmer air temperatures)

1.5. Moisture pathways and sources in precipitation extremes

Moisture transported into a region is a critical component of regional moisture availability and climate. It returns to the surface as precipitation, shaping a region's annual water balance. There are three physical moisture sources that drive precipitation: moisture already present in the atmosphere, continental sources through local evapotranspiration, and moisture advected from neighboring water bodies (Horan *et al.*, 2023; Yang *et al.*, 2023). However, the first two sources cannot fully explain changes in precipitation, particularly extremes. Intense moisture transport leads to extreme precipitation, while the lack of it leads to water scarcity. Extreme precipitation also occurs when marine sources supply abnormal amounts or when additional sources contribute. Extreme precipitation will have different hydroclimate and hydrological causes depending on the sources of moisture.

From a moisture balance perspective, evaporation and precipitation are crucial in controlling atmospheric storage. The connection between evaporative sources and precipitation at a specific location can be understood by studying the spatiotemporal trajectories of moist air parcels and observing the changes in specific humidity (decrease–precipitation and increase–evaporation) to locate the moisture sources. This is effectively achieved using the Lagrangian transport approach. The Lagrangian-based moisture backtracking analysis is commonly used due to its relatively better accuracy in determining moisture sources and sinks. Tracking air parcels provides a time record of their locations, atmospheric humidity, and thermodynamic conditions (Sodemann, Schwierz and Wernli, 2008a).

A significant portion of precipitation in India happens during the Indian Summer Monsoon (ISM), with moisture transported primarily from neighboring oceanic basins. The primary sources include the central Indian Ocean, Arabian Sea, GB, Red Sea and neighboring Gulf (Pathak *et al.*, 2017). The major contributions come from the central and southern Indian Ocean, with some intermittent contributions from the Arabian Sea, local recycling, and other remote sources (Dey and Döös, 2021). The Bay of Bengal also contributes, but it primarily serves as a pathway for air parcels from the central and south Indian Ocean. Extreme precipitation over central India results from anomalous moisture uptake from the Arabian Sea (Pathak *et al.*, 2017) supported by intense LLJs, and despite the weakening of monsoon circulation, decreased moisture-laden depressions from the Bay of Bengal, and reduced local moisture supply, there has been an increase wide-spread extreme precipitation events in this region (Roxy *et al.*, 2017). In summer, the strongest extreme precipitation events primarily draw moisture from the Arabian Sea, followed by the western Indian Ocean (near Madagascar), and the Caspian Sea (Hunt, Turner and Shaffrey, 2018). Establishing climatologies of these primary moisture sources during dominant weather patterns helps characterize their attributes, enhances predictability, and reveals potential links to climate modes. Any deviations from established sources or alterations in these links will manifest in the magnitude of precipitation and duration of the event. If ARs are present, they can transport moisture from tropical-subtropical and/or extratropical regions (Cordeira, Ralph and Moore, 2013). They enhance moisture transport through continuous moisture accumulation via evaporation over open waters, lateral convergence from surrounding areas, or even contribution from distant sources (Knippertz and Wernli, 2010; Sodemann and Stohl, 2013). This enables ARs to persist longer by replenishing depleted moisture, primarily through precipitation, along their paths. Thus, during ARs, the sources of moisture supply can vary or deviate from the normal, which should be tracked in case of events.

1.6. Objectives and Research Gaps

With the primary goal to explore ARs in India and their potential linkages to extreme weather, such as heavy precipitation, floods, etc., the following objectives are formulated.

Objective 1: Investigate the role of ARs during the second most devastating flood in Kerala in August 2018.

Research questions:

a. Did ARs play any role in this flood?
b. What are the synoptic conditions that orchestrated the flood?
c. What are the primary sources of moisture supply contributing to the extreme precipitation during the Kerala flood event?

Objective 2: Studying ARs in Himalaya, thermodynamics, and precipitation mechanisms of extreme ARs.

Research questions:

a. Do ARs occur in the Himalayan region?
b. Compare ARs identified using two algorithms for AR detection.
c. What are the spatio-temporal patterns characterizing AR in Himalaya?
d. What are the mechanisms driving precipitation during the largest-intensity ARs events in two distinct topographical regions within the AR: near mountain foothills and plains?
e. Can analyzing moisture sources in the two basins (Indus and Ganga) within ARs help explain their respective roles in local precipitation intensity?
f. Can the vertical profile of atmospheric stability reveal important atmospheric conditions leading to the type of precipitation formation, and possible mechanism?

Objective 3: Quantifying the Impacts of ARs on Himalayan Hydrology

Research questions:

a. What is the extent of AR events' impact on precipitation and water discharge in the Indus and Ganga Basin?
b. What is the average contribution of ARs annually and seasonally to rainfall?
c. How much do ARs contribute to precipitation in the basins and the mountains? Can AR explain the seasonal precipitation variability over the mountains?
d. What is the fraction of seasonal precipitation extremes related to ARs?
e. Are major floods in the two basins associated with ARs?

1.7. Organization of the thesis

Chapter 1: Introduction

In this chapter, a brief overview of ARs is provided, spanning their historical context and recent global and regional studies that uncovered their global presence and diverse impacts, with a focus on extreme precipitation and related floods. We delve into AR's presence and impacts in India. We briefly discuss the significance of ARs over the Himalaya, and why their presence may be important from a climatological impact perspective. We briefly discuss the moisture pathways during events and the importance of contributing sources to extreme precipitation in India. Towards the end of this chapter, we list the objectives of this thesis based on the research gaps identified.

Chapter 2: Literature review and problem formulation

This chapter provides a comprehensive review of past studies, the quantitative definition of ARs, that lead to a diverse approach for their identification, climatological contributions of ARs to regional precipitation, and precipitation impacts of ARs that leads to major floods.

Chapter 3: Major Flood in Kerala in August 2018: Role of ARs

In Chapter 3, we investigate the role of ARs in the second most devastating Kerala flood in August 2018. IVT and IWV are computed and compared against the 85th percentile climatological values. ARs are identified through visual inspections of IVT above the threshold and verified using an AR identification algorithm. We assess the synoptic characteristics of the lower and mid-troposphere to reveal anomalous activity leading to the extreme event. Lastly, the sources of moisture for extreme rainfall are diagnosed and their percent contributions to moisture in Kerala are computed to identify the locations of excess moisture supply.

Chapter 4: Studying Himalayan ARs, thermodynamics and precipitation mechanisms of extreme ARs

In this chapter, we present a modified algorithm to identify ARs in the Himalayan region. The climatological characteristics of ARs, and their categorization into groups of different impacts, are shown for different segments of the detection transect, which aligns with the Himalayan arc. Further, the top 16 AR events impacting the two Himalayan Basin−Indus (8) and Ganga (8) are selected for detailed analysis involving the computation of the moisture budget terms to determine the horizontal movement of moisture and the sources and sinks, track parcels, and quantify the contributions of various sources to moisture in the target regions. The thermodynamic properties (temperature and moisture) of the atmosphere during ARs were analyzed.

Chapter 5: Quantifying the Impacts of ARs on Himalayan Hydrology

In this chapter, the multifaceted impacts of ARs on the regional hydroclimate in the Himalayan Basins−Indus and Ganga, are assessed and quantified from a climatological perspective. The average annual and seasonal contributions of ARs to average and extreme rainfall are quantified for all grids in the affected area, as the number of years/seasons with ARs to the total number of years. Furthermore, the average fractions of winter snowfall over the basins are quantified, and the AR contributions to average precipitation (rainfall, snowfall) in Hindu Kush, Karakoram, Western, Central, and Eastern Himalaya are also shown.

Chapter 2

Literature Review

2.1. Quantitative Definition of AR

Ralph *et al.*, (2018) provided a qualitative definition for ARs in GoM, even though prior studies that identified ARs (Lavers *et al.*, 2012; Guan and Waliser, 2015) and/or tracked them (Leung and Qian, 2009; Sellars, Gao and Sorooshian, 2015) have offered numerous quantitative definitions that are valuable for analysis and modeling. These quantitative definitions emerged from addressing specific research objectives. Ralph *et al.*, (2018) has left the basic criteria open for future studies, which has benefitted the AR research community, and emphasized the significant impact of various criteria, including dataset choice, on AR statistics in climate simulations (Shields *et al.*, 2018; Ralph, Wilson, *et al.*, 2019).

In the 1990s, AR were described as concentrated regions of water vapor flux in the lower troposphere (below 500 hPa), with lengths about five times their widths (Newell *et al.*, 1992). Zhu and Newell, (1998) used global numerical model-based wind and humidity data (12-hourly, 7 pressure levels, for 3 years) from European Centre for Medium-Range Weather Forecast (ECMWF) to compute perturbations to mean flow and separate ARs from the background moisture flux. They found that 95% of the estimated total flux $11 \times 10^8\ kg.s^{-1}$ at 40˚S was transported by only 5 ARs, each transporting $\sim 2.2 \times 10^8\ kg.s^{-1}$, which is 38% more than the Amazon river's flux, despite occupying < 10% of that latitude. Ralph, Neiman and Wick, (2004) used readily available SSM/I measurements to identify ARs in the western USA, and noted regions of IWV > 2 cm, extending over 2,000 km (continuous regions), and less than 1,000 km wide in composite cross-plumes of daily averaged water vapor maps. Observations from dropsonde NOAA P-3 aircraft at multiple cross-sections of AR revealed strong low-altitude winds and water vapor were ahead of a cold front, with 75% of low-level flux (<500 hPa) concentrated within a 565 km stretch (or 440 km for 800-500 hPa) and approximately 4 km altitude (Ralph, Neiman and Wick, 2004). Within IWV > 2 cm region, 75% of the flux is in the lowest 2.25 km altitude and occurs with LLJ winds (Ralph, Neiman and Rotunno, 2005). Ralph *et al.*, (2006) identified LLJs between 100 m to 4 km during AR conditions offshore the California coast using a wind profiler at Bodega Bay. Following Ralph, Neiman and Wick, (2004) method, (Neiman *et al.*, 2008) defined ARs, that intersected west coast USA between $32.5^{\circ}N - 52.5^{\circ}N$ during 1998-2005, as plumes (since IWV lacks the horizontal transport component of ARs they referred them as 'plumes') with IVW > 2 cm, over 2,000 km long, and less than 1,000 km wide, and this method was followed also by Guan et al. (2010) but only for ARs that struck the Californian coast. Neiman et al. (2009) developed a method to detect coastal AR conditions that often led to floods using winds from radars and IWV from GPS-recorded at 1 km altitude (~925 hPa), as SSM/I lack information overland. So far, most analyses mainly relied on visual inspection.

Gorodetskaya *et al.*, (2014) also defined ARs as long (>2000 km), narrow (<1000 km) IWV-enhanced corridors. They refined identification in polar regions by using lower thresholds (~1cm) as they noted that AR-IWV dropped below 2 cm near Antarctica, but remained anomalous compared to the zonal means. At point locations, Ralph et al. (2013) determined AR conditions at the Bodega coast using stations/GPS receiver data for IWV (> 2 cm), upslope IWV flux (> 15 cm $(m.s^{-1})$) (from wind profiler at 1 km MSL) and persistent criteria of 8 consecutive hours. These methods are ideal for regional AR investigations when in-situ observations (high-quality data) are available.

Lavers *et al.*, (2012) introduced an automated algorithm for the reanalysis data to identify ARs by their central axis (maximum IVT regions) based on IVT (300 – 1000 hPa) and percentile-derived thresholds. They defined a detection transect over Britain (spanning between $50° - 60°N\ at\ 4°W$) and a fixed latitudinal threshold (median value of maximum IVT at 1200 UTC distribution corresponding to the 86.1th percentile) for the winter season (October-March) of 1998-2005. The transect was meant to identify ARs directed toward the region and associated with the highest impacts. The AR is identified if the axis is more than 2,000 km, assuming 1000 km wide. The algorithm was used to detect ARs (1979-2012) in western Europe and western USA using ERA-Interim ($0.7° \times 0.7°, 300 - 1000$ hPa), but the threshold was computed for each 5° latitudinal band and for the entire winter season. If the detected axis exceeds roughly 1,500 km it is considered as AR (Lavers and Villarini, 2015b). A temporal criterion of 18 hours was also applied in both studies to focus on events that led to extreme precipitation. Nayak et al. (2016) defined ARs as long and narrow regions with a minimum length of 950 km because the detection latitude was located deep inland of the central USA. They used a fixed threshold of $550\ kg.m^{-1}.s^{-1}$ for one month and followed the Lavers *et al.*, (2012) algorithm for AR identification. Nayak and Villarini (2017) followed the AR criteria by Nayak et al. (2016) but incorporated daily-varying thresholds (percentiles were calculated for each day) in the algorithm to identify ARs.

Guan and Waliser, (2015) adopted the long, narrow features with poleward movement to detect ARs universally, without the need for a detection transect. Their algorithm uses instantaneous IVT, geometric criteria, and monthly-varying 85th percentile thresholds (computed from 6-hourly IVT distribution of 5 months centered on the month of interest) not lower than $100\ kg.m^{-1}.s^{-1}$. AR criteria include length >2,000 km, length/width >2, and mean poleward component > $50\ kg.m^{-1}.s^{-1}$(meridional requirement), consistency, and coherence of IVT within the elongated shape. The algorithm was improved a few years later (Guan, Waliser and Ralph, 2018; Guan and Waliser, 2019) to incorporate tracking ability across time over an AR's life cycle, to identify ARs embedded in high moisture latitudinal bands, and without the consistency requirement (mean $\overrightarrow{IVT}$ direction should be within 45˚ from its overall AR orientation) thus ARs with certain portions being zonal can still be detected. Pan and Lu (2019) described ARs as long and narrow corridors of enhanced moisture transport, with length >2000 km, length/width ratio > 2, and distinct from tropical cyclones (using turning angle series $\propto_{sum} < 360$). These two studies compete whether cyclones should be considered or removed from the identification. Now, as the length criteria for ARs were not formally defined, previous studies have generally considered 2,000 km, though few studies have used smaller limits of 1,400 km (Mundhenk, Barnes and Maloney, 2016) or 1,500 km (Kamae *et al.*, 2017; Thapa, Endreny and Ferguson, 2018), width between 300 – 1,000 km, length/width ratio > 2 or unspecified, which all depend mostly on thresholds used (some used IVT > $500\, kg.m^{-1}.s^{-1}$, or IVT >$250\, kg.m^{-1}.s^{-1}$), etc. Essentially all AR studies rely on objective, quantitative methods to distinguish ARs from the background (O'Brien *et al.*, 2022).

2.2. Identification of ARs

ARs are commonly identified in an Eulerian framework using two variables: (1) IVT or/and (2) IWV. Both variables are subjected to appropriate thresholds and geometric criteria to identify ARs. IVT ($kg.m^{-1}.s^{-1}$) [atmospheric column-integrated horizontal water vapor transported in an atmospheric column] is computed from reanalysis data using specific humidity, zonal and meridional winds at various pressure levels, and integrated from the surface to the upper troposphere (Zhu and Newell, 1998; Lavers and Villarini, 2013b). Contiguous grid cells with IVT exceeding specific thresholds are isolated, and geometric and proximity criteria are applied to determine ARs. There is no universal definition of IVT thresholds, but it is usually set above 2 or 3 standard deviations from the mean value. Some use anomalies based on zonal latitudinal bands (Zhu and Newell, 1998), for example, Gorodetskaya *et al.*, (2014) used temperature-dependent IWV thresholds at different latitudes, significantly above the mean saturated IWV; or on zonal and meridional values (Jiang and Deng, 2011). Thresholds can be absolute like $250\, kg.m^{-1}.s^{-1}$ (Rutz, Steenburgh and Ralph, 2014), or $500\, kg.m^{-1}.s^{-1}$ (Sellars *et al.*, 2013) or they may be derived from statistical distributions like values at the 85th to 95th percentiles of daily IVT distribution, which varies across space and time. In certain cases, it is a combination of spatiotemporally varying percentile values and a fixed lower threshold (Guan and Waliser, 2015). IWV ($kg.m^{-1}$ or cm) [column-integrated water vapor present in the vertical column of air (https://glossary.ametsoc.org/wiki/Precipitable_water)]. Also known as "Total Column Water Vapor" or "Precipitable Water". It can be estimated directly from microwave remote sensing satellites like SSM/I, or polar orbiting Geostationary Operational Environmental Satellite (GOES) (Ralph, Neiman and Wick, 2004; Ralph, Neiman and Rotunno, 2005; Ralph and Dettinger, 2011), or by integrating specific humidity at various pressure levels using reanalysis data (Rutz, Steenburgh and Ralph, 2014). SSM/I provide reliable observations but (a) IWV measurements can degrade during heavy rain, (b) possible surface wind interference during rain, (c) irregular areal and temporal coverage, and (d) generally not available over land. Though GOES offers continuous data, cloud cover can contaminate it (Ralph, Neiman and Wick, 2004).

Continuous and uniform gridded high-resolution IWVs are taken from reanalysis or model-derived data; these are the best proxy for observations. In extra-tropics, ARs are typically identified using IWV with characteristic dimensions (along and across) required to exceed 2 cm, wind speeds above 12.5 m/s in the lowest 2 km, and having an elongated shape, usually between 400–500 km wide and extending thousands of kilometers. Rutz, Steenburgh and Ralph, (2014) identified ARs using IVT (contiguous region above $250\ kg.m^{-1}.s^{-1} \geq 2000$ km) and IWV (contiguous region ≥ 2 cm). The value $250\ kg.m^{-1}.s^{-1}$ was based on largely subjective analysis of various cool-season ARs that penetrated the west coast USA and corresponded well with precipitation patterns. IWV is used as a proxy for IVT as it closely depicts filamentary forms of enhanced IVT in extra-tropics. However, IVT is preferred for AR detection as it is strongly related to orographically induced precipitation (Neiman *et al.*, 2009). The choice between these methods depends on the purpose of the study and location. Relying solely on IWV, may not provide moisture origins or pathway information, especially in tropics where IWV is consistently high.

Previous studies have developed automated AR identification algorithms based on intensity and/or geometry thresholds, capable to detect ARs instantaneously or track their life span. Here, we will focus only on instantaneous AR identification. Most AR algorithms are developed for regional analysis in the USA (Ralph *et al.*, 2006; Lavers and Villarini, 2013a) and Western Europe (Lavers *et al.*, 2012). The outputs from regional algorithms may not consistently agree among themselves or with ARs identified by global algorithms, but they are often in agreement on moderate (IVT $> 500\ kg.m^{-1}.s^{-1}$) or strong (IVT $> 700\ kg.m^{-1}.s^{-1}$) ARs or longer events even when reanalysis data used is different (Ralph, Wilson, *et al.*, 2019; Rutz *et al.*, 2019; Lora, Shields and Rutz, 2020). The Atmospheric River Tracking Method Intercomparison Project or ARTMIP (Ralph, Wilson, *et al.*, 2019) facilitated comparisons and offered valuable insights and recommendations for use (Rutz *et al.*, 2019). In this thesis, three algorithms were used and are briefly described below. Two algorithms require to specify a rectangular boundary over the study area while the other requires a detection transect. The Lavers *et al.*, (2012) algorithm was modified to identify ARs intersecting the Himalaya foothills. A detection transect can be defined in the region of interest to identify the central axis (maximum IVT region) of ARs that intersected it. The placement of the transect is not restrictive and can be defined precisely as desired. This algorithm has been widely for regional AR analysis (west coast USA (Barth et al., 2017), Europe (Lavers and Villarini, 2015a, 2015b) central USA (Lavers &Villarini, 2013a; Nayak et al., 2016; Nayak & Villarini, 2017), South Asia (Thapa, Endreny and Ferguson, 2018; Yang *et al.*, 2018)). However, the algorithm cannot distinguish cyclones from ARs, but as seen the AR dates with the cyclone center located within the study area are removed (Nayak, Villarini and Lavers, 2014). The Guan et al. (2018) “tARget” algorithm globally detects ARs instantaneously using IVT. The rectangular box size can vary but has little effect on AR counts (Park, Son and Kim, 2021). The algorithm first identifies AR shapes and then their axes, but it may identify ARs with minimal regional impacts if their axis does not intersect the concerned region. It uses monthly-varying percentiles (varying between 85th to 95th) with a fixed lower threshold of $100\ kg.m^{-1}.s^{-1}$ to extract ARs. The axis should be over 2,000 km, length/width ratio of 2, poleward component > $50\ kg.m^{-1}.s^{-1}$ to be an AR. This algorithm also detects high IVT grids due to cyclones and considers them AR-related if they occur very close to ARs. Such associations have resulted in the mutual strengthening of their IVT intensities and precipitation (Cordeira, Ralph and Moore, 2013; Zhang, Ralph and Zheng, 2019). The algorithm by Pan and Lu (2019) also uses a rectangular box over the study area and employs two thresholds: a local 85th percentile IVT smoothened with Gaussian Kernel density to extract ARs, and the 80th% quantile IVT over the region and season to exclude weak moisture transport. Within the object's shape, the trajectory (or central axis) is determined and smoothened using weighted centroids. It then checks the length (> 2000 km), length/width ratio (>2), and accumulated turning angle criteria ($\alpha_{sum} < 360°$) of the trajectory. The last criterion filters cyclone but also eliminates ARs that coincide with cyclones. Grid cells impacted by cyclones are only eliminated if they are located far away from ARs. If they are connected to the main body of ARs, the cyclone-related IVT can be considered part of the AR. While many algorithms exclude cyclones entirely as they differ from ARs (Newell and Zhu, 1994; Zhu and Newell, 1994; Zhang, Ralph and Zheng, 2019), some attempt to retain them while removing only specific portions (Guan and Waliser, 2019; Guo *et al.*, 2020).

2.3. AR in South Asia and India and Himalaya

2.3.1. Climatological importance

ARs also contribute significantly to regional mean precipitation beyond their roles in extreme events. In Europe between October – March and western USA during October – January, ARs contribute nearly 30% and $35 - 50\%$ to the total precipitation, respectively (Lavers and Villarini, 2015b). In Western Washington, 96% of the annual peak daily flows (1998-2009) in four watersheds (two each in Olympic and western Cascades) occurred during ARs landfall, with floods characterized by anomalous warming ($4 – 6°C$ in lower-troposphere), strong low-level water vapor fluxes and weak static stability. ARs brought mostly excess rainfall, and elevated the melting level to $\sim$1.9 km in top the 10 events, significantly higher by ~1 km in the four basins (Neiman *et al.*, 2011). During 2004–2010, 45 winter AR events in Sierra Nevada, Western USA, contributed $30 – 40\%$ of the annual snowfall. Interestingly, just two AR events in 2005 and one in 2008 dominated the contributions. Their extreme nature is evidenced in their capacity to deposit four times the daily snowfall of non-AR storms (Guan *et al.*, 2010). On South America's west coast, high AR frequency favors winter-spring north of 43°S, and summer-autumn south of this latitude. The Andes induced precipitation during AR events, contributing over $40 - 60\%$ of annual precipitation (Viale *et al.*, 2018). They also account for $\sim 50\%$ of the

Andes' annual snowfall (Saavedra *et al.*, 2020). Among all storms in the western USA between 1948-2002, $16\text{–}32\%$ were associated with ARs, and on average ARs contributed $31\text{–}52\%$ of annual precipitation in this region (Lamjiri *et al.*, 2018). In certain regions of Antarctica where annual precipitation events are infrequent and brought by rare intrusions of maritime air, ARs (3 days/year) contributed around $25\text{–}35\%$, $35\text{–}45\%$, and $60\text{–}70\%$ of extreme precipitation based on the 90th, 95th, 99th percentiles of 3-hourly precipitation, respectively, i.e., 70% of the 1% of precipitation events come during ARs (Wille *et al.*, 2021). When ARs approach polar regions, they become important to snowfall and melt processes in the cryosphere (Wille *et al.*, 2019), they contribute $10-20\%$ of the total snowfall across East Antarctica (Wille *et al.*, 2021). ARs contribute to annual precipitation in Antarctica (Gorodetskaya *et al.*, 2014), especially in the eastern region (above 3000 m a.s.l.) (Maclennan *et al.*, 2022).

Most ARs are beneficial for water supply. In California, ARs are the primary source of water in the state (Eiras-Barca *et al.*, 2021). They contribute about $20\text{–}50\%$ of the state's precipitation totals, with area-average yearly contributions between $0\text{–}54\%$ (Dettinger *et al.*, 2011). Historically, California's late 2012 – early 2014 drought was exacerbated by the scarcity of large storms, like ARs, which are essential for precipitation and drought relief (Dettinger and Cayan, 2014). Most droughts in the western USA (74% in Washington, Oregon, and 40% of persistent droughts in California) end abruptly when ARs arrive (Dettinger, 2013). In California's Central Valley, unintentional catastrophic levee breaks in river systems and agricultural flood plains are common during ARs (81% of breaks), while the rest have occurred due to snowmelt. However, the breaks (intentional and planned overflow designed), especially in fall/winter promote vegetation establishment through the deposition of sediments during ARs. This intern restores ecosystems and sustains floodplain habitats (Florsheim and Dettinger, 2015). When ARs make landfall along the west coast USA, at the low-latitudes, they influence precipitation amounts in the northern regions and wildfires in the dry interior, Mojave, Central, Northern, Sonoran Basin, Range, Central and Southern California. This highlights the sensitivity (vegetation/wildfires) of dryland ecosystems in the interior southwest to interannual variability in landfalling ARs (Albano, Dettinger and Soulard, 2017).

2.3.2. Extreme cases

ARs are important to the global water cycle and are linked to extreme precipitation and flooding. They are well-studied in mid-latitude regions where they contribute significantly to heavy precipitation. In northern California, ARs were responsible for all seven major floods between October 1997- February 2006, for instance, one AR event produced over 250 mm of rain in two days (16th – 18th February 2004) and ~100-175 mm in nearby areas (Ralph *et al.*, 2006). Mountains enhance the AR's impact. In late December 2005 (29th – 31st), a short-lived AR (peaked IVT of $700\ kg.m^{-1}.s^{-1}$) caused heavy precipitation on the windward slopes of Coastal Range (some locations received over 150 mm in 24-hour) and Sierra Mountains, resulted in major floods, mudslides, and street flooding in San Francisco and Reno (Smith *et al.*, 2010). ARs extend beyond coasts to inland regions. In Montana's Glacier National Park, which is ~800 km away from the coast, ARs have led to record rainfall and flooding (Bernhardt, 2006). During a two-day AR event (1st– 2nd May 2010), Kentucky, western and central Tennessee experienced over 400 mm of rainfall surpassing the 1000-year recurrence interval for 48 hours of rainfall and resulting in a historic flood with damages totaling $2 billion (Hayes, 2011). This very high impact had moisture transported from the tropics (Gulf of Mexico and Caribbean Sea) and increased IWV to 6.5-7.5 cm over central USA (Moore *et al.*, 2012). In western Europe (Britain, France, Norway), 8 of the top 10 annual precipitation maxima happened during ARs, underscoring their role in extreme events (Lavers and Villarini, 2013b). Their effects were observed far inland in Germany and Poland (Lavers and Villarini, 2013b). Precipitation is considered AR-related if the AR occurs "near" the precipitated region (Lavers and Villarini, 2015b; Gimeno *et al.*, 2016). AR-precipitation generated 10 of the highest winter flood peaks (1817-2019) in the Rhine River (one of the biggest rivers in Europe) catchment, amplified by the orographic effects of mountains in France and Germany. The flood peaks were preceded by intense ARs (~average peak $500\ kg.m^{-1}.s^{-1}$) arriving from the subtropical Atlantic with a lag of 2-7 days (Ionita, Nagavciuc and Guan, 2020). On 4th January 1995, an intense AR (966 $kg.m^{-1}.s^{-1}$) over the California coast produced intense precipitation. This led to a week-long stream flow peak above flood stages in the Russian River, resulting in an estimated loss of $1 billion over 3-days. It was one of the most damaging events is 40 years. (Corringham *et al.*, 2019).

In various parts of the world, ARs were uncovered as the main drivers of extreme precipitation. In the Madeira Archipelago, Portuguese islands, 6 out of 7 intense winter events in 2009/2010 were associated with frontal systems and AR. They brought over 125 mm/day for four days in December 2009 and up to 273-387.1 mm on 2nd February 2010, with precipitable amounts reaching 60 kg/m^2, which is two or three times than the mean (1979-2009). The mountain ridge in the central area influenced the AR-precipitation intensity (Couto, Salgado and Costa, 2012). In Portugal, 9 out of 10 extreme precipitation events (above 95th percentile of climatological precipitation) were linked to ARs (Ramos *et al.*, 2018). In northern and southern Morocco, Africa nearly 50% of extremes (above 99th percentile of wet days) come during ARs (Khouakhi *et al.*, 2022). The Moulouya River discharge in Morocco increased by 40% in AR presence (Paltan *et al.*, 2017). ARs transport moisture, energy, and heat to polar regions; for example, ARs amplify the warming of the Artic troposphere (Komatsu *et al.*, 2018), or melt ice and slow the recovery rate of sea ice in Bren-kara Seas and central Artic (Zhang *et al.*, 2023). The conveyance of warm moist air by ARs to Greenland was one of the reasons that melted ice sheets in the 2012 melt episode (Neff *et al.*, 2014). Thus, ARs exert diverse impacts across regions globally beyond conventional boundaries, contingent on their characteristics. New Zealand experienced a high AR frequency year-round (Guan and Waliser, 2015), significantly influencing precipitation patterns. Between 1980-2018, 7 to 10 heaviest precipitation days at 11 stations across New Zealand, and the most costly floods between 1970-2018 were linked to ARs (Reid *et al.*, 2021). In areas with glaciers like the west coastal mountains, ARs have a dual impact, producing extreme snowfall (maximum AR IVT: $800\ kg.m^{-1}.s^{-1}$) or melt events (AR IVT: $1600\ kg.m^{-1}.s^{-1}$) (Little et al. 2019). Melts occurred because ARs increased surface temperature upon landfall and released high rainfall (and/or snowfall) rates that increased available energy fluxes (Little et al. 2019). ARs also transport heat to the poles (meridional latent and sensible heat) contributing to global thermodynamic equilibrium (Shields *et al.*, 2019). On 6th February 2011, an AR made landfall in the Southern Alps, New Zealand, and caused exceptionally warm (2 times the normal) and very moist atmospheric conditions (vapor pressure ~2 times the normal) on the Brewster Glacier. High surface air temperatures (11.5˚C), enhanced atmospheric humidity, and heavy rainfall (133 mm/day) led to continuous melt rates of 3-4 mm w.e. per half-hourly(Kropač *et al.*, 2021).

Landfalling ARs contributed significantly to hydrological extremes globally, often associated with other extremes beyond precipitation (Waliser and Guan, 2017). They trigger $40–75\%$ of wind extremes (above the 98th percentile) along with 40% of the world's coastlines, including the Indian coasts. During AR events, the most probable (probability of ~0.1) wind speeds (2 m/s) get doubled (4 m/s) and in rare events (probability of 0.02) they can surge from ~8 m/s to 12 m/s (Waliser and Guan, 2017). Furthermore, ARs were associated with $15–50\%$ of the annual sea level maxima on the west coast USA, which is driven by high wind speeds (exceeding 15 m/s) that pushed the water towards the coast through the inverse barometric (Khouakhi and Villarini, 2016). In less frequent cases, ARs caused intense sea ice reduction in marginal Antarctic ice zones by bringing warm, humid, and cloudy weather from mid-low latitudes (Liang *et al.*, 2023). They caused pond formation in Antarctica due to surface meltwaters, potentially accelerating sea ice disintegration (Bozkurt *et al.*, 2018). The melting of large Antarctic ice shelves due to rising temperatures is accelerated (partly) by ARs and raises concerns about their stability. ARs from the Atlantic Ocean reached North Africa and impact highland mountains. From March to April between 1981-2017, AR events, on average, brought 1.5 times the precipitation of non-AR events, along with warmer (+1.5°C) conditions compared to the climatology, while very extreme AR events are linked to large-scale sensible heat transport that led to more rain-on-snow precipitation, increased snow-melt and discharge (Bozkurt *et al.*, 2021).

Global AR studies showed that ARs landfall has the highest tendency in extra-tropics (on average 16 AR days/year) than in tropics or poles (8─4 days/year) (Guan and Waliser, 2015; Gimeno *et al.*, 2016), and contributed to global/local water resources, and shape hydrological extremes (Paltan *et al.*, 2017). However, as seen in Paltan et al. (2017) the contribution of ARs to South Asia for extreme streamflow (based on exceedance probability, the flow which exceeded 10% of the time) is less than 20%, including Himalayan-fed basins, possibly related to coarse resolution ($0.75° \times 0.75°$) data used i.e., ERA-Interim (ECMWF Re-analysis Interim) (Cucchi *et al.*, 2020). Recent regional studies in East Asia showed peak AR frequency occurred in summer (June-July), closely related to the strength of the East Asian Summer Monsoon (EASM) (Pan and Lu, 2019; Park, Son and Kim, 2021; Mahto *et al.*, 2023). Zhu and Newell, (1998) suggested that the overall monsoonal water vapor transport depends on small spatial scale anomalous water vapor flux within the monsoon system**.** This season also corresponds to the highest frequency of AR genesis over the Western North Pacific (Guan and Waliser, 2019). Additionally, both ARs and their associated extreme events become more frequent if the preceded winter has an El Niño event (Kamae *et al.*, 2017).

2.3.3. Assessing the frequency and scope of AR impact in India

A few major hydrological events of large economic losses in South Asia were recently linked to the presence of ARs (Nanditha *et al.*, 2023). For example, Lakshmi and Satyanarayana, (2019) observed that heavy precipitation events between 30th November-1st December 2015, and the major flood on 1st December 2015, in Chennai city, southeast India, was caused by ARs (peaked IVT $\sim 800\ kg.m^{-1}.s^{-1}$, extended 3,500 km AR, and lasted over 48 hours), alongside a cyclone. Moisture may have arrived from the Pacific Ocean (between $5° - 15°$N) that sustained the ARs (> 36 hours) as specific moisture sources were not tracked. In February 2013, an intense snowfall event that occurred in northern India and Nepal, accompanied by flash floods in Pakistan, was also linked to the presence of an AR event (Thapa, Endreny and Ferguson, 2018). Lakshmi and Satyanarayana, (2020) studied the frequency of AR landfall on India's coasts between 1980-2015, and classified their associated heavy precipitation events (HPEs) into three rainfall categories (abbreviated as Cat): Cat01(rainfall <64.4 mm/day), Cat02 (64.4 mm/day<rainfall<124.4mm/day) and Cat03 (rainfall >124.4 mm/day. The west coast of India experienced the highest frequency between June-August ($40 - 50\%$ of Cat03 HPEs are linked to ARs, surpassing other categories and seasons), while the east coast has the highest between October-December (17-28% Cat03 HPEs and <4% of Cat01 and Cat02 are linked to ARs). The seasonal preference of ARs in summer on the west coast than in other seasons (e.g., in winter as in mid-latitude) may be a distinctive characteristic of tropical ARs, which is similarly observed by Kamae et al. (2021) for ARs in East Asia/Western Pacific. Yang *et al.*, (2018) identified ARs in Bay of Bengal during 1979-2011 using ERA-Interim reanalysis (6-hourly, $1.5° \times 1.5°$), and found that ARs frequently hit the southern Himalayan foothills, in Bangladesh, Burma, and occasionally India. ARs were most frequent in spring-summer and autumn-winter, with 50% lasting over 18 hours, and led to extreme precipitation (>90th percentile of above 1 mm daily precipitation). The monthly IVT threshold over a $1.5°$ latitudinal band increased from $24°$N to $25.5°$N and decreased to $27°$N. Recently, Mahto et al. (2023) found that$18 - 24\%$ (28% in Western Ghats and Central India) of extreme precipitation (>95th percentile daily rainfall) were related to ARs. Furthermore, 72% of floods in India between 1985-2020, including the top ten largest floods happened during ARs.

The presence of ARs over the Himalayan mountain range is of critical concern to its regional and global influences on the climate. Many AR detection algorithms often miss ARs in these regions or identify only a small fraction (see Figures 2 and 3 in Lora, Shields and Rutz, (2020)). Studies on ARs and their hydrological impacts in Himalaya are limited and scattered. Thapa et al. (2018) examined extreme precipitation during 1979-2013 in western Nepal and found that over 35% of the annual maximum precipitation events happened during ARs. Yang *et al.*, (2018) did not account for ARs originating from western sources, including the Arabian Sea and the Mediterranean Sea, as a result, ARs in the WH and CH were not detected. Liang and Yong (2020a) studied AR impacts on the Asian monsoon regions, including the Indian subcontinent, but their high IVT threshold ($500\ kg.m^{-1}.s^{-1}$) rarely identified ARs in the WH. However, orographic barriers like the Himalaya can be highly vulnerable to AR impacts due to the potential for moisture uplift (Neiman *et al.*, 2013; Hughes *et al.*, 2014; Rutz, Steenburgh and Ralph, 2014). ARs over the Himalaya are important both from a global and regional climatic perspective.

Chapter 3

AR Connection to a Major Flood in Kerala (South India)

After:

Lyngwa, R. V. & Nayak, M. A. (2021). Atmospheric river linked to extreme rainfall events over Kerala in August 2018. Atmospheric Research, 253, 105488, DOI: 10.1016/j.atmosres.2021.105488 (IF: 5.96)

Executive Summary

The previous chapters briefly provided an overview of the evolving knowledge about ARs, highlighting their distinct characteristics, significance to global water resources, and increasing importance in meteorological research. While the qualitative definition of ARs published in 2018 was based on mid-latitude AR studies, the focus should expand beyond mid-latitudes, to lesser-explored regions like India (South Asia), as their presence in various latitudes including the tropics has only recently been revealed. There are qualitative and quantitative approaches to define ARs and will mainly depend on the research purposes and region of interest. The quantitative definition uses threshold (absolute or relative) and specific criteria (≥ 2000 km in length, < 1000km, etc.) on IWV or IVT for AR identification, and for studies attributing extremes to ARs, generally, relative methods are recommended (O'Brien *et al.*, 2022). Upon landfall, ARs induce a wide range of impacts, encompassing extreme precipitation, floods to wind extremes, etc. while also bringing beneficial water supply and contributing to the regional climatology, globally. These ARs' impacts are often influenced by the orientation, duration, intensity of the ARs (events), and the topography of the affected region. As only recently ARs are found over India, could they have been related to high-impact events in this subcontinent? The next chapter presents a critical hydrological event where we aimed to understand the complex atmospheric dynamics behind the August 2018 flood event in Kerala by analyzing the role of ARs. It begins with observation of the pre-and during-flood precipitation patterns over Kerala, followed by identifying ARs using IVT (visually and verified using an AR algorithm) and IWV, studying the characteristics feature to confirm ARs, and comparing them to their climatological values to reveal their extremeness. This chapter also examines the synoptic overview of atmospheric variables to uncover the factors contributing to this extreme weather, like the complex interaction of the polar jet and monsoon trough, depression over the Bay of Bengal, and systems sustaining moisture influx from the Indian Ocean. In addition, the parcels that released precipitation during the flood in Kerala were tracked using HYSPLIT to gain insight into the locations of excess moisture.

Abstract

A multi-day atmospheric river (AR) in the second week of August 2018 was pivotal in causing extreme precipitation over the southwest coast of India that eventually led to record-breaking floods in the state of Kerala. Integrated water vapor transport (IVT) analysis depicted an intense and long-duration CAT 5 AR stretching from the Arabian Sea across South India into the Bay of Bengal. A high-pressure ridge over the eastern Arabian Sea and western India and a trough over the Bay of Bengal forming a subsection of monsoon wave train was observed ahead of the flood event. The monsoon trough was exacerbated by the synchronous effect of a polar westerly jet trough that created an anomalous low-pressure region covering central and eastern India and a quasi-stationary depression over the Bay of Bengal. The system favored a continuous supply of moisture from the Indian Ocean into Kerala. To locate major sources of moisture, the air parcels that rained out to generate extreme precipitation are tracked backward using the Hybrid Single Particle Lagrangian Integrated Trajectory model (HYSPLIT). The backward trajectory analyses reveal that on 13th August more than 60% of the moisture was contributed from the Central-Eastern Indian Ocean, with some intermittent contributions from the Arabian Sea; while on 14th–16th August, about 25–30% was contributed from the Arabian Sea.

3.1. Introduction

The poleward transport of moisture in the lower troposphere has a significant role in driving the global precipitation distribution and maintaining the global water cycle. More than 90% of the total midlatitude poleward transport takes place in narrow corridors known as atmospheric rivers (ARs) (Zhu and Newell, 1998). Intense moisture vapor transport plays an important role in water resources of midlatitude regions and is often associated with extreme hydrometeorological events such as extreme precipitation and severe floods (Ralph *et al.*, 2006; Leung and Qian, 2009; Ralph and Dettinger, 2011; Paltan *et al.*, 2017; Chen *et al.*, 2019). Many studies have identified that the majority of extreme precipitation events in mid-latitude regions were associated with ARs. ARs are defined as long, narrow, and transient systems of strong horizontal water vapor transport from the tropics to extra-tropics. They are usually associated with low-level jet streams ahead of cold fronts of extratropical cyclones (Ralph, Neiman and Wick, 2004; Bao *et al.*, 2006; Zhang, Ralph and Zheng, 2019). Moisture-laden winds in ARs can deposit an enormous amount of precipitation over mountainous coastal regions where they make landfall or by an ascent in the warm conveyor (Ralph, Neiman and Rotunno, 2005; Ralph *et al.*, 2006; Neiman *et al.*, 2008; Dettinger *et al.*, 2011; Konrad and Dettinger, 2017). ARs also play a significant role in inland precipitation climatology by contributing to heavy precipitation and consequent flooding across the southwestern and western USA, where they penetrate further over lesser complex terrain (Neiman *et al.*, 2013; Rutz, Steenburgh and Ralph, 2014). Moisture is fed into an AR from various sources, either via local convergence and evaporation along its track (Bao *et al.*, 2006; Dacre *et al.*, 2015) or in some cases from advective sources like tropics/subtropics (Sodemann and Stohl, 2013). ARs have received substantial attention in the mid-latitude regions as they are recognized among the key drivers of extreme precipitation episodes in the USA (Ralph *et al.*, 2006; Leung and Qian, 2009; Lavers and Villarini, 2013a; Rutz, Steenburgh and Ralph, 2014; Nayak, Villarini and Bradley, 2016), Europe (Lavers *et al.*, 2012; Lavers and Villarini, 2013b), South Africa (Blamey *et al.*, 2018; Viale *et al.*, 2018; Ramos *et al.*, 2019), and Antarctica (Gorodetskaya *et al.*, 2014), and key mechanisms of the associated damages (Leung and Qian, 2009; Dettinger *et al.*, 2011; Ralph and Dettinger, 2012; Barth *et al.*, 2017; Konrad and Dettinger, 2017; Corringham *et al.*, 2019). The duration of ARs, ranging from a single time step to multiple days, is directly proportional to the extent of their hydrological impacts. Extreme storms and floods are generated in ARs that last for an average duration of 20 hours, and more persistent ARs are capable of generating streamflow that is significantly higher than the average (Ralph *et al.*, 2013). In addition to hydrologic extremes, ARs are often associated with damaging winds (Beaufort Wind Scale of $\sim 8-12$ (Waliser and Guan, 2017)) and increased chances of storm surges (Khouakhi and Villarini, 2016). In contrast to intense ARs (in terms of vapor transport), less-intense long-duration ARs are shown to have supplied beneficial moisture for water supply and alleviated water scarcity in many instances (Guan *et al.*, 2010; Dettinger *et al.*, 2011; Dettinger and Cayan, 2014; Florsheim and Dettinger, 2015; Albano, Dettinger and Soulard, 2017).

Guan and Waliser, (2015) conducted a global-scale AR study and detected a significant number of ARs making landfall over different regions of the globe. They also highlighted the lack of investigations in many regions such as northeastern North America, Central America/Caribbean, South/East Asia, Australia, New Zealand, Caribbean, northwestern, and southwestern Africa. Although the presence of ARs over the Asian monsoon regions seems atypical and, perhaps objectionable to some, the important study by Guan and Waliser, (2015) detected a significant number of ARs over the region, see their Figures. 3 and 8. Following Guan and Waliser (2015), Pan and Lu (2019) identified ARs during the summer Asian monsoon (June–August) that triggered extreme precipitation and consequent flooding in the Yangtze River Basin in China using a new modified AR-identification algorithm. With a 6-hourly evolution, they showed that many ARs travel from the Arabian Sea, via Bay of Bengal, South China Sea, and Southeast Asia and terminate in the Pacific Ocean. Though it is now known that landfall frequency of ARs over Indian coastal regions is significant (Guan and Waliser, 2015; Paltan *et al.*, 2017; Sellars *et al.*, 2017; Waliser and Guan, 2017; Pan and Lu, 2019), there are major gaps in investigating the impact of ARs on the regional hydrology. The concept of ARs causing extreme events over the Indian subcontinent has not been appreciated and explored to its merits, considering the ARs and extreme precipitation nexus exist closely as mentioned earlier. Over the tropical belts, a few recent studies have investigated the role of ARs in driving extreme rainfall outbursts and consequently causing catastrophic floods. Lakshmi and Satyanarayana, (2019) found that during the December 2015 floods in Chennai, India, heavy precipitation events were caused by persistent AR of duration greater than 18 hours. Yang *et al.*, (2018) identified 149 ARs over the Bay of Bengal in the period 1979 to 2011; most of them occurred in the monsoon period of May and October and lasted for more than 18 hours. They also observed that a quarter of the ARs identified were associated with tropical cyclones, which indicates their influence on the longitudinal transport of water vapor. Thapa et al. (2018) examined the seasonal climatology of ARs (1979–2013) in the Himalayan region of Nepal and found that the highest frequency occurs in September–November followed by December–February, June–August, and March–May. They also noted major contributions (78%) of ARs to daily precipitation in the October–May season. Over East Asia and North Western Pacific, Kamae et al. (2017) observed the highest frequency of ARs in boreal summer (June–July). They found that ARs in these regions are associated with the variability of the East Asian Summer Monsoon and modulated by Pacific and Indian Ocean sea surface temperature anomalies, with strong influence by the El Niño-Southern Oscillation (ENSO) in winter.

The geographical location of India, surrounded by oceans on all three sides in the south constitutes a land–ocean thermal contrast accompanied by the large pressure gradient between the Tibetan plateau and Mascarena, which risks socioeconomic assets to frequent hydrometeorological extremes. The Kerala flood of 2018 caused more than 500 deaths and inundated 775 townships (NDMA, 2018; Rajan et al., 2018), many of which remained submerged for more than two weeks (Kurian et al., 2018). The flood affected millions of people residing in the region and resulted in approximately 3.7 billion dollars in damage to property and agriculture (News Asia, 2018). As per Central Water Commission of India (CWC) reports, the state received 2394.4 mm of rainfall from 1st June to 19th August 2018 in comparison to the expected 1649.5 mm, and the most excess rains happened in the first three weeks of August when the state received roughly three times the normal rainfall of that period. There was extreme flooding in thirteen of the fourteen districts of Kerala state, when a severe spell of rainfall occurred from August 13th–17th August. The flood of August 2018 was the second most disastrous flood term between 1951–2015 precipitation data, Mishra and Shah (2018) noted that 1-day maximum precipitation received on 15th August 2018 exceeded the 95th percentile by about 30 mm. Such precipitation extremes are very rare and have seldom been observed in the last six decades (1951–2017) in Kerala. Generally, extreme flood events in India are attributed to extreme precipitation and/or failure of reservoir operations, but further investigations into the causes of those extreme precipitations have not been extended. The hydroclimatic aspects of this flood and the hydrological impacts have not been studied. Investigations into the atmospheric dynamics during those events are important to provide insightful or new information as to what initiated them.

In this study, we aim to understand the major meteorological features of the August 2018 flood event, with focus on:

(1) the identification of ARs over the region during this event,

(2) the dynamical features of the atmosphere that may have orchestrated the moisture flow into the region, and

(3) identifying oceanic moisture sources of the extreme rainouts and estimating the percentage contribution made from each source to the rainfall event.

This paper is organized as follows.

In Section 3.2, we present the data and explain the methods used for AR identification and moisture tracking. The results from our analyses are given in Section 3.3, and major conclusions are presented in Section 3.4.

3.2. Data and methodology

The daily rainfall data from rain gauge measurements and estimates based on remote sensing satellites are used in this study to understand the spatial and temporal distribution of rainfall over Kerala during the flood event of August 2018. The rainfall observations for August 2018 collected by the India Meteorological Department (IMD), Pune (www.imd.gov.in) are obtained from official reports published by CWC, India. The details about these station data used in our study are presented in the supplementary material (SM; S3.1 and Table S3.1). The satellite data from Global Precipitation Measurement Integrated Multi-Satellite Retrievals (GPM IMERG), which is the latest version of available global satellite precipitation data, were downloaded at a daily time step with a horizontal resolution of $0.1° \times 0.1°$. Sharifi et al. (2016) in their comparison of GPM-IMERG, TRMM-3B42, and ERA-Interim, with ground station data in Iran found that at the daily scale, GPM-IMERG performs better than other products, especially for precipitation exceeding 15 mm/day intensity, and underestimates the precipitation slightly at some places at the monthly and seasonal scale. They also found that GPM-IMERG showed a better correlation with ground data at a daily scale in comparison to other products. However, the quality of any predicted variable depends greatly on the model's ability to simulate it and have a good agreement with the observations, which, in the case of precipitation estimates from remote sensing, is location-dependent (Stohl and James, 2004; Stein *et al.*, 2015). However, as will be shown in the results, GPM-IMERG data matches qualitatively well with ground-based observations taken during the Kerala flood event. As one of our major objectives is to identify ARs during the event, different approaches from previous studies will be considered herein. Neiman *et al.*, (2008) and Ralph, Neiman and Wick, (2004); Ralph *et al.*, (2017) have implemented integrated water vapor (IWV, also known as total precipitable water), estimated mostly from satellite images of SSM/I and SSMIS (Special Sensor Microwave Imager/Sounder), to identify ARs by applying the AR criteria of length ≥ 2000 km, width ≤ 1000 km, and IWV > 2 cm. However, IWV does not include wind velocity—the transport component of ARs; this limits IWV to clearly define AR structures. In other studies (Zhu and Newell, 1998; Lavers *et al.*, 2012; Ralph *et al.*, 2017), an alternative method to identify ARs is to compute IVT from atmospheric reanalysis products. IVT is calculated at each location by taking the vertical summation of layer-averaged specific humidity, u-wind, and v-wind (details are given below) to compute the total zonal and meridional components of water vapor transport. Then a threshold value, usually taken as the 85th percentile of daily IVT distribution, is estimated at each location to characterize the presence of strong moisture transport. An AR is then identified as a contiguous region of IVT exceeding the prespecified threshold, having length ≥ 2000 km and width ≤ 1000 km, and persisting for longer than 18 hours (Lavers and Villarini, 2013b; Nayak, Villarini and Lavers, 2014; Guan and Waliser, 2015). In this study, the Pan and Lu (2019) algorithm is also used to identify ARs during the event. Furthermore, IVT is used as the main indicator as it is shown to produce more reliable results in AR identification and precipitation impact assessment than IWV (Neiman *et al.*, 2002; Nayak, Villarini and Lavers, 2014; Rutz, Steenburgh and Ralph, 2014). Numerically, IVT is computed using wind fields of zonal *u* (m/s) and meridional *v* (m/s) wind speeds and specific humidity q in kg/kg at different pressure levels starting from the surface $\sim 1000\ hPa$ to $300\ hPa$ using the following equation

$$IVT = \sqrt{\left(\frac{1}{g}\int_{1000}^{300} qudp\right)^2 + \left(\frac{1}{g}\int_{1000}^{300} qvdp\right)^2} \tag{1}$$

where, g is the acceleration due to gravity $\sim 9.81\ m/s^2$ and dp is the pressure difference between two adjacent pressure levels (in Pa). The layered average specific humidity and horizontal winds between two pressure levels are integrated below $300\ hPa$ as water vapor is mostly concentrated in the lower troposphere, ignoring the levels above $300\ hPa$ will have negligible impact on the output (Zhou, 2005; Payne and Magnusdottir, 2014) Atmospheric reanalysis datasets from global reanalysis product by ECMWF called ERA5 (fifth generation ECMWF *Re*-Analysis) (Hersbach, Bell, Berrisford, Hirahara, Horányi, Muñoz-Sabater, Nicolas, Peubey, Radu, Schepers, Simmons, C. Soci, *et al.*, 2020), are used to compute daily IVT for all the years from 1979-2018 and in identifying major atmospheric and meteorological features during the flood event. ERA5, with its multiple improvements in simulating the Earth's processes, uses the latest assimilation methods and the latest version of Earth system model capable of providing better estimates of atmospheric variables as compared to ERA-Interim (Albergel *et al.*, 2018; Hersbach *et al.*, 2019). It has a spatial resolution of $0.25° \times 0.25°$ and is available at 137 pressure levels at an hourly temporal resolution. Hoffmann et al. (2019) compared ERA5 and ERA-Interim in their analysis of the trajectories of the free troposphere and stratosphere at a global scale, and found that ERA5 provides better representations of the mesoscale and synoptic scale features of the atmosphere. These highlight substantial improvements in spatial and temporal estimates using ERA5. Thus, in this study, the model's spatial and temporal resolution are tuned to obtain a better representation of atmospheric features for the analysis of the Kerala event. The meteorological variables from ERA5 adopted herein include IWV, wind speed (u, v, and w), specific humidity, geopotential height, mean-sea level pressure (MSLP), and temperature for 1979–2018. The IWV data in ERA5 is computed by taking the vertical integral from the lowest level ($1000\ hPa$) to the nominal top level of the atmosphere expressing the total amount of water with the exclusion of precipitation.

The rainfall in Kerala can originate from local evaporation, moisture transported by winds from distant sources, and, in certain instances, the moisture already present in the atmosphere (not all moisture can be drained from air parcels) over the region. Over longer periods, it is found that the major contribution to rainfall is effectively from the first two sources (local evaporation and advection), and minute contributions from the third source (Brubaker, Entekhabi and Eagleson, 1993; Trenberth, 1999). To effectively determine the source–sink relationship of water, a Lagrangian moisture source diagnostic is adopted, by tracking the path of air parcels that reached the target region. This leads us to two objectives: first, to identify the sources of moisture input into Kerala during the flood event, and second, to estimate the percentage contribution of each source to the rainfall event. For the first objective, a global particle trajectory model HYSPLIT of the National Oceanic and Atmospheric Administration's (NOAA), Air Resources Laboratory (ARL) named Real-Time Environmental Applications and Display (READY, http://www.ready.noaa.gov) is used herein for tracing the moisture source (Draxler and Hess, 1998; Stein *et al.*, 2015; Rolph, Stein and Stunder, 2017). The inputs for this model include meteorological datasets such as u and v wind components, vertical velocity, temperature, pressure, and ground-level winds ($\leq 10\ m$). It is to be noted that an online model is used with the available datasets from the National Centers for Environmental Prediction's (NCEP), Global Data Assimilation System 1 (GDAS1) model with horizontal resolutions of $1.0° \times 1.0°$ (~111 km). In the HYSPLIT model, the backward trajectories for parcels at multiple vertical levels: 500 m AGL (m AGL: meters above ground level) (~943 hPa), 750 m AGL (~910 hPa), 1000 m AGL (880 hPa), 3000 m AGL (~660 hPa), and 6000 m AGL (~430 hPa) are computed until the mixing ratio is very low (i.e., $<$ 0.2 g/kg) or the endpoint of the trajectory is reached. Throughout their trajectories, the air parcels may have multiple moisture uptakes and losses. The moisture uptake/gain within the boundary layer is due to evaporation and the losses are due to precipitation. When moisture uptake by an air parcel happens within the boundary layer (mixing boundary layer, as estimated by HYSPLIT) or close to its upper boundary, the location where the uptake takes place is identified as a moisture source (Sodemann, Schwierz and Wernli, 2008a), as it is assumed that turbulent fluxes exchange moisture between the air parcel and the surrounding boundary layer air. When the increase of moisture occurs in a parcel well above the boundary layer, its sources cannot be identified with certainty, since the uptake could result from a mixture of oceanic as well as terrestrial moisture traveling from any other locations, which cannot be ascertained. In our analysis, we have selected only air parcels that precipitated at the target region, defined by a decrease in the average mixing ratio of the selected parcels at each released location (time 't' = 0) such that, $\Delta q_t - \Delta q_{t-\Delta t} = -\Delta q$, and predominantly traveled within the boundary layer (see Figure 3.9(a)). For the second objective, i.e., to compute the fractional contributions from different sources to Kerala rainfall, the following equation is used following the method described by Sodemann, Schwierz and Wernli, (2008).

$$f_{m,t} = \frac{\Delta q_{m,t}}{q_n} \qquad (2)$$

where, q_n is the mixing ratio of the air parcel at the time of extreme rainfall (t = 0), $\Delta q_{m,t}$ represents the moisture increase (i.e., gained at t; which is found by taking the moisture difference between time 't' and the time prior to that 't – $24\,hr$') at any location in time t steps before the rainfall event. The value $\Delta q_{m,t}$ is discounted every time there is a loss of moisture (rain) in the trajectory from time $t = -t \ to \ t = 0$ (target region) and the updated value is used to get the actual fraction. Hence, $f_{m.t}$ is the fractional contribution of time $-t$ to rainfall at $t = 0$. Since the location of the parcel at time *t* is known using HYSPLIT, we know the sources of positive $f_{m,t} \times 100$ percent contributions. In our analysis, we have computed the attributed fraction of each location to the rainout. We performed computations for multiple parcels and at six-hourly time steps, which are later aggregated to single daily values.

3.3. Results and discussion

3.3.1. Rainfall distribution.

The rainfall observations from IMD rain gauges showed that many stations distributed throughout Kerala recorded high rainfalls over multiple successive days, with the highest one-day total rainfall of 400 mm recorded in Nilambur on 9th August alone and the second highest of 350 mm recorded in Peermmade on 16th August (Figure 3.1). At the end of the first week of August from 8th–10th (Figure 3.1a-b), many stations had received rainfall of magnitude more than 70 mm per day. These observations indicated that the antecedent rainfall had already added moisture to the soil layers before the next storm. From 14th to 19th August another severe storm set in and heavy rainfalls were recorded almost throughout Kerala (Figure 3.1d-f), which induced extreme flood levels at several stream gauges throughout the region. Figure 3.2 shows the rainfall generated from GPM-IMERG. On 14th and 15th August, rainfall above 50 mm covered almost entirely the state of Kerala with higher rainfall concentrated in the northern part on 14th August and the south-eastern part on the next day. The daily gauge data were not uniformly available throughout Kerala during the event and were missing on many days of August. Notwithstanding the limited availability, point observations, whenever available, were valuable in validating the GPM-IMERG estimates. Hence, we leveraged both the point measurements and GPM-IMERG data to locate the regions of heavy rainfall for tracking their moisture sources (shown in Figures 3.9 and 3.10). The spatial distribution of rainfall from GPM and IMD are seen to match reasonably well, though it can be observed that at many locations GPM slightly underestimated the extreme rainfall during the Kerala floods; for example, in Figure 3.2b the highest rainfall estimates from GPM were in the range 230 mm to 260 mm, whereas IMD highest rainfall observations were in the range 260 mm to 290 mm (Figure 3.1e). Although this is a single event, it highlights that GPM estimates should be carefully evaluated for hydrological impact assessments, especially in the case of extreme precipitation events.

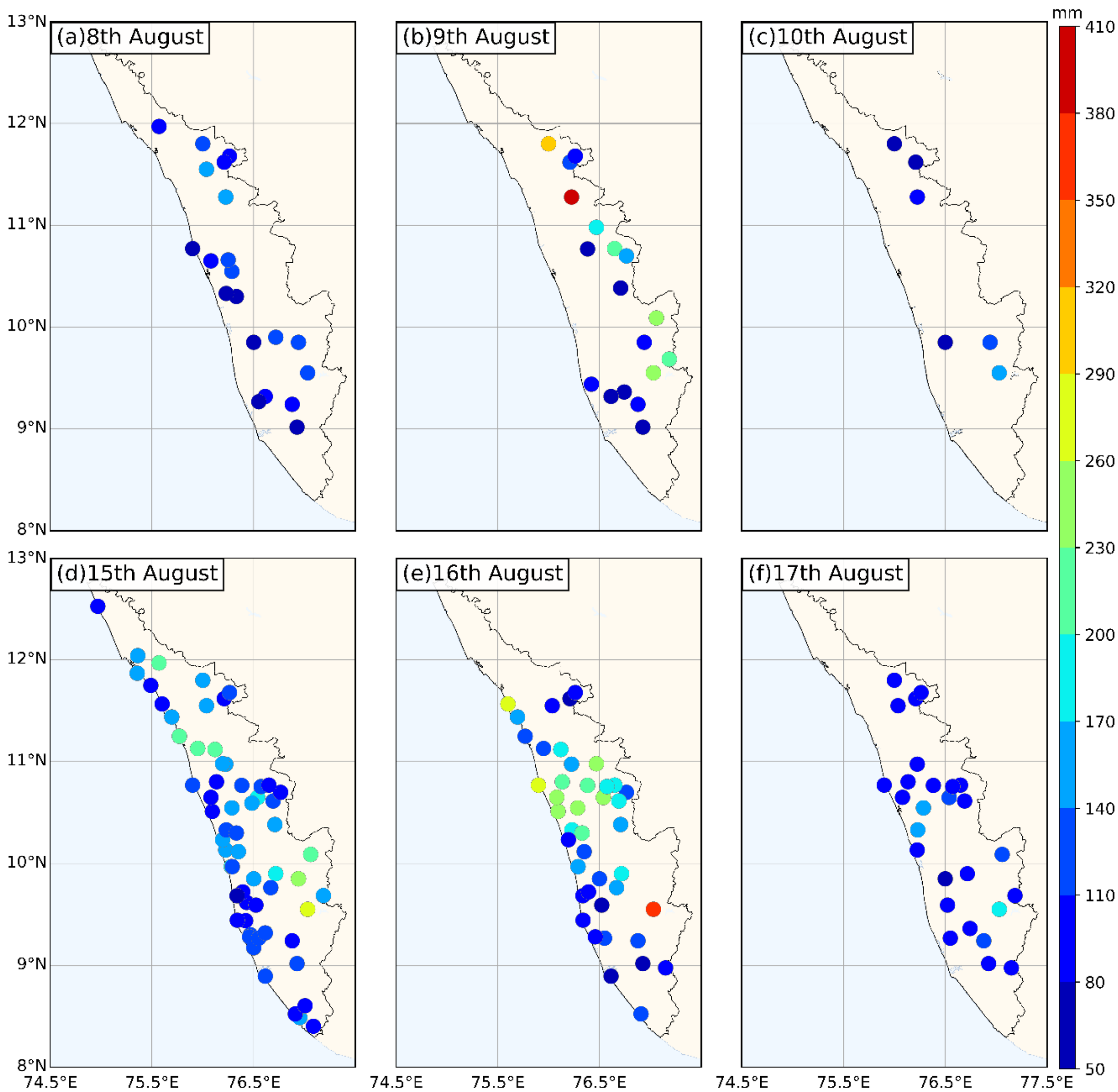

Figure 3.1: *Daily rainfall (mm) at multiple rain gauge stations of IMD (a) 8th (b) 9th (c) 10th (d) 15th (e) 16th (f) 17th, August 2018 as available from IMD. Rainfall for a day is from 08:30 AM Indian Standard Time (IST) of the previous day to 08:30 AM IST of the day.*

3.3.2. Atmospheric rivers

The IVT threshold to identify ARs varies depending on location and season; for example, Lavers *et al.*, (2012) used $520\text{–}630\ kg.m^{-1}.s^{-1}$ as the criteria for the AR identification based on long-term data (1980–2010) over the British Isles. Rutz, Steenburgh and Ralph, (2014) in their study over the western USA set a threshold value of $250\ kg.m^{-1}.s^{-1}$ based on daily values, and Nayak et al. (2016) used $550\ kg.m^{-1}.s^{-1}$for AR identification over the central USA for the floods of spring 2013. Over the Indian subcontinent, the average IVT during monsoon season is in the range of $100\ kg.m^{-1}.s^{-1}$ over northern India to $600\ kg.m^{-1}.s^{-1}$ in the tropical Indian Ocean near the coasts (figure not shown).

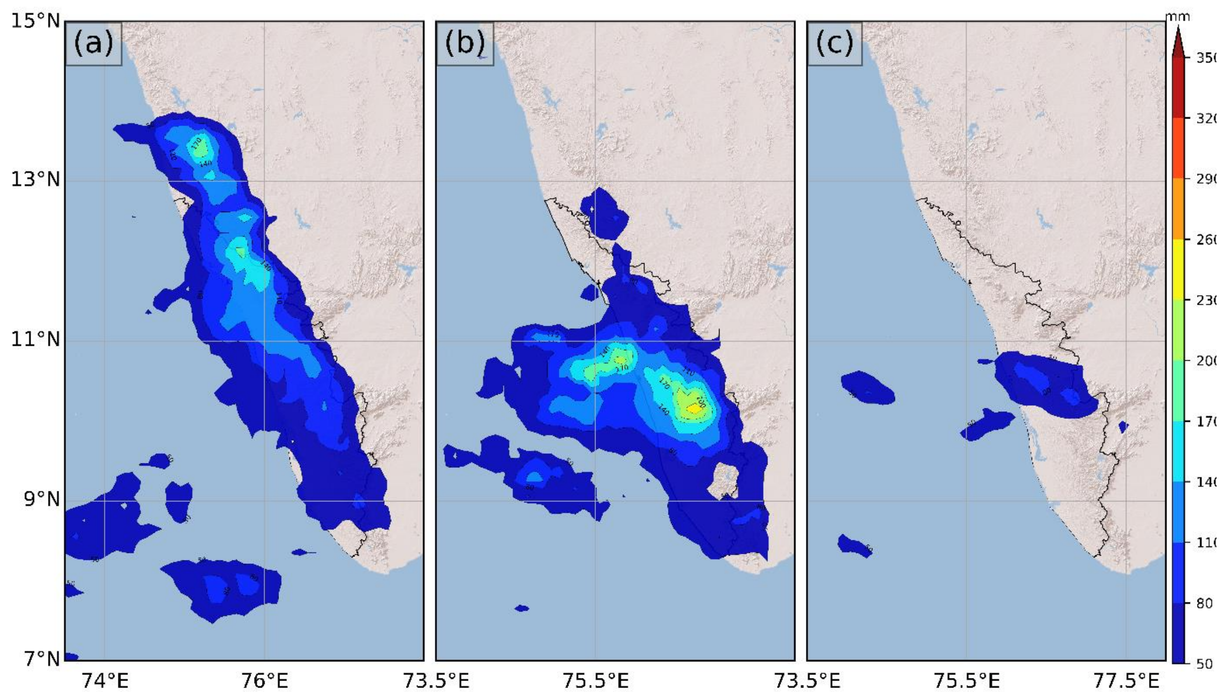

Figure 3.2: *Rainfall (mm) estimated from GPM-IMERG datasets for (a) 14th (b) 15th, and (c) 16th August 2018. GPM rainfall sum for a day is taken from 00:00:00 Z to 23:59:59.99 Z on that day (Z: Zulu or UTC: Universal Time Coordinated)). Hence, the 15th August rainfall from IMD can be compared with 14th August of GPM.*

An illustrative map of IVT during the Kerala flood of 2018 is shown in Figure 3.3 An elongated and narrow structure of intense IVT having a magnitude as high as $1000\ kg.m^{-1}.s^{-1}$ at the core (southeast India) along the center-line of its length (stretching a length > $4000\ km$, and width ≈$1500\ km$) with a west-east direction (Zhu and Newell, 1998; Lavers and Villarini, 2013a; Nayak, Villarini and Lavers, 2014). This structure closely fits the description of AR characteristics (Ralph *et al.*, 2018) and indicates the presence of an intense AR during the Kerala 2018 flood. The change in AR strength as it crosses over south India and Thailand reflects the depletion of moisture in AR due to the high mountain barriers in the Western Ghats and northern parts of Thailand during orographic rainfall. The gradient of IVT (900 $kg.m^{-1}.s^{-1}$ to 850 $kg.m^{-1}.s^{-1}$ (15˚N, 75˚E); 700 $kg.m^{-1}.s^{-1}$ to 550 $kg.m^{-1}.s^{-1}$ or drop as low as 250 $kg.m^{-1}.s^{-1}$ in Kerala) on crossing the Western Ghats shows that slightly less intense AR (although 850 $kg.m^{-1}.s^{-1}$ is still high) penetrates inland and further crosses over into Bay of Bengal. In Figure 3.3, moisture within the AR was fed from the Arabian Sea, the Bay of Bengal, and the South China Sea, and depletes on crossing through complex terrain in south India and Thailand.

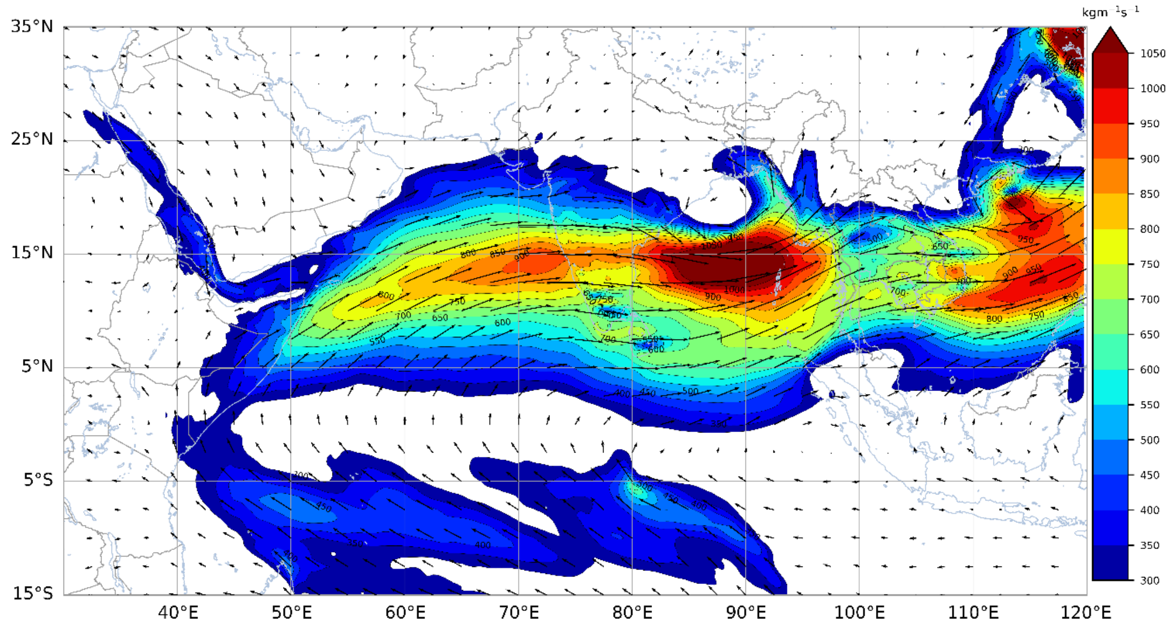

Figure 3.3: *Vertically integrated water vapor transport (IVT; $kg.m^{-1}.s^{-1}$) shaded (magnitude shown in the color bar) with IVT wind fields corresponding to the magnitude of IVT; using ERA5 datasets for 13th August 2018.*

The severity of the AR in a climatological context is shown in Figure 3.4. Figure 3.4a-b shows the climatology of IVT and IWV for 13th August. The climatology is obtained by taking the mean value of all 13th August days from 1979 to 2017, and the 13th August value for a year is taken as the 7-day moving average from 10th–16th August of that year centered at 13th August. This is done to smooth out any short-term fluctuations in the data (i.e., cancel noises, if any) at each grid point. Figure 3.4c-d shows the IVT and IWV for 13th August 2018. Both IWV and IVT showed intense moisture and its transport on 13th August 2018 in this region as compared to their climatology; however, it is observed that IVT provides a better depiction of AR than IWV. It can also be noted that the AR orientation of AR-landfall with topography has not been previously investigated over India, it is shown to be a critical factor in terms of precipitation and flooding impacts over the West Coast of USA (Neiman *et al.*, 2011, 2013; Hughes *et al.*, 2014). A large fraction of moisture in ARs transported by strong low-level winds is forced upslope of the mountains and, upon orthogonal orientation, the ascent results in higher rainfall and runoff. A similar observation was made by Neiman *et al.*,

(2011) for the top 10 annual peak discharges on Green and Queets Rivers that corresponded to the zonal orientation of landfalling ARs. However, in this study, an orthogonal orientation of the AR to the Western Ghats is observed, which closely relates to heavy rainfalls over Kerala during the event.

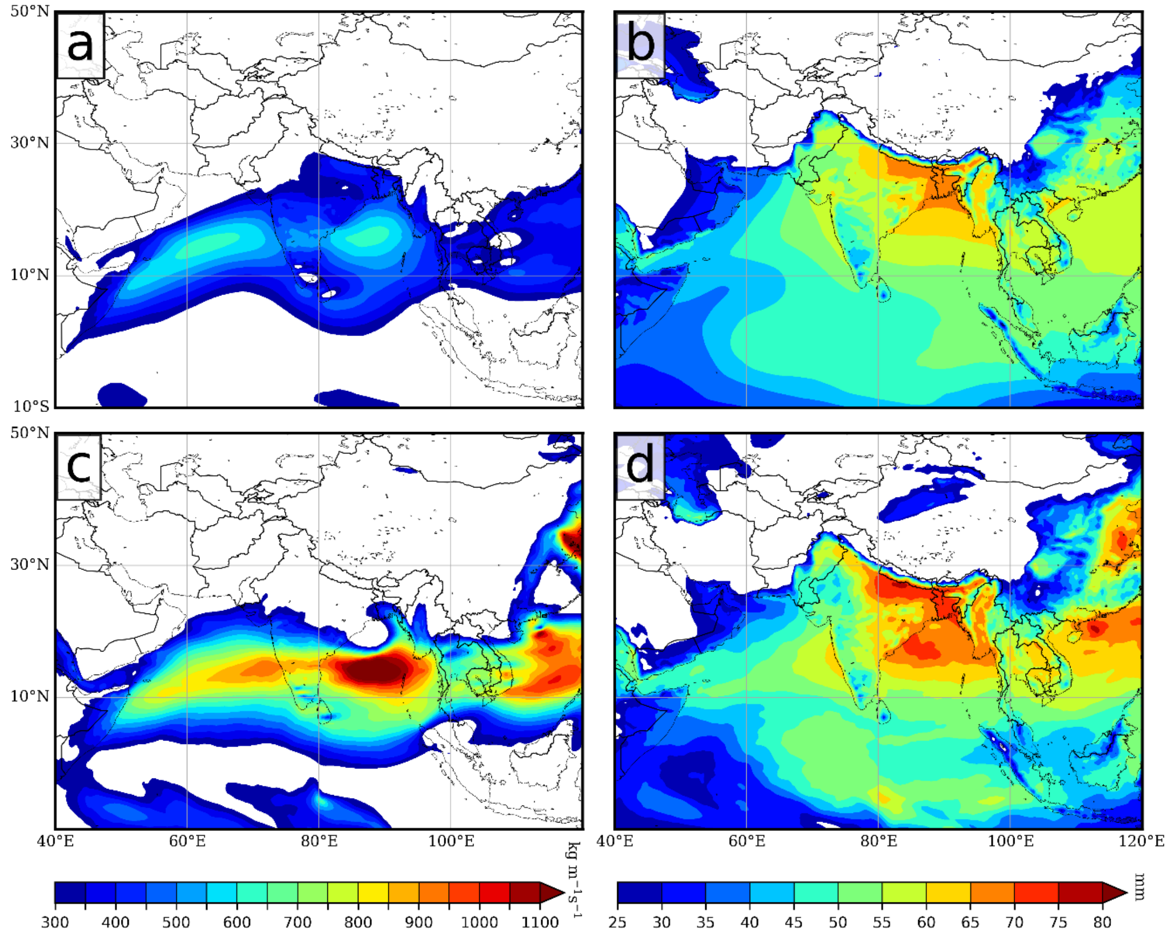

Figure 3.4: *(a) IVT ($kg.m^{-1}.s^{-1}$; shaded) climatology and (b) IVW (mm; shaded) climatology taken for 39 years (1979–2017) for 13th August 2018 (c) IVT and (d) IWV average for four timestamps (00UTC, 06UTC, 12UTC, and 18UTC) for 13th August 2018.*

To gain further insight, the algorithm by Pan and Lu (2019) is implemented to objectively identify the AR during the event. The 85th percentile IVT threshold is computed for each grid, and those values that exceed this threshold are retained for detection of the AR pathway (i.e., contiguous grid cells exceeding the threshold). The AR trajectories are computed from the AR pathway to deduce their geometric features (see Pan and Lu (2019) for more technical details on the algorithm). An example for 13th August 2018 is shown in Figure S3.2 of SM, which depicts a similar structure of the AR as identified visually in Figure 3.3. The area of the AR is 10,807,886.25 km^2 with a trajectory length of 4953.43 km, based on its 30% nearest neighbors (or NN30), a width of 2182 km, and a length/width ratio of 2.3 with a total turning angle of 0.71˚. The details of the results are presented in SM in Table S3.1 where we have shown the geometric features estimated from different nearest neighbor choices. It is to be noted that the trajectories computed by this method do not capture the center of the AR, which would ideally link the grids of maximum IVT at each cross- section within the isolated AR pathway. This is due to the nearest neighbor method being implemented here. The AR trajectory captured here is in close agreement with the ones identified by Pan and Lu (2019) (See their Figure 8b-c). This further confirms the presence of an AR over India that led to the extreme precipitation event. The AR persisted over $96\ hr$ (12th –15th August 2018) (Fig. S2) and is categorized as the most severe CAT 5 category based on the criteria given by Ralph, Rutz, *et al.*, (2019). Recently, Liang and Yong (2020) used a higher threshold value of $500\ kg.m^{-1}.s^{-1}$ for India and East Asia to distinguish ARs from the large-scale monsoonal transport of intense moisture. Using this threshold, the AR observed here would be classified as intense.

Detailed analysis of IVT at 6-hourly time steps showed that on 12th August 2018 at 0 UTC high IVT was observed in the central Bay of Bengal and eastern Arabian Sea. This intensification increases in the Bay of Bengal (> $1000\ kg.m^{-1}.s^{-1}$) with a slight increase in the central and eastern Arabian Sea (>$900\ kg.m^{-1}.s^{-1}$) at 6 UTC. At 12 and 18 UTC, IVT is above $1000\ kg.m^{-1}.s^{-1}$ at both these locations with a well-formed elongated shape of maximum IVT. On 13th August 2018, this increase in IVT strength was observed in the western Arabian Sea at 0 UTC and 6 UTC, which rapidly evolved as the tail end of the AR. The strengthening continued on 13th August at 12 UTC and 18 UTC to 14th August 0 UTC to 6 UTC. From 14th August 12 UTC to 15th August 18 UTC the leading edge of the AR shifted northwestward (west Bengal, Bihar, and Jharkhand) associated with a cyclone development (Figure S3.3). This weak cyclone feature helped increase the moisture in the atmosphere in the Bay of Bengal and fueled the AR.

3.3.3. Synoptic characteristics

At the lower pressure level (850 hPa), there is a weak monsoon trough over east India and a relatively strong ridge over northwestern India on 10th August (Figure 3.5a). The trough over east India and the Bay of Bengal intensified over the next three days, as can be inferred from the development of the low-pressure system in the Bay of Bengal and increased gradient in the height contours (Figure 3.5b-d). Simultaneously, the tropical cyclone Bebinca formed in the South China Sea on 9th August and continued through the next week, seemingly emerging from the second trough of the quasi-stationary monsoon wave train. In this figure, we also note that intense surface heating preceding the flood event caused a persistent thermal low over much of southwest China, northwest India adjoining regions of Pakistan, Afghanistan, Iran, Arabia, Persian Gulf, Egypt, Sudan, etc. A clear demarcation of warm and cold air masses is visible in the mid-level atmospheric regime ($500\ hPa$, Figure S3.4).

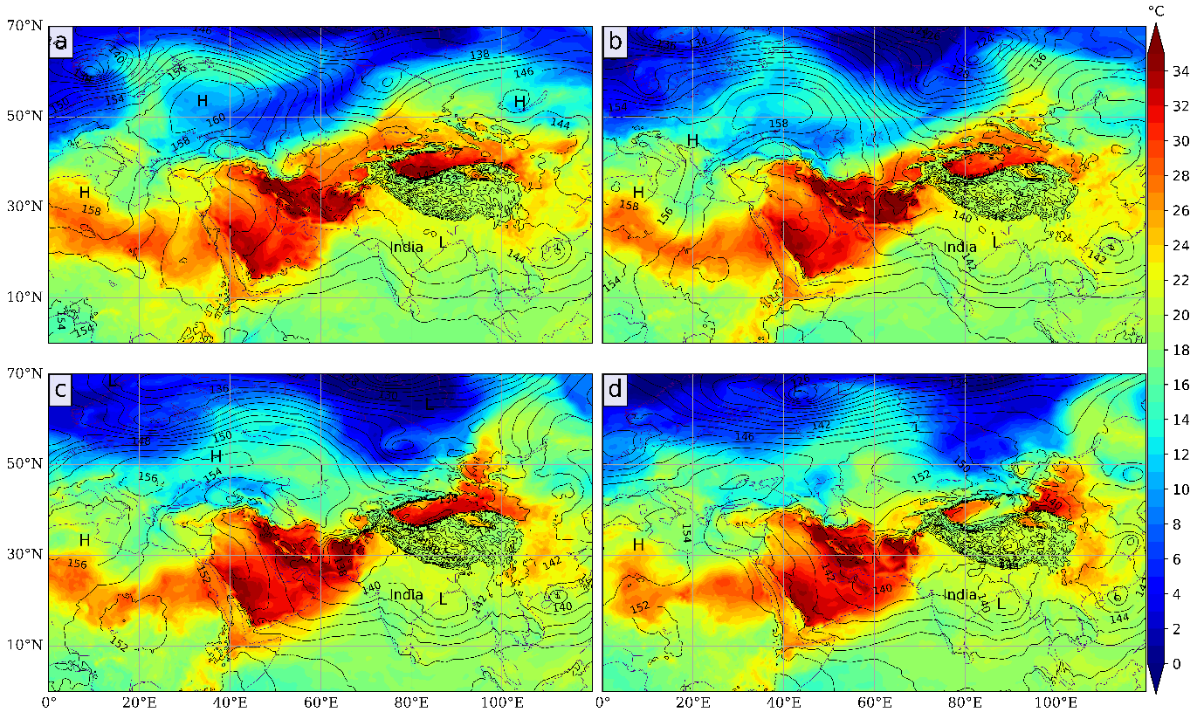

Figure 3.5: *Geopotential heights and temperature at 850 hPa (contour lines represent geopotential heights in the dam, at an interval of 2 dams) and shaded contours represent temperature (in ◦C) at 12:00UTC on (a) 10th, (b) 11th (c) 12th, and (d) 13th August 2018.*

To better understand the synoptic features of the event, the mid-tropospheric flow pattern is analyzed at 500 hPa height anomalies and wind vectors, are shown in Figure 3.6. This Figure reveals an eddy-driven polar jet stream present throughout the extreme rainfall event, extending along $50-70°N$ and $60–100°E$ belt. The eddy-driven nature of these jets is inferred from the lower-level wind patterns (Woollings et al., 2010). On 10th August, a cyclonic wave-breaking can be observed near $62°E–60°N$, but over the next days, the cyclonic low again merges with the jet stream. On 12th August, we noticed that the trough of the jet, longitudinally aligning with India ($75°–80°E$), is intensified and its maximum amplitude stretches southward to around $40°N$, as compared to the normal jet position of $50°N–60°N$. The jet diverges momentum flux southward and feeds onto the monsoon wave train, which results in an anomalous decrease in pressure over the entire India, the Bay of Bengal, and most Southeast Asian countries in both lower- and middle-troposphere (Figures 3.6c-d and Figures S3.4c-d). The significant decrease of pressure over India and Bay of Bengal exacerbated the monsoon trough and generated cut-off lows there that persisted for several days (Figures 3.6, 3.7, S3.4, S3.5). This decrease in pressure in the Northern hemisphere is synchronous with the increase of pressure in the southern hemisphere (Figure S3.6) near Madagascar. The detailed quantitative analysis of jet streams and wave-breaking impacts on the synoptic-scale flow regimes is beyond the scope of this paper; we, however, direct the reader to relevant studies on this topic (Branstator (1995); Held (1975); Hoskins et al. (1983); Lorenz and Hartmann (2001); O'Rourke and Vallis (2016); Woollings et al. (2008); Yu and Hartmann

(1993), among others). The Madden-Julian Oscillation (MJO), known for causing fluctuation in tropical weather through eastward propagation of clouds and rainfall near the equator, was also suspected to influence this event. Observing phase diagrams (Wheeler and Hendon, 2004) obtained from the Australian Government Bureau of Meteorology (http://www.bom.gov.au/climate/mjo/) for July–September 2018, shows the progression of MJO eastwards through different phases or locations (dependent on geography and climate), we observed that MJO was near Maritime during July and in the western Pacific Ocean for August 2018. This normally suppresses the convective processes of monsoon in India. Therefore, the intensifying low pressures in the Bay of Bengal and South China Sea seem more evidently due to the unusual impact of the polar jet stream.

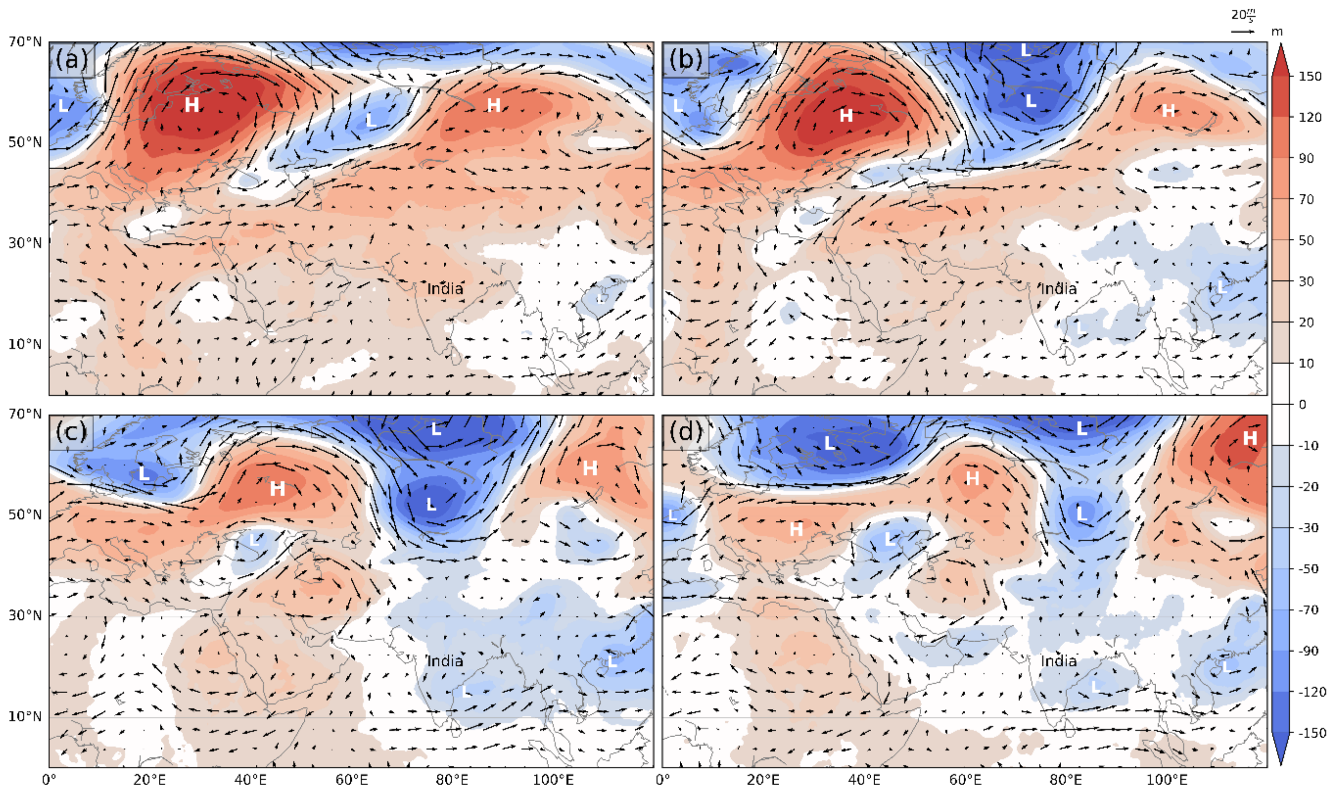

Figure 3.6. *500 hPa geopotential height anomalies for (a) 10th, (b) 11th, (c) 12th, (d) 13th, August 2018. The anomalies are computed at 06:00UTC of each day. For any given day of the year 2018, the climatological mean was taken as the average of that day for all years from 1979 to 2017.*

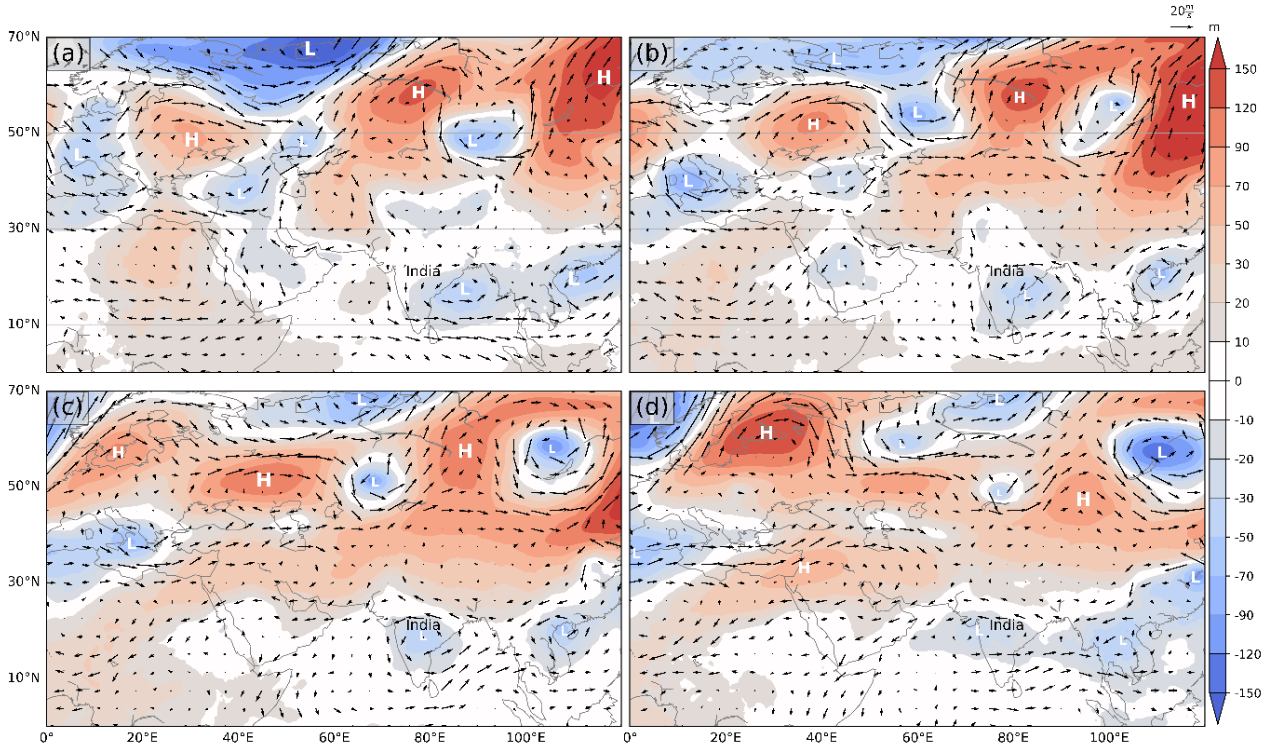

Figure 3.7: *Same as Figure 3.6 but for (a) 14th, (b) 15th, (c) 16th (d) 17th, August 2018.*

3.3.4. Convergence

The vertical ascent of the moisture-laden winds into Kerala is shown in Figure 3.8 for different days before and during the extreme rainfall days (taking the average of 500 hPa and 850 hPa levels values). There is a strong uplift (>1 $Pa.s^{-1}$) of air parcels over the windward side (west side) of the Western Ghats from 13th to 15th August and, as expected, subsidence can be seen on the leeward side (east side) of the mountains. Though the atmospheric pressure system advected warm air from the Arabian Peninsula towards northern India and then south, the heat advection into the study region is rather slow, as can be seen from the temperature gradient in Figure 3.5. Thus, it can be inferred that the ascent of air due to warm-air advection did not play a major role in the uplift of the air during the event. From this discussion, we deduce that the extreme precipitation was generated through the orographically-induced ascent of moist air parcels; this is a typical signature of landfalling ARs over complex-terrain coastal regions.

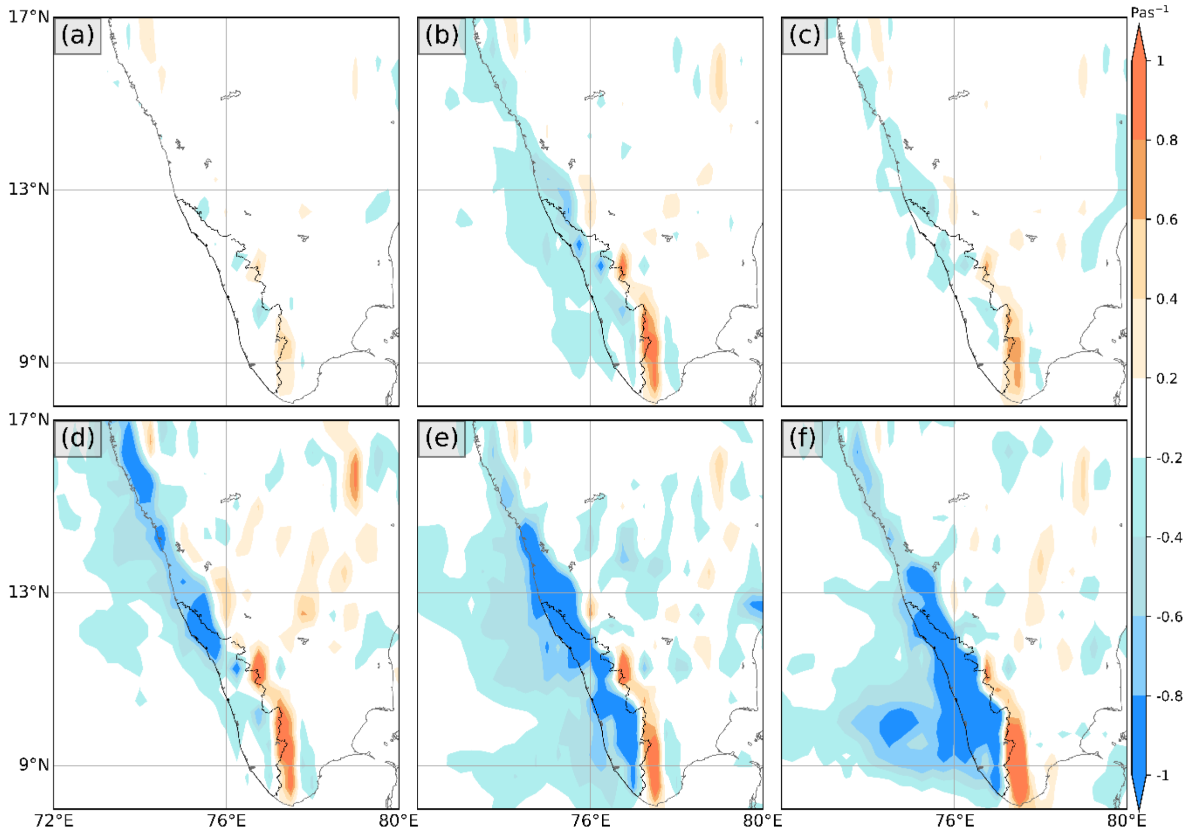

Figure 3.8: *Vertical wind speed ($Pa.s^{-1}$) for days of August 2018 on (a) 3rd (b) 7th, (c) 9th, (d) 13th, (e) 14th, and (f) 15th using ERA5 data; the blue shaded (negative) shows the ascent of air and the coral shaded (positive) shows descend of air; taking an average for two* $500\ hPa$ *and* $850\ hPa$ *vertical winds.*

3.3.5. Moisture sources

To identify the moisture sources during the event using Lagrangian trajectory analysis, we release air parcels from multiple vertical levels (as mentioned in the methodology section) at various locations in the region that have recorded high rainfall during the event (12th–15th August). The parcels' locations were decided based on the station and GPM-IMERG maps. One such location is just ahead of the orographic barriers enclosed in corners $11.09417°N, 76.0552°E$ *and* $10.66944°N, 76.144°E$. At each level, 12 parcels are released at the start of diagnosis (13th August 2018 at 12 UTC) which sums up to a total of 60 parcels released from all the levels. The backward trajectories of the parcels that ended up in Kerala at 12 UTC of 13th August are shown in Figure 3.9. This time corresponded with the instance AR identified on 13th August. We see that the lower-level parcels ($\leq 1000mAGL$) have well-organized trajectories as compared to the upper-level parcels ($\geq 3000mAGL$). Most of the lower-level parcels enter the boundary layer (before 5th August) somewhere near the eastern Indian Ocean ($15°S – 25°S, 100°E – 110°E$) where they hold relatively lower moisture contents (mixing ratio ~2 $g.kg^{-1}$). As the parcels travel through the Indian Ocean and the Arabian Sea, they accumulate large quantities of moisture and the mixing ratio reached 16 $g.kg^{-1}$) before landfall over

Kerala. The upper-level parcels travelled above the mixed boundary layer throughout their course and as explained earlier, their true moisture sources cannot be ascertained. Also, these parcels did not contribute significantly to the rainout over Kerala (drop in mixing ratio at 12:00UTC is ~0.25 $g.kg^{-1}$). The trajectories were also computed using GDAS (0.5° × 0.5°) and were found similar to those using GDAS1, except for the parcels released above 1000 m AGL (Figure S3.7) Hence, to locate the major sources of moisture and their fractional contributions to the Kerala rainfall event, we focus only on the lower-level parcels (i.e.,500 m AGL, 750 m AGL, and 1000 m AGL) with the final number of 36 parcels used to compute the fractional contribution). The parcels at each of the three levels were spatially average at all locations along their path. To obtain a single representative as shown in Figure 3.10 these values were further averaged for the three levels. This method gives the average value of moisture at all locations in the trajectory (Figure 3.10). The moisture trajectories provided a timeline of air parcels' locations, days before the rainout event; they do not necessarily represent the major axis of the AR since the parcels attained sufficient moisture only after reaching the northern portion of their track to be considered in the AR, which is at the time of the AR event. This is observed in Figure 3.9 (a) where mixing ratio is very high nearing Kerala, in the vicinity of the AR.

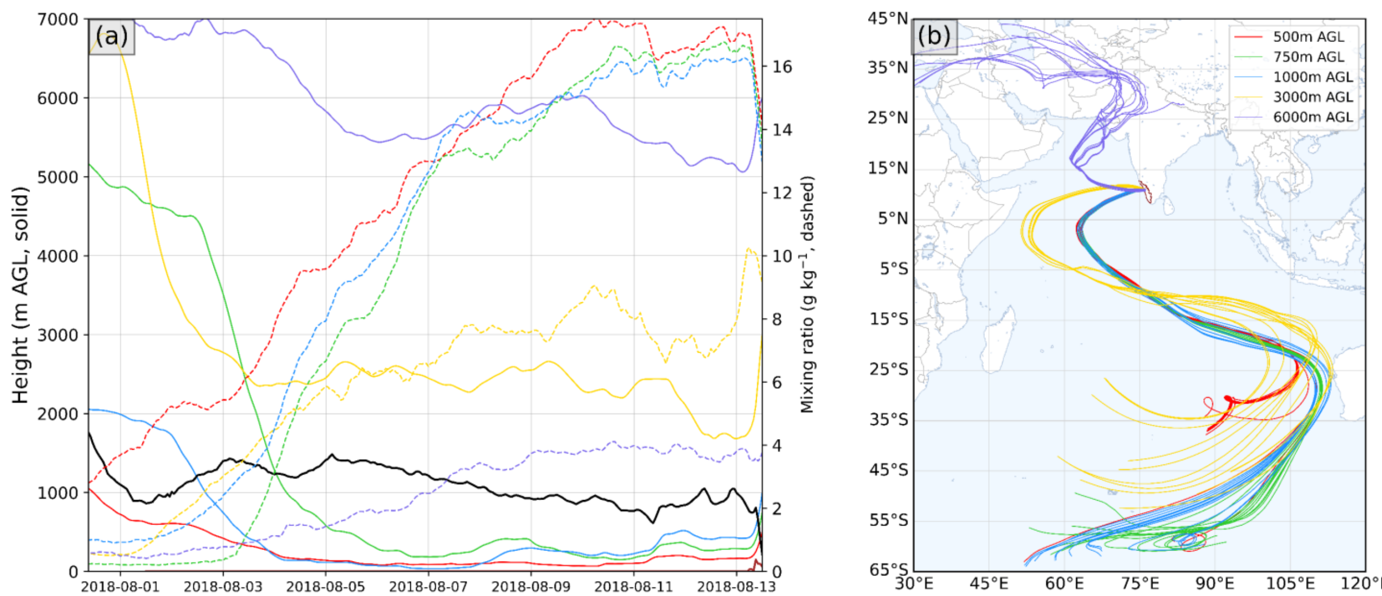

Figure 3.9: *(a) The average position of parcels (m AGL; solid lines) released at different heights (shown in the legend), and their corresponding moisture ($g.kg^{-1}$; dashed lines) are shown by matching colors for different vertical levels; the boundary layer is shown in black solid line; y-axis on the left shows the height of the parcel (m AGL); y-axis on the right shows the mixing ratio ($g.kg^{-1}$); x-axis shows the time. (b) The trajectories and path of parcels (advected moisture) ending at 12:00UTC on 13th August 2018, as traced by HYSPLIT within the defined region. Twelve parcels are released at each height at the start, and each color represents parcels belonging to the same group.*

Figure 3.10 shows the fractional contribution of moisture from various sources (taken as the average of lower-level parcels, i.e., $\leq 1000\ m\ AGL$) to a total of $3.09\ g.kg^{-1}$ rainout at 12 UTC on 13th August over a region where heavy rainfall was recorded that day. As can be observed, the majority of the moisture originated from the tropical central and eastern Indian Ocean ($\sim 60\%$) with minor contributions from the Arabian Sea. Another region in the southern part of Kerala that experienced heavy rainfall on 15th August is also examined for its moisture sources Figure S3.8. We find that approximately $20\text{–}30\%$ of moisture originated from the Arabian Sea, located next to the rainfall region, and $70\text{–}80\%$ was contributed from the Indian Ocean, which is far from Kerala. There is a possibility that a lower amount of moisture coming from these far, albeit strong sources of moisture, actually reaches Kerala, since trajectories beyond some point in time are overwhelmed by computational and modelling errors (Sodemann, Schwierz and Wernli, 2008a). The trajectory of other days (Figure S3.8 to S3.11 in SM) during the event showed that they rained marginally before reaching the Arabian Sea and picked up moisture again before the final loss over Kerala. A similar case for the extreme rainfall in central India in 2016 stems from increased contribution in the Arabian Sea ($5°N - 30°N, 50°E - 75°E$) (Roxy *et al.*, 2017). Strong moisture advection from the Arabian Sea during this event is evident in Figure 3.3 shown by the IVT vectors. A closer observation of the wind fields in Figure S3.5a showed that the winds from 12th -13th August intensified till 15th August (Figure S3.5b), which suggests a cyclone may have played some role in the 15th August event. The moisture sources for the Western Ghats are dominated by transport from the Indian Ocean with some contributions from the Arabian Sea (Nieto *et al.*, 2019) and any increase from these two sources can trigger extremes. Importantly, increased contribution from the Arabian Sea will mainly impact the adjacent land as any increase from the Indian Ocean (especially the east and south Indian Ocean) will likely rain midway or not reach the Indian continent. Other oceanic sources that might have added to the rainfall during the event were all above $\sim 800\ hPa$ with location traced to the north and western Arabian Sea, central and eastern Indian Ocean, and continental regions from Pakistan, Afghanistan, Turkmenistan, and some parts of the Middle East countries. There is a uniform increase in specific humidity in the eastern Indian Ocean and east Arabian Sea prior to the rainfall event. Most of the parcels after the 8th or 9th day from the release time travel above the MBL and therefore moisture uptake sources cannot be identified as sources. The analysis presented here showed that $60\text{–}80\%$ of the moisture during extremes can be tracked to the source, while 10% comes from above MBL and the remaining oceanic or continental moisture was already present in the air parcels before the diagnosis end time and are not considered as major sources of contribution to the event. Detailed diagnoses of moisture source contribution during extreme precipitation events are limited. Studies by Cadet and Reverdin (1981); Clemens and Oglesby (1992) have used the moisture budget approach of IVT for quantifying the contribution of moisture to India from the Arabian Sea, Bay of Bengal, and South Indian Ocean during the monsoon season (JJAS). Their analysis showed that 66– 70% of water vapor flux on the west coast of India comes from the south Indian Ocean and 30– 34% comes from the Arabian Sea. Their approach considered the total evaporation and precipitation in those regions without any information on the contribution to specific events, which is important to attribute specific regions that contributed to extreme events. This method can provide only a general idea of large regions that act as sources of moisture on average. The small modification that we made in the method by Sodemann, Schwierz and Wernli, (2008) (showed the contribution of each source (with moisture uptake) to the target region) has helped to identify the locations where moisture was picked up and the percentage contribution from them to the extreme event even if the parcel losses moisture during its path before reaching the target region.

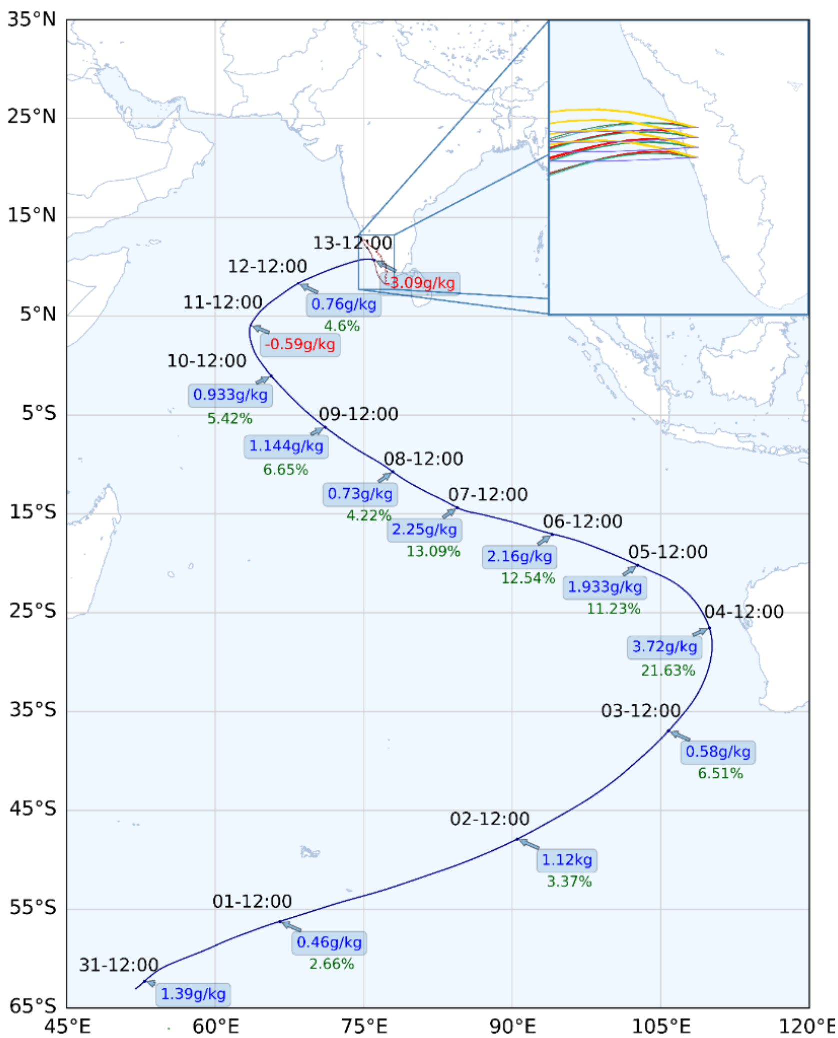

Figure 3.10: *Moisture sources and their fractional contributions for 13th August rainout at 12:00UTC. The moisture path traced by the parcel (average) is shown in navy color, moisture gained at each time is shown in blue enclosed within a light blue box, and the percentage contribution of moisture to the rainout from various sources is shown in dark green. The timestamp is given in black color; the map (top right corner) shows the parcels released within the region defined for diagnosis. Daily values shown are aggregated from the 6-hourly*

analysis. (For interpretation of the references to color in this figure legend, the reader is referred to the web version of this article)

3.4. Conclusion

The heavy to extreme rainfall events in Kerala, India, in August 2018 led to widespread flooding that impacted thirteen of the state's fourteen districts, and triggered landslides in many hilly areas. This study examines the atmospheric conditions during the event and identifies atmospheric rivers in relation to the Kerala 2018 flood. The major moisture sources for the abnormally high rainfall amounts that led to extreme precipitation are also identified. Station rainfall observations showed that Kerala received heavy rainfall in June–August 2018 that exceeded the climatological normal of the period (CWC, 2018). The majority of precipitation during the flood event occurred on the 13th, with many stations recording daily rainfall amounts exceeding 70 mm. A strong, narrow, and long moisture transport (Figure 3.3) band depicting an AR played a key role in transporting moisture from the Arabian Sea into the study region. Both visual inspection and an IVT-based algorithm identified a long-duration AR that lasted for about 96 hours from 12th to 15th August. Such storms with IVT >$700\ kg.m^{-1}.s^{-1}$ are rare in the tropics as compared to the mid-latitudes (Sellars *et al.*, 2017). On a scale that characterizes AR events based on maximum IVT and duration, the AR during the flood event is categorized as extreme AR CAT5 (Ralph, Rutz, *et al.*, 2019). The multi-day occurrence of AR observed here was effective in generating extreme precipitation tunneling-in large quantities of warm oceanic moisture from the neighboring oceans. The presence of ARs during this event explains the contribution to rainfall (that crossed the 95th percentile) received by Kerala in 2018. An increase in the kinetic energy (850 hPa) over the Arabian Sea was also observed for 12th – 15th August 2018. This increase was 3–4 times the threshold ($40\ m^2.s^{-2}$) taken as that of the monsoon onset period (Kumar et al., 2020). The orientation of the AR normal to the mountains in Kerala played a key role in the orographic uplift of moisture and downpours.

From the Lagrangian moisture tracking method, it is noted that air parcels on these days have high moisture near the Indian Ocean and increased in moisture on nearing the Arabian Sea and Kerala at the instance when the AR is observed. Thus, it can be inferred that these parcels contribute to the formation of AR and eventually deposit high rainfall in the windward region. A limitation in this, is the use of a low-resolution (GDA1) for moisture source identification and tracking. The multiday occurrence of AR impacted the wetness of the soil and exacerbated the flood. The detailed behavior of summertime ARs has not been examined yet over India, perhaps because of the presence of high-water vapor plume during monsoon that covers the entire area. In this study, both IVT and IWV captured the enhanced moisture originating from the Arabian Sea, where IVT is seen to represent AR structure more clearly. However, distinguishing ARs and monsoon circulation over the Indian subcontinent is still an open challenge. It is of interest to the authors to further investigate this challenge in our future works and to extract ARs from the background monsoon circulation. The selection of higher threshold values as done recently by Liang and Yong (2020) to delineate the AR area for tropical regions will help to identify strong ARs but eliminate the weak ones.

To intuitively strengthen our results the atmospheric dynamics prevalent during the event are analyzed in detail. The synoptic overview of the daily evolution of pressure, temperature and pressure anomalies revealed a mechanism for the intensified low pressure in India. It was found that the trough of a polar westerly jet induced low-pressure anomalies, which simultaneously co-acted with the monsoon trough over Orissa and the Bay of Bengal creating a depression in the Bay of Bengal. The quasi-stationary high-pressure ridge located over north-western India steered the moisture flow from the Indian Ocean to Kerala. The warm moisture-laden winds upon striking the Western Ghats barrier resulted in a deep convergence of moisture and eventual rainout.

Overall, we conclude that the flood event in Kerala during August of 2018 was triggered by extreme precipitation events associated with an intense and long-duration CAT 5 atmospheric river. A view of extreme events that lead to major floods from an AR perspective is important to understand the cause of heavy precipitation, especially in densely populated regions that have costly effects. Such intense ARs are most likely to affect heavy precipitation (Mahoney *et al.*, 2016). Hence further research is required to quantify the effect of anthropogenic factors in translating extreme precipitation to state-wise floods. These factors include operations of reservoirs, rapid encroachment of floodplain areas, conversion of forest areas to urban cities, and other land use practices.

APPENDIX-A: Supporting Information

Text S3.1: Information related to rain gauge data of Indian Meteorological Department (IMD).

The details on IMD station precipitation observations are originally described in Parthasarthy & Mooley, (1978). These daily data are archived at the National Data Centre (NDC), IMD, Pune, India. A day's precipitation observation from IMD is the accumulated precipitation over the past 24 hour ending at 08:30 hour Indian Standard Time (0300 UTC) of the day. The rainfall records collected at various locations throughout India are subjected to quality controls such as completeness of the data, error removal, location verification, and validation of the date and time of the collection, etc. The monthly rainfall values in a year are compared with the monthly mean of the station and its standard deviation ($mean \pm 2\sigma,\ mean \pm 3\sigma$) to ensure consistency. All the records to be archived are verified for duplicates, typing errors, and verified with original manuscripts. Examinations and tests are carried out to remove any extreme outliers, which are entirely not consistent with the climatology. The extreme values observed at one station are compared with neighboring stations for spatial consistency and to filter out erroneous values. In order to enrich the quality of data, additional rainfall records are collected from state governments and private organizations, which are again treated for quality control and used to verify the IMD data, especially for location matching (Rajeevan *et al.*, 2006; Jaswal, Narkhede and Shaji, 2014; Pai *et al.*, 2014). The Symons' 5-inch diameter rain gauge was used as standard at all places (Parthasarthy & Mooley, 1978). More information on data collection and quality is available from IMD http://rcc.imdpune.gov.in/Training/SASCOF12/CDMS_Daythree/Data_qua_URJ.pdf. The CWC report analysis referenced here is based on rainfall records of 67 stations of IMD spread across the entire state covering both hilly and plain regions.

Table S3.1: List of stations and their related information.

Sl. No.	**Station Name**	**District**	**Location**		**Elevation (m)**
			Latitude (˚N)	**Longitude (˚E)**	
1.	Alathur	Palakkad	10.63	76.55	65
2.	Alwaye PWD	Ernakulam	10.12	76.35	7
3.	Alappuzha	Alappuzha	9.55	76.33	2
4.	Ambalavayal	Wayanad	11.62	76.20	922
5.	Angadipuram	Malappuram	10.97	76.23	39
6.	Aryankavu	Kollam	8.89	77.17	135
7.	Chalakudy	Thrissur	10.30	76.33	14

8.	Chengannur	Alappuzha	9.32	76.62	45
9.	Cherthala	Alappuzha	9.70	76.33	10
10.	Chittur	Palakkad	10.70	76.73	300
11.	Enamakkal	Thrissur	10.5118	76.0936	3
12.	Ernakulam South	Ernakulam	9.97	76.28	7
13.	Haripad	Alappuzha	9.28	76.45	12
14.	Idukki	Idukki	9.83	76.92	895
15.	Irinjalakuda	Thrissur	10.34	76.21	8
16.	Irikkur	Kannur	11.97	75.55	156
17.	Kannur	Kannur	11.87	75.37	14
18.	Karipur AP	Malappuram	11.13	75.95	79
19.	Kayamkulam	Alappuzha	9.18	76.50	5
20.	Kayamkulam AGRI	Alappuzha	9.17	76.52	4
21.	Kochi C.I.A.L.	Ernakulam	10.15	76.40	8
22.	Kochi I.A.F.	Ernakulam	9.97	76.23	-20
23.	Kodungallur	Thrissur	10.22	76.20	5
24.	Kollamkode	Palakkad	10.6139	76.6908	99
25.	Kollam RLY	Kollam	8.88	76.60	19
26.	Konni	Pathanamthitta	9.23	76.87	175
27.	Kottayam	Kottayam	9.58	76.52	30
28.	Kozha	Kottayam	9.75	76.57	
29.	Kozhikode	Kozhikode	11.25	75.78	8
30.	Kudulu	Kasaragod	12.5283	75.00	85
31.	Kumarkam	Kottayam	9.62	76.43	1
32.	Kupaddy	Wayanad	11.68	76.27	889
33.	Kunnamkulam	Thrissur	10.65	76.07	17
34.	Kurudamannil	Pathanamthitta	9.35	76.74	13
35.	Manjeri	Malappuram	11.12	76.13	106
36.	Mananthavady	Wayanad	11.80	76.02	900
37.	Manantoddy	Wayanad	11.80	76.01	900

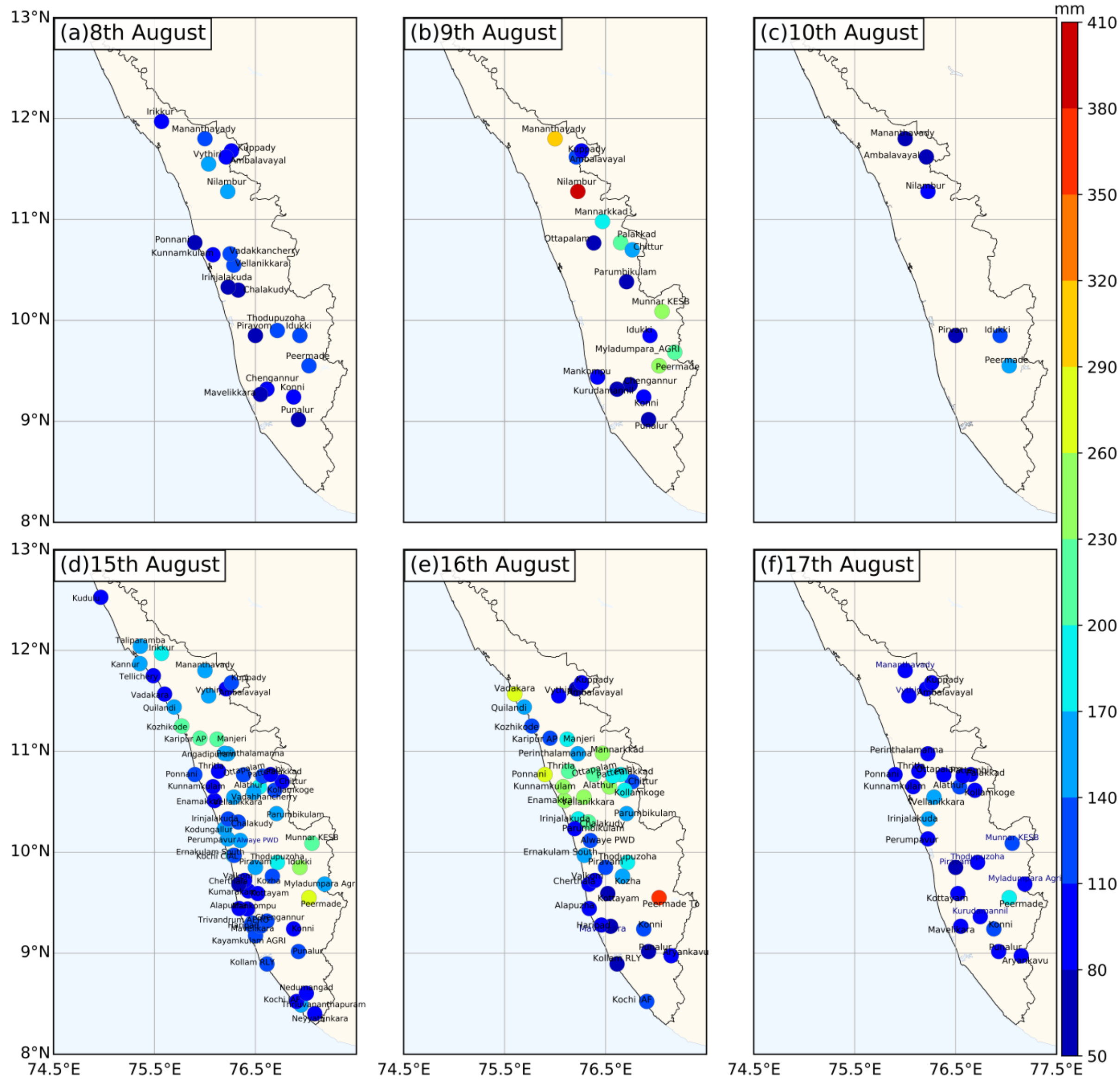

Figure S3.1: *Daily rainfall (mm) at multiple rain gauge stations of IMD for different days of August 2018 during the event. The rainfall for a day is recorded from 08:30AM Indian Standard Time (IST) of the previous day to 08:30AM IST of the day. The color scheme gives the magnitude of rainfall for the day.*

S3.2: AR and AR trajectory

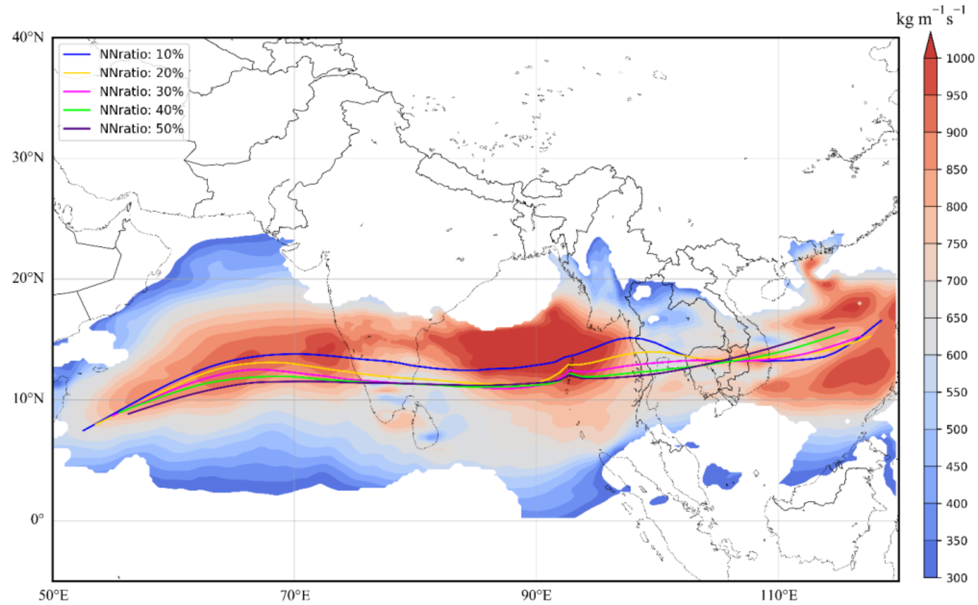

Figure S3.2. *An AR detected using the AR identification algorithm by Pan and Lu (2019) with trajectories representing the center of AR formed by connecting the centroids of IVT weighted of all cross sections on AR pathway (shaded region). The centroids are found by considering different nearest neighbors' ratios (NN) shown at the top left represented by different colors. The initial starting points of maximum IVT is defined for the specified region (0 – 30°N and 50 – 120°E) then all the contiguous grids exceeding their threshold are extracted as AR pathways or preliminary AR pathways.*

Nearest Neighbors (NN): In this detection algorithm at least 5 choices of NN ranging from NN10 to NN50 were used (shown in different colors in the plot, sensitivity analysis was shown in Pan and Lu (2019)). The NN10 trajectory (in blue) followed the center of AR mass closely, however, the NN10 is highly sensitive to local turbulences in the AR pathway as shown by Pan and Lu (2019). The NN50 missed to follow the path of maximum IVT, did not capture the curvature, and over-smooth the trajectory. The trajectory obtained is of shorter length and this affects the other metrics (shown in Table 2). The NN20, NN30 NN40 showed intermediate ranges of length between the two trajectories, and their values are shown in the table below. In order to reduce the sensitivity to the choice of NN ratios, the weighted average was used in the calculation of IVT direction and centroid.

Table 2: AR metrics

NN ratios	*Length (km)*	*Area (km^2)*	*Width (km)*	*LWratio*	*Turning angle (°)*
10%	5213.045	10807886.25	2073.239	2.51	-15.205
20%	5145.695	10807886.25	2100.374	2.45	-2.62
30%	4953.425	10807886.25	2181.902	2.27	0.71
40%	4738.554	10807886.25	2280.841	2.08	0.27
50%	4532.851	10807886.25	2384.346	1.90	1.91

S3.3: Atmospheric rivers on multiple days during the 2018 Kerala flood event

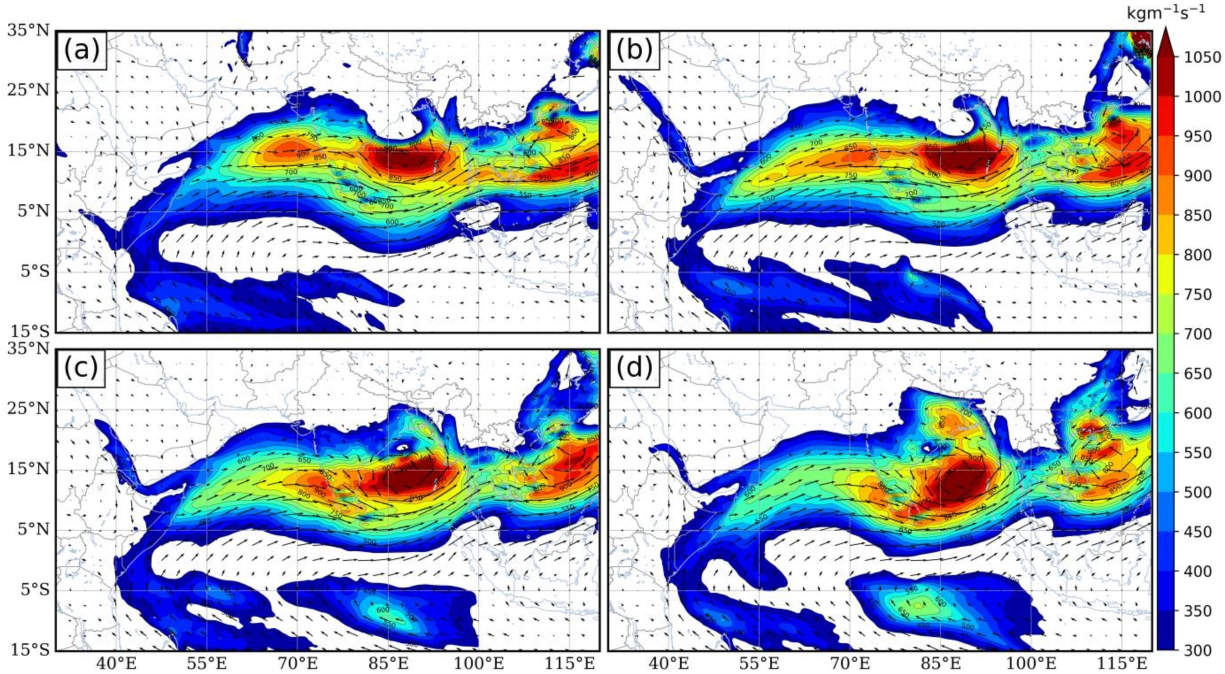

Figure S3.3: *Atmospheric rivers identified during the heavy rainfall events in Kerala on (a) 12th, (b) 13th (c) 14th, and (d) 15th August 2018. At each grid cell, IVT vector comprised of column-integrated $q \times u$ and $q \times v$, which give the magnitude of moisture (q) and their transport directions by the horizontal winds (u and v) at a grid point.*

S3.4: Geopotential Heights and Temperature at 500hPa

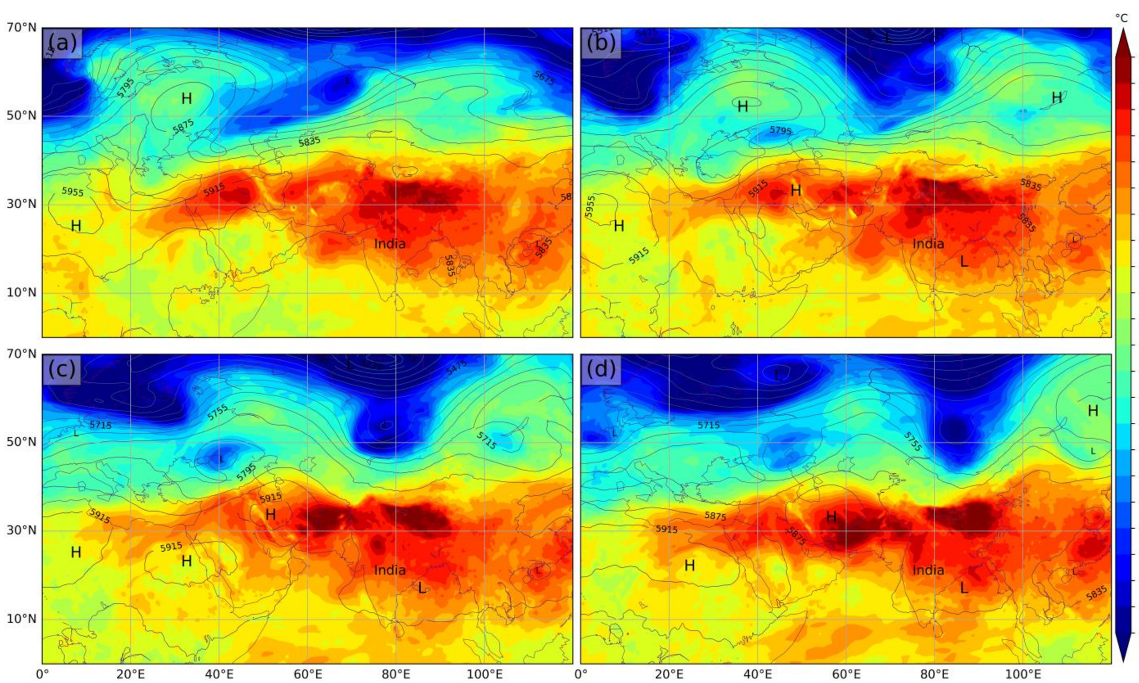

Figure S3.4: *Geopotential heights and temperature at 500hPa (geopotential heights in dam shown by contour lines) and shaded contours represent temperature (in ˚C) at 12:00UTC on (a) 10th, (b) 11th (c) 12th, and (d) 13th August 2018.*

S3.5: Geopotential Height and Wind Fields at 850hPa during the 2018 Kerala flood event.

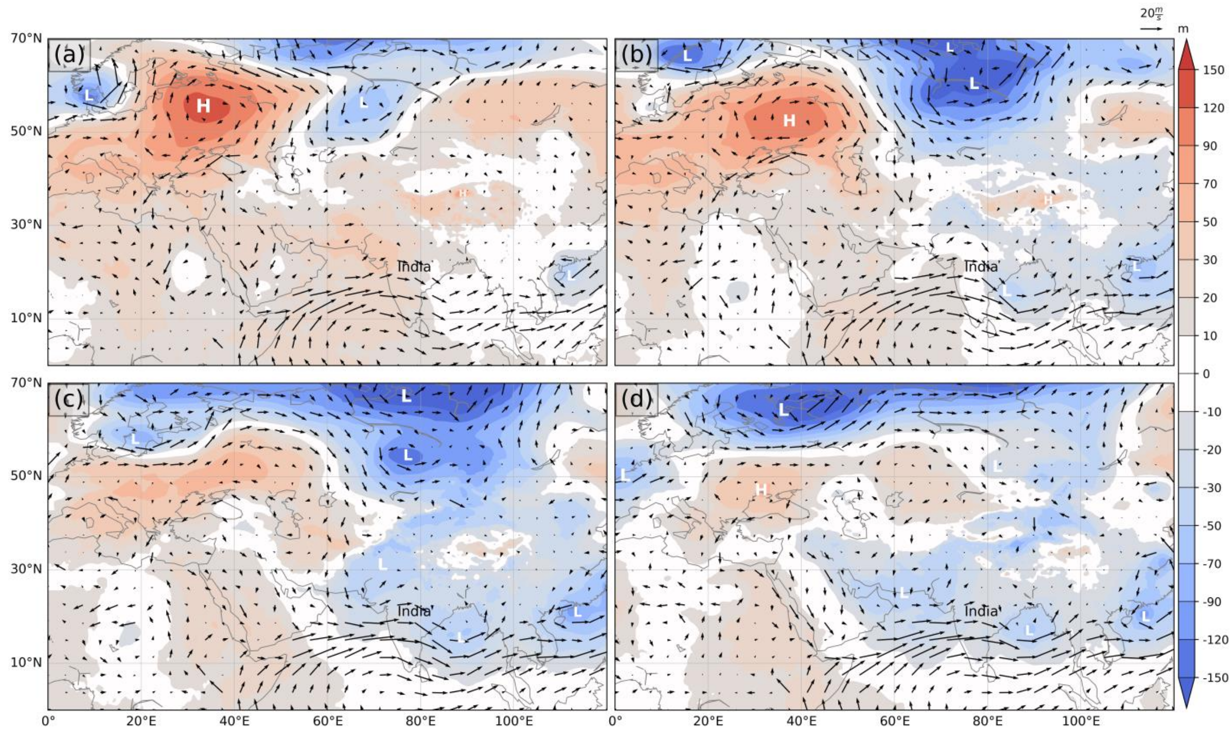

Figure S3.5a: *850hPa geopotential height anomalies for (a) 10th, (b) 11th, (c) 12th (d) 13th, August 2018. The anomalies are computed at 06:00UTC of each day.*

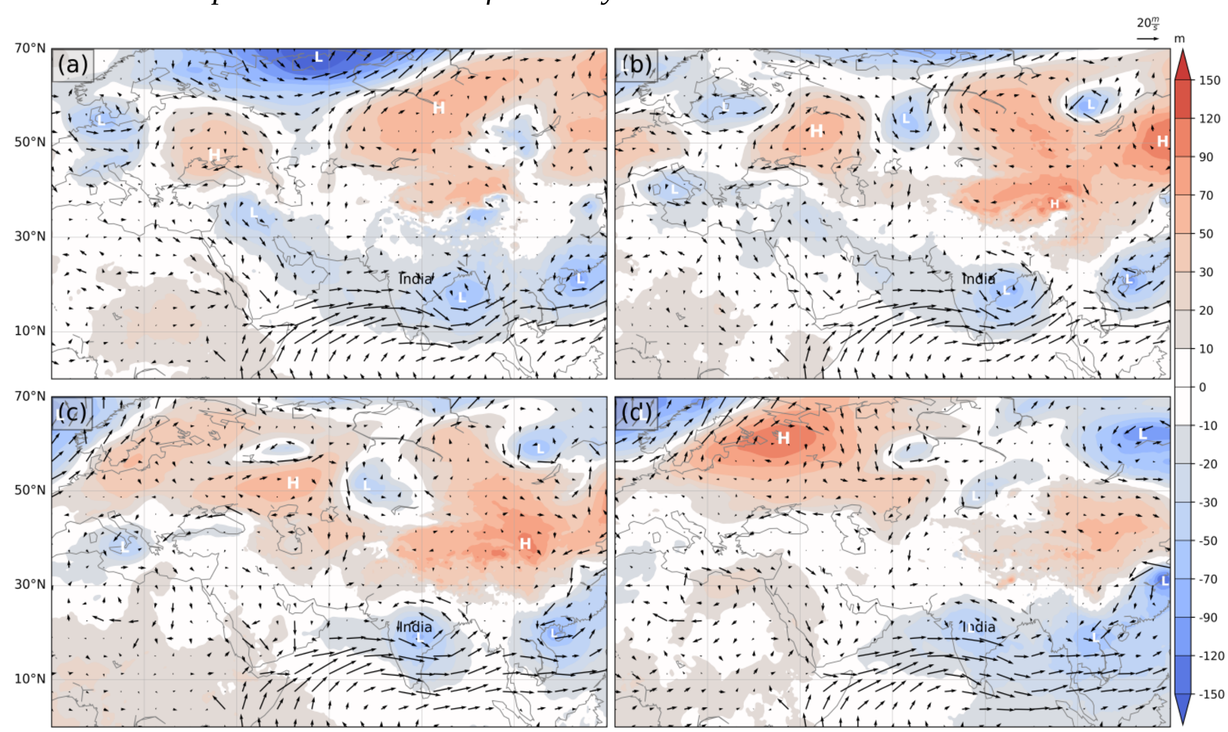

Figure S3.5b: *850hPa geopotential height anomalies for (a) 14th, (b) 15th, (c) 16th (d) 17th August 2018. The anomalies are computed at 06:00UTC of each day.*

S6: Mean Sea Level Pressure

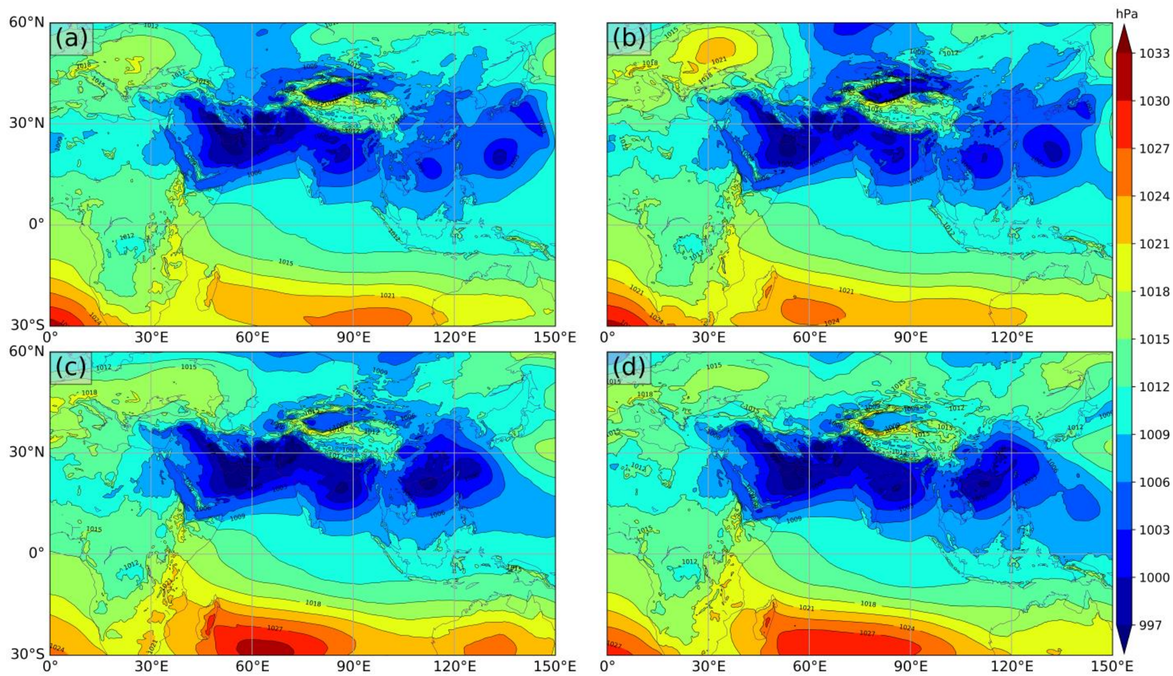

Figure S3.6: *mean sea level pressure on (a) 7th (b) 9th (c) 13th and (d) 15th August 2018*

S3.7: Tracks of parcels release in Kerala and their moisture content and position in the troposphere

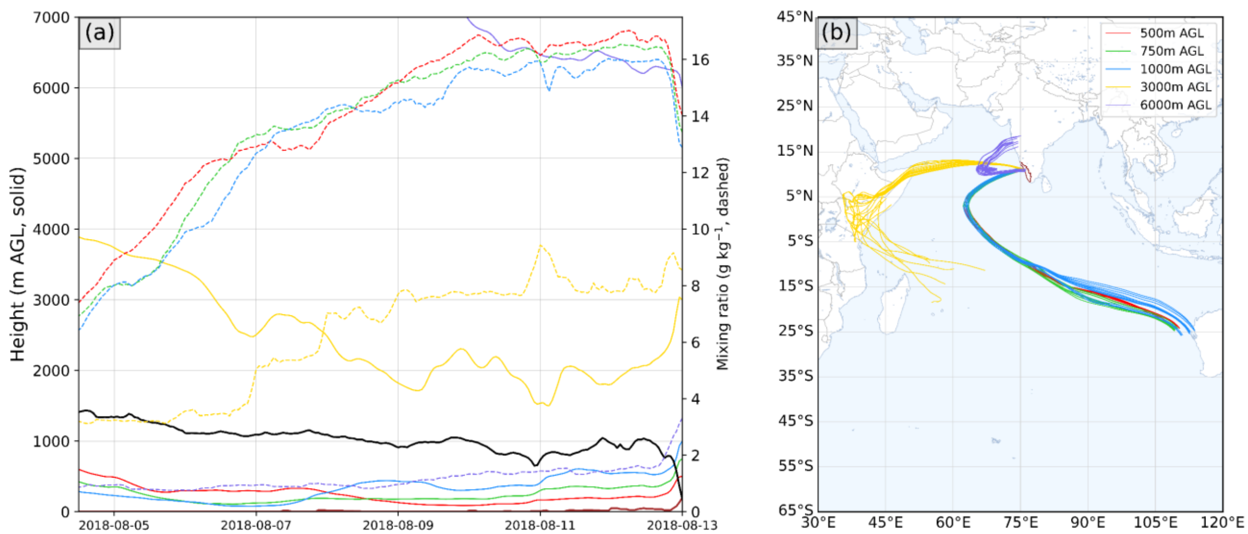

Figure S3.7: *(a)The average parcels' position (m AGL; solid lines) released at 500 m AGL, 750 m AGL, 1000 m AGL, 3000 m AGL, and 6000 m AGL and their respective moisture ($g.kg^{-1}$; dashed lines); the boundary layer is shown in black solid line, (b) The trajectories of air parcels ending at 12:00UTC on 13th August 2018 shown by different colors.*

S3.8: Moisture sources and fractional contribution on 15th August 2018

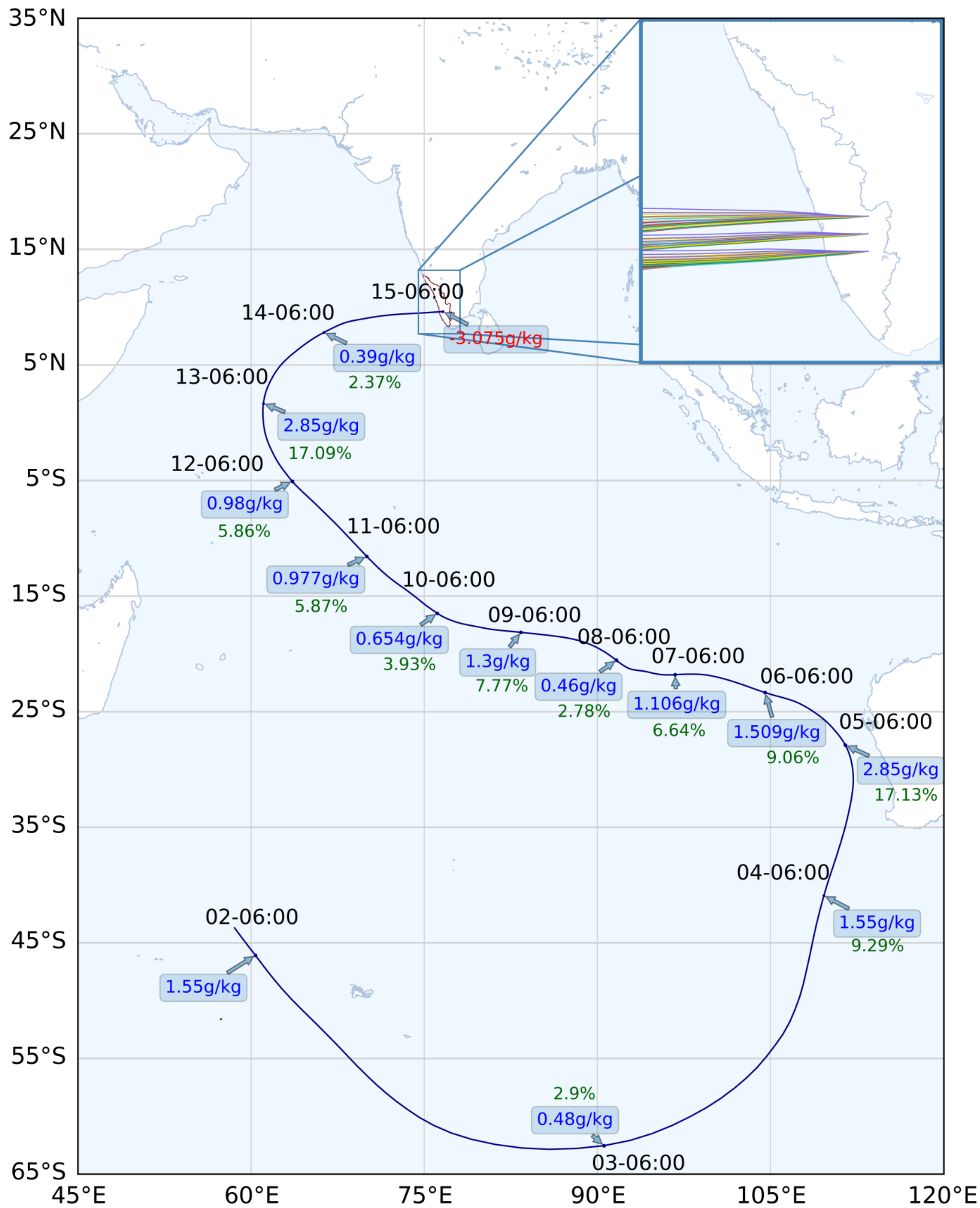

Figure S3.8: *The fractional contribution of moisture from various sources (blue colour enclosed in a light blue box) to Kerala on 15th August 2018 at 06 UTC. Here the parcels at levels 500mAGL, 750mAGL, 1000mAGL and 1500mAGL are average spatially at each time stamp and at each level and the path traced by the parcel (average) is shown in navy colour. The level 1500mAGL is also considered as the parcel was observed to have travelled very close/within the mixed boundary layer in this case. The location selected for backtracking covered the districts of Idukki, Ernakulam and Kottayam which have been observed to receive high rainfall.*

S3.9: Moisture sources and fractional contribution on 12th August 2018 at 6UTC

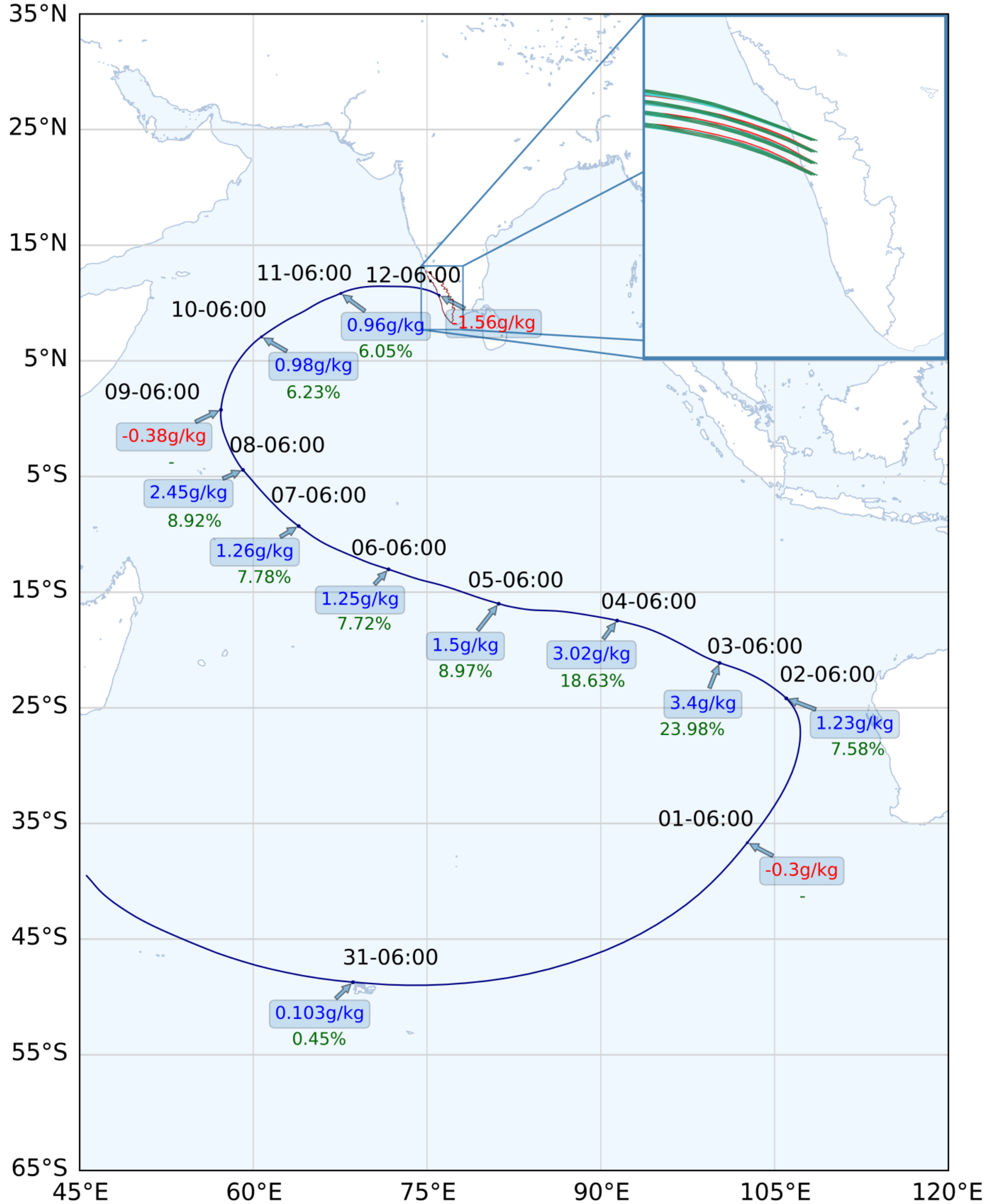

Figure S3.9: *Same as figure S3.8 but for 12th August 2018 at 06UTC.The location selected covers the districts of Malappuram, Palakkad and Thrissur.*

S3.10: Moisture sources and fractional contribution on 14th August 2018 at 18UTC

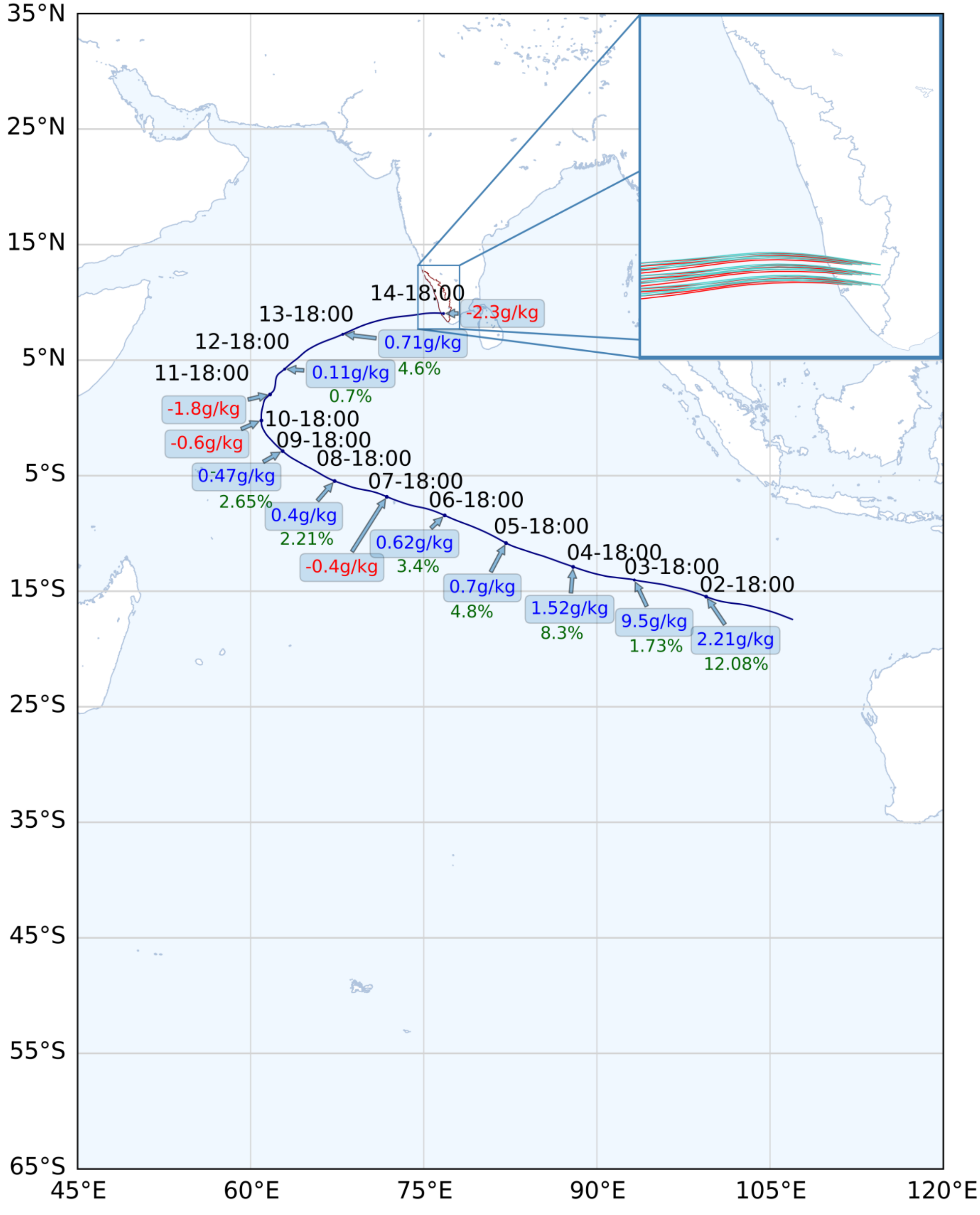

Figure S3.10: *Same as figure S3.8 but for 14th August 2018 at 18 UTC. The location selected covers the districts of Alappuzha, Kollam and Thiruvananthapuram.*

Figure S3.11: Moisture sources and fractional contribution on 15th August 2018 at 12 UTC

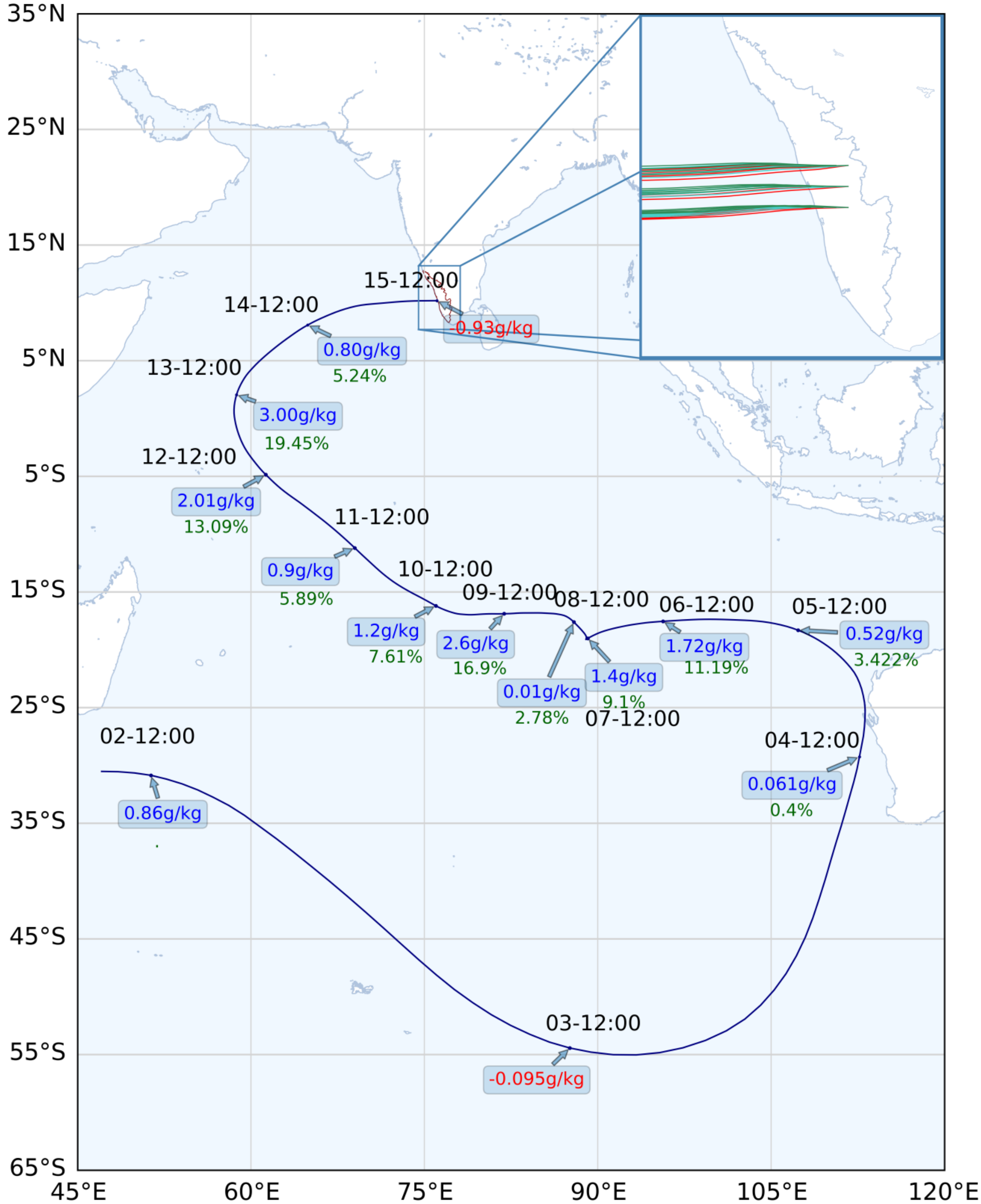

Figure S3.11: *Same as figure S3.8 but for 15th August 2018 at 12 UTC. The location selected covers the districts of Malappuram and Palakkad*

Chapter 4

Studying Himalayan ARs, thermodynamics and precipitation mechanisms of extreme ARs

After:

R. V. Lyngwa, M. A. Nayak, and M. F. Azam; Himalayan Atmospheric Rivers: Thermodynamics of extreme Atmospheric rivers and their precipitation mechanisms in two major Himalayan basins

Executive Summary

Chapter 3 demonstrates the connection between the severe August 2018 flood in Kerala and high-impact precipitation associated with an AR event. The intense and long-lived AR belonging to Category 5 on the AR scale was oriented perpendicular to the Western Ghats. We identified key contributing factors that led to the flood and found that saturated soil conditions, an intensified low pressure on the monsoon trough, and the influences of the polar jet on India played major roles. Moisture mainly originated from the Indian Ocean, with some contributions from the Arabian Sea. Here the focus has been shifted from ARs affecting the coastal region in south India to ARs impacting the high mountains in north India, situated deep inland. This chapter studies ARs that hit the south-facing Himalayan arc, and focus on their characteristics, precipitation impacts, and mechanisms leading to precipitation. It begins with a step-by-step procedure of the AR algorithm used, including modifications for efficient AR identification over this region. A comparison with results using another established global AR detection algorithm is briefly mentioned. This chapter presents AR characteristics such as intensity, duration, annual and seasonal frequency. The analysis then focuses on extreme precipitation impacts in two large Himalayan Basins-IB and GB. For this, the top eight AR events from each basin are selected, and precipitation one day during the event and the day following it are assessed, to understand the impact of the ARs on the magnitude and extent of the affected area. Here, the moisture budget equation is used to break down the precipitation processes into different terms explaining the transport of moisture, sources, sinks, and the rate of changes of atmospheric moisture. The terms were also averaged for two areas of distinct topographical characteristics to better understand the importance of topography in addition to the physical mechanisms. The average track of parcels arriving in the impacted areas is traced with Lagrangian trajectory analysis using HYSPLIT, making it feasible to locate the major sources of moisture supply along the tracks. In addition, the local atmospheric conditions during the events were analyzed using SkewT-log*P* diagrams for different locations within the AR, to provide a general idea of the complexity of atmospheric processes (moisture, temperature, winds, cloud formation) leading to precipitation.

Abstract

In extra-tropics, moisture is transported efficiently within the lower troposphere in narrow bands of poleward movement called Atmospheric rivers (ARs). In this study, ARs that penetrated the Himalaya, South Asia, are identified using 6-hourly Integrated Vapor Transport (IVT) fields in an AR detection algorithm tailored for the Himalaya. We focus on the top 8 AR events (Categories 3-5) with substantial precipitation impacts in the Indus Basin (IB) and Ganga Basin (GB). These ARs released over 150 mm/day of precipitation (exceeding the 99th percentile of non-zero daily precipitation distribution) along their central axis and mountain landfall locations. Even the headwaters experienced precipitation above 65 mm/day, and the plain received up to 50 mm/day. Two regions were selected to show the Himalaya's significance in influencing precipitation intensity: near mountains and over plains. In almost all events, high precipitation falls near mountains. High-intensity precipitation resulted from strong positive convergence, and positive advection, with small atmospheric storage changes. Tracking backward the precipitated air parcels at these areas revealed that excess moisture came from the north and western Arabian Sea, the north and eastern Bay of Bengal, and the Middle Eastern Seas. Within ARs, two locations of high IVT and intense precipitation, the troposphere was saturated. Near mountains, mildly unstable air is forced along steep topography and generates orographic precipitation, while near/on-axis, mildly unstable air undergoes vertical ascent driven by warm air lifted over cold air, generating frontal precipitation. This study provides insights into the characteristics of ARs impacting the Himalayan. The results indicate that ARs are transport mechanisms of oceanic moisture to mainland India and the Himalaya, however, they remained relatively understudied and lack comprehensive insights for practical applications.

4.1. Introduction

The Himalaya, a group of parallel mountain chains running in a northeast to southwest direction for approximately ~2700 km, home to nearly 40,000 glaciers that cover an incredible area of ~41,000 km^2 with an estimated volume of ice of 3500 km^3 (Farinotti *et al.*, 2019; Jackson *et al.*, 2023). The ice mass in this region is the third-largest on Earth and rightfully called the "Third Pole" (Xu *et al.*, 2009; Bolch *et al.*, 2019). These mountains are also referred to as "Asia's water tower", sustaining the major Himalayan river system— Indus, Ganga, and Brahmaputra (Figure 1)— that are nourished by seasonal precipitation in summers and glacier- and snow-melts in dry seasons. Nearly $50 - 60\%$ of the world's population living in and around these mountainous regions rely on the water resources derived from these mountains. Moreover, those residing outside the basins also benefit from the water release through the melting of snow and ice of these mountains. The three basins stretch approximately 2.75 million square kilometers of which ~20% is irrigated area (Azam *et al.*, 2021).

Precipitation deposited over these mountains and basins is the main source of water input to the land and water systems. The two major South Asian climatic systems known to transport and deposit a bulk of the yearly precipitation are: the Indian Summer Monsoon (ISM), which is active in summer seasons (June-September) and provides precipitation mainly to CH and EH (Bookhagen and Burbank, 2010), and the Western Disturbances (WDs), mainly active in winter-spring seasons (November-March) and primarily contribute precipitation to the WH and western CH. In addition to these well-known moisture transport systems, the presence of ARs over these regions may have been overlooked. ARs are distinct meteorological phenomena characterized by narrow forms, high moisture content (precipitable water, ≥ 20 mm in mid-latitudes (Ralph, Neiman and Wick, 2004)), robust wind speeds (surpassing 15 m/s), low-level dynamic reaching up to 3-4 m/s in height, and possess transient nature (Zhu and Newell, 1998). ARs are known widely to contribute significantly to the water supply in various regions around the globe (Dettinger 2011; Lakshmi and Satyanarayana 2020; Lavers and Villarini 2015a; Moore et al. 2012; Prince et al. 2021; Viale et al. 2018), but their role in the Himalayan regions are relatively poorly known and lesser explored, which may be important.

ARs manifest as river-like filaments in the lower troposphere, transporting approximately 90% of excess energy, and moisture from the extra-tropics to the poles year-round while occupying < 10% of the global circumference of a given latitude (at one timestep about 4 to 5 ARs are found across a latitude) (Zhu and Newell, 1998). The original concept of ARs encompasses the idea of the abundant supply of moisture from subtropical regions, however, sources of moisture for ARs were found even beyond the subtropical regions (Cordeira, Ralph and Moore, 2013; Gimeno *et al.*, 2016), and thus the tropical and extratropical sources were included in the definition of an AR (Ralph *et al.*, 2018). The definition highlighted the "typical" association of ARs to LLJ streams ahead of an extra-tropical cyclone's cold front because it was based primarily on ARs over the western USA. Emerging studies revealed that ARs can exist independently of extra-tropical cyclones, expanding their significance beyond this relationship. In diverse regions, of tropics and extra-tropics, ARs were found to be associated with various synoptic weather systems. For example, AR activities were observed during boreal monsoon in South and East Asia (Lakshmi, Satyanarayana and Chakraborty, 2019; Park, Son and Kim, 2021).

The Himalayan ranges in South Asia form an important physical barrier to moisture transported from the Bay of Bengal, Arabian Sea, and Indian Ocean and from the Mediterranean Sea, Black Sea, and Atlantic Ocean (Boschi and Lucarini, 2019). The atmospheric moisture these mountains extract sustains the ecological balance and contributes to environmental health. Recently, with more field work, advancements in remote sensing, and modelling, it was discovered that many Himalayan glaciers show diverse changes of different rates in size and volume over the past 5-6 decades. Mass losses are prevalent in WH, CH, and EH and more gains or near balance in the Karakoram (Hewitt, 2005; Azam *et al.*, 2018; Bolch *et al.*, 2019).

Numerous studies worldwide focused on ARs' impacts, and have perceived a range of AR effects, from causing high-impact disasters through extreme rainfall (Lavers and Villarini, 2013b; Kamae *et al.*, 2017; Waliser and Guan, 2017; Young, Skelly and Cordeira, 2017) to providing vital water resources (Dettinger *et al.*, 2011; Florsheim and Dettinger, 2015). Studies also pinpointed areas of heightening the risk of landfalling ARs (along the western USA. and western Europe, etc.) at present and for future, and have made strides in AR forecasting and prediction abilities (Lavers *et al.*, 2020). The Himalayan regions are also naturally prone to water-induced hazards, due to climate, topography, and geological formations. In this context, these mountains assume an important role in intensifying hazards by determining water vapor loss from ARs. The severity impact of ARs (or AR events) depends on the interaction with local topography, besides intensity, duration, integrated water vapor transport direction, AR orientation, and synoptic scale. Notably, regions with uneven terrains intensify the impacts by effectively extracting moisture from ARs through orographic processes (Lamjiri *et al.*, 2017; Viale *et al.*, 2018). For instance, over California mountain complex in west coast USA, precipitation was four times greater on the windward side of coastal and inland mountains than on less elevated areas around the mountains (Smith *et al.*, 2010). Recently few studies have recognized ARs as the leading cause of major flood events in south India (Lakshmi and Satyanarayana, 2019; Lyngwa and Nayak, 2021). (Lakshmi and Satyanarayana 2020) found that 40% of extreme precipitation was linked to the presence of ARs landfalling over the Indian coastlines. A study found that nearly 35% and 70% of the annual and non-monsoon precipitation maxima in western Nepal, occurred during ARs (Thapa, Endreny and Ferguson, 2018). Recently, Nash et al., (2021) studied the synoptic characteristics related to ARs that impacted the High Mountain Asia.

The moisture transported into a region from neighboring water surfaces is the most important component in moisture recycling and the climate system. It returns to the surface as precipitation, and influences a region's annual average precipitation. Intense moisture transport generally leads to excess precipitation, while weak transport deprives regions of water supply. India receives substantial precipitation during boreal summer months, due to the greater height of moisture in the atmospheric column in tropical regions. High amounts of the moisture transported out of the tropical waters over South Asia is intercepted by the Himalaya. Moisture transport in the tropics is highly dependent on the divergent (or convergence) part of the wind fields (Trenberth, 1991). Moreover, precipitation is directly associated with the field of convergence rather than with high values of water vapor flux (Starr, Peixoto and Livadas, 1958; Tan *et al.*, 2022) or moisture derived from evaporation in situ. In the tropics, precipitation also exceeds evaporation because the trade winds converge with moisture (Seager, Naik and Vecchi, 2010). Additionally, atmospheric moisture also precipitates due to strong convective heating primarily during summer monsoons (Baisya *et al.*, 2018). Since the association between the water vapor changes, atmospheric processes, precipitation, and evaporation are constrained by the moisture budget equation, this analysis is performed to study the dynamic/thermodynamic processes associated with ARs and precipitation generation (Starr and Peixoto, 1958; Peixoto and Oort, 1992). The analysis breaks down the individual terms of moisture budget to will help understand the regional modification to precipitation intensity during ARs. While many studies have focused on studying the characteristics of ARs, there is relatively little focus on the processes that contribute to AR moisture.

A typical signature of AR-generated precipitation is the absence of upward vertical motion of lower tropospheric moist air due to convection, and instability is mainly initiated by the motion of fronts in the atmosphere and the presence of high mountains (Smith *et al.*, 2010; Cordeira, Ralph and Moore, 2013). Our analysis confirms these signatures, as detailed in the sections ahead. ARs of different types (classified based on three distinct circulation patterns (Tan *et al.*, 2020)) associated with extreme precipitation (above the 90th and 99th percentile of daily winter precipitation) in western North America, were due to the dominant role of moisture convergence (mostly the mean moisture by transient winds) than due to local rate of change of moisture (Tan *et al.*, 2022). A comprehensive investigation of the moisture budget equation in different sectors of AR (post-frontal, frontal, pre-frontal, and pre-AR) was shown by Guan et al., (2020). Their findings revealed specific-sector dominance of different terms: post-frontal showed moisture loss, moisture advection, and reduced precipitation; frontal exhibited gain in mass convergence (component of moisture flux convergence), and higher precipitation; pre-frontal involved high moisture content, positive moisture advection but reduced precipitation; and pre-AR showed weak moistening of atmosphere, weak positive advection that produced minimal precipitation (Guan, Waliser and Ralph, 2020). Precipitation is also modulated by the AR characteristics (orientation, intensity, duration, etc.), their associated weather systems, and topography (Hughes *et al.*, 2014; Lamjiri *et al.*, 2018; Albano, Dettinger and Harpold, 2020). In addition, a strong positive correlation is found between bulk bias AR IVT direction and convergence in the frontal and pre-frontal (Guan, Waliser and Ralph, 2020). In AR events studies, the water vapor changes over a region are strongly correlated with the moisture flux convergence (non-local moisture sources) (Mo *et al.*, 2019) rather than evaporation (Zangvil *et al.*, 2010) but as pointed out above that may be valid for certain regions within the AR. The addition of moisture influences the local change in water vapor content (integrated water vapor or IWV). Precipitation rate is linearly correlated to the dynamical convergence of water vapor (Norris *et al.*, 2020). Moist air propagating in the lower atmosphere (<1 km) is a critical ingredient to moisture flux convergence associated with orographic precipitation enhancement in midlatitude coastal mountains (Neiman *et al.*, 2011). The processes driving the signs (and strength) of moisture flux convergence is the asymmetrical balance between its components: advection and mass convergence. For example, a strong positive moisture flux term is driven primarily by a significant positive mass convergence term with a minor role of the advection term, which is mostly driven by the physical environment of the AR. Conversely, when the advection term dominates, the moisture flux becomes negative. These dynamics exhibit large variations across selected subregions but generally display low magnitudes when considering the overall selected region (Norris *et al.*, 2020). Their study also highlighted that by increasing the uncertainty range for the temporal fidelity of the observed time-difference IWV, the closer it gets to the moisture budget closure.

As regional precipitation depends greatly on atmospheric circulation, we also examined moist air parcels' track history before precipitation during AR events to gain insights into the possible driving circulation that influenced their paths (Tan *et al.*, 2022). While the computation of integrated water vapor fluxes can reveal the paths of moisture transport, it may not directly pinpoint the sources and sinks of water vapor (Wei *et al.*, 2012). However, by tracking the changes in specific humidity along the path of air parcels it becomes possible to determine the sources' location and establish the connections between precipitation at one location to the contributing evaporation sources. If additional variables are tracked it can provide more information on the parcel's characteristics (e.g., air temperature, pressure, etc.) over time. The losses and gains of moisture by air parcels along their path indicate the locations that influence moisture content within the parcels related to thermodynamic changes particularly if these incidences occur within the boundary layer (Sodemann, Schwierz and Wernli, 2008b). The most important sources of moisture supply to events on land are generally found along the path of transport, with the sources over oceans playing the greater role in initiating the transport (Wei *et al.*, 2012). The major oceanic sources contributing to precipitation in South Asia include the Arabian Sea, Bay of Bengal, Indian Ocean, and moisture arriving from the Seas of Middle East (Pathak *et al.*, 2017). The variability in moisture supply from these sources can directly impact the precipitation over the subcontinent. Similarly, variability of moisture sources due to alterations in precipitation processes, moisture transport, or evaporation can also lead to precipitation variability, for instance, during the positive phase of ENSO, moisture contribution from the Arabian Sea, Bay of Bengal, and Indian Ocean increases, particularly there is anomalous convection (subsidence) in western (eastern) Indian Ocean and excess moisture is transported to continental regions (Horan *et al.*, 2023). This also leads to wetter conditions over eastern Africa due to ENSO. Therefore, in addition to tracking the parcels' path, we quantify the relative contributions of the sources to atmospheric moisture reaching the target region before precipitating following the method by Sodemann et al. 2008). The moisture leading to precipitation is discounted and adjusted based on prior evaporation and precipitation processes in the Lagrangian approach for backward trajectory analysis. This approach has been used to study the natural dynamic and thermodynamic mechanisms influencing air mass flow evolution in time (Fremme and Sodemann, 2019; Keune, Schumacher and Miralles, 2022; Hochman *et al.*, 2023). The objectives in this chapter include (1) study their characteristics, such as intensity, duration, seasonality, etc. (2) identify major physical mechanisms for extreme precipitation, analyze their thermodynamic properties, and distinguish tropospheric instability near mountains and plain areas, (3) understand the thermodynamic and dynamics nature of extreme ARs, by locating the major sources of moisture carried by them. The objectives (2) and (3) focus on the top 8 AR events in IB and GB.

4.2. Materials and Methods

Meteorological data used in the study, include specific humidity (q; 'kg/kg'), precipitation (P; 'm'), evaporation (E; m of water equivalent); zonal winds (u; 'm/s'), meridional winds (v; 'm/s'), etc., from ERA5 (Hersbach, Bell, Berrisford, Hirahara, Horányi, Muñoz-Sabater, Nicolas, Peubey, Radu, Schepers, Simmons, Cornel Soci, *et al.*, 2020) of the ECMWF (European Centre for Medium-Range Weather Forecasts). This data has a high horizontal resolution of $0.25° \times 0.25°$ (~31 km globally), a high vertical spatial resolution of 37 pressure levels, and a high temporal resolution of hourly available since 1950. ERA5 has improved performances over its predecessors, especially in simulating the dynamics of the lower atmosphere, where ARs are located. It provides a better representation of precipitation over core tropical land regions and a more accurate portrayal of atmospheric circulations, cyclones, etc. (Hersbach *et al.*, 2019; Hersbach, Bell, Berrisford, Hirahara, Horányi, Muñoz-Sabater, Nicolas, Peubey, Radu, Schepers, Simmons, Cornel Soci, *et al.*, 2020). Here, q, u, and v were retrieved at six-hour intervals (00, 06, 12, and 18 UTC for a given day), which is preferred for several key reasons, it (1) aligns with the common time intervals used in AR detection algorithms with reanalysis datasets (Rutz, Steenburgh and Ralph, 2014; Guan and Waliser, 2015; Mundhenk, Barnes and Maloney, 2016; Brands, Gutiérrez and San-Martín, 2017), (2) provides sufficient temporal details of AR events and captures gradual changes of AR characteristics (Ramos *et al.*, 2015; Nash and Carvalho, 2020), (3) found minor differences in AR characteristics when the temporal resolution is varied from 6-hourly to 1-hourly or from 6-hourly to 3-hourly (Rutz, Steenburgh and Ralph, 2014; Guan and Waliser, 2015, 2017; Shields *et al.*, 2018), and (4) is easily-manageable on a desktop machine compared to hourly data, with only slight compromise on the level of information about AR characteristics. For instance, if an AR is detected at 06 UTC, we include data from 01 to 05 UTC in the AR-duration assessment, while if no AR is detected at any one-time step, only 5 hours of data may be missed at most.

Daily gridded ($0.25° \times 0.25°$) rainfall observational data from the India Meteorological Department (IMD) are used to observe rainfall intensity over India during the main AR events. The Shepard's inverse distance weighted interpolation (Shepard, 1968) is used (assuming that stations within 1.5 degrees around the grid point have similar rainfall characteristics) to develop this gridded data from 6955 observed sites (Pai *et al.*, 2014).

The topographic gradient map was generated using Global Digital Elevation Model (DEM) data from NASA's Shuttle Radar Topographical Mission (SRTM) (Farr *et al.*, 2007) of the United States Geological Survey (USGS https://earthexplorer.usgs.gov/). The SRTM 1 Arc-Second Global, void filled using ASTER (Advanced Spaceborne Thermal Emission and Reflection Radiometer) GDEM2, GMTED2010 (Global Multi-Resolution Terrain Elevation Data 2010) and NED (National Elevation Dataset), has a spatial resolution of 30m x 30m, and much lower absolute vertical error than its predecessor, SRTM 90m. Visual verification confirmed the absence of mission tiles or voids over our study region. The data was projected from WGS1984 to the UTM coordinate system and resampled to 10 km by 10 km for gradient calculation.

The date and time of cyclones over the Arabian Sea, Bay of Bengal, and continental India are collected for the study period 1982–2018 from the Regional Specialized Meteorological Centre (RSMC, www.rsmcnewdelhi.imd.gov.in), India, for tropical cyclones over the North India Ocean.

4.3. Methods

4.3.1. Integrated water vapor transport

One of the key characteristics of ARs is the strong horizontal moisture flux in the lower atmosphere. Horizontal moisture flux is difficult to directly observe and is rather estimated, unlike visual identification of ARs using Integrated Water Vapor (IWV) from satellite images (Ralph, Neiman and Wick, 2004; Neiman *et al.*, 2008; Ralph and Dettinger, 2011). We require q, u, and v to compute the horizontal moisture flux at different atmospheric levels, which is then integrated from 1000 hPa to 300 hPa to yield $\overrightarrow{IVT}$. Here, the IVT magnitude at each location is calculated from integrated zonal and meridional moisture fluxes, as shown in Equation 3 below.

$$IVT = g^{-1}\sqrt{\left(\int_{1000hPa}^{300hpa} qudp\right)^2 + \left(\int_{1000hPa}^{300hpa} qvdp\right)^2} \qquad (3)$$

where, "IVT" is in $kg. m^{-1}. s^{-1}$, "q" is in $kg. kg^{-1}$, "u" and "v" are in $m. s^{-1}$, "g" is the acceleration due to gravity (9.81 $m. s^{-2}$), and "dp" is the atmospheric layer thickness in Pascals ($kg. m^{-1}s^{-2}$). In the present study, IVT is computed at a 6-hourly scale from 1980-2018 considering only periods with available satellite data.

4.3.2. AR Identification Algorithm for Himalaya

In this study, we modified the AR algorithm by Lavers *et al.*, (2012) (L_{AR}2012) because (i) it is simple to set a detection transect (ii) flexible thresholds can be used based on regional climate, and (iii) it has been successfully applied in different parts of USA and Europe (Lavers and Villarini, 2013b, 2015a, 2015b; Nayak, Villarini and Bradley, 2016; Barth *et al.*, 2017; Nayak and Villarini, 2017).

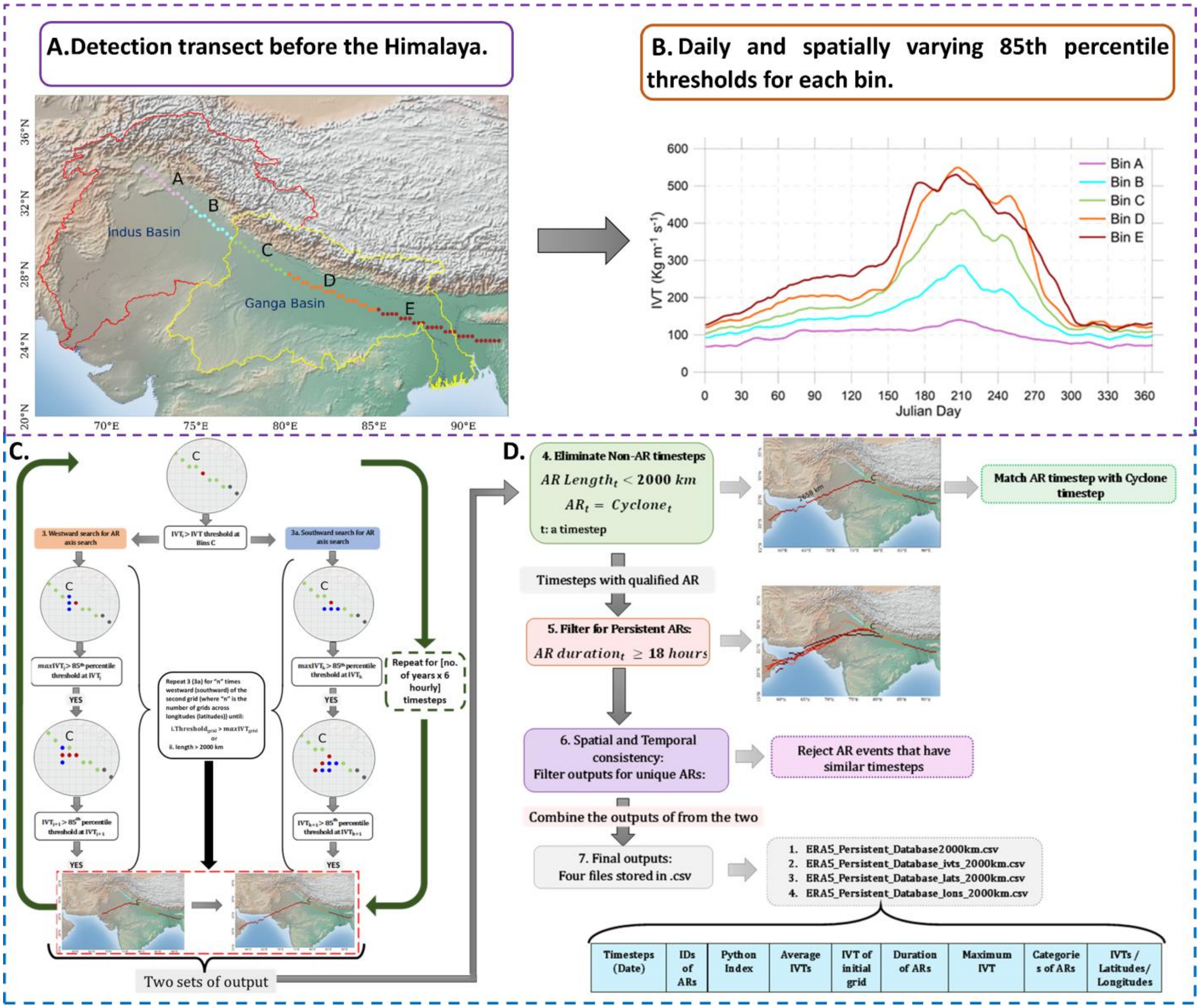

Figure 4.1: *Flowchart of the algorithm used for detecting ARs over the Himalaya. Top panels (a and b) are the primary steps in the algorithm, Panel a: the detection transect (composed of ERA5 grids, and represented by different colors for bins A - E) established south of the Himalaya. IB and GB boundaries are shown by thin and yellow lines respectively. Panel b: Daily IVT thresholds of the bin. Bottom panel: Main steps in the AR identification algorithm, Panel c: The step-by-step processes in the grid-wise search for the AR major axis.*

The working of the AR algorithm is shown in Figure 4.1. [1] A geographical detection transect following the Himalayan arc was defined just south of the Himalayan range (average elevation < 200 m), spanning ~2,000 km from $72°E$ to $92°E$, excluding rugged terrains where moisture depletion may hinder AR identification (Figure 4.1A). [2] To distinguish potential ARs from the background moisture, the 85th percentile IVT thresholds (Lavers and Villarini, 2013a; Nayak, Villarini and Lavers, 2014) were computed for 366 days at all grids, instead of a single threshold for the entire transect (Lavers *et al.*, 2012) and time period (Lavers and Villarini, 2013b). To reduce high IVT variability, we segmented the transect into five bins (Figure

A, bins A-E) based on the climatological latitude-dependent IVT variations. Bin thresholds are then computed as the spatial average of grid thresholds within the bin and the resultant time series are shown in Figure 4.1 (Panel B). [3] The algorithm focused on identifying the major axis of potential AR features. At each timestep, the grid with the highest IVT on the transect, exceeding the bins' threshold is designated as the primary grid of the axis (maroon-colored dot in Panel C, e.g., grid "i" on Bin C). The second grid (say grid "j" in maroon) forming the major axis is chosen from three adjacent grids west of the primary grid "i" (center, north, and south cells shown in blue) with the highest IVT ($\mathrm{maxIVT_j}$) that also exceed the grids' 85th percentile threshold. The subsequent grid (say grid "j+1") search continued westward from the second grid "j" and retained if the IVT is above the threshold, but terminates if (1) the selected grid's threshold does not exceed its $\max \mathrm{IVT}$, or (2) the axis length reaches 2,000 km. Features with axes longer than 2,000 km were identified as ARs and their corresponding timesteps were recorded as AR timesteps. The 2,000 km length criterion is consistent with previous studies (Wick, Neiman and Ralph, 2013; Guan and Waliser, 2015; Ralph, Rutz, *et al.*, 2019, 2019; Shearer *et al.*, 2020). The width criterion was not considered as features longer than 2,000 km typically fulfill the shape requirements of being an AR (Rutz, Steenburgh and Ralph, 2014). Similarly, the search was performed in the southward direction from the first grid "i" (step 3) and all timesteps designated as AR timesteps were compiled. The outputs obtained from the searches are a series of grids forming an axis for the timestep (Panel C, bottom red color box). The two processes are repeated for "$6\text{ hourly} \times \text{no. of days} \times \text{no. of years}$" timesteps and the outputs from each search are stored simultaneously and separately. Criteria for qualifying an axis as AR's is applied sequentially. [4] Since cyclones can occur simultaneously near ARs, these timesteps were removed from AR timesteps compiled in step [3], as they are considered distinct features (Zhou, Kim and Guan, 2018; Guan and Waliser, 2019). In this study, only the period from 1982 to 2018 was considered for investigation as the cyclone timesteps were available only from 1982 onwards. [5] Short-lived ARs with a duration less than 18 hours, (three continuous 6-hourly timesteps) were excluded, as they typically produce low precipitation as observed for ARs in western USA (Albano, Dettinger and Harpold, 2020), northwest coast Europe (Eiras-Barca *et al.*, 2021), and west coast of India (Lakshmi and Satyanarayana, 2019) (axes of an AR event that persisted over 18-hours are shown by different shades in Panel D). The long-duration AR is referred to as an "event" or "AR event" and its total time period is referred to as AR duration. [6] To ensure uniqueness, records from the westward and southward searches were merged and reviewed. If an event was repeated or matched in at least one time step, then the event with the smaller average IVT magnitude was removed, while unique events were unmodified and stored. This maintains spatial and temporal consistency. The final ARs are stored with information on AR event characteristics, including timesteps, duration, latitudes, longitudes, maximum and average IVTs, IVT of the first grid, and AR categories in .csv files (Panel D). The average IVT magnitude of an AR event is the average over the major axes of that event.

4.3.3. Scheme to categorize AR effects in Himalaya

The identified ARs are examined to understand their potential regional impacts. Most ARs are largely beneficial for water supply, for instance, such as in California, where ARs contribute $\sim 50\%$ of the annual precipitation (Eiras-Barca *et al.*, 2021). The impacts vary with AR intensity, duration, and locations, and adopting a practical approach to understanding these impacts holds significance from a water resources perspective. Ralph et al. (2019b) designed an objective scale to categorize ARs and associate their likely impacts for the western USA, using two important variables: peak instantaneous IVT magnitude of AR event and duration of AR conditions over the location. This scale, akin to the scale for hurricanes and tornadoes (Fujita, 1970), aims to assist water managers, policy-makers, and emergency managers in making informed decisions during AR storms, with categories ranging from Category 1 to Category 5 (Category is abbreviated as Cat, hereafter). The categories range from beneficial, Cat 1 and Cat 2, having short duration and low IVT magnitude; to balanced and occasionally hazardous as Cat 3 and Cat 4 with short to long durations, and most damaging as Cat 5 with long duration. Since this scale (Ralph, Rutz, *et al.*, 2019) was based on ARs that made landfall on the west coast USA., they selected $250\ kg.m^{-1}.s^{-1}$ as the lower limit for IVT threshold and adjust the scale based on increments of $250\ kg.m^{-1}.s^{-1}$. As the scale is location dependent and much more useful in regions of dominant AR storms, this scale can also be very useful to classify ARs in the Himalaya. Climatologically, the Himalaya differs from the USA., leading to varying IVT thresholds across seasons and latitudes. Generally, non-monsoon days have thresholds below $250\ kg.m^{-1}.s^{-1}$, and the overall magnitude of IVT thresholds decreases from Bin A to E (Figure 4.2, Panel A-2). The threshold of $250\ kg.m^{-1}.s^{-1}$ used in the USA scale (Ralph, Rutz, *et al.*, 2019) is too high for the Himalya, where IVT is generally low. To accommodate this difference, the scale was modified to propose a region-specific AR categorization as shown in Table 4.1, based on instantaneous peak IVT (maximum IVT) ($IVT_{\max}$) of the first grid on the transect of each major axis of AR events. Unlike the previous scale (Ralph, Rutz, *et al.*, 2019; Guan, Waliser and Ralph, 2023), in this categorization even the ARs with $IVT_{\max}$ below $250\ kg.m^{-1}.s^{-1}$, referred to as "weak ARs", were considered and classified under "Cat0". This will account for the importance of such ARs, as observed in cold climes of polar regions, such ARs play an important role in regional precipitation (Gorodetskaya *et al.*, 2014; Mattingly, Mote and Fettweis, 2018; Nash *et al.*, 2018; Wille *et al.*, 2019). Certainly, Table 4.1 can be improved to better describe AR impacts in the Himalaya, for future operational uses. Currently, this categorization helps analyze the climatology and local impacts of ARs of various intensities in Himalaya.

Table 4.1: A scheme to categorize ARs in the Himalayas based on their intensity ($kg.m^{-1}.s^{-1}$) and duration (hours). The categories are labelled from 0 to 5 with mostly beneficial categories being Cat 0 to Cat 2, and mostly hazardous are Cat 3 to Cat 5, following (Ralph, Rutz, *et al.*, 2019).

Table 4.1: Categorization of Himalayan ARs

IVT_{max} $(kg.m^{-1}.s^{-1})$ \ AR Duration (hrs)	≤ 24	$24-48$	≥ 48
≤ 250	0	1	2
$> 250-500$	1	2	3
$> 500-750$	2	3	4
$> 750-1000$	3	4	5
$> 1000-1250$	4	5	5
> 1250	5	5	5

4.3.4. Diagnostic Computation of Moisture Budgets of top AR events

The relationship between the terms in the moisture budget is constrained by the moisture continuity equation, which has two major terms leading to precipitation, moisture convergence into the closed system (Control Volume), and large-scale vertical motion (local evaporation). For a column of air from 1000 hPa to 300 hPa, at each grid, assuming hydrostatic balance is given by the following equation (Trenberth and Guillemot, 1995)

$$\frac{\partial IWV}{\partial t} + \nabla.\overrightarrow{IVT} = E - P + R \tag{4}$$

where,

$\frac{\partial IWV}{\partial t}$ is the time change of vertically integrated moisture content or the atmospheric storage; IWV is the mass integral of q (kg/kg) or total precipitable water $(kg.m^{-2})$; $\overrightarrow{\mathrm{IVT}}$ is instantaneous IVT vector $(kg.m^{-1}.s^{-1})$, analogous to aerial runoff (Peixóto and Oort, 1983), t is the time (s); ∂t is the time step (1 hour in this analysis); P is the precipitation rate (solid and liquid phases) over '∂t' (mm); E is evaporation rate over '∂t' (mm), which includes transpiration from vegetated land; and R is the residual between the budget terms, possibly related to reanalysis data assimilation method for which the magnitudes can be nontrivial or comparable to moisture flux divergence magnitudes (Minallah and Steiner, 2021)

$$IWV = \frac{1}{\mathrm{g}} \int_{1000\,hPa}^{300hPa} q\, dP \tag{5}$$

The negative of $\nabla.\overrightarrow{\mathrm{IVT}}$ gives the Moisture Flux Convergence, which is shown in the results. The flux terms, $-\nabla.\overrightarrow{\mathrm{IVT}}$ can be split into its component parts as shown in Equation 6: vertically integrated horizontal advection of moisture (right-hand side, first term), vertically integrated water vapor convergence (right-hand side, second term), and the surface terms (right-hand side, third term).

$$-\nabla.\overrightarrow{\mathrm{IVT}} \quad = -\frac{1}{g}\int_{1000\ hPa}^{300hPa} \nabla.(\bar{V}q)dP$$
$$-\nabla.\overrightarrow{\mathrm{IVT}} \quad = -\frac{1}{g}\int_{1000\ hPa}^{300hPa} \bar{V}.(\nabla q)dP - \frac{1}{g}\int_{1000\ hPa}^{300hPa} q(\nabla.\bar{V})\ dP + \frac{1}{g}q_s\bar{V}_s\nabla p_s \tag{6}$$

and,

$$\vec{\mathrm{V}} \quad = \hat{\imath}\frac{1}{g}\int_{1000\ hPa}^{300hPa} q.\bar{u}\ dP + \frac{1}{g}\hat{\jmath}\int_{1000\ hPa}^{300hPa} q.\bar{v}\ dP \tag{7}$$

$\hat{\imath}$ and $\hat{\jmath}$ are unit vectors along zonal and meridional directions; q_s is the specific humidity near the Earth's surface, $\bar{V}_s$ is the wind vector near the Earth's surface. The surface terms ($\frac{1}{g}q_s\bar{V}_s\nabla p_s$) is introduced when the divergence operator $\left(\nabla = \mathrm{i}\frac{\partial}{\partial x} + \mathrm{j}\frac{\partial}{\partial x}\right)$ is taken inside the vertical pressure integral of IVT, splitting the divergence of IVT into its components parts, and it is not included here, because it is often very small compared to the other terms in the equation (Seager *et al.*, 2007; Seager and Vecchi, 2010; Guan, Waliser and Ralph, 2020), and 'q' is assumed to be zero at the top pressure level. All units are presented in '$mm.day^{-1}$' for ease of comparison.

To minimize the impact of changing wind directions related to small weather systems in fine spatiotemporal resolution data (Minallah and Steiner, 2021), we performed the budget analysis at an hourly scale using ERA5. 'R' in equation (4) represents errors arising from multiple sources, including coarse spatial/temporal discretization, few atmospheric pressure level segmentation, physical parameterization, data assimilation limitations, and methodological errors (approximate numerical solution), that hold no physical interpretation, but remains significant and cannot be ignored (Dominguez *et al.*, 2006). They introduce biases in the moisture budget, resulting in the non-closure of the mass balance. They stem from numerical methods differing from those used in the models, and the diagnostic evaluation of divergence (or convergence), i.e., $\nabla.$, being the largest single error source(Seager and Henderson, 2013).

The advection term describes horizontal air movement between locations impacting local humidity hence precipitation. Cold, dry air advection reduces the humidity and temperatures over land, while it enhances large-scale evaporation and moisture transfer over oceans (Aemisegger and Papritz, 2018). Conversely, warm, moist air advection increases land temperature and humidity (You, Tjernström and Devasthale, 2021), while decreasing ocean evaporation (Seager *et al.*, 2003). The convergence/divergence term indicates moisture accumulation/dispersion in an area due to winds. Here, it is assumed that no water vapor exits through the top of the control volume (300 hPa) since q is near zero. The equation may then be written as Peixoto and Oort, (1992)

$$\langle\frac{\partial IWV}{\partial t}\rangle + \langle\nabla . IVT\rangle = \langle E\rangle - \langle P\rangle + \langle R\rangle \tag{8}$$

where, the bracket $\langle . \rangle$ denotes a spatial average over the control volume. Calculating the spatial averages reduces spatial displacement errors and allows for an appropriate characterization of the regional moisture budget. Thus, the regional-scale moisture budget was computed for Indian regions of IB and GB that have IVT $\geq 300\ kg.m^{-1}.s^{-1}$ for strong ARs, and $\geq 200\ kg.m^{-1}.s^{-1}$ for weak ARs: (1) ahead of the detection transect, near/in elevated terrains, and (2) behind the transect, for plain regions with slope gradient < 2%(computed using the DEM of SRTM derived from USGS (Figure S4.1).

4.3.5. Three dimensional trajectories of air parcels during AR events

The paths of air parcels that precipitated during the top AR events are tracked using the HYbrid Single Particle Lagrangian Integrated Trajectory (HYSPLIT) model version 5.2.1 (Draxler and Hess, 1997; Stein *et al.*, 2015). These paths represent the time-integrated advection of parcels in space (Draxler and Hess, 1998) and are essentially viewed as simple trajectories.

In HYSPLIT, air masses are modeled as particles advected by Eulerian mean wind fields (3-D wind vectors) within the model domain. If the position vector of the particle is 'Z' (latitude, longitude) at 't', the advection equation is used to determine the first guess (iterative approximation) locations ($Z'(t + \Delta t)$) (Draxler and Hess, 1998) following the iterative scheme of Petterssen, (1940)

$$Z'(t + \Delta t) = Z(t) + V(Z, t). \Delta t \tag{9}$$

where 'Z(t)' is the initial position and 'Δt' is the integrated time step, then the final location is determined as follows

$$Z(t + \Delta t) = Z(t) + 0.5[V(Z, t) + V(Z', t + \Delta t)]. \Delta t \tag{10}$$

HYSPLIT simulations are driven by gridded meteorological data from various sources. Here, we used hourly ERA5 data for sufficient accuracy of trajectory calculations. This includes 'u', 'v' winds, vertical velocity field, temperature, humidity, geopotential height from 1000 hPa to 1 hPa; and surface variables like boundary layer height, 2 m temperature, 10 m u-and-v winds, and surface pressure. Surface values are important to avoid interpolation to the surface, between data levels and local terrain well above sea level.

We selected two locations for the trajectory analysis and major moisture sources tracking within the AR shapes, as similarly described in moisture budget analysis: near mountain foothills and plain regions Since multiple trajectories yield a robust representative of transport, we released five parcels at 2500 m above ground level (m AGL), i.e., above low-level terrains within moisture-rich lower troposphere, to avoid potential inaccuracies from undulating surfaces, and model levels below 1000 hPa that may intersect the ground and generate unrealistic trajectories by extrapolation(Draxler and Stunder, 1988; Bowman *et al.*, 2013). Here, backward trajectories are computed up to 7 days preceding the defined time, aligning with the maximum residence time of moisture in the atmosphere (Trenberth, 1998) (or <10 days as in Durán-Quesada et al., (2010) and Numaguti, (1999)). This minimizes errors in parcel's estimated locations, as longer durations become less reliable due to errors in wind fields (Bowman *et al.*, 2013), i.e., 20% travel distance errors for long-range back-in-time transport using analyzed fields (Stohl, 1998; Stohl and Seibert, 1998). Nie and Sun, (2022) also omitted the last 4 days from their 14 days backward trajectories due to significant differences in results, diverging to different locations after 10 days with very low moisture. HYSPLIT provides hourly outputs, including potential and ambient temperatures, precipitation, mixing depth, relative humidity (RH), solar radiation, terrain height, pressure, and parcel altitude.

4.3.6. Assessing key moisture sources

The average trajectory (average of five parcels released at 2500 m AGL) is computed to estimate the parcels' average moisture, air temperature, and atmospheric position. The parcels in section 3.5 were selected with RH >70%, and q should decrease at the target area. The major moisture sources of precipitation at the target area are identified using the Lagrangian moisture source diagnostic by Sodemann, Schwierz and Wernli, (2008), which assesses moisture uptake and release by a parcel from the increase and decrease in q, respectively, along its trajectory $\left(\frac{\Delta q}{\Delta t}\right)$. The fractional contribution (F) of the uptake amount (Δq_n; difference of 'q' at two consecutive timesteps, and 'n' is the location at a timestep) to moisture in the parcel 'q_n' (say) at each uptake location along the trajectory, is computed as $F_n = \frac{\Delta q_n}{q_n}$. The diagnostics then begin at the end of the backward trajectory and proceed to each timestep up to the timestep before precipitation. Starting from the end, if there is moisture uptake (Δq_n) at the next timestep ('n'), the fractional contributions of all previous moisture uptake (F_m) amounts (Δq_m (say) at 'm' locations/timesteps before 'n') with respect to this new uptake is updated $\left(F_m = \frac{\Delta q_m}{q_n}\right)$, whereas if moisture is released (of 'Δq_n^0' amount) at the next timestep ('n'), q gained in the previous steps (Δq_m) before the released is discounted proportionately as in equation (11). This method is applied to all timesteps with moisture uptake and release in the preceding steps to determine the final moisture content before precipitating at the target area. Moisture contribution (%) is computed at timesteps with moisture gained and within the mixed boundary to identify the major moisture sources, with their percentage determining their significance in precipitation over the target area. Sources of any moisture uptakes above the boundary layer cannot be reliably pinpointed as it may be due to convection, turbulence, ice-water phase change, or physical inconsistencies (Sodemann, Schwierz and Wernli, 2008a), however, recent studies have considered moisture gained immediately above the boundary layer to be indirectly related to surface evaporation of strong convection and mixing (Fremme and Sodemann, 2019). The overall relative contributions from different sources to precipitation are estimated by summing contributions at each timestep, with adjustments to moisture grained above the boundary layer. The identification of major moisture sources is performed 24 hour intervals to avoid very short-term variability, and this interval does not significantly alter the overall understanding of moisture sources.

$$F'_m = \frac{\Delta q'_m}{q_m}, \Delta q'_m = \Delta q_m + \Delta q_n^0 \times F_m, for\ all\ m > n \tag{11}$$

4.3.7. Atmospheric conditions and stability

The thermodynamic properties of the atmosphere were examined at four main locations within the AR boundary using Skew-T -Log*P* diagrams. Selected pairs of locations with heavy precipitation near the mountain foothills, left of the axis, right of the axis, and on axis, were compared for atmospheric stability, saturated levels, and energy available for vertical ascent, influencing precipitation in ARs.

For Skew-T -Log*P* plots, dew point temperature is approximated using the Bolton equations (Bolton, 1980) as

$$e = 6.112 \times exp\left[\frac{17.67 \times T_d}{(T_d + 243.5)}\right] \tag{12}$$

$$e = e_s \times \left(\frac{RH}{100}\right) \tag{13}$$

where, 'e' is vapor pressure (Pa), 'e_s' is saturated vapor pressure (Pa), and T_d is the dew point temperature (˚C). We also used the Magnus Tetens equation for dew point calculation and found comparable results (not shown in the manuscript). It was observed that above 500 hPa, RH slightly exceeds 100%, indicating supersaturation. The variables computed include Convective Available Potential Energy (CAPE), representing the potential energy (J/kg) inherent in temperature (virtual) and moisture stratification between a reference air parcel (T_{vp}) and its environment (T_{ve}) [$CAPE = R_d \int_{EL}^{LFC} \left(T_{vp} - T_{ve}\right) dp$, where R_d is the gas constant]; Level of free Convection (LFC), representing the height at which a denser and stable air parcel lifted adiabatically along dry adiabat until saturation becomes warm and less dense than its environment and rises freely; Environmental Level (EL), representing the height at which a warm and moist parcel rising along a saturated adiabat cools below its environment temperature, it is also the highest level of instability (Persing and Montgomery, 2005); Convective inhibition (CIN), representing the energy (J/kg) required to lift a parcel to LFC [$CIN = -\int_{surface}^{LFC} R_d \left(T_{vp} - T_{ve}\right) dp$]. For positive CAPE (to promote convection) CIN must be negative, thus CIN may be interpreted as the negative of CAPE. It is also essential for CIN to be non-zero yet not excessively large to prohibit convection/deep convection (Wallace, Wallace and Hobbs, 2006).

4.4. Results and Discussions

4.4.1. Climatological variations of IVT

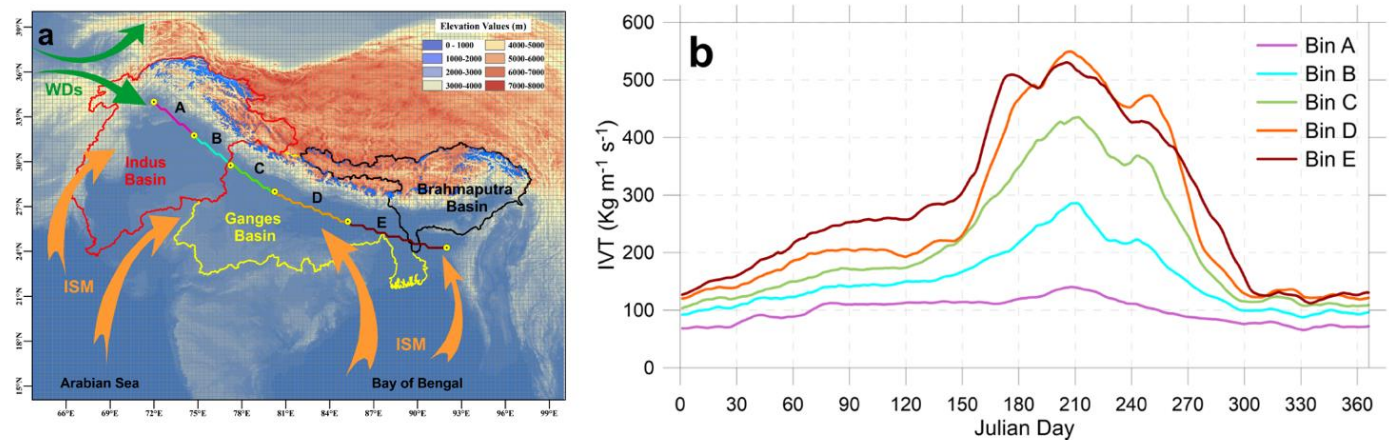

Figure 4.2: *Study region and climatological IVT of the 85th percentile thresholds in Himalaya. Panel a, is the study region over South Asia, with major basins highlighted in red for the IB, yellow for the GB, and black for the Brahmaputra basin. The detection transect at the Himalayan front is shown as a line with different colors representing the segments of each bin labelled from "A" to "E". The typical path and direction of atmospheric flow during ISM in summer and WDs in winter are shown by arrows in orange and green colors, respectively. The glacierized regions are shown by bright blue color in the Himalaya, which were retrieved from the GAMDAM inventory* (Nuimura *et al.*, 2015)*. The grid mesh in grey color is the ERA5 horizontal grids at a spatial resolution of* $0.25° \times 0.25°$*. Panel b is the climatological 85th percentile IVT for all the bins, details of which are provided in the Data and Methods sections.*

Figure 4.2 (a) shows the AR detection transect in the plains before the mountains, which is overlaid on a few ERA5 grid cells. The daily IVT thresholds corresponding to each segment of the transect (different colors) are shown in Figure 4.2 (b). They exhibit noticeable variations across seasons that emphasize the strong latitudinal disparities in moisture transport. Moreover, moisture transports are lowest during the winter-spring period (late September to late March) with magnitudes mostly below $250\ kg.m^{-1}.s^{-1}$, then abruptly increase up to $500\ kg.m^{-1}.s^{-1}$ from mid-spring to mid-autumn (April to September). These variations are due to wind speed and moisture content (Sarkar, Kuttippurath and Patel, 2023), related to seasonal variations in major circulations and air temperature. These are also latitude-dependent with Bins A and B exhibiting mostly extratropical and Bins C, D, and E being mostly tropical. The thresholds in IB (Bins A and B) are lower than the traditionally adopted value of $250\ kg.m^{-1}.s^{-1}$ (Rutz, Steenburgh and Ralph, 2014; Gershunov *et al.*, 2017), while GB (Bins C, D, and E) has higher thresholds and larger seasonal variations. Large variability in regional IVTs is influenced by the strength and reach of WDs and ISM, for example, Bin A is highly influenced by cool-season WDs in winter and spring and slightly affected by ISM, Bin B is influenced by WDs in winter-spring, and mildly by ISM in summers, Bins C, D, are influenced weakly by WDs and moderately by ISM, while Bin E is strongly influenced by ISM (Riley *et al.*, 2021), and summer cyclones (Sil *et al.*, 2021) due to its close proximity the Bay of Bengal. The variability in IVT during non-monsoon and monsoon may be caused by ARs.

4.4.2. Characteristics of ARs in Himalaya and their annual trends

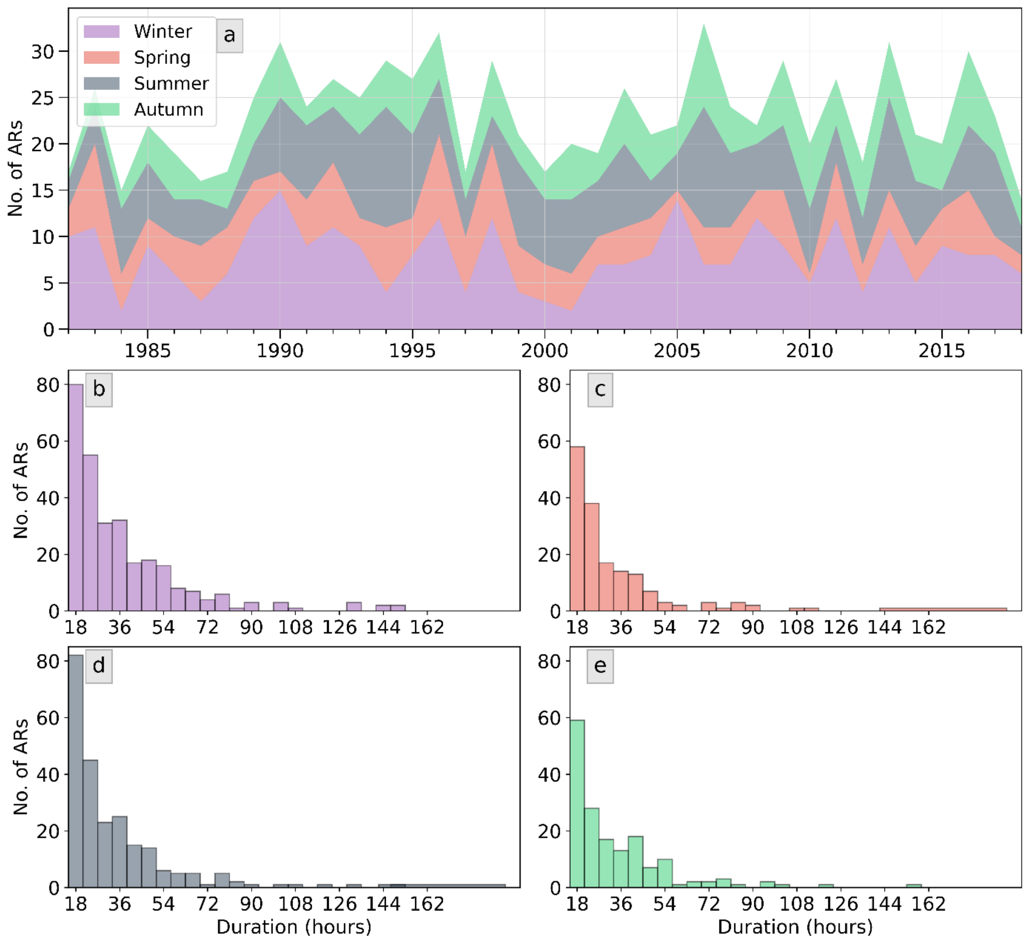

Figure 4.3: *Characteristics of ARs over the Himalaya: Panel "A" shows the yearly and seasonal frequency of ARs over the period 1982 to 2018. Panels "B", "C", "D", and "E" show the frequency of ARs and duration for Winter, Spring, Summer, and Autumn, respectively.*

ARs occur consistently each year and across all seasons with varying frequency between 1982 and 2018 (Figure 4.3A). The annual average number of ARs is 24, with the lowest (15) in 1984, and the highest (33) in 2006. The AR frequency variations may coincide with the variability of climate modes like El Niño and Indian Ocean Dipole (IOD) (Guirguis *et al.*, 2019; Lakshmi and Satyanarayana, 2020; Xiong and Ren, 2021). In 1984, there was no El-Niño (Niño3.4 index had negative SST anomalies all year, dropping below -1°C in the last two months) and a negative IOD (but above -1°C all year except April), while 2006 had El-Niño (positive SST anomalies from June-December, and above 1°C in December) and positive IOD (for July-

December, but below 1°C) Comparison was also made with values from https://psl.noaa.gov/data/timeseries/monthly/NINO34/, https://psl.noaa.gov/gcos_wgsp/Timeseries/DMI/).

Seasonal analysis showed that winter ARs are most frequent, followed by summer ARs, and likely due to the association of ARs and frequent storms (WDs) in these regions. The average frequency of ARs is 8 in winter (December-February), 5 in spring (March-May), 6 in summer (June-August), and 5 in autumn (September-November) over 1982-2018 (Figure 4.3A). Winter frequency here is higher than in Nash et al., (2021), and is attributed to less stringent thresholds in our algorithm. Most ARs have short durations of 18 hours, although some last over 72 hours (3 days), especially in winter and autumn (Figures 3B to 3E). Similarly, the median duration in winter and autumn (nearly 30 hours) is higher than in spring and summer (nearly 24 hours). Persistent ARs in western USA typically occur between October-December and January-March. In Payne and Magnusdottir, (2016), persistent ARs were supported by moisture feedback supply through moist dynamics rather than just strong winds. Comparing our findings with those from Guan and Waliser, (2019) suggests some similarity in their main characteristics (Section 2 and Figures S2a and S2b in SI) but differences in seasonal frequency exist. This is because the present algorithm identified more ARs in winter and autumn (without a lower threshold), while the Guan and Waliser, (2019) algorithm identified more ARs in spring and summer (using variable monthly thresholds to extract ARs from high moisture background, and only AR portions that co-occurred with cyclones). The approach led to a higher average frequency using the Guan and Waliser, (2019) method.

Based on the slope of linear regression of ARs with time (year), we found that seasonal AR frequency in autumn increases at 0.87 ARs/decade (p-value < 5%) in GB and decreases at 0.1 ARs/decade in IB (p-value > 5%) and in spring AR frequency decreases at 0.36 ARs /decade in IB (p-value < 5%) and 0.1 ARs/decade in GB (p-value > 5%), while the trends for other seasons are not significant even at 10% significance level (Figure S4.3).

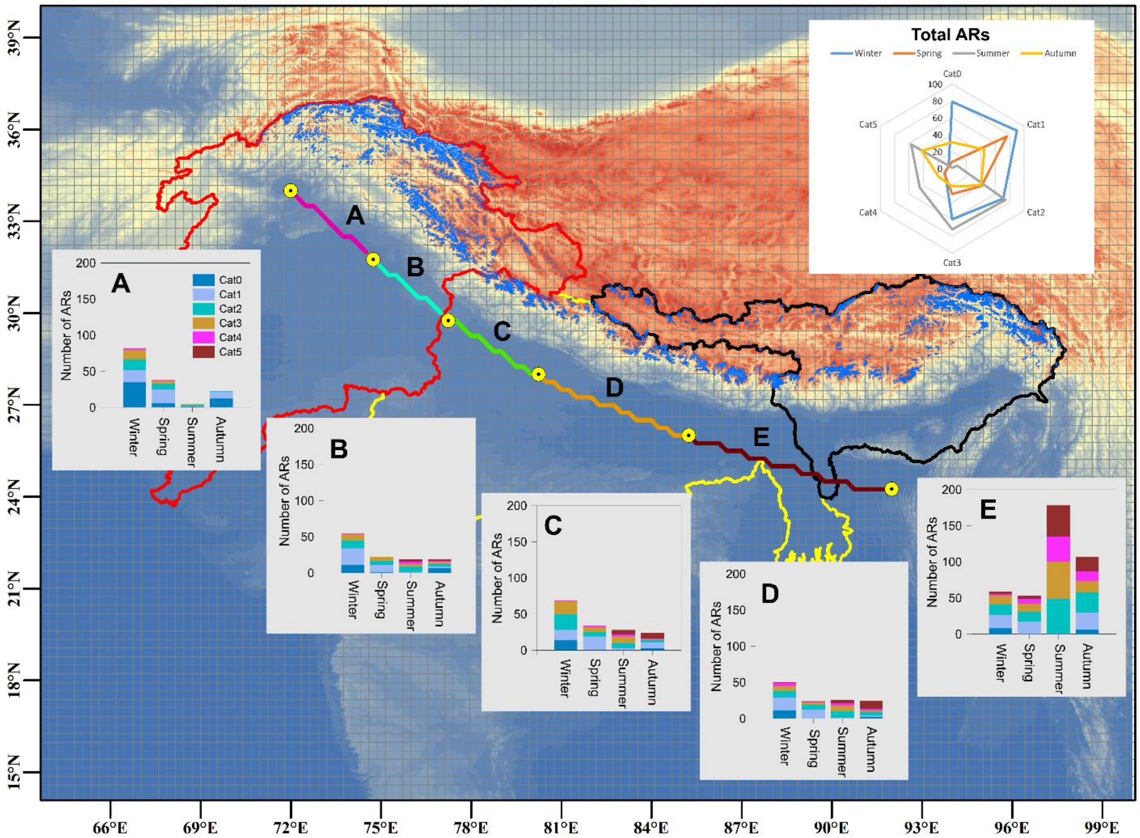

Figure 4.4: *Seasonal distribution of categorized ARs in Himalayan: The panels labelled from A to E shows the seasonal distribution of different category ARs i.e., from Cat0 to Cat5, for bins A to E respectively. The radar diagram at the top right illustrates the fractional distribution of the categorized AR in each season.*

ARs are grouped based on maximum IVT and duration for each season in different bins (Figure 4.4). When an AR is forecasted, the focused statistics facilitate a prompt assessment of the potential impact of an AR, which can help prepare swift responses. All bins except Bin E, have the highest frequency of ARs in the winter season possibly linked to increased WD activity. The seasonal frequency is below 50, except in winter, while in Bin E it is above 50 for all seasons. The large difference between Bins A and E reflects the influence of moisture transport on IB and GB. In the radar diagram, winter-spring ARs belong to Cat0-Cat3 mostly under Cat0-Cat1 (beneficial), while summer ARs are mostly Cat2 or higher with a majority under Cat3 (beneficial and hazardous).

4.4.3. Assessing the impact of intense AR events on regional precipitation

The importance of ARs to a region most markedly manifests in their ability to influence the region's hydrology (Michaelis *et al.*, 2022). AR-landfall impacts two key regional hydrometeorological variables: precipitation and temperature. AR-related precipitation variations are additionally shaped by geographical factors like regions' location, land characteristics, and topography, which ultimately affect the region's hydrological response to ARs (Chen *et al.*, 2019).

To illustrate the impacts of the Himalayan ARs on regional precipitation, the top two AR events (highest IVT and long durations) that affected each basin are shown in Figure 4.5. In all four IVT panels, a region of an intense and narrow band of IVT is seen in the Arabian Sea and some in parts of India. The ARs in IB have high IVT ($> 500\ kg.m^{-1}.s^{-1}$) in northwest India, the Arabian Sea, and the southward slopes of the Himalaya. Precipitation maps for two days following the AR timestep (Panels a1-a2 and b1-b2, with adjusted time overlap for precipitation from IMD (IST) and IVT from ERA5 (UTC)) showed intense precipitation along the AR tracks, in mountainous regions of central and western India. At the location where ARs hit the Himalaya, precipitation exceeded 150 mm/day, and beyond this location (Lesser and Greater Himalaya of elevation ranging between $3{,}700 - 6{,}100$ m), in regions of decreased IVT precipitation exceeded 65 mm/day. Additionally, the ARs triggered widespread precipitation (< 50 mm/day) in surrounding areas, highlighting their extensive spatial impact. These mountains are crucial for generating orographic precipitation, and essential water resources for the downstream plains (Azam *et al.*, 2021), while also being the chief cause for flash floods and landslides (Rao et al., 2016). On the west coast of USA, Ralph *et al.*, (2006) found that major orographic precipitation in California resulted from AR interaction with coastal mountains. In GB, ARs have high IVT (> $500\ kg.m^{-1}.s^{-1}$) in the northwest India, central Arabian Sea, and Bay of Bengal. Similarly, it can be observed that higher precipitation (>50 mm/day) is found in mountains, foothills, and hilly areas.

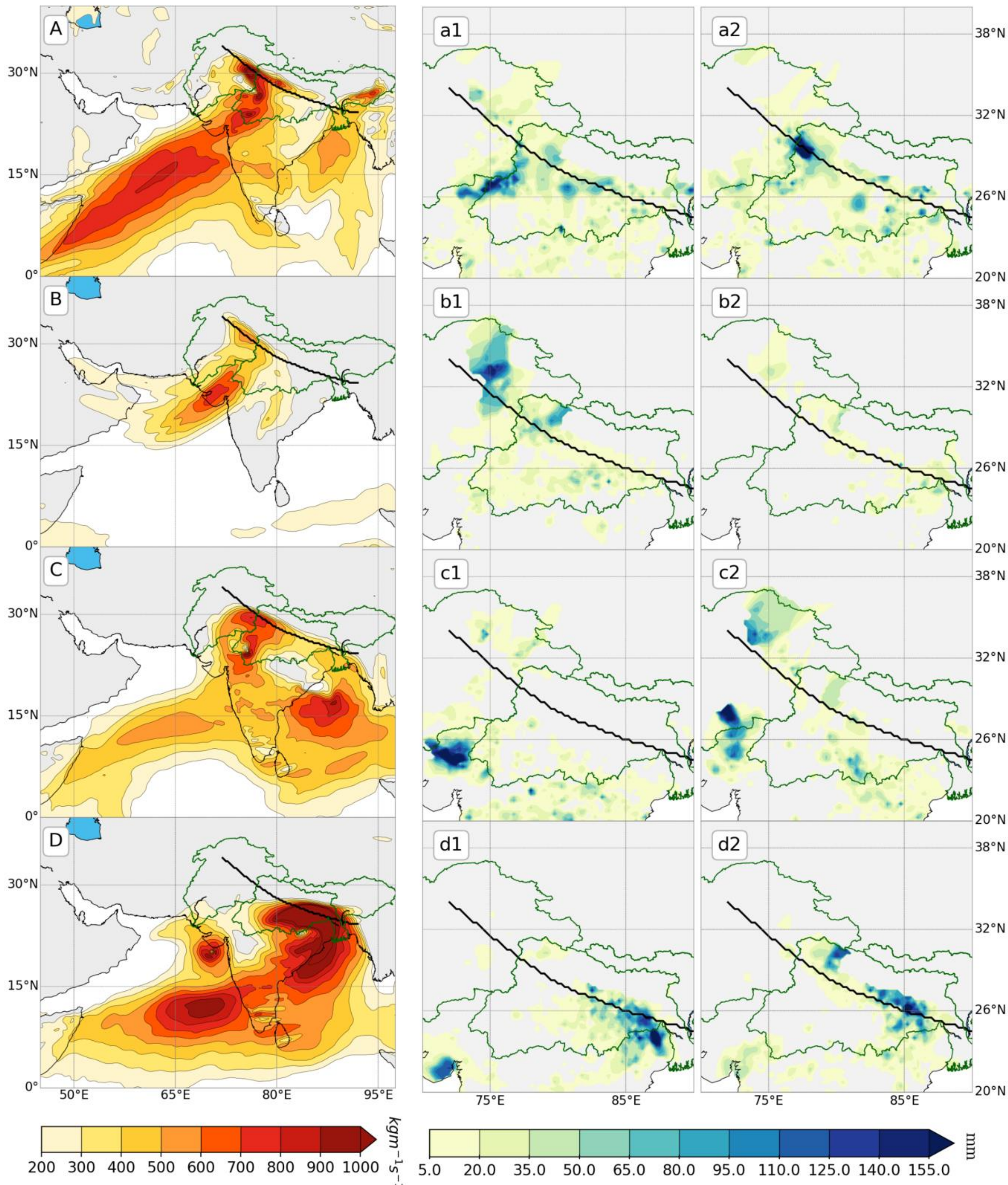

Figure 4.5: *Impact of AR on precipitation: Panels A to D show IVT ($kg.m^{-1}.s^{-1}$) during the highest and second highest intensity ARs, with durations of more than 3 days, over the IB: panel A shows an AR on the 26th July 1983 at 18 UTC, and panel B shows an AR on 18th February 2003 at 12 UTC, and over the Ganga basin: panel C shows an AR on 06th September 1992 at 12 UTC, and panel D for AR on 21st September 2007 at 00UTC. The panels a1 to d2 show the second- and third-day precipitation totals (in mm; IMD) after the AR occurred.*

We compared precipitation during the four events with extreme climatological thresholds over the region, i.e., the 95th (around 70 mm) and the 99th percentiles (between 90-125 mm) for wet days > 2 mm per day, to understand the scale of AR-induced extreme precipitation. The one-day precipitation exceeded 150 mm at multiple locations (Panels a1 to d2), surpassing the 99th percentile. Such heavy precipitation occurs infrequently over a year (with return periods of 20 and 100 years for the 95th and 99th percentile, respectively), and contributes a major fraction of the annual basin precipitation. To establish the strong AR-high-impact precipitation link, 6 more intense AR events for each basin were analyzed (Figures S4–S5), with 9 out of the 12 generated heavy precipitation, particularly over the mountains. Most winter ARs primarily affect mountains and influence the region's glacier mass balance. Himalya have around 39,660 glaciers (Nuimura *et al.*, 2015) that may be impacted by ARs. ARs, known to transport warm moist air (Shields *et al.*, 2019) from tropical basins, alter snow accumulation patterns in elevated regions (Neiman *et al.*, 2008; Guan *et al.*, 2013, 2016) depending on how far inland they reach. From this Figure 4.5, we suggest careful studies to understand AR influence on Himalayan glacier mass balance.

4.4.4. Major mechanisms leading to precipitation during extreme AR events

Figure 6 shows the moisture budget terms (using equations 4 and 5) at each grid for a timestep of one AR event: 18th February 2003 12 UTC (event: 16th February 2003 06UTC to 19th February 2003 00UTC; IVT_{max} = 671.6 kg.m^{-1}.s^{-1}; and duration = 66 hours; CAT4 AR) (Total moisture flux convergence is shown in Figure S4.6). IVT and IVT vectors within the AR shape (IVT≥ 300 kg.m^{-1}.s^{-1}) are shown in Figure 4.6A, with peak values at mountain foothills and along the axis. IVT decreased strongly when southwesterly winds over India encountered the south-facing Himalayan slopes. The dipole pattern in the advection and rate of IWV change around the AR axis (blue line) is evident, and visibly distinct over the Arabian Sea. Dacre *et al.*, (2015) also observed a dipole pattern of an AR (1st February 2002 06UTC) in the North Atlantic Ocean. Topography influences disrupted patterns of the spatial distribution of positive and negative values of moisture flux (Minallah and Steiner, 2021). A strong moisture gradient about the axis suggests a potential cold front. The contrasting fields and magnitude differences on either side of the axis led to moisture accumulation along it that eventually precipitated, likely due to warm air movement, from the south-east, over the cold air in the west. This reflects the complex interaction between dry, denser air (west) and moist, warm air (east).

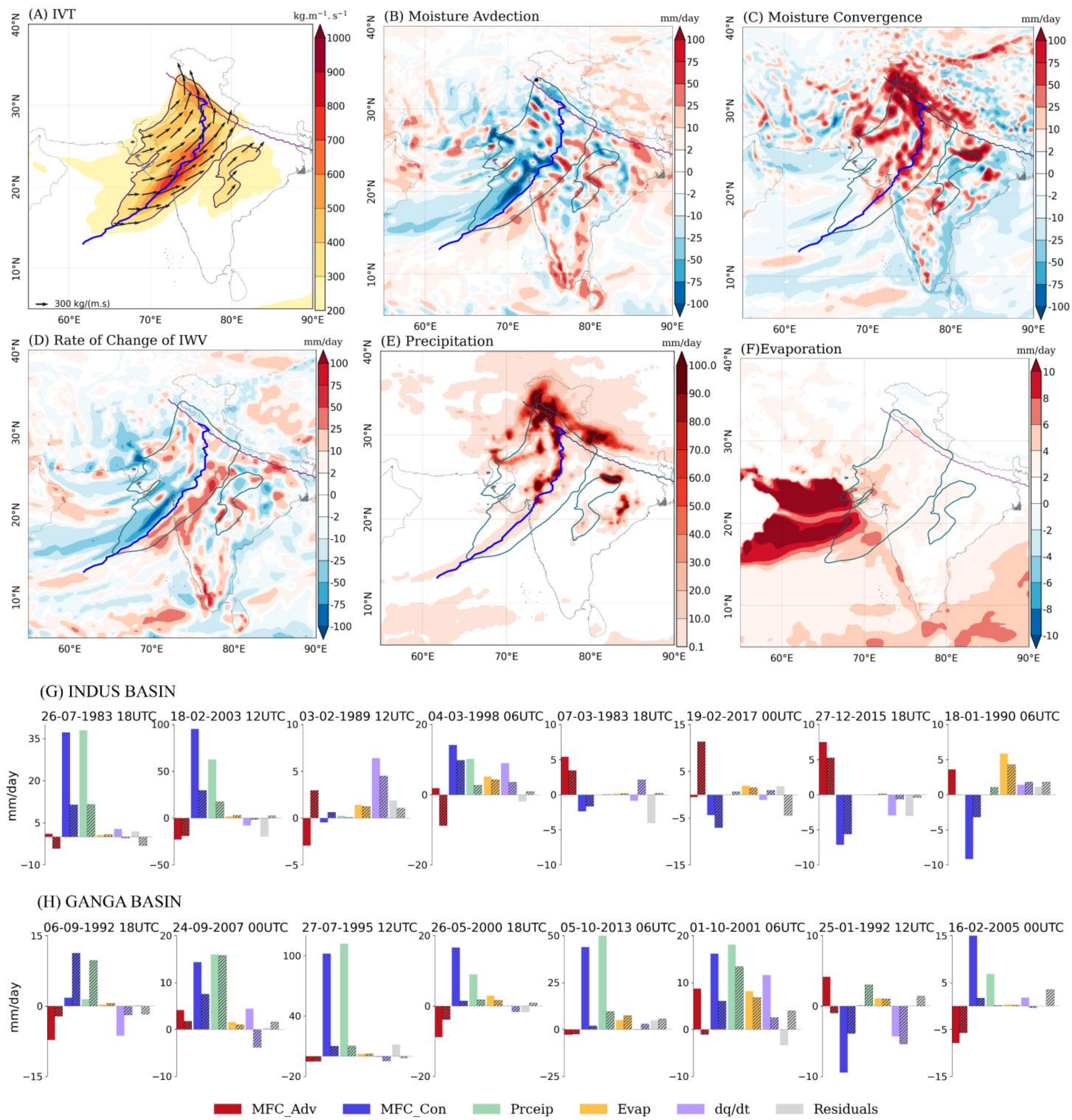

Figure 4.6: *Moisture budget components during ARs: Instantaneous IVT of AR at 12UTC 18th February 2003. The AR's boundary of IVT of* $300\ kg.m^{-1}.s^{-1}$ *is indicated in dark purple lines, and only IVT vectors equal to or exceeding this magnitude are shown by arrows. The major axis of the AR at the given time step is depicted in blue. (B) vertically integrated moisture advection, (C) vertically integrated mass convergence, (D) rate of change of IWV, (E) Total precipitation, and (F) Evaporation. Positive values are in red shades and negative values are in blue shades in (B)-(F) and the axis is the same as in (A). The moisture budget terms for different dates during the top AR events are shown in panel (G) for IB and (H) for GB Basin, shaded are for near mountains, and shaded with hatches for the plains. All units are expressed in mm/day except for (A).*

In moisture advection (Figure 4.6B), there is moisture displacement (negative values) by cold dry air from the northwest that reduced local moisture and resulted in weaker or no precipitation over the Arabian Sea and western India (Figure 4.6E). Moisture depletion also occurred at the foothills due to the dynamical forcing of moist air to ascend over the mountain barrier, leading to orographic precipitation. There is a moisture increase (positive values) in the east of the axis, generated by the abrupt lifting of warm air over the air in the west. Cold air (denser air) moves eastwards and replaces warm air (less dense air) eventually, is driven by disproportionately large and spatially extensive moisture advection (strong negative values). Strong positive moisture convergence along the axis, near/over the mountain, indicates net moisture inflow and an increase in IWV, driven by low pressure (Figure 4.6C). Typically, low-level convergence along a cold front is associated with low-pressure, and the ascent of moist warm air (slantwise ascent; Figures 8 and 9 in Ralph, Neiman and Wick, (2004)) condenses and precipitates. The rate of IWV change (Figure 4.6D) (difference between IWVs, one hour before and one hour after the time of interest and divided by the time interval) closely resembles moisture advection. Moisture decreased (negative values) due its transport away by cold, drier winds, while near/in mountains moisture decreased by orographic precipitation. Moistening (positive values) due to converging winds, and accumulations from warm air ascended on the warmer side, ia also reflected in IWV change. At the axis, there is a near-zero change in IWV indicating that high moisture convergence (high IVT) is balanced by precipitation released. Guan et al., (2020) observed a similar case for the pre-frontal region of an AR in the western USA. Figure 4.6E shows the highest precipitation are along the axis, mountain regions, and low hilly terrains, with even low precipitation occurring at distances away from the impact location. AR-precipitation along the axis resulted from high moisture convergence (Norris et al., 2020), and was triggered by the ascent of warm moist air. The dipole advection around the axis formed a moisture transport channel. Moreover, moisture convergence dominates the total moisture flux convergence and significantly influences the moisture within the AR (Smith *et al.*, 2010). Topography and air mass interaction enhance precipitation intensity within the AR. East of the axis, high moisture accumulated (Figure 4.6D) did not result in heavy precipitation, likely due to lacking dynamic/thermodynamic mechanism for moisture-to-precipitation conversion. This area also coincides with the positive moisture advection. Figure 4.6F shows higher evaporation in the northern Arabian Sea, though it is comparatively smaller than other terms.

The area average budget terms for two distinct regions within IB and GB are shown in Figures 6 G and H. Across the events, precipitation is higher near the mountains compared to the plains, highlighting the role of high terrains in promoting instability and more moisture losses. In IB, in the first event, strong positive convergence and small positive advection largely influenced precipitation magnitude rather than evaporation and atmospheric storage. In the second event, high negative advection reduced precipitation magnitude despite high positive convergence. In GB, the first event has lower precipitation at the foothills than in the plains, due to large negative advection and minimal/no contribution from evaporation. High precipitation in the plains comes from larger positive convergence than negative advection, evaporation, and atmospheric storage. This AR bifurcated (Figure 4.5 Panel C) before reaching the Himalaya, and deposited much precipitation over the plains. Moreover, high precipitation occurred in the mountains well ahead of the AR boundary (Figure 4.5, Panels c1, c2). In the second event, both regions experienced high precipitation from positive convergence and advection, and a small contribution from evaporation (though slightly higher in mountains, contributing to increased atmospheric storage). In other events in IB (on the 3rd, 5th, 6th, 7th, and 8th) we observed small precipitation in mountains and plains, as the AR-IVT boundary did not overlap with the region of maximum precipitation, similar to findings in Dacre *et al.*, (2015) (in Figure S4.7, we also exclude precipitation area within AR boundary that are located outside the IB boundary). Widespread precipitation with maximum intensity over the Sulaiman Ranges, Hindu Kush, and Western Himalaya, occurred near the AR boundary. The non-overlap of IVT with maximum precipitation may stem from different meteorological processes associated with ARs (Gimeno *et al.*, 2021) or reduced spatial extent of AR-IVT, where magnitude drops below the threshold from moisture depletion as ARs propagate over the mountains. High IVT over oceans and coastal areas dissipates upon AR landfall or encounter mountains, as seen in west coast USA where an AR-identification algorithm missed AR-landfall area because its IWV < 20 mm (Mahesh *et al.*, 2023). In IB, such regions have positive advection, small/negative convergence, high evaporation, and positive atmospheric storage. Plains have small precipitation as the large convergence term is balanced by large negative advection. In both cases, excess moisture from convergence and evaporation only increased the atmospheric moisture storage. Most events occurred in non-monsoon and ARs arrived from the west and south-west, except for the first event that occurred in July and had a south-west and north-east orientation. The small residual term generated may be related to the nonlinear effects or factors as described earlier.

In GB, the top events mostly occurred between July-October, coinciding with the monsoon, and causing high precipitation related to increased moisture content in warmer tropical atmospheres. Furthermore, precipitation was higher in mountains than in plains (except at one event), which is attributed to strong positive convergence. On 25th January 1995 at 12UTC, precipitation was very low near the mountain foothills, as this AR-region did not overlap with the maximum precipitation area (See Figure S4.8). This AR event is similar to those seen in IB, which have a west-to-east orientation and deposited most precipitation in the neighboring mountain ranges. In most cases evaporation was low, moisture was due to convergence, and precipitation was mainly controlled by dynamic responses, while in a few cases with high evaporation (1998 and 2001) thermodynamics plays a role in precipitation (Vittal *et al.*, 2016).

4.4.5. Tracks of AR moist air and key sources of moisture supply

To understand where moisture comes from during AR events, the air parcels that precipitated within ARs are tracked backward to locate their position in space over different past times. The trajectories are used to identify the locations of relatively large moisture uptakes. They can also provide insights into the possible circulations influencing the tracks (Nie and Sun, 2022).

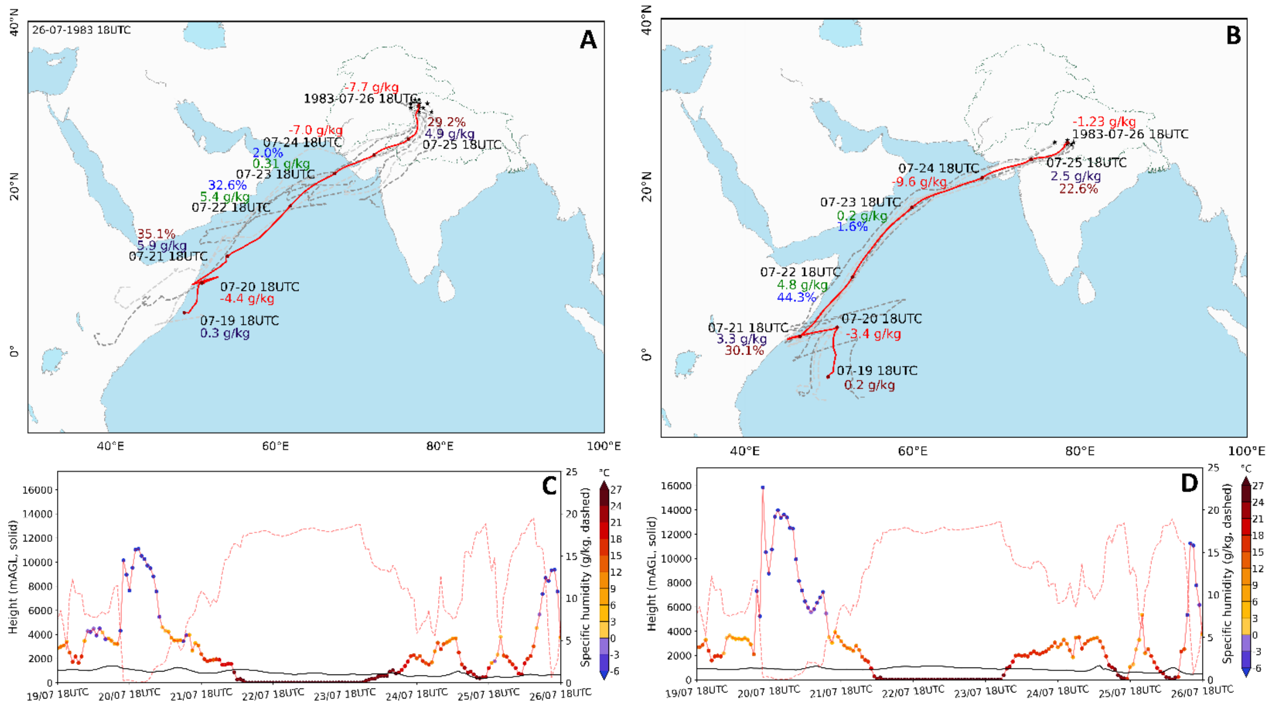

***Figure 4.7**: Top panels: The trajectories of air parcels released at 26th July 1983 at 18UTC, within the AR boundary (as defined in the budget analysis), from locations Behind (Panel A), and ahead (Panel B) of the detection transect. The light and dark grey dashed lines represent trajectories of five air parcels released at 5000 m AGL and 2500 m AGL, respectively, and the red solid line represent the average trajectory of air parcels. Moisture gained within (outside) the mixed boundary layer is shown by green (dark blue), and the percent contribution of source to moisture at the target region is shown in blue (maroon). The moisture lost as precipitation is shown in red. Bottom Panels: Panels C and D show the vertical profiles of the average track at 26th July 1983 at 18UTC. The particle position in the atmosphere is shown in red solid line, specific humidity by the red dashed line, mixed boundary layer by the black line and the scatter plots represents the parcels' position and air temperature is shaded with values indicated on the colorbar.*

Figures 4.7 A and B shows the tracks of 10 air parcels released in the lower- and mid- troposphere behind (near mountain foothills) and ahead (plains) of the transect for the last-8 days. The parcels predominantly travelled from southwest in both cases, following along east Africa and Arabia coastline before entering India. Varying trajectory lengths indicate different travel speed of air parcels within the same time frame. Short trajectories are mostly the parcels that travelled in the lower tropospheric levels, which are warmer and have higher specific humidity. While, longer trajectories involved upper tropospheric parcels, colder with very little specific humidity. Only two locations in the Arabian Sea (Figures 4.7 A and B, values highlighted in green) were determined strongly as the major sources, however, the vertical profile (Figures 4.7 C and D) revealed that after 21st July 1983 the parcel travelled mostly below the mixed boundary layer or close to it before it crossed the coast after 23rd July 1983, and the moisture increased which maybe locally sourced. The parcels arriving near the mountains lost 7.7 g/kg compared to 1.23 g/kg lost by parcels arriving at the plains in agreement with the moisture budget analysis. As the moisture source tracking was computed at 24-hour intervals, the value at the specified location reflects the total moisture loss since the 24-hour prior. The Arabian Sea contributed 34.6% to the total moisture arriving near the mountains before precipitation, while the rest came from other sources in the atmosphere above the basin (29.2%) and the rest was from other source (35.2%, Persian Gulf, Red Sea, Arabian Peninsula). The average parcel position showed that in the Arabian Sea, warmer low-level parcel with increased specific humidity, rose upto ~9000 m AGL over land with reduced temperature resulting in precipitation. In the plains, nearly 46% of the moisture reached came from western Arabian Sea, 22.6% from land and nearly 30% from other sources. The warmer air parcels' temperature at the surface of the Arabian Sea indicated a warmer sea surface (> 27°C), leading to enhanced sea-air interaction and moisture uptake. Similarly, warming of the Arabian Sea surface temperature was associated with the northward shift of the Tibetan Plateau Summer Monsoon (or westward shift of the ISM), that increased moisture advection from the Indian Continent and Arabian Sea over the south Tibetan Plateau (Zhang *et al.*, 2022). Warming of the Arabian Sea and increased surges of moisture flux into central India was also noted by (Roxy *et al.*, 2017), though their study was only for central Indian plain region (19°-26°N; 76°-86°E). Extreme precipitation events of large societal impacts in central India were often linked to strong convections that drew moisture from the Arabian Sea (Gupta *et al.*, 2005; Suthinkumar, Varikoden and Babu, 2023). A prominent component of the ISM is the LLJ (Findlater, 1969; Krishnamurti and Ramanathan, 1982), a warm season narrow stream of high speed winds (20-50 m/s, and maximum wind at 850 hPa i.e., between 800 to 1.5 km altitude) developed in response to the strong temperature gradient, wind balance and wind driven upwelling variations in northwest Arabian Sea (Findlater, 1969; Fischer *et al.*, 2002), and transport moisture from the Arabian Sea to India (Joseph and Simon, 2005). Warming in the Arabian Sea intensifies the meridional pressure gradient and strengthens the LLJ that increases moisture loading from the Arabian Sea (Li *et al.*, 2022). ARs are known to co-occur with LLJs, and are located ahead of the maximum of cold fronts' of extratropical cyclones, or in some cases, ARs occur with just LLJs without extra-tropical cyclones (Gimeno *et al.*, 2014, 2021) as observed in this case. During this season, heavy precipitation at the Himalayan foothills have been reported (Kotal, Roy and Bhowmik, 2014; Ranalkar *et al.*, 2016a), and mainly attributed to monsoonal heavy precipitation and changes in mid-latitude circulation systems, however, excess moisture transport by ARs was lesser known to be the potential cause of extreme precipitation.

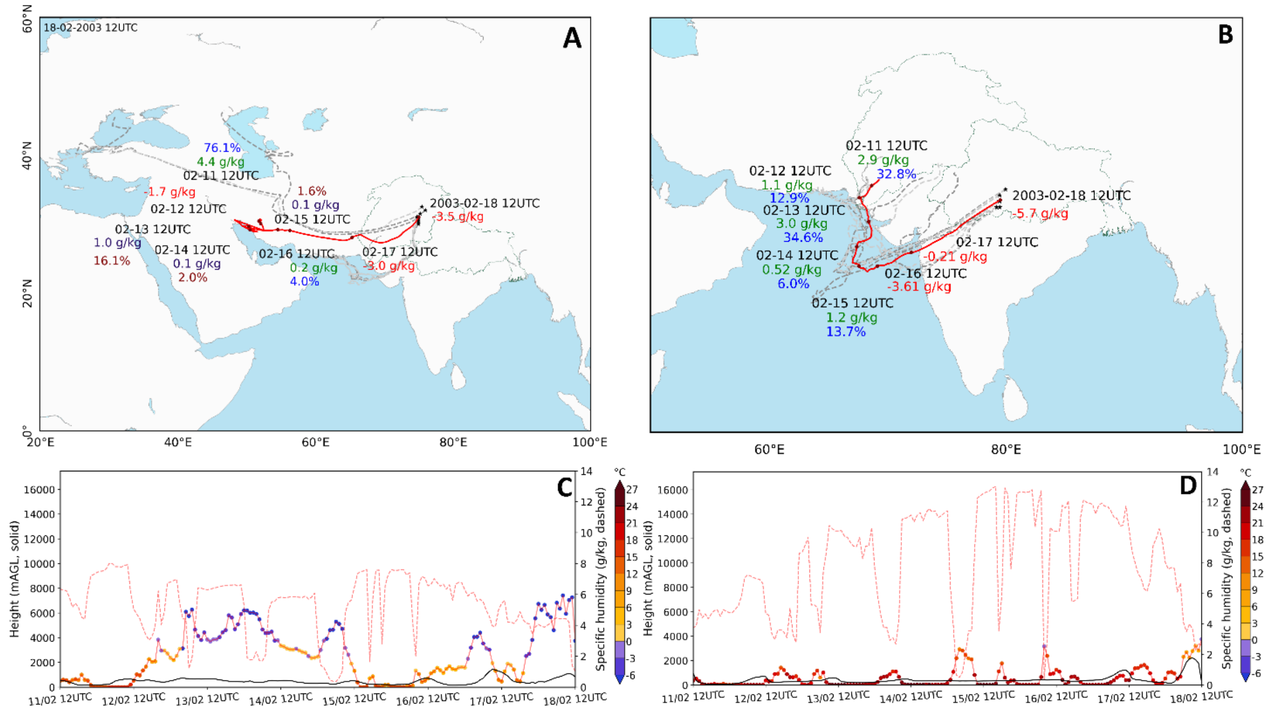

Figure 4.8: *Similar to Figure 4.7 but for air parcels released on 18th February 2003 at 12UTC.*

Figure 4.8 shows parcels' trajectories released on 18th February 2003 at 12UTC at two locations, near mountain foothills (Figure 4.8 A) with high convergence and precipitation, and in the plains (Figure 4.8 B) with the highest moisture accumulation and precipitation. The parcel at mountain foothills have trajectories that show two patterns: one arrived from the seas and lands of Middle East (west), and the other from the Arabian Sea (southwest). The parcels arriving from the west travelled much faster than parcels from the southwest, as they travelled mostly at higher altitudes. They also possessed low moisture loading (< 8 g/kg; see also Figure S4.8a) and resulted in slightly low average moisture loss of -3.5 g/kg (-0.3 g/kg in Figure S4.8a) at the target region compared to moisture loss at the plains of -5.7 g/kg. These parcels also released nearly 3 g/kg in the 24-hours before arriving at the target region. Two locations near the Arabian Sea and the Persian Gulf are identified as the major source of moisture supply with a total contribution of 80%, and the rest 19.7% was traced from other sources (Iran, Mediterranean or Caspian Sea can be the sources as the parcels travel immediately above the mixed boundary layer, but with low moisture (Figure S4.8a)). Moisture uptake began in the Mediterranean and Caspian Sea, with parcels mostly located at mid-to-upper troposphere with very low temperatures (<-3°C). These could indicate cold air intrusions from the northwest of India that descended into the tropics. Within the mixed boundary layer the temperature is upto 18°C, and they may be related to the cold air advection by subtropical westerlies (WDs, which manifest as eastward moving cyclone with defined upper level tropospheric troughs that often extent to lower troposphere (Dimri *et al.*, 2015) during this season

(Cannon *et al.*, 2016)). In the plains, most selected air parcels traced back to locations in the east Arabian Sea and western India. The short distance travelled indicates slower travel rate of parcels than the parcels arriving from the west as in Figure 4.8 A. The major moisture sources are north-eastern Arabian Sea and Persian Gulf that contributed nearly 100% of the moisture for precipitation from 16th to 18th February 2003. The parcels mainly travelled close to the surface or immediately above the mixed boundary layer, with higher specific humidity and very warm temperatures (Figure 4.8 D). Parcels from both (near the mountains and plains) depicts the presence of two type of air masses: the cold-dry air advected over long distances from the northwest of India, and warm-wet air masses displaced slowly from the southwest of India. Along the boundary of these air masses (assumed to be weak cold front), moisture from the Arabian Sea produced rainbands (frontal) which further enhances the LLJ through latent heat released from warm air thereby enhance the moisture transport, i.e., increase mass convergence along the AR (Hu and Dominguez, 2019). It can be understood that ARs transported the moisture from the Arabian Sea to India, and deposited it through air mass interaction and by orographic lift.

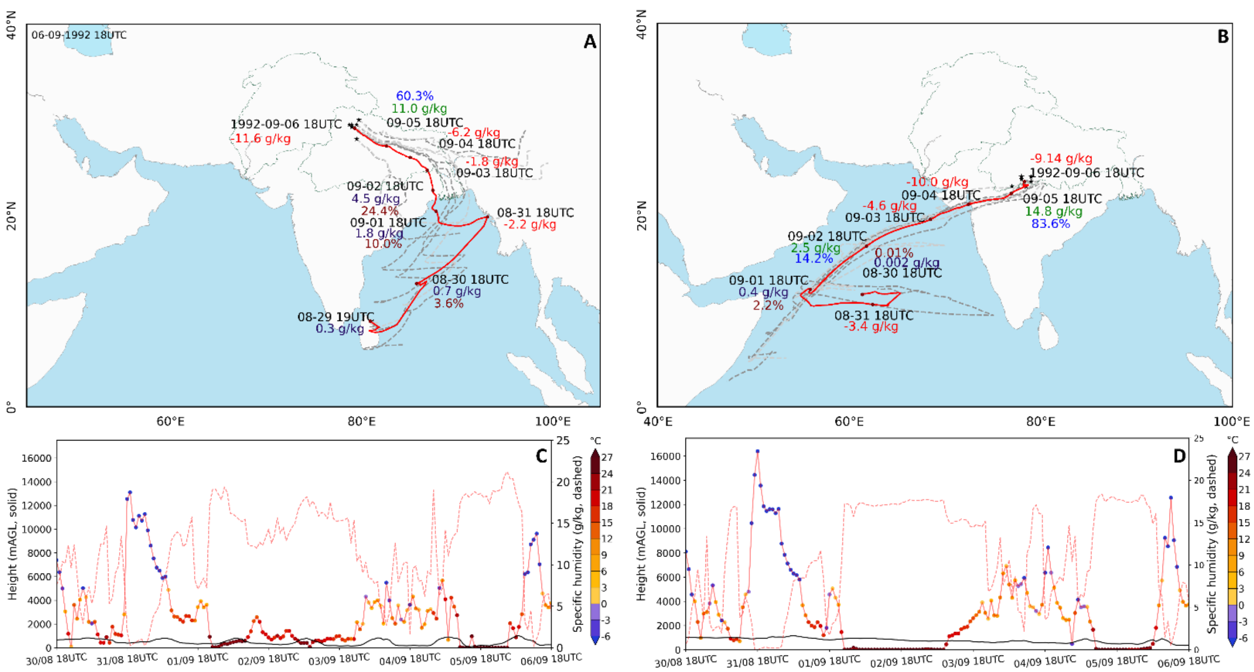

Figure 4.9: *Similar to Figure 4.7 but for air parcel released on 06 September1992 at 18UTC.*

The trajectories for the AR event on 6th September 1992 at 18UTC are shown in Figure 4.9. The parcels that arrived at/near the mountains have trajectories over east central India and Bays of Bengal. Parcels travelled over the Bay of Bengal and entered India from the Bengal delta. The parcels released ~8 g/kg at -48 hrs and -72 hrs, and gained ~11.6 g/kg 24 hrs before precipitating it. While the parcels in the plains have tracks that traced back to the Arabian Sea. The main sources of moisture includes the central Arabian Sea and moisture from the coastal northeast Arabian Sea to inland, and moisture recycling within the landmasses of the basins (as observed by Pathak et al. (2017)). These patterns resemble the AR-IVT patterns as shown in Figure 4.5, with the major sources of moisture overlapping the regions of high IVT i.e., in north Bay of Bengal, central and northeast Arabian Sea. In both the cases, the parcels carry high moisture content with the maximum reaching 20 g/kg and were warmer (Figures 4.9 C and D). These parcels predominantly travelled between the mid-to-lower troposphere except on 31st August 1992 and the hour before precipitation in the target region.

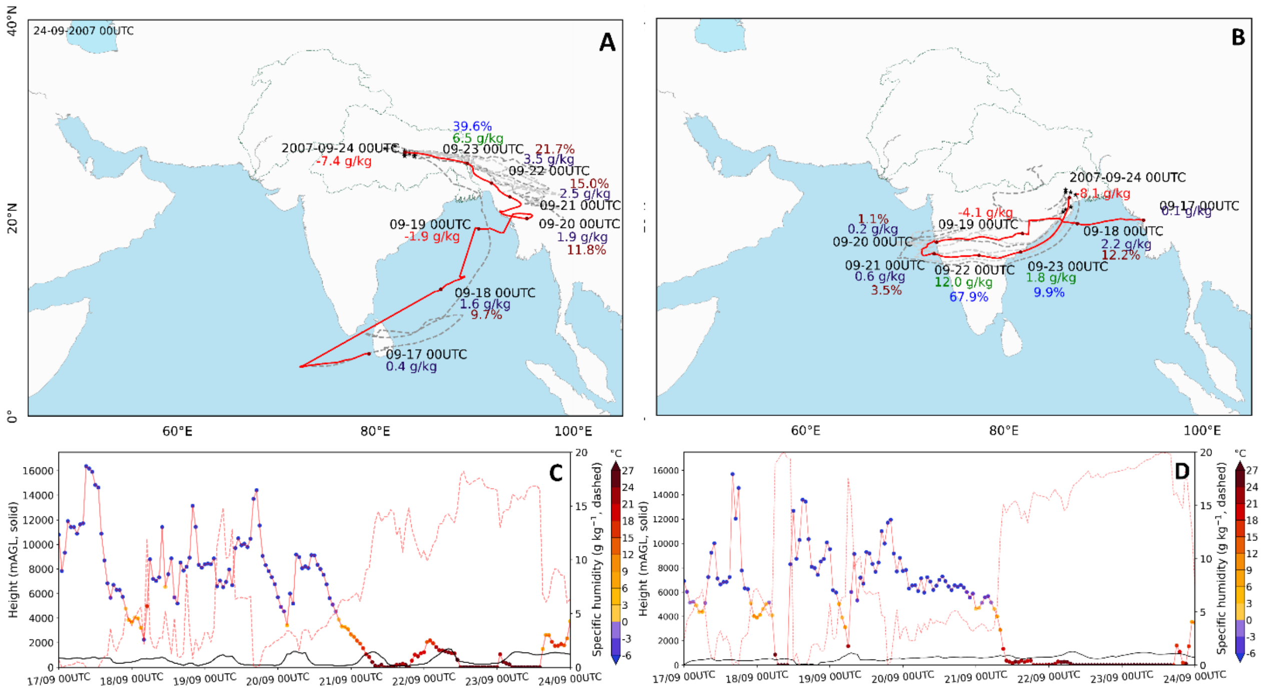

Figure 4.10: *Similar to Figure 4.7 but for air parcel released on 00UTC 24-09-2007*

On 24th September 2007 at 00UTC, the parcels near the mountains and plains have tracks in the Bay of Bengal (Figures 4.10 A and B), mirroring the IVT patterns during the event. Near mountains, the moisture released was -7.4 g/kg in the last 24 hrs, with approximately 40% originated from the Bengal delta. The profile showed that the parcels entered the mixed boundary layer at -96 hrs marked by sudden increase in moisture content and air temperature (Figures 4.10 C and D). In the plain region, the selected parcels released moisture of -8.1 g/kg in the last 24 hrs, which overlapped with region of highest IVT in the AR. Parcels traced back to the Bay of Bengal, then the Arabian Sea in the lower troposphere, and from the Arabian Sea to the Bay of Bengal in the upper troposphere. This suggested to be the reversal of winds in the upper layer, contrasting with the lower-level counter-clockwise wind movement. The parcels were cold and less moist before they entered the boundary layer -72 hrs prior to reaching the target area.

We also tracked the parcels of other AR events, except those where the AR shape does not coincide with precipitation in the mountains, as they show patterns similar to Figure S4.8b. The events that happened during non-monsoon seasons have their tracks extended to the west, sourcing moisture from Seas of the Middle

East. The parcels have low moisture loadings even though they travelled within the boundary layer or immediately above it and may be attributed to lower temperatures leading to reduced moisture carry capacity. The moisture was also lost may along the mountain ranges before they arrived at the target region. While parcels in most of the summer AR events have their tracks in the Arabian Sea and Bay of Bengal, carried greater moisture loadings and have warmer air temperatures (Figure S4.8d-8f). Such characteristics may amplify hydrological responses over affected area. In one case, the parcel travelled from the west but had low contribution to precipitation due to multiple prior instances of precipitation before it arrived at the target area (Figure S4.8d). The main oceanic contributors to continental moisture in India during the ISM was also tracked to the Red Sea, Arabian Sea and the India Ocean (Pathak *et al.*, 2017). And during extreme precipitation events in ISM, large moisture contribution from the Arabian Sea is well-documented in previous studies (Pathak *et al.*, 2017; Roxy *et al.*, 2017), primarily attributed to the increase intensity of LLJs. Despite this evidence, ARs as a mechanism for transporting oceanic moisture to mainland India and Himalaya remain relatively understudied and lack comprehensive insights for practical applications. Precipitation extremes are becoming more intense and may be related to strengthening of the transport features (dynamic response), that sustained moisture channels from the ocean to the subcontinent (Algarra *et al.*, 2020).

4.4.6. Analyzing vertical stability profiles of AR events

Figures 4.11-4.14, are the instantaneous profiles of atmospheric conditions during the AR events. For the purpose of conciseness, we have described here only the top two events of IB and of GB, as they occurred in different season and/or have contrasting conditions. Within the AR shape we selected multiple locations for analysis and comparisons: two near the mountain foothills, two behind the AR axis, two on, and two ahead of the axis where heavy precipitation occurred. The locations on either side of the axis are selected such that they are at similar latitudes.

Main Similarities

In three of the events (referred to as the 1983 event for 26th July 1983 at 18UTC (Figure 4.11), as the 2003 event for 18th February 2003 12UTC (Figure 4.12), and as the 2007 event for 24th September 2007 at 00 UTC (Figure 4.14)), the locations foothills selected ahead (marked as M1 and M2) of the transect, near mountain have saturated tropospheric conditions. This condition includes saturation (RH> 99%) throughout the troposphere or only at certain altitudes (e.g., < 780 hPa in M1, Figure 4.11) with near saturation (RH >88%) throughout. A region of rapid change in air and dew point temperature was noted at mid-troposphere (~500 – 700 hPa), which is accompanied by reduced saturation, and in some cases, there was strong shear in wind speed (1983 and 2007 events). This region represents cooler unstable air (temperature decreased much faster than the normal lapse rate) and suggested the presence of low-pressure. This may be related to cold air intrusion from northwest India. Below 800 hPa, southeasterly winds dominated (2.57-48.0 m/s) with high specific humidity (16-20 g/kg, for summer-autumn events and for winter specific humidity is 8-10 g/kg). The southeasterly low-levels winds veered to southerly with increasing height for the 1983 and 2003 events, which indicated ascent and deflection of low-level winds by mountains, while for the 2007 the winds remain southeasterly throughout the column but showed wind shear magnitude. Water drops formed upto 500 hPa (indicated by srwc) in the summer-autumn events and up to 700 hPa in the winter event. Snow crystals formation peaked between 400 – 600 hPa (indicated by sswc) in most events except for the winter event where it extended from 850 hPa to 300 hPa. This is related to the vertical environmental temperature at different season. The atmosphere showed weakly stability (low CAPE, low CIN) in the three events favoring weak/no vertical ascent of parcels, however, the presence of mountains nearby may have forced the vertical uplift of parcels. This generated precipitation between 1.3─19.3 mm/hour as a result.

At locations marked 1 and 2, the tropospheric condition varied from saturated at lower and upper levels or only at the lower levels to near-saturation at mid-levels (500-700 hPa). Winds were predominantly southwesterly except in the 1992 event and 2007 event (location 1). Snow crystal formation in upper levels exceeded water droplet formation in lower level, and the non-zero values in droplet formation have contributed precipitation here. Despite very high CAPE (upto 1155.1 J/kg) and low CIN (upto – 39.4 J/kg), precipitation was below 6 mm/hour, which indicated that CAPE and CIN alone were insufficient for heavy precipitation. Precipitation efficiency was also found to depend on moisture available (Lepore, Veneziano and Molini, 2015) and convergence of air into the region (Derbyshire *et al.*, 2004). The mid-dry and unstable region is also observed at 1 and 2, and much more pronounced for the 2003 event.

At locations labelled as A1 and A2 on axis, the troposphere was either saturated (near-saturation) as seen in Figure 4.11, 4.13 (A2), and 4.14, or saturated only at the lower troposphere and dry aloft as in Figure 4.12 and 4.13 (A1). Winds veered from southwest to west or southeast to south but less pronounced than those near mountains. Southwesterlies or westerlies prevailed throughout the troposphere with shear in magnitude, and wind veered at lower levels and mid-upper indicated the presence of warm air. It was noted that CAPE was higher compared to that near mountains, and with low CIN promoted instability and encouraged convective storm activity. This resulted in precipitation (1.8 – 12 mm/hour), which was almost at par with precipitation near the mountains. A weak thermal inversion was present at lower levels upto 800 hPa, which indicated warms and cold air masses, and the alteration of the thermal inversions indicated air mass interactions. And thus, precipitation was generated by convection.

In 3 and 4, near-saturation (RH: 81%-95 %) prevailed throughout the troposphere (except for the 2007 and 1992 events, when saturation was only at mid/low-levels). In all the events, snow crystal or water drops formation was almost negligible (srwc and sswc < 0.1 g/kg). High precipitation was notably very low (<1.2 mm/hour), despite conditions favorable for convection were present, high CAPE, low CIN, high specific humidity was available and warms surface temperatures. The potential energy was translated mainly to vertical ascent of parcels, while moisture increased to upper levels, indicating accumulation e.g., in 2003 the low-level dryness is related to higher surface air temperature (~24˚C), and even though high specific humidity extended upto 450 hPa precipitation was low (0.6 mm/hour). This event showed agreement with the time change in IWV and advection term of moisture budget analysis. The accumulations is due to the lack of convection (low CAPE and higher CIN) or precipitating mechanism to trigger precipitation. In almost all the events, there was slightly warmer surface air temperature at these locations (including at A1 and A2) compared to other locations, which is related to warmer tropical air.

Main Dissimilarity:

The event on 06th September1992 at 18UTC (the 1992 event) showed different conditions, with either near saturation (RH = 91%) or dry conditions at M1 and M2. There was high CAPE (1441.9 J/kg (M1) to 1671.9 J/kg (M2)) and low CIN (-45.1 J/kg (M1) to -24.1 J/kg (M2)) and specific humidity in lower-levels, favorable for deep convection and strong vertical ascent. However, this only resulted in ascent without high precipitation (below 0.6 mm/hour), and related to incomplete saturation as the air temperature was high (27 - 29˚C). This may also be due to winds (weak wind shear) that prevailed southeasterly throughout and almost parallel to the south-facing side of mountains (longitudinal length), indicating importance of orientation (perpendicular vs parallel impact). In this case high precipitation occurred in the plains (Figures 4.13, 1,2, 3, 4, A1 and A2) consistent with moisture budget analysis.

The summer-autumn events possessed higher specific humidity (upto 20 g/kg) and winds (mostly between 0-20 m/s, except when near a cyclone the winds speed can go upto 49 m/s) as compared to the winter event that possessed much higher wind speeds (9-49 m/s) and much lower specific humidity (upto 10 g/kg). This is related to the surface air temperatures on different seasons, warmer in summer-autumn than in winter, highlighting the seasonal characteristics of ARs. The vertical profile of environmental air temperature in summer ARs does not decrease (lapse rate) as rapidly as observed for winter ARs. In most cases, high specific humidity extended to mid troposphere (~500 hPa) for locations near the mountain foothills on and ahead of the AR axis, while behind axis high specific humidity is mainly below mid-troposphere. There is a strong distinction in atmospheric column of specific humidity in winter and summer-autumn events, however even in winter the specific humidity was high near mountains and ahead of AR axis compared to on/before the AR axis.

Overall, orographic effect led to high hourly precipitation near mountain foothills (orographic uplift of moist air) despite very low CAPE (weak updraft) and CIN energy (enough for water particles to coalesce effectively), while precipitation in the plains, on axis may be linked to the gradual ascent of warm air over cold air, that triggered intense convective precipitation within an hour as CAPE was high and CIN was low CIN and high moisture was available. This is similarly for locations behind the axis, but with lower magnitude in CAPE, CIN, humidity, and precipitation. These two cases support that precipitation probability increases with higher CAPE (Dixon, 2008) and low CIN (Raymond, Sessions and Fuchs, 2007). Ahead of the axis, the troposphere has higher CAPE and low CIN, however, this energy only resulted in upward vertical acceleration without translating heavy precipitation. Thus, this indicate that precipitation link to CAPE and CIN magnitude increase only upto certain CAPE values. Very high CAPE was also found to negatively correlate with high precipitation intensity (Dong *et al.*, 2019), and for the tropics, precipitation does not correlate well with CAPE (Barkiđija and Fuchs, 2013). High CIN (the energy barrier required for an air parcel to rise above the surface to the LFC (Level of Free Convection)) also undermines the strong relationship between precipitation and CAPE (Kirkpatrick, McCaul and Cohen, 2011), as observed at 3 and 4 (2003 event), at 3 (1983 event). In this case, topography, and precipitating mechanism due to cold and warm air interaction, played a crucial role. As seen above, topographic effect can override weak convective condition, force uplift of moist air and intensify precipitation

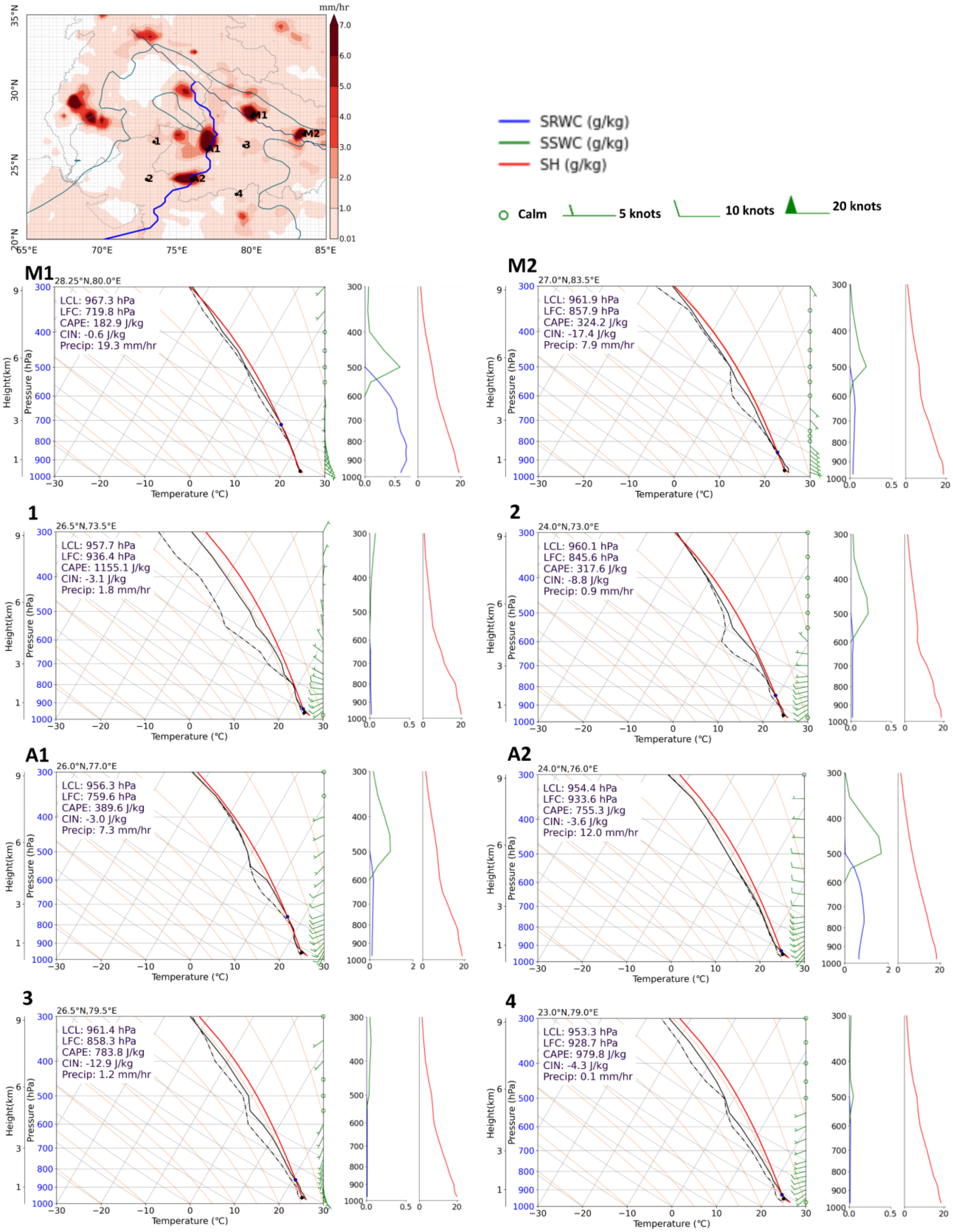

Figure 4.11: *Skew T-logp diagrams on 26th July 1983 at 18UTC for different locations (marked and labelled, with the coordinates shown at the top of each subplot) within the AR boundary. Vertical temperature profile of environmental, dew point, and air parcel are shown in black solid, black dashed, and red solid lines, respectively. Profile of winds are shown by barbs (knots, circle (calm air) = 0 m/s, small barb (5 knots) = 2.57 m/s, full barb (10 knots) = 5.14 m/s, and pennant (20 knots) = 10.28 m/s). The middle column is the vertical*

profile of specific rain water content (g/kg; srwc) shown in blue, and specific snow water content (g/kg; sswc) shown in green. The specific humidity (g/kg; q) is shown in the last column as red line.

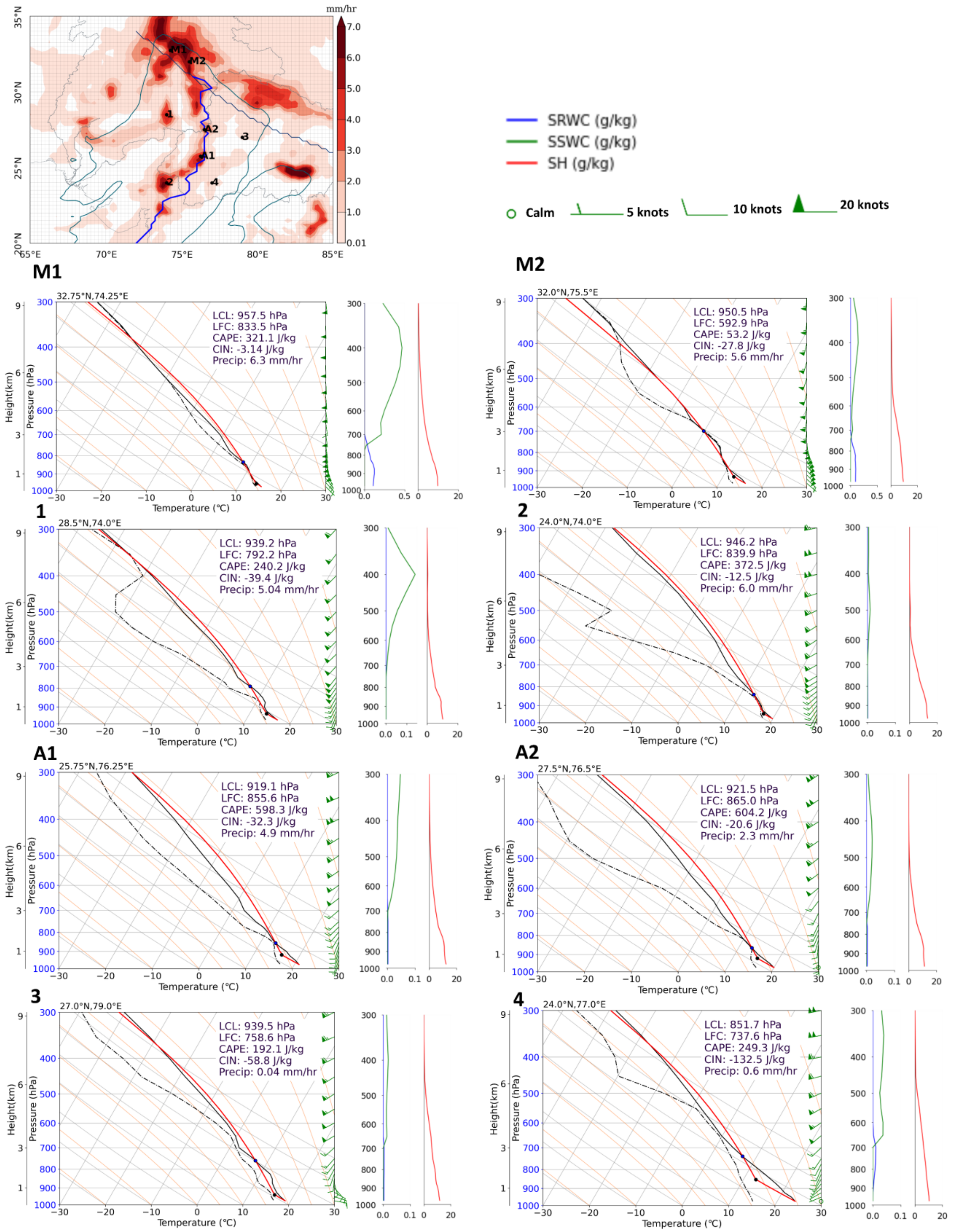

Figure 4.12: *Similar to Figure 4.11 but for 18th February 2003 12UTC.*

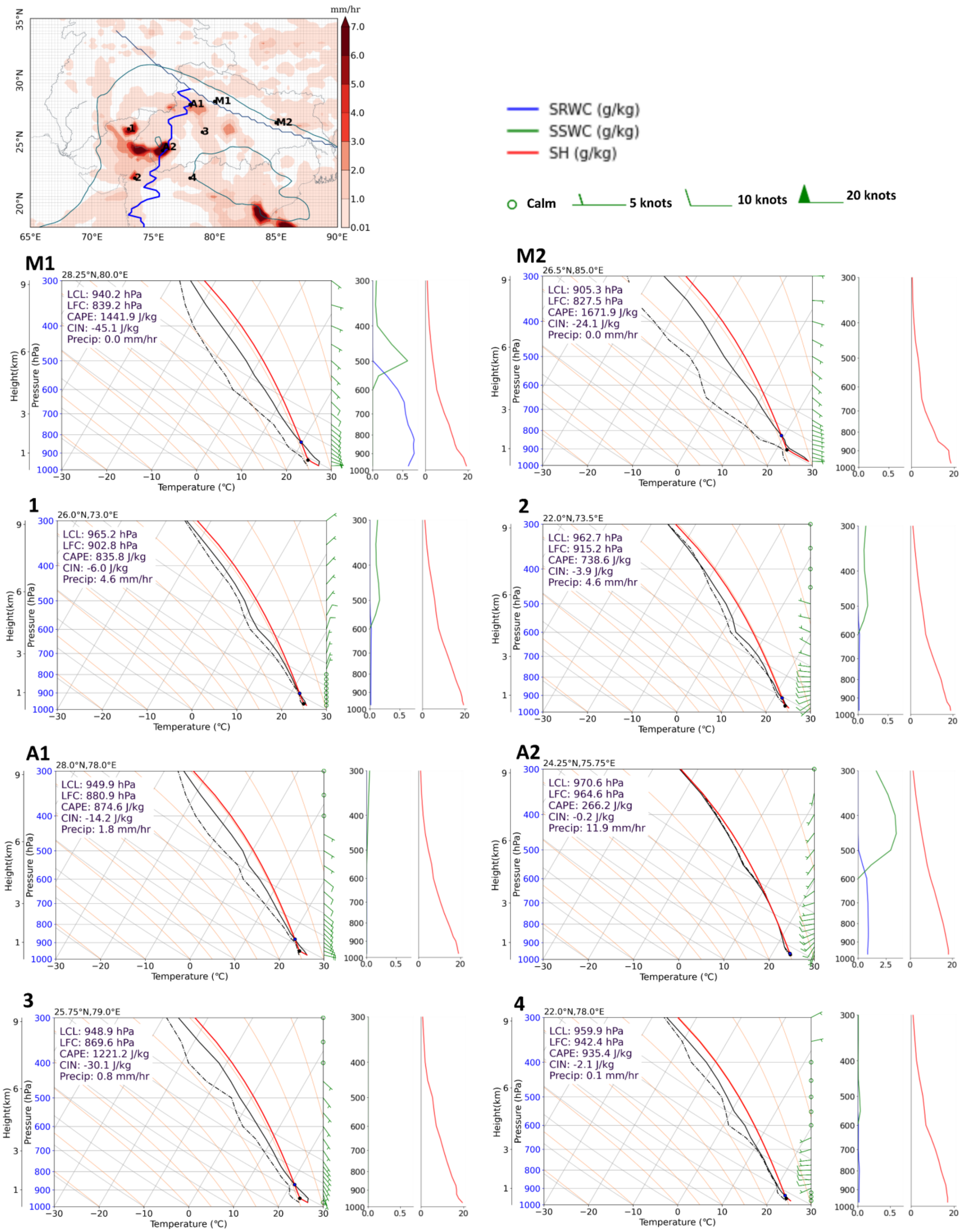

Figure 4.13: *Similar to Figure 4.11 but for 06th September1992 at 18UTC.*

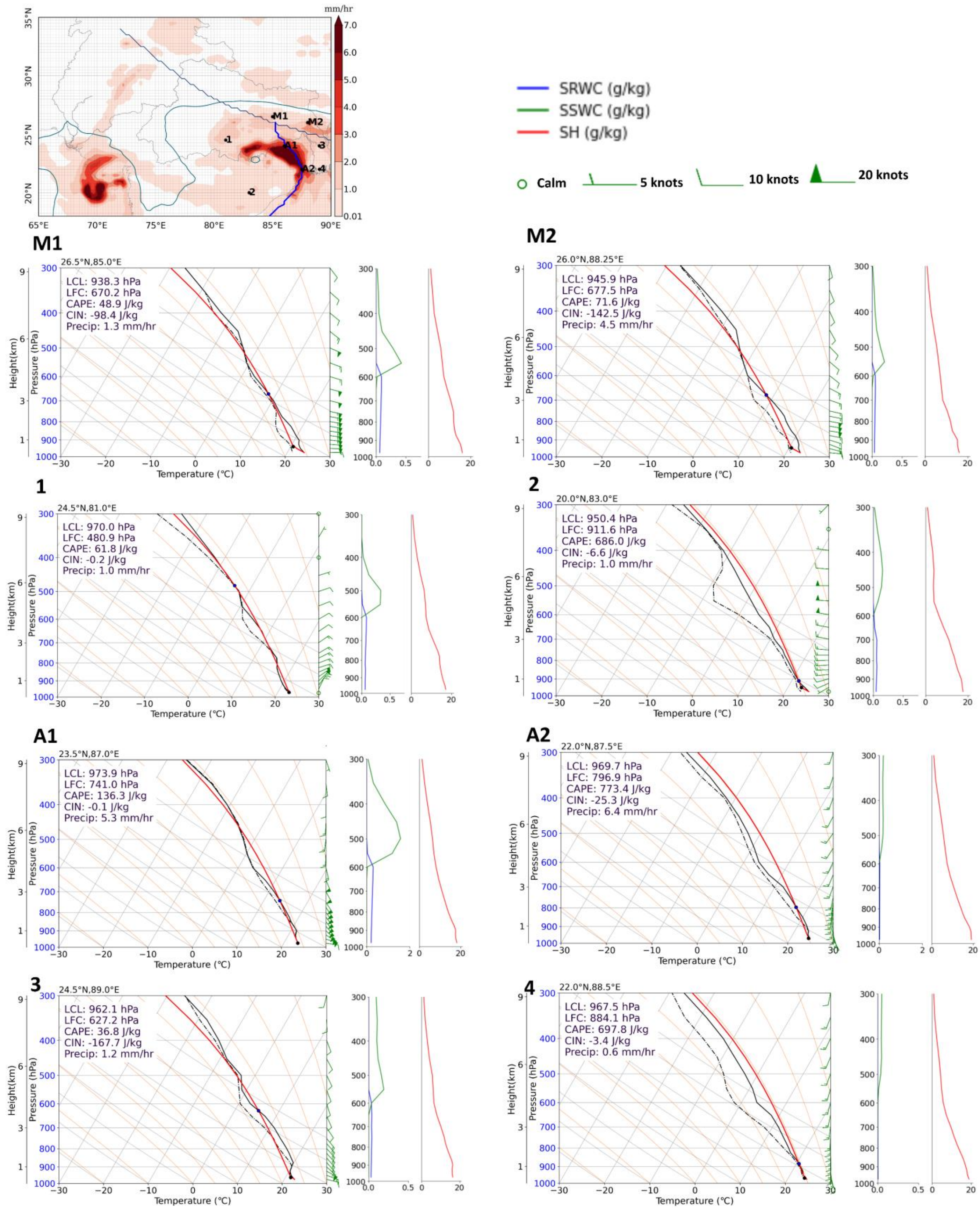

***Figure 4.14**: Similar to Figure 4.11 but for 24 September 2007 at 00 UTC*

4.5. Conclusion

The Himalaya form an important physical barrier to moisture transport in South Asia, extracting vital precipitation for two Himalayan basins ─ IB and GB. This study examines ARs that penetrated the Himalaya from the south. A modified regional AR identification algorithm, detection transect (placed in lesser terrain, south of the Himalaya), and daily 85th percentile IVT thresholds are used to identify ARs, every 6-hourly, from 1982 to 2018. The threshold captures the seasonal and regional climatic IVT variations across latitudes and identifies even weak ARs often neglected over these regions with traditional $100\ or\ 250\ kg.m^{-1}.s^{-1}$ thresholds. The intensity generally increases towards the tropical regions, Bin A (consistently <$120\ kg.m^{-1}.s^{-1}$ year-round), Bin B ($90 - 250\ kg.m^{-1}.s^{-1}$) located in extra-tropics, and Bin C ($100 - 400\ kg.m^{-1}.s^{-1}$) located in the sub-tropics. Weak ARs may be less intense than extra-tropical ARs, however, they surpass their climatological thresholds over Himalaya. Bins D and E (in tropics) have higher thresholds ($120 - 550\ kg.m^{-1}.s^{-1}$), even in non-monsoon months, especially Bin E. ARs occurred year-round, averaging 24 ARs/year, with most in winter (8/season), followed by summer (6/season), spring and autumn (5/season each). They typically last for 18 hours but some persisted for 72 hours or longer. Seasonally, winter and autumn ARs have a longer median duration (30-hours) than spring and summer ARs (24-hours). Winter ARs are frequent in Bins A-D and mainly belong to Cat0 and Cat1, which provide beneficial precipitation. Other seasons had fewer ARs in various categories. Summer and autumn ARs in Bins B-D have more Cat5 ARs (primarily destructive). While Bin E has more ARs in each season, most in summer (Cat2 – Cat5), then autumn (Cat0 – Cat5), winter (Cat0 – Cat5), and spring (Cat1 – Cat5), with notable Cat4 and Cat5 ARs occurrences.

In the top AR events of IB and GB, precipitation exceeded 150 mm/day (> 99th percentile) in AR-affected Himalayan areas, and even in mountains beyond the impacted area 65 mm/day precipitation occurred. These regions coincided with reduced AR-IVT, suggesting ARs' extension into the high mountains, impacting them. ARs also induce nearly 50 mm/day around their boundaries. Hence, extreme AR events have a wide-reaching impact, extending into the headwaters of IB and GB and surrounding areas in the plains.

Heavy precipitation occurred in regions of high IVT, near the mountains, and along/near the AR axis in plains, and the minimal changes in atmospheric storage indicated the effective translation of AR moisture to precipitation. Understanding the processes contributing to AR precipitation is as important as AR characteristics, moisture budget analysis revealed that excess moisture leading to extreme precipitation was imported from neighboring water bodies. Changes in atmospheric column/storage were driven mainly by horizontal advection, with some contributions from evaporation. High-intensity precipitation resulted from strong positive moisture convergence, combined with positive advection, and no changes or decreased atmospheric storage. While low-intensity precipitation resulted from weak or large negative convergence, with low positive or large negative advection, increased evaporation, and net accumulation in atmospheric storage. It was also noted that large negative advection and convergence, or negative advection with minimal convergence led to removal of existing moisture and drying up of the atmosphere. Since this analysis did not account for all atmospheric water (liquid and frozen water), or non-linear terms, it has potentially introduced some error terms, which is one of the drawbacks of this analysis.

Backward tracking of precipitated air parcels for 7 days revealed moisture sources and travel paths likely influenced by seasonal atmospheric circulations or dominant weather systems. Summer-autumn events have tracks mostly in the tropic (low-levels, warmer ~27˚C, moist up to 20 g/kg) over India, Pakistan, the Arabian Sea or Bay of Bengal (mostly parcels reaching the plains), while winter-spring events have tracks in the sub-extratropic (12 – 20˚C, and moisture < 6 g/kg) over the Middle Eastern Seas/land, Pakistan, and even Europe (mostly parcels reaching near mountain foothills), or arrived from Arabian Sea with high moisture loadings (Figure 4.8). In most events, excess moisture came from the north and western Arabian Sea, north and eastern Bay of Bengal, and from the seas of the Middle East, and in some cases, moisture was also gained over land by evaporation.

Near the mountain, the troposphere was mostly saturated throughout, mildly unstable (low CAPE: <350 J/kg, low CIN: -0.6 to -145 J/kg), and in some cases stable layer started from mid-level. There was warm air advection and ascent, leading to high precipitation (up to 19.3 mm/hour). On axis, the troposphere was saturated throughout, or only low levels, more unstable (CAPE: 390 to 875 J/kg, and CIN: -0.2 to -25 J/kg), and precipitation was comparable to mountain precipitation. The two locations of high IVT and intense precipitation within ARs had saturated tropospheric air, and two different precipitation mechanisms at play: orographic uplift near mountain foothills, and air mass interactions or frontal lift in the plains. Thus, the severity of AR impacts depends on the interaction with local topography, besides intensity, duration, IVT direction orientation of winds, and synoptic-scale dynamics associated with ARs.

These investigations suggested that ARs are mechanisms of transporting oceanic moisture to mainland India and the Himalaya, besides ISM and WDs. However, they remained relatively understudied and lacked comprehensive insights for practical applications in these regions. Thus, further investigations along these lines are necessary to provide more insights and a critical understanding of their importance to society and ecology over these regions.

APPENDIX-B: Supplementary Information

S4.1: Terrain gradient map

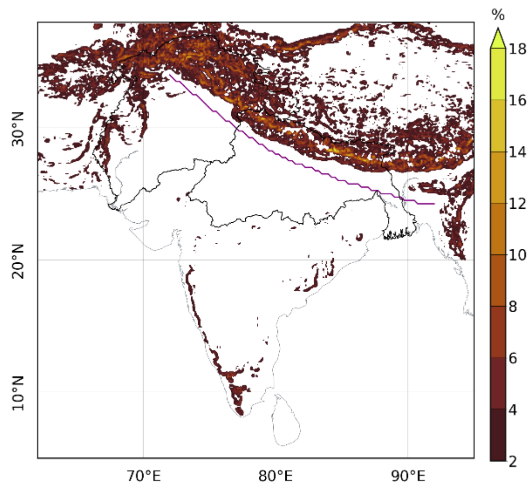

Figure S4.1: *Gradient of slopes computed using SRTM DEM (30m by 30m) retrieved from USGS (United States Geological Survey). Basin boundaries are highlighted in black for IB and GB. The detection transect is shown in purple.*

S4.2: Comparison of Frequency and Duration of ARs from the Guan and Waliser, (2019) and modified Lavers *et al.*, (2012) algorithms

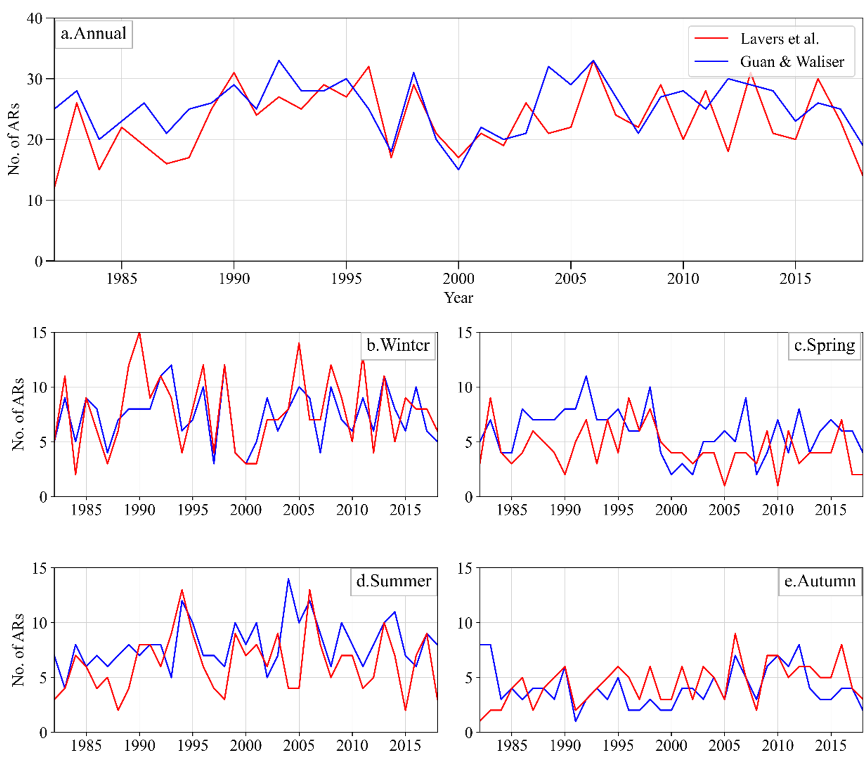

Figure S4.2a*: Comparing ARs from two AR detection algorithms: Annual and seasonal frequency of ARs using GWAR2019 (blue lines and the LAAR2012 (blue lines). Panel "a" shows the annual frequency for the* *years from 1982 to 2018, while panels "b", "c", "d", and "e", show winter, spring, summer, and autumn frequencies, respectively.*

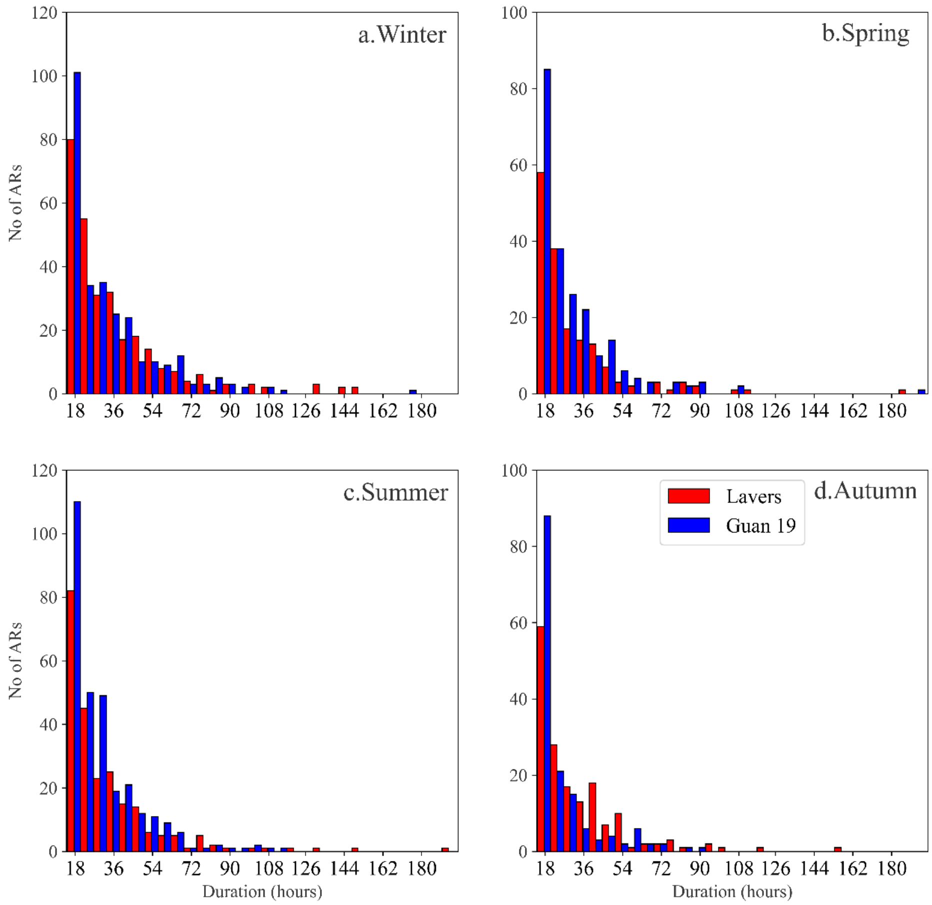

Figure S4.2b: *Comparing the seasonal durations of ARs obtained from two algorithms: The distribution of AR durations for AR events obtained from the GWAR2019 in blue color and the LAAR2012 in dark blue color for different seasons.*

To understand and measure the uncertainties among AR algorithms that emerge using various methods, AR criteria, and input data, the ARTMIP was established as a collaborative effort for this mission and guide researchers to select the most favorable algorithm for their specific research objectives (Shields *et al.*, 2018). As mentioned in the earlier section, the most evident disagreement among the algorithms (detecting ARs based on the same set of data) lies in the ability to detect "weak AR" (Lora, Shields and Rutz, 2020). In this section, we used ARs identified by the Guan and Waliser, (2019) AR detection algorithm (Guan and Waliser, 2019) (GW_{AR}2019) over our study region for comparison with the present ARs.

Following the minimum duration criterion for persistent ARs as described in this article, we also select only those AR events that exist over 18 hours from the ARs identified by Guan and Waliser, (2019) for the Himalaya. We noted that a similar number of ARs are identified by Guan and Waliser, (2019) for most years, although for some years this algorithm identified many more ARs and increase the annual average frequency to 25. More ARs were identified in spring, summer, and autumn seasons, but the highest increase is in summer. This arises mainly because the two AR identification algorithms adopt different approaches to compute the IVT thresholds, and different minimum values of IVT to identify potential ARs. For example, in the $GW_{AR}2019$ algorithm for each grid cell, a monthly IVT threshold is calculated based on 85th percentile values of 6 hourly IVT during the 5 months centered on the month considered (but not lower than $100 kg.m^{-1}.s^{-1}$). This threshold is increased from 85th to 87.5th and so on by increments of 2.5 till the 95th is reached, and it is applied for IVT objects that fail the qualify the AR requirements at the first step (using 85th percentile threshold). While in the $L_{AR}2012$ the AR threshold is calculated for all the days in a year as described in the Method Section earlier. Another important criterion is that cyclones occurring very close to ARs are considered as part of the AR in case of the $GW_{AR}2019$ algorithm, and hence these days are counted as AR days. The $G_{AR}2019$ algorithm identified 942 ARs while the modified algorithm of $L_{AR}2012$ identified 857 ARs over the period 1982 to 2018.

Figure S4.2a illustrates the comparison of AR frequencies at annual and seasonal intervals using the two algorithms. The number of ARs per year in either case is always greater than 15, and the annual frequency patterns are nearly similar, for example, the frequencies are higher between 1988 and 1997 (consistently above 25) and between 2000 and 2010 (consistently above 20). Seasonally, we observed ARs to be present in each year with varied frequency, for example, the winter and summer seasons have larger variances in comparison to the spring and autumn seasons, and this variability is evident when using either of the two algorithms (Figures S4.2a b, c, d, and e). The $GW_{AR}2019$ algorithm identified many more ARs for nearly all the years in summer, and in spring for the years before 1995 and after 2003, while in winter and autumn, this algorithm identified slightly fewer ARs than those identified by the $L_{AR}2012$ algorithm. Similarly, we performed a side-by-side comparison of the durations of AR events identified by both algorithms (Figure S4.2b), and we found that most AR events have a short duration of only 18 hours. It is also observed that many of the events identified by $GW_{AR}2019$ have short durations (less than a day), especially in winter and autumn, and rarely these identified ARs have long durations longer than 126 hours. In spring and summer, however, there are comparatively more AR events that have durations as long as 3 days. The differences in the duration of events are again related to the reasons mentioned above. The discrepancies observed here are, however, reasonable and can be considered to be within the uncertainty range of AR detection algorithms. More details on the differences among AR algorithms can be found these papers (Shields *et al.*, 2018; Rutz *et al.*, 2019; Lora, Shields and Rutz, 2020).

Using the ARs from $GW_{AR}2019$, we also match the dates of the 16 highest-intensity ARs as shown in Figures 4.5, S4.2a, and SI4.2b for the IB and GB as identified by the $L_{AR}2012$ algorithm. We found that out of 14 events 10 events in $GW_{AR}2019$ match those found by the $L_{AR}2012$. From these comparisons, it can be regarded that both algorithms are efficient in identifying intense and impactful ARs in the Himalaya.

S4.3: Seasonal Trends in AR Frequency

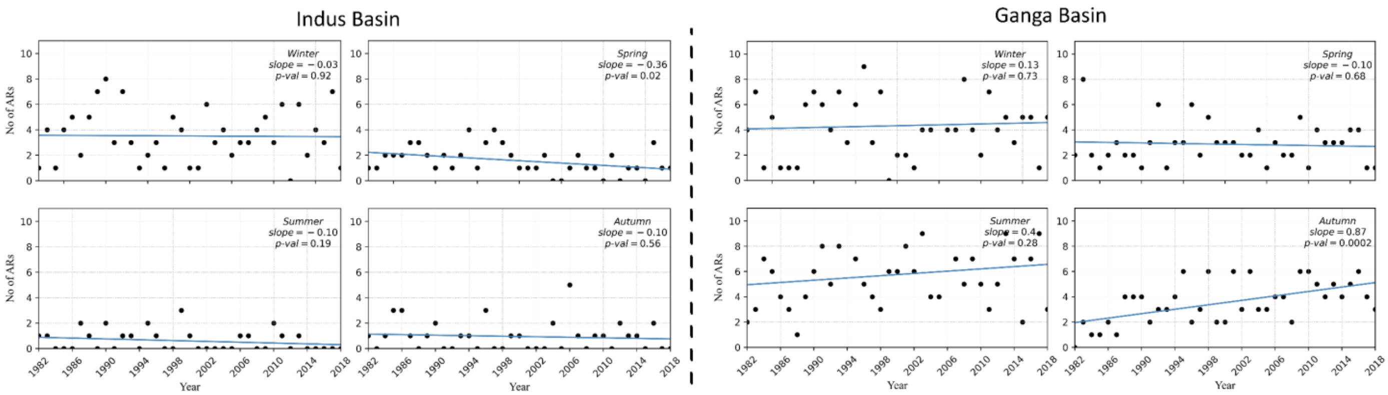

Figure S4.3: *Long-term seasonal trend of AR frequency in IB and GB: The frequency of ARs per season (black dots) and the fitted trendline (in blue; slope is taken per decade) are shown for IB (left panel) and GB (right panel) for winter (December–February), spring (March–May), summer (June–August), and autumn (September–November) from 1982 to 2018. The AR frequency in each season is regressed on time (year) as an independent variable.*

S4.4: AR and AR-related Precipitation in IB

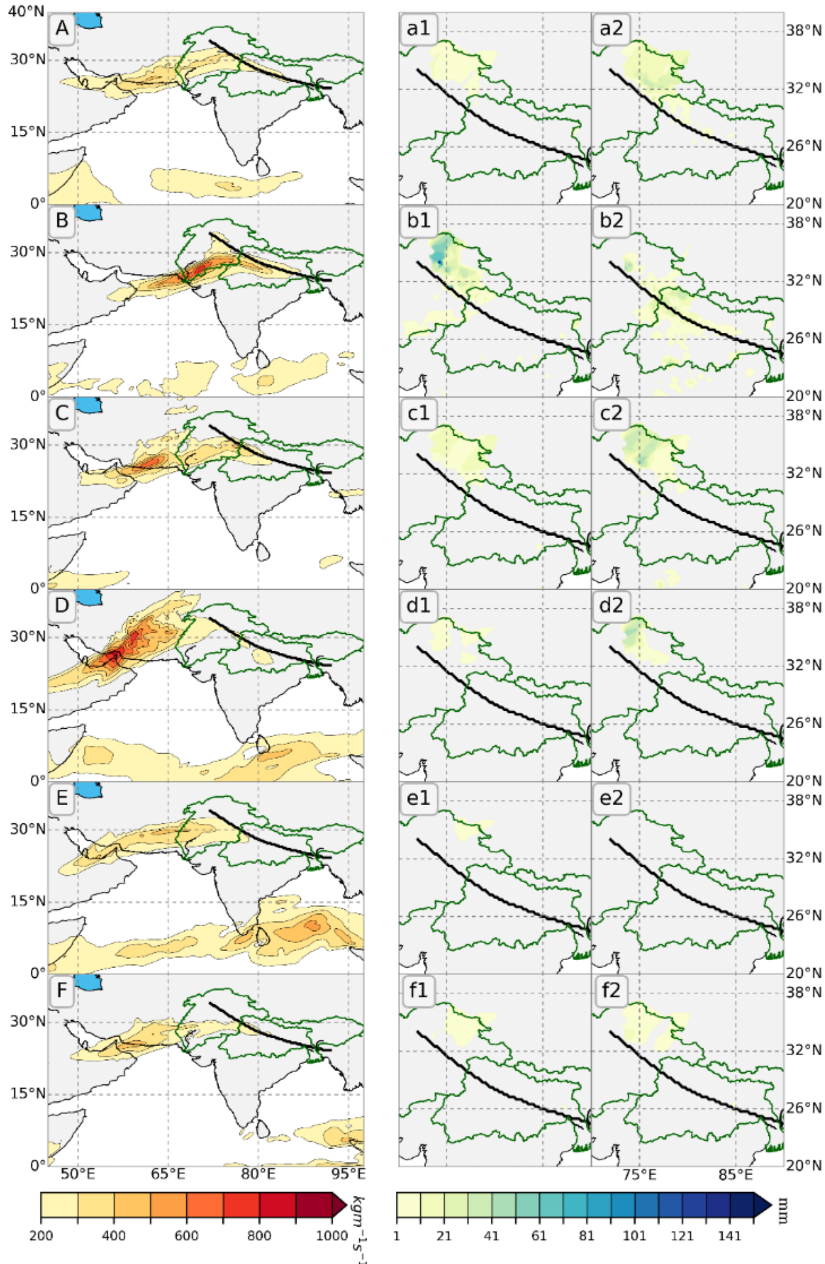

Figure S4.4: *Top ARs in Indus Basin: The top third to eight AR events in the Indus Basin (Bin A and Bin B) selected from the AR database are shown on the left panels (A to F), and the corresponding precipitation on the second and third day after the first day of the AR events are shown on the right panels (a1 to f2). The dates of the events are (A) 02-02-1989 (B) 02-03-1998 (C) 06-03-1983(D) 15-02-2017 (E) 25-12-2015 and (F) 15-01-1990 (in Figure SI 2, left panels). The AR for panels (A) and (B) fall under Cat 4, with maximum IVT of* $567.5\ kg.m^{-1}.s^{-1}$ *and* $517.2\ kg.m^{-1}.s^{-1}$ *respectively; ARs in panels (C), (D), (E) and (F) are Cat 3, with maximum IVT of* $477.6\ kg.m^{-1}.s^{-1}$, $387.6\ kg.m^{-1}.s^{-1}$, $362.5\ kg.m^{-1}.s^{-1}$ *and* $352.6\ kg.m^{-1}.s^{-1}$ *respectively. These ARs are confined mostly in the northern Arabian Sea and in countries of Iran, Pakistan and Afghanistan. The precipitation observations from Indian Meteorological Department (IMD) (Figure S4, panels a1- f1) show that precipitation is mostly along the tracks of the ARs and in higher reaches of the Himalayas (elevation > 4000 km).*

S4.5: AR and AR-related Precipitation in GB

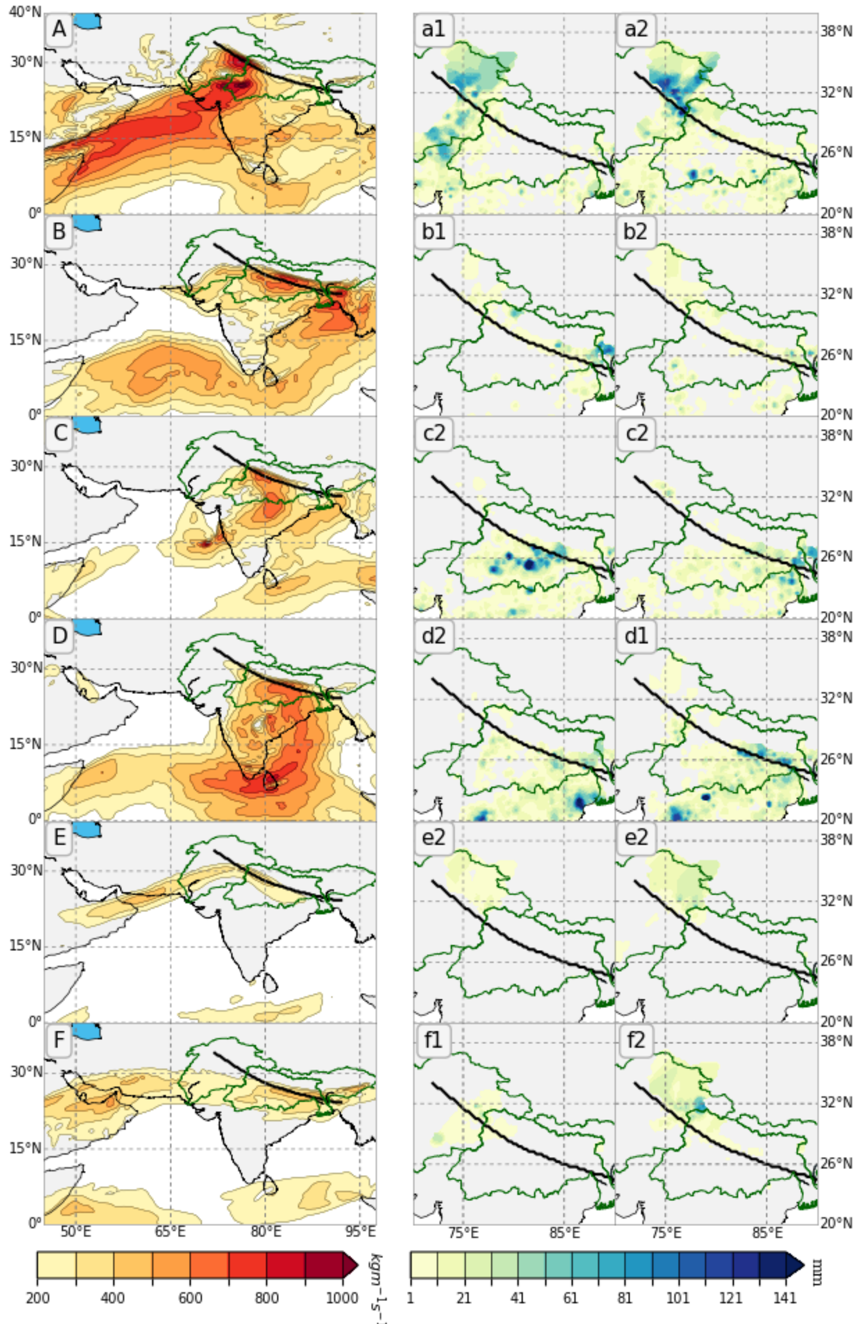

Figure S4.5: Top ARs in Ganga Basin. *The ARs occurred on (A) 25-07-1995, (B) 24-06-2000, (C) 03-10-2013, (D) 29-09-2001, (E) 23-01-1992, and (F) 12-02-2005. The ARs in (A), (B), (C) and (D) belong to Cat 5, with the highest IVT of* $1130.1\, kg.m^{-1}.s^{-1}$, $823.7\, kg.m^{-1}.s^{-1}$, $818.5\, kg.m^{-1}.s^{-1}$ *and* $813.98\, kg.m^{-1}.s^{-1}$ *respectively, and ARs in (E) and (F) belong to Cat 4 with the highest IVT value of* $572.2 kgm^{-1}s^{-1}$ *and* $559.6 kgm^{-1}s^{-1}$ *respectively. (Right panel) Figure SI 3 (a1-f1) shows precipitation observed above 140 mm in regions where the ARs make landfall, and greater than 50 mm along their tracks in most of these events.*

S4.6: Total IVT Convergence Term for 2003 AR event

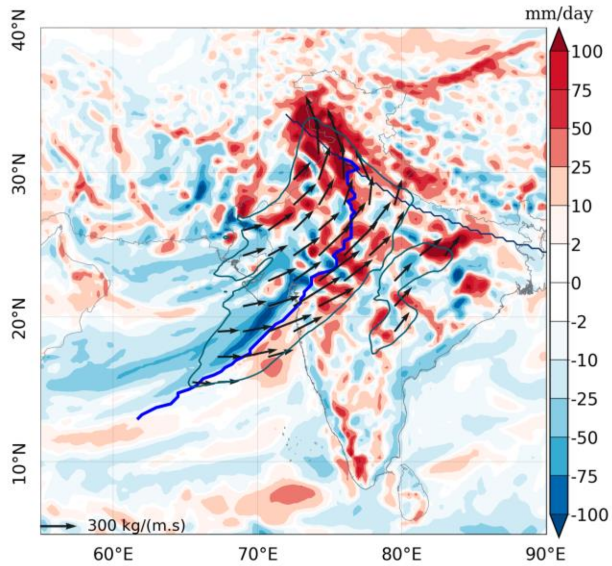

Figure S4.6: *Total IVT convergence term at 12UTC 18th February 2003.*

S4.7: Precipitation in mountains during AR events

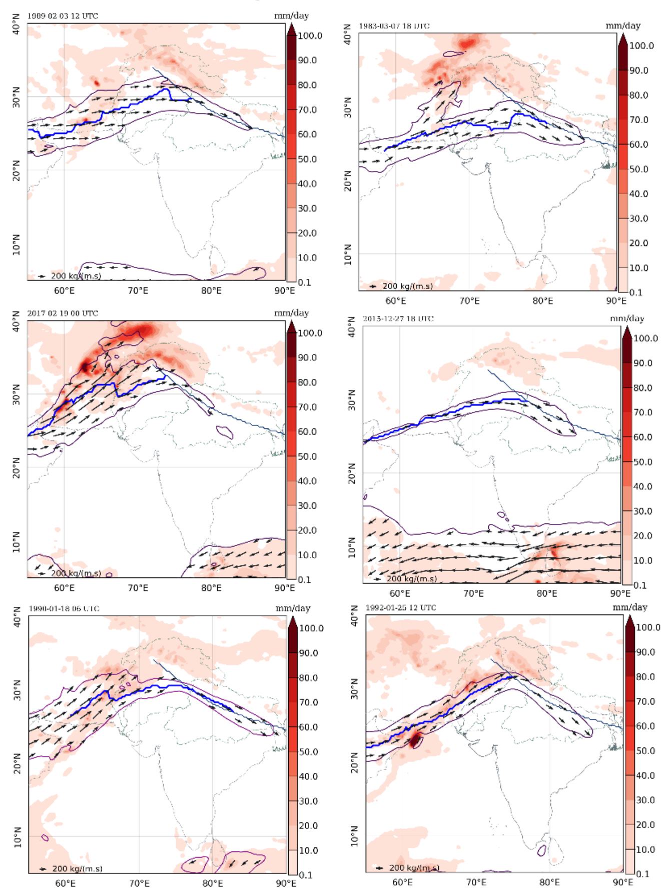

Figure S4.7: *ARs impact mountain precipitation. Precipitation at the selected timesteps of AR events is shaded and the corresponding values are shown by the colorbar. The AR boundaries for IVT of* $200\ kg.m^{-1}.s^{-1}$ *are* *shown in purple color, IVT vectors with this magnitude and greater as shown by arrows and the detection transect is shown by dark green color.*

S4.8: Trajectories of Air Parcels and Moisture Sources during AR Events

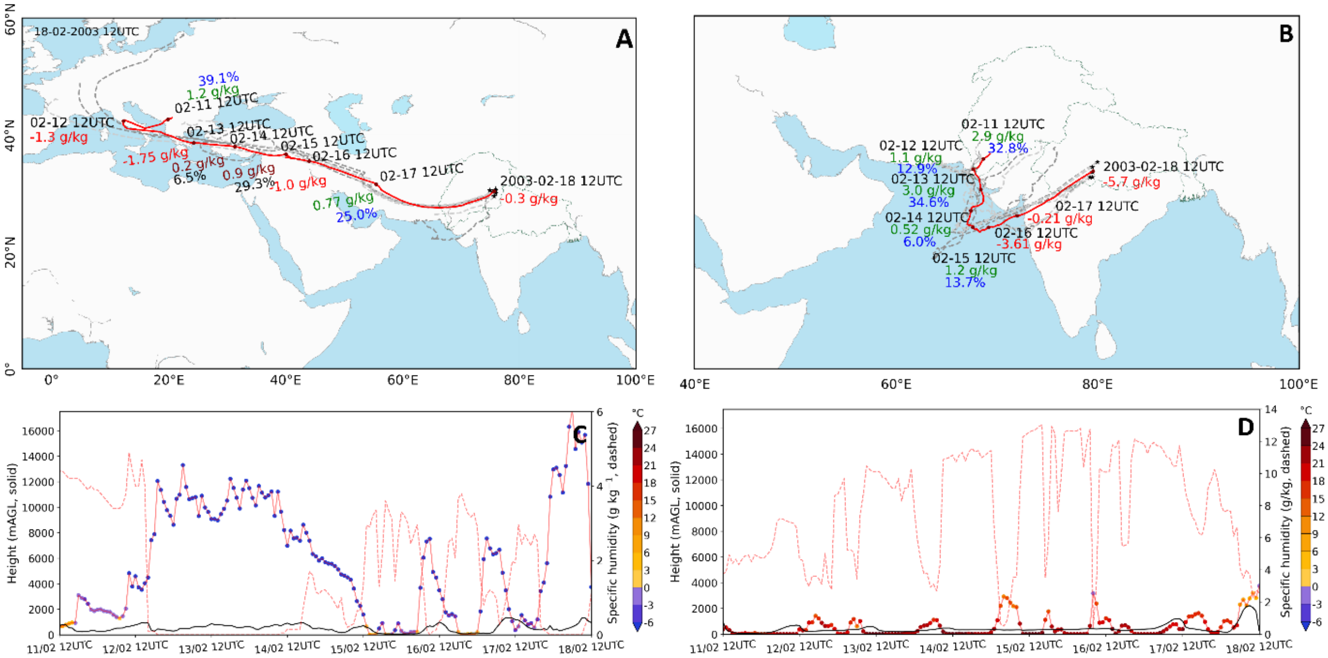

***Figure S4.8a**: Top panels: The trajectories of air parcels released at 18th February 2003 at 12UTC, within the AR boundary (as defined in the budget analysis), from locations ahead (Panel A), and behind (Panel B) the detection transect. The light and dark grey dashed lines represent trajectories of five air parcels each released at 5000 m AGL and 2500 m AGL, respectively, and the red solid line represent the average trajectory of air parcels. Moisture gained within (outside) the mixed boundary layer along the average trajectory is shown by green (dark blue), and the percent contribution of source to moisture at the target region is shown in blue (maroon). The moisture lost as precipitation is shown in red. Bottom Panels: Panels C and D show the vertical profiles of the average track at 18th February 2003 at 12UTC. The particle position in the atmosphere is shown in red solid line, specific humidity by the red dashed line, mixed boundary layer by the black line and the scatter plots represents the parcels' position and air temperature is shaded with values indicated on the colorbar.*

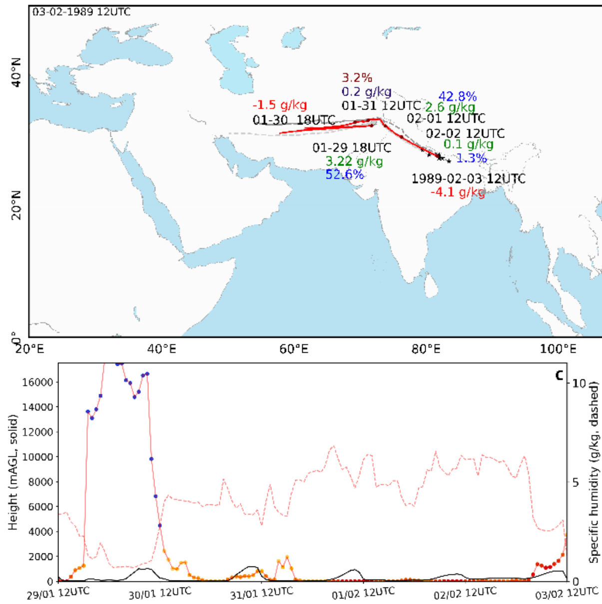

Figure S4.8b: *Similar to Figure 4.8a but for 03rd February 1989 at 12UTC.*

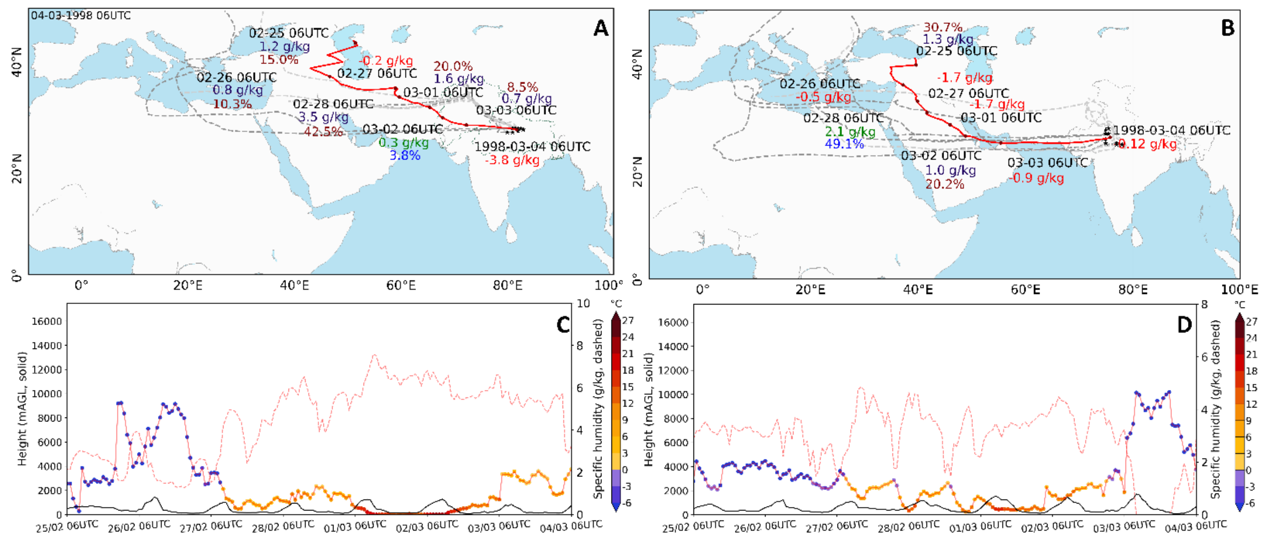

Figure S4.8c*: Similar to Figure 4.8a but for 04th March 1998 at 06UTC*

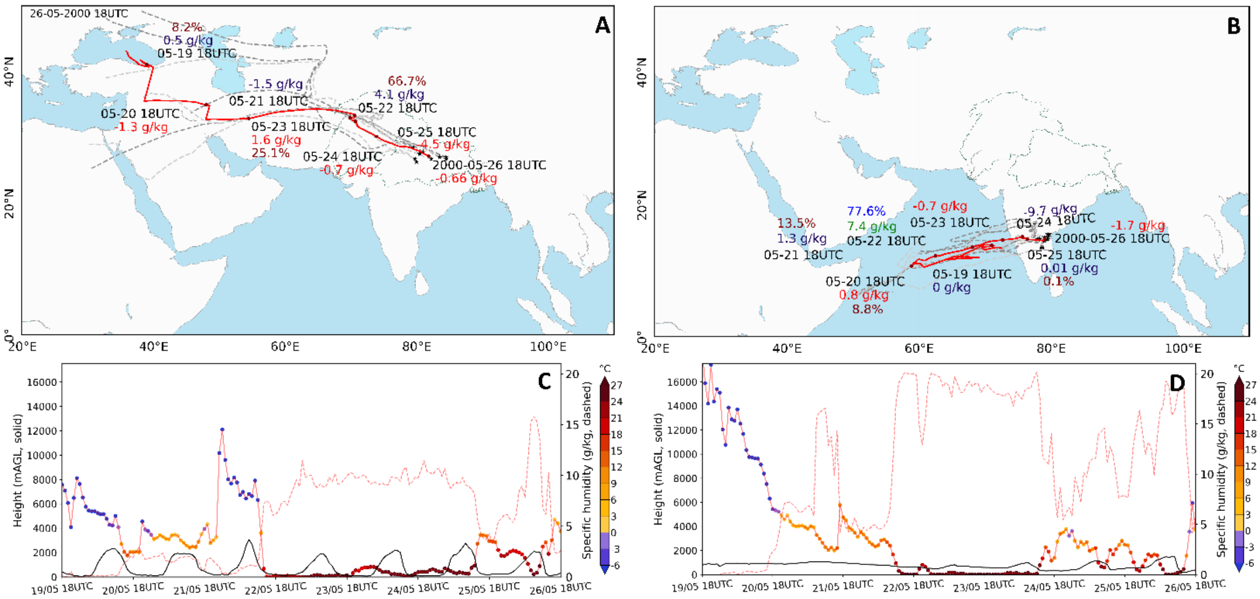

Figure S4.8d: *Similar to Figure 4.8a but for 26th May 2000 at 18UTC.*

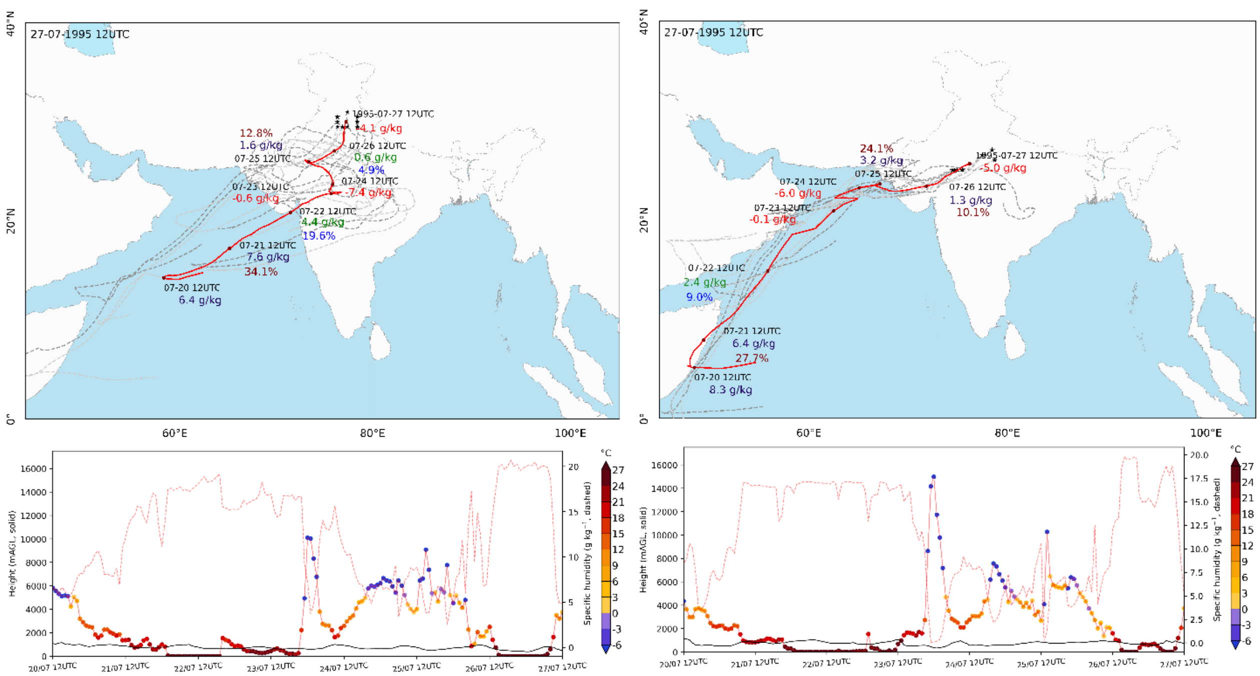

Figure S4.8e: *Similar to Figure 4.8a but for 27th July 1995 at 12UTC.*

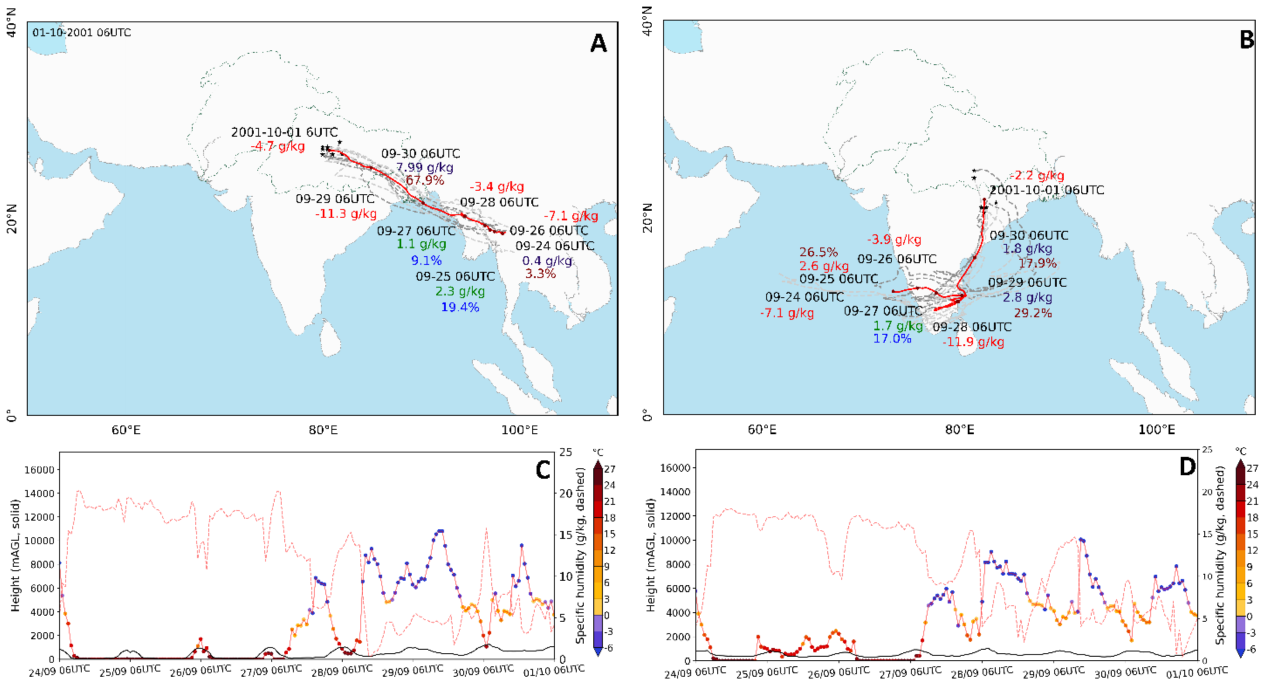

Figure S4.8f: *Similar to Figure 4.8a but for 01st October 2001 at 06UTC.*

Chapter 5

Quantifying the Impacts of ARs on Himalayan Hydrology

After:

Lyngwa, R. V., Nayak, M. A. & M. F. Azam. Large fraction of winter precipitation variability in two major Himalayan basins explained by Atmospheric Rivers. *Journal of Climate*, pp.1-30, DOI: https://doi.org/10.1175/JCLI-D-22-0599.1

Executive Summary

Chapter 3 presented the annual and seasonal characteristics (intensity, frequency, duration) of ARs in the Himalayan region during 1982-2018. Most Himalayan ARs impacting the subtropical-extratropical latitudes are predominant in winter, providing a beneficial water supply (Categories 0-2) but, occasionally in summer or autumn they can cause catastrophic (Categories 3-5). While ARs affecting the topical latitudes have more ARs across seasons and tend to cause more havoc than benefits (Categories 1-5). Notably, many winter ARs are less intense and transient (exist between 18-24 hours; IVT ≤ $250\ kg.m^{-1}.s^{-1}$). The top AR events in IB and GB have significant one-day precipitation impact along the AR axis and landfall areas in the mountains, with their impact extending to high mountains and nearby areas. High precipitation at these locations was due to a strong convergence of moisture from distant sources. Near the mountain, precipitation is orographic due to the forced ascent of less stable moist air, while on-axis the moist unstable air ascends by frontal processes or different air mass interaction or even by convection. Additionally, it showed that heavy precipitation events are associated with tracks over the tropics, drawing excess moisture from the north and eastern Arabian Sea, some form the north Bay of Bengal and continental sources, while small contributions came from extratropical sources. Surely these ARs will exert impacts in these regions, but how much do ARs impact the Himalayan regions? Chapter 4, will focus on answering this important question through a detailed analysis of the long-term contributions of ARs to precipitation, how these contributions vary spatially and seasonally in the two Himalayan Basins, and their impact on extremes will highlight their importance. This study will help to explain the driver of hydrological variability which are key to water resources and risk management. This chapter begins by demonstrating the influence of two intense AR events, one in each basin, on precipitation and water levels, that led to the largest floods. It then outlines the methods to identify AR-affected regions, along with quantification techniques. The main analysis assessed AR contributions to four key aspects: seasonal and annual precipitation, winter precipitation, seasonal extremes, and major floods. This study revealed that ARs contribute throughout the year, with the highest contribution in winter in IB and northern GB. Coefficients of determination were computed for winter precipitation, as it has the highest AR contribution, in Hindu-Kush (HK), Karakoram (KA), Western (WH), and Central Himalaya (CH) with respect to AR-related precipitation, which showed that the variability is explained largely by ARs.

Abstract

Atmospheric rivers (ARs) have the potential to generate large-impact hydrometeorological events over mountainous topography. In this study, we investigate ARs' impacts on the hydrology of the Indus Basin (IB) and Ganga Basin (GB), two highly populated basins of the Himalaya. We used the recently developed 37-year-long ERA5-based AR database over the Himalaya to explore the influence of ARs on total and extreme precipitation, snowfall, and floods over these basins. We find that ARs contribute; 25% to the annual rainfall in the IB and; 15% to the GB. Over the mountainous regions, ARs contribute more than 50% to winter precipitation in Karakoram (KA), Hindu–Kush (HK), Central (CH), and western Himalaya (WH), and respectively explain over 75%, 57%, 42%, and 30% of their interannual variability. The seasonal rainfall extremes over the mountain foothills are most often (50%– 100%) associated with ARs in winter and spring, whereas the summer and autumn extremes over the plains and mountain foothills appear moderately associated with ARs (10%– 40%). The two most catastrophic flood events (2014 Kashmir flood and 2013 Uttarakhand flood) in these basins are found to be linked with category 5 ARs. Upon further examination of floods over a long period, we noted that 56% and 73% of the floods in IB and GB, respectively, are related to ARs. Thus, our results establish that the variance of ARs is a major source of hydroclimate variability in the two Himalayan basins.

5.1. Introduction

Atmospheric rivers (ARs) are moisture-rich plumes concentrated in the lower part of the troposphere and are identified as transient filamentary features (Zhu and Newell, 1998) having a lifetime spanning from several hours to generally 3 days or more (Zhou, Kim and Guan, 2018). Upon landfall, ARs bring intense precipitation in coastal regions (Neiman *et al.*, 2008; Konrad and Dettinger, 2017), in the mountainous regions (Leung and Qian, 2009; Thapa, Endreny and Ferguson, 2018; Chen *et al.*, 2019; Nayak, Azam and Lyngwa, 2021), and can even infiltrate deep inland through valleys and plains (Rutz, Steenburgh and Ralph, 2014; Mahoney *et al.*, 2016; Nayak, Villarini and Bradley, 2016). When lifted orographically, they are known to deliver copious rainfall at lower altitudes and snowfall at higher altitudes (Neiman *et al.*, 2008). ARs are often related to extreme hazards such as floods, landslides, destructive surface winds, etc. (Paltan et al. 2017; Ralph and Dettinger 2011; Waliser and Guan 2017); when viewed in certain favorable contexts, however, they emerge as essential sources of moisture supply, alleviate droughts, and decrease water scarcity (Dettinger et al. 2011; Dettinger and Cayan 2014). ARs have been extensively examined in connection with high-impact precipitation events, especially over mountainous regions adjacent to oceans. In the western USA, for example, winter ARs produce twice the precipitation as compared to non-AR storms (Neiman *et al.*, 2008). AR impacts are amplified by the presence of mountains, e.g., the west coast of South America receives; 15% more of the

AR-related precipitation than North America due to the Andes (Viale *et al.*, 2018). In another study on the impacts of inland penetrating ARs in Europe, rainfall and/or snowfall produced by ARs are found to be the major cause of all extreme floodings in the Rhine catchment (Ionita, Nagavciuc and Guan, 2020). A study by Paltan et al. (2017) on the impacts of global ARs found that ARs contribute approximately 11% to the annual snowpack in limited areas of the Himalaya. Since ARs are known to deliver snowfall and rainfall depending on the region's location, topography, and atmospheric conditions, it becomes critical to understand how ARs modify the hydrology of these regions. AR and precipitation connections in the Himalayan basins are understudied. Previous works were focused on improving precipitation observations over HK, KA, and Himalaya and conducted topographic-related precipitation extremes studies (Palazzi, von Hardenberg and Provenzale, 2013; Riley *et al.*, 2021). Recently, a few studies have initiated the exploration of ARs in South Asia. Yang *et al.*, (2018) identified ARs over the Bay of Bengal that landed over coastal India, Bangladesh, Bhutan, Myanmar, and Nepal at $24°N$ and those that penetrated inland into Eastern Himalaya (EH) at $27°N$. They also found that many extreme rainfall events at the foothills of EH are related to ARs. Other studies in South Asia have focused on ARs in the coastal mountainous regions in South India (Lakshmi and Satyanarayana, 2019, 2020). Thapa et al. (2018) identified ARs in Nepal and examined their frequency and contribution to annual and non-monsoon (October–May) precipitation extremes at six grid cells covering Nepal. However, this study excluded most regions in the two Himalayan basins and did not attempt to identify ARs and assess their impacts on HK, KA, and WH. Nash and Carvalho (2018) focused on monthly frequencies of ARs in KA, WH, CH, and EH, while Nash et al. (2022) investigated the synoptic atmospheric patterns and dynamic mechanisms associated with different types of ARs during December–May over High Mountain Asia (HMA). While acknowledging the frequent occurrence of ARs over the Himalaya, the two studies did not consider their hydrologic impacts. This represents an important research problem since estimating the impact of ARs on the hydrology of the two major snow- and glacier-rich basins can help manage water resources in the region that supports the livelihood of roughly a billion people.

The two Himalayan basins, IB and GB observed the largest floods in September 2014 and June 2013, respectively. The September 2014 Kashmir flood killed nearly 460 people (Rehman et al. 2016; Vithalani and Bansal 2017), affected 2.5 million people, destroyed 2.4 million acres of cropland, impacted 4000 villages, and caused an economic loss of over $15 billion (Vithalani and Bansal 2017). The June 2013 Kedarnath flood in Uttarakhand killed roughly 5000 people and caused an economic loss of $400 million (Bhambri et al. 2016). The Kedarnath flood was a complex cascading catastrophe, which triggered a Glacier Lake Outburst Flood in the region (Das et al. 2015). Though both floods have been extensively studied, the role of ARs in the Kashmir flood has not been ascertained nor there is any assessment of ARs' impact in the Kedarnath flood. In this study, we show that these events were accompanied by category 5 ARs (Ralph, Rutz, *et al.*, 2019) (Figures 5.1a, b) that triggered extreme precipitation, which translated into disastrous floods (Figure 5.1 and Fig. S5.1 in the online supplemental material; further details are given in the results section). These results underscore the impacts of ARs over the Himalaya.

The objectives of the present study are

(1) To estimate the impact of ARs on seasonal and annual total precipitation and extremes in IB and GB,

(2) To estimate the impacts of ARs on winter rainfall and snowfall in the mountains of IB and GB, and

(3) To identify the major floods related to ARs. The remainder of the paper is organized as follows.

Section 5.2 provides a brief description of the study area. Section 5.3 describes in brief the AR database, precipitation, floods, and discharge data used in this study which is followed by a detailed description of methods implemented to quantify the AR impacts on the hydrology of IB and GB. Section 5.4 presents the relative contribution of ARs to the annual and seasonal precipitation, including precipitation extremes and floods in the basins with a discussion of their impacts. The results and discussions of our findings are then summarized and concluded in section 5.5.

5.2. Study area

The Himalaya, located in South Asia, extend, ~2,500 km from west/northwest to east/southeast across Pakistan, India, China, Nepal, and Bhutan. They are landlocked by the Tibetan Plateau in the north, the HK and KA in the west, the Yunnan Plateau in the east, and the Indo-Gangetic Plains in the south. The high mountains (~8,000 m MSL) impede moist air transported from the tropical waters of South Asia, the Atlantic Ocean, and seas of the Middle East and results in precipitation via orographic lift (Figure 5.1c, d) (Bookhagen and Burbank 2006). The two basins covered areas of 1,120,000 and 1,087,300 km^2, supporting 312.5 and 637 million people, respectively (Azam *et al.*, 2021). They have distinct climatic regimes that are controlled by latitude, altitude, and location relative to the atmospheric flow of the Indian summer monsoon (ISM) and western disturbances (WDs). The climates within these basins show great variation across their geographical extents, which become even more intricate in the upper regions due to the complex mountain terrains. For example, it is arid and semiarid in lower IB (~200 mm yr^{-1}) and humid to arid in northern IB (1500–2000 mm yr^{-1}) (Laghari et al. 2012; Archer et al. 2010); in GB, western regions are arid to semiarid (350 mm yr^{-1}), eastern regions are typically tropical (hot with abundant precipitation in summer; 2000 mm yr^{-1}), and in the northern parts the climate transition from tropical to alpine (2000–3000 mm yr^{-1}) (Anand et al. 2018).

Of the two precipitation drivers preeminent to Himalayan basins, the ISM contributes 60%–80% of their annual precipitation, though in IB mostly the south-facing WH receives precipitation from the ISM. The

ISM is a tropical wind regime that brings precipitation during boreal summer months, set in motion by two intense pressure centers in central and south Asia, related to temperature differences between land and surrounding water bodies. Another driver of precipitation [40% and 25%– 35% of the annual precipitation in IB and GB, respectively (Barros et al. 2006; Lang and Barros 2004)] is the WDs (also called upper synoptic systems or extratropical storms), which are active mainly in winter and spring due to the large latitudinal temperature differences in subtropics. WDs deliver precipitation through orographic lift when the upper levels are rich in moisture. They originate in the Middle Eastern Seas (Bookhagen et al. 2005; Dimri 2006) and propagate eastward across semiarid and arid lands before reaching these basins. Precipitation is predominantly snowfall above 2,500 m MSL (headwater of these basins) and rainfall in the lesser elevation plains (Lang and Barros 2004). The annual precipitation variability during WDs mainly leads to variations in glacier accumulations (Kaab et al. 2012). The accumulated snow and ice every winter in the upper reaches serve as important reservoirs for spring water yield. Meltwaters contribute the highest to the annual streamflow in IB (40.6% in northern IB), while rainwater dominates in GB (66% in northern GB) (Lutz et al. 2014). Snow and ice meltwaters are indispensable for the Himalayan water resources especially when monsoon onset is delayed. Any changes in the seasonal/annual contributions by the dominant precipitation regimes potentially impact roughly a billion inhabitants there (Immerzeel et al. 2020; Pritchard 2019).

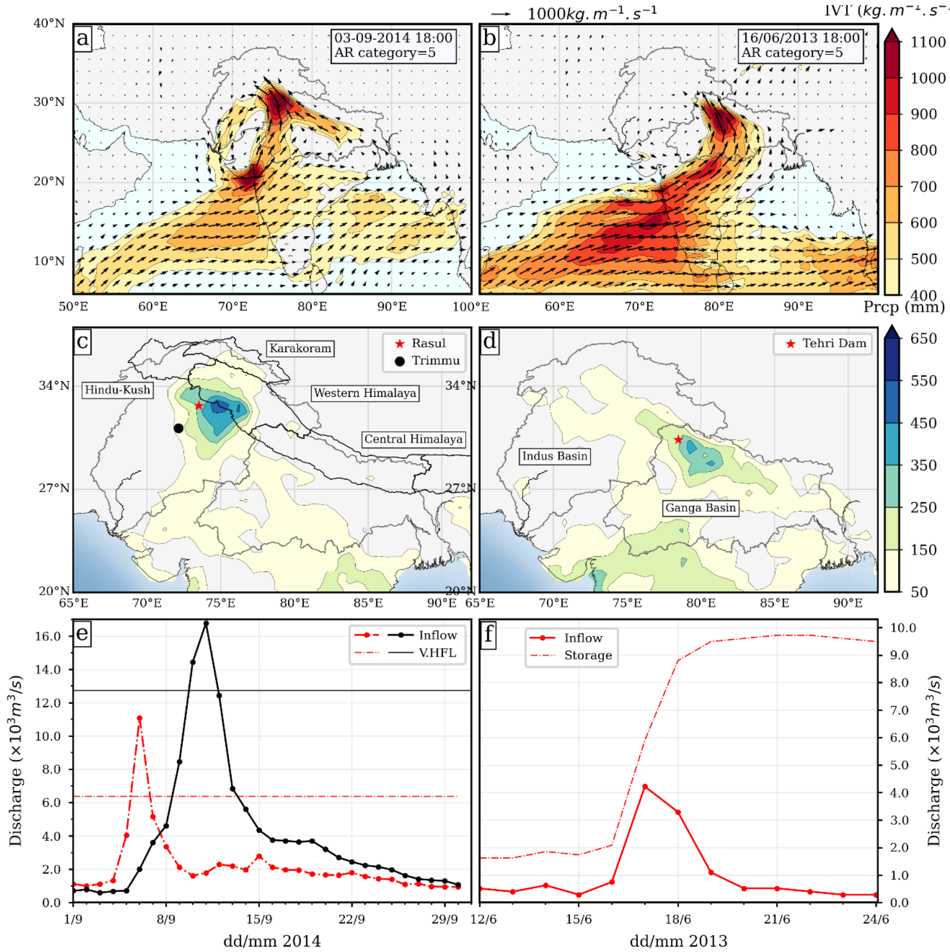

Figure 5.1*: IVT ($kg.m^{-1}.s^{-1}$)) for two ARs (a) 3rd September 2014 at 1800 UTC (AR event: 3rd–th6 September) and (b) 16th June 2013 at 1800 UTC (AR event: 12th–18th June); (c), (d) the total accumulated precipitation (mm; using WFDE5) for the AR events. The star and circle (solid) represent the discharge measuring stations in Jhelum River and Chenab River, respectively, in (c), and the star in (d) represents the location of the Tehri Dam at Bhagirathi River. (e), (f) the discharges ($m^3.s^{-1}$) at the gauge stations/dam. In (e) the discharge and very high flood level are shown by dashed lines for Rasul and by solid lines for Trimmu in IB, and in (f) the discharges are shown by solid lines and storage by dashed line at Tehri dam in GB. The basin's boundary is shown by light gray lines in (a)–(d); boundaries of HK, KA, WH, and CH are shown by black lines (Bolch et al. 2012) in (c).*

5.3. Materials and methods

5.3.1. Data

We used the recently developed European Centre for Medium-Range Forecasts reanalysis version 5 (ERA5) (Hersbach et al. 2020) based AR database for the Himalaya over 1982–2018 (Nayak, Azam and Lyngwa, 2021). This database provides multiple characteristics of AR events including location, intensity (average IVT of AR axes), duration, maximum IVT, and categories of AR events. The ARs are identified if they intersect the detection transect located south of the Himalaya (Figure 5.2, green line) and fulfill the AR criteria (see Text S5.2 for details). The algorithm of Nayak et al. (2021) uses relative IVT thresholds to extract locally extreme IVTs. As in (Lavers *et al.*, 2012), only ARs that persist for at least 18 hours are considered. Moreover, only the timesteps of ARs without cyclones are retained. A brief description of the regional algorithm used for the identification of ARs in the Himalaya is given in Text S5.2.

We also used the "tARget" algorithm by (Guan and Waliser, 2019) to identify ARs in this study region, and we found that nearly 82% of the AR days match (Figure S5.10) with the ARs in Nayak et al. (2021); the detailed result based on "tARget" ARs are given in the supplemental material. In the main manuscript, however, we focused on the results obtained using ARs by Nayak et al. (2021) because the algorithm 1) is region specific for the Himalaya, 2) is capable of identifying persistent ARs of low intensities, and 3) excludes all cyclone-related impacts. We also added a section in Text S5.7a, b to discuss the limitations of the present Nayak et al. (2021) approach.

Hourly rainfall and snowfall flux (aggregated to daily) from Water and Global Change (WATCH) Forcing Data ERA5 (WFDE5; Cucchi 2021; Cucchi et al. 2020) are used to analyze the precipitation patterns over the IB and GB over the period 1982– 2018. WFDE5 are recent global meteorological data developed by applying the WATCH Forcing Data (WFD) methodology (Cucchi 2021; Cucchi et al. 2020) on ERA5. ERA5 is bias corrected for the number of wet days per month using CRU TS4.03 (Climate Research Unit; Harris et al. 2014) and for the precipitation totals using GPCCv2018 (Global Precipitation Climatological Centre; Schneider et al. 2016), and upscaled to half-degree ($0.5° \times 0.5°$) spatial resolution to conform with CRU resolution. Corrections for unrealistic precipitation phase (rainfall or snowfall) relative to large elevation differences between ERA5 and CRU TS4.03 grids were applied, for example, a phase was changed if at a timestep (hourly) the bias-corrected air temperature for a grid at a certain elevation is beyond the respective monthly minimum CRU air temperature records for rainfall and monthly maximum CRU air temperature records for snowfall (Cucchi et al. 2020).

We also used high-resolution daily gridded rainfall observations from the IMD (https://dsp.imdpune.gov.in (Pai *et al.*, 2014)) with a spatial resolution of $0.25° \times 0.25°$ from $1982 - 2018$. These data are developed using gauge station observations interpolated into grids using Shepard's method (Shepard 1968). In this dataset, the daily rainfall total for any day (say 5 June 2020) is defined as rainfall collected from 8:30 AM IST (Indian Standard Time) of the previous day (i.e., 4th June 2020) to 8:30 AM IST of that day. Since the AR dates are in UTC (Universal Time Coordinated) and rainfall observations are in IST, to match an AR day we take 1 day ahead in the rainfall day. IMD extent, however, does not include parts of IB and GB outside India, hence results based on IMD rainfall are reported in the supplemental material.

Important details for flood events in India (location, start date, end date, etc.) are retrieved from Dartmouth Flood Observatory's (DFO) flood database developed by Najibi and Devineni (2018), which is publicly available at https://dataverse.harvard.edu/dataverse/dfo1985to2015 for the 1985– 2015 period. These are large flood events (i.e., over a 10-year recurrence period) that have been validated using information from various sources and have been mapped for changes in surface water extent during floods by DFO using remote sensing satellites. More information regarding the collection and validation of the flood events can be found in the cited paper and link provided above.

The daily discharge for IB was obtained from the Federal Flood Commission, Government of Pakistan (FFC-GOP 2014) at Rasul and Trimmu barrages. Due to the unavailability of discharge in GB, we used the reservoir storage data of Tehri Dam from the India Water Resource Information System (WRIS 2013). For the flood days, we used reservoir releases provided by Tehri Hydro Development Corporation (THDC) to compute inflows [Q in (m^3/s)] to the dam from a simple mass balance model, ignoring evaporation and infiltration losses

$$Q_{in} - Q_{out} = \frac{\Delta S}{\Delta t} \tag{14}$$

where, $Q_{out}(m^3/s)$ = release from reservoir. ΔS (m^3) = change in storage during the period $\Delta t(s)$.

5.3.2. AR impacts on annual and seasonal rainfall

A day is considered an AR day if an AR is detected for at least one-time step (out of the four available, 0, 06, 12, and 18 UTC) on that day. For the assessment of AR impacts on precipitation, we defined the regions within 250 km from the AR major axis as regions with AR-affected precipitation, which is consistent with previous studies on AR-related precipitation (Mahoney *et al.*, 2016; Nayak and Villarini, 2017, 2018). Hatchett et al. (2017) also used 250 km to link avalanche events to ARs (or AR precipitation) when the AR major axis is found upstream of the events and within 250 km. It has been observed that regions closer to the AR major axes have more rainfall (Nayak, Villarini and Bradley, 2016), and showed a stronger positive relationship with on-axis AR IVT (Nayak, Villarini and Bradley, 2016) than rainfall at 300 km away from the axis. Thus, precipitation can be expected to be more surrounding to the AR axes that have higher atmospheric IVT, than the regions which are far from the axis. As mentioned earlier, the Himalaya block and deflect moisture transports, coming from the west, south, and east, therefore ARs will also be deflected from their path on impinging upon the mountains. In addition, since the AR detection transect was defined along the Himalayan foothills, before elevated terrains, the AR axes were not identified beyond the detection transect where AR IVT is dispersed in the Himalaya. To counter this hindering and dispersing effect of the Himalaya, we consider precipitation if it happens during an AR time step within a 350 km band around the detection transect, and only those grids that have IVT above the threshold are used to identify ARs as AR-related precipitation. The "350 km" was also considered to include the northern reaches of IB, HK, and KA. In this way, on a particular AR time step, we assess grids within 250 km from the AR axes and those that have IVT above the threshold within 350 km from the detection transect for AR impacts on precipitation (referred to here as AR grids). Now, when there is more than one AR time step in an AR day, we compute the union set of AR grids for that day by combining each set of AR grids of each time step. Then the precipitation (daily) in the AR grids during AR days is defined as AR-related precipitation. For this analysis, we did not include one day each before and after an AR event i.e., any possible differences in the lag/lead times of AR-derived precipitation (Shu, Shamseldin and Weller, 2021; Wang, Wei and Ma, 2021), as we cannot exactly determine the AR-related precipitation without knowing the AR axes. Hence, we believe that our estimates of AR contributions to precipitation are conserved. Relative contributions of AR-related precipitation are estimated at annual and seasonal scales, such as winter (December–February), spring (March–May), summer (June–August), and autumn (September–November).

AR contribution to annual (seasonal) precipitation is computed as temporal and spatial averages: 1) spatial analysis (temporal averages at each grid) for rainfall in IB and GB, and 2) region-wide analysis (winter average precipitation over a region) for rainfall and snowfall in HK, KA, WH, and CH. For the spatial analysis of AR contributions, we compute the average of annual (seasonal) precipitation and AR-related precipitation for the study period at each grid cell and then compute the contribution as follows

$$\%\ contribution\ at\ a\ grid\ cell = \left[\frac{\frac{\sum_{i=1}^{i=N}(P_{AR})_i}{N}}{\frac{\sum_{i=1}^{i=N}(P)_i}{N}}\right] \times 100\% \qquad (15)$$

where,

$(P_{AR})_i$ is total precipitation on AR days of ith year (season) at a grid cell $(P)_i$ is total precipitation on all days of ith year (season) at a grid cell N is total number of years (seasons).

In regional analysis, we compute the daily spatial sum of rainfall and snowfall over each region on AR days and all days. Since the detection transects over IB and GB is stretched from HK to EH, the ARs detected at HK, KA, WH, and CH impact almost their entire region, respectively. Hence, the daily spatial sum computed by considering either only those grids that experienced AR or all the grids within a region on AR days would be very similar. Also, in this case, the regions have comparatively smaller areas than the basins. The annual average AR-related rainfall/snowfall is then computed by dividing the total AR rainfall/snowfall for all years by the number of years and scaling the values by the area of the region (though the area can be taken as $\text{area} = \text{no. of grids} \times 25\ \text{km} \times 25\ \text{km};$ taking $1° = \sim 100$ km, here we have scaled the winter precipitation by the number of grids as we have also summed precipitation for the number of grids within regions in the numerator). Mathematically, it can be written as

$$Annual\ average\ rainfall/snowfall = \frac{\frac{\sum_{i=1}^{i=N}(S_{AR})_i}{N}}{No.of\ grids\ within\ the\ region} \quad (16)$$

where, $(S_{AR})_i$ is Annual sum of AR-related rainfall/snowfall over the region for the ith year and N is total number of years (seasons).

We also compute the coefficient of determination (R2) between precipitation totals and AR-related precipitation for the winter season for HK, KA, WH, and CH, as a measure of ARs' influence on the interannual variability of winter precipitation in the mountainous regions.

5.3.3. AR impacts on extreme rainfall

To assess the AR impacts on seasonal extreme precipitation, we find the maximum daily rainfall at each grid for each season and for all years. We fixed 60 mm as the minimum threshold (~80th percentile in the winter season, Figure S5.3) to define daily maxima for IMD, and 40 mm for WFDE5 (as 60 mm appears rare in IB in winter and spring (Figure S5.5a), e.g., only 10 grids satisfy 60 mm criteria, and three have all their extremes related to ARs in winter). These fixed thresholds of 60 and 40 mm were adopted to avoid maxima of smaller magnitude that may not have large perceivable impacts. The grids with the number of seasonal maxima ≥ 7 (return period of roughly 5 years, in some cases smaller) are retained for further analysis. We then compare the dates of these maxima with AR dates to classify them as AR-related extremes when the dates match. The AR contribution to extremes is then computed as

$$\%\ contribution\ at\ each\ grid\ cell = \frac{SM_{AR}}{SM} \times 100\% \quad (17)$$

where, $SM_{AR} =$ number of years with AR-related seasonal maxima, $SM =$ total number of years that have seasonal maxima precipitation above 40mm for WFDE5 and 60 mm for IMD.

5.3.4. AR impacts on floods

We also assessed the number of flood events reported in these basins that are related to ARs. An AR-related flood event is defined as follows: 1) the flood should have occurred within the AR grids around the AR axis on an AR day, 2) the flood should have happened within 7 days after an AR event to account the time of concentration, and 3) floods that have happened 2 days before the AR event to account for high IVT already present in the region before the AR is identified and for the time steps ARs are present very close to the transect but were not identified by the algorithm.

5.4. Results and discussion

5.4.1. Patterns of Annual and Seasonal Rainfall

The annual rainfall shows significant spatial variation in both basins (Figure 5.2a) mainly due to variations in topography and the influence of the main precipitation drivers. Mountainous regions, particularly CH and its eastern foothill, receive the highest rainfall. Seasonal rainfall (Figure 5.2d–o) further illustrates remarkable spatial variations and regional distribution of rainfall among the seasons in each basin. In IB, the highest rainfall happens in summer and is limited only to the south-facing WH (Figure 5.2j). Rainfall magnitude reduces rapidly from WH toward the plain areas in the south IB and the northern most IB (in KA). This is related to monsoon airflow propagating westward toward northwest India with reduced atmospheric moisture, which is extracted mostly by WH (Fowler and Archer, 2006). The rainfall in IB is also brought by interactions between WDs coming from the west and the monsoon propagation from the east, and often such interactions produce extreme rainfall and generate floods (Pai and Bhan, 2014). In winter, the highest rainfall (70–240 mm per winter) is in central-north IB (WH and lower HK, Figure 5.2d), while rainfall is less than 15 mm per winter in KA (data not shown). This pattern is similarly observed in spring, with an average rainfall of 50–300 mm found only in central-north IB (Figure 5.2g), though a large part of western IB receives greater than 50 mm on average. The rainfall in winter and spring is mostly associated with WDs approaching from the west/southwest. In autumn, as in summer, the band that receives the maximum rainfall (200–350 mm per autumn) is to the southeast of WH (Figure 5.2m), which is related to moist winds associated with the ISM. GB receives the lowest rainfall, less than 65 mm, in winter except in the north (115–140 mm) (Figure 5.2d), and the highest rainfall in summer with 400 mm distributed throughout the basin, the highest is in CH (750–1140 mm, Figure 5.2j). In spring, rainfall between 100 and 400 mm is found in the north and east GB, and less than 50 mm is found in the remaining areas of the basin (Figure 5.2g). The autumn rainfall (Figure 5.2m) bears similar patterns to summer rainfall though the magnitudes are comparatively lower. The east–west rainfall gradients in summer and autumn imitate the monsoon progression across GB basin (in June) (Bookhagen and Burbank, 2010) and the monsoon retreat (in October) in autumn. Though some portion of the summer and autumn rainfall is related to cyclones that made landfall at the Indian coastline or those that moved inland from the Arabian Sea and Bay of Bengal during the pre- to post-monsoon (Sattar and Cheung, 2019). We found similar spatial patterns for the annual and seasonal rainfall in both basins except for the northern IB when IMD is used; details are provided in the supplemental material (section S5.6).

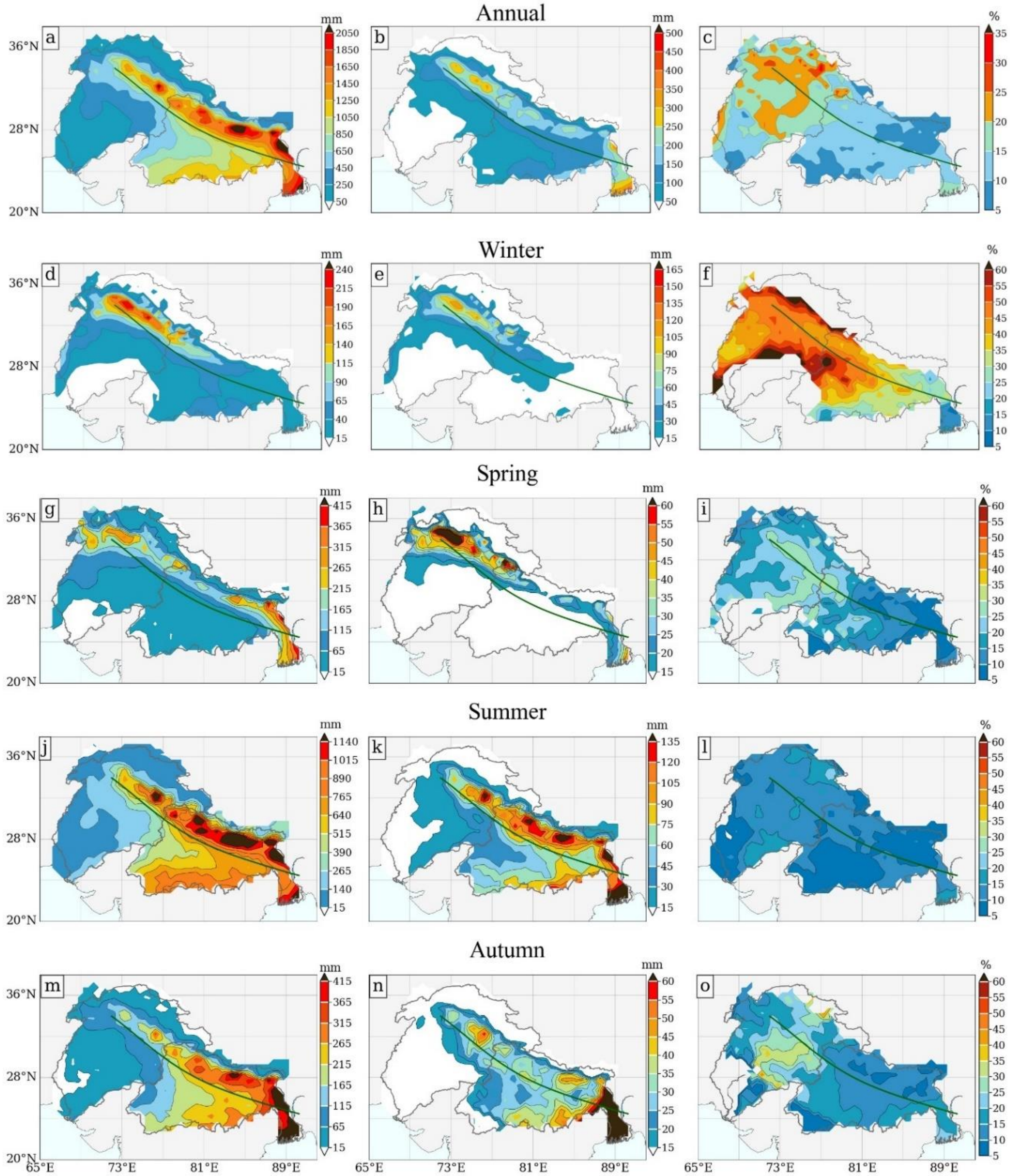

Figure 5.2: *(left) Spatial distribution of annual and seasonal average rainfall (mm/year and mm/season), (center) annual and seasonal average AR-related rainfall (mm/year and mm/season), and (right) the fractional contributions (%) over the period* 1982–2016 *using WFDE5. The basin outlines and the detection transect are shown by light gray lines and the dark green line, respectively. Note that grid cells with annual (seasonal) average rainfall < 50 mm (< 15 mm), shaded in white, are not shown in the fractional contribution.*

5.4.2. ARs' contributions to annual and seasonal rainfall

The spatial patterns of AR-related rainfall are similar to annual rainfall in both basins, albeit with smaller magnitudes. On average, ARs contribute nearly 20%–30% to the annual rainfall in north IB and over isolated patches in south IB (Figure 5.2c). In GB, 5%–15% of the annual rainfall happens during ARs, with higher fractions; ~20% in the lower east in response to ARs' frequent landfall north of the Bay of Bengal during summer and autumn. On average, rainfall in IB (KA, HK, WH, and southern plains) is more influenced by ARs than rainfall in GB. Similar spatial patterns are noted for annual, AR-related rainfall and AR contributions (%) in both basins when IMD rainfall data are used (Figure S5.6), and discrepancies were found in the northernmost reaches of IB, where mountain elevation exceeds 3000 m (mostly in KA) (more details are given Text S5.6). The highest AR contribution to seasonal rainfall is found in winter (Figure 5.2f), contributing up to 50% of comparatively high rainfall (40–120 mm, Figure 5.2e) in central IB (WH) and northwest GB (west of CH) and even higher fractions of above 60% for comparatively low rainfall (less than 40 mm) is found in the south and northern reaches of IB. In GB, ARs contribute 50%– 60% of winter rainfall in the northwest which gradually reduces to 10% in the south GB. The higher contributions from ARs in the central IB and northwest GB during winter are likely due to winter ARs frequently originating in the Arabian Sea and mostly striking the WH and western part of CH (see Figure 4 in Nayak et al. (2021)). These ARs deposit the bulk of their moisture in the mountains and release additional moisture when deflected along the Himalayan Range.

In spring (Figure 5.2h), AR-related rainfall is the highest in north IB (mostly in WH and HK), and southeast GB. On average, ARs contribute 15%– 30% in IB and 10%– 30% in GB, with the highest AR contribution of 35% found in the mountains of IB and northwest GB (Figure 5.2i). In summer, ARs have a higher impact on rainfall in the north IB (WH) and in GB (except the west) (Figure 5.2k). ARs contribute to 15%– 20% of rainfall in IB except in the south, and ~15% in the north (CH) and southeast of GB (Figure 5.2l). For autumn season, ARs contribute nearly 20% in southern GB, while the contribution decreases gradually to 15% in northern GB. In IB, ARs contribute about 5%– 40% on average to the autumn rainfall with contributions between 25% and 40% for rainfall in north and southeast IB. Higher fractions of AR contribution for high rainfall are found mainly in the mountain regions, though higher fractions are also observed for comparatively low rainfall (in KA), especially in winter and autumn. We also observed higher fractions of rainfall in southeast lower IB (lowland areas with less than 200 m MSL), which may indicate the preferred passage of ARs along this region.

The higher AR contribution in the regions beyond the WH (i.e., KA and HK) may be related to ARs that penetrate through mountain gaps or cross over the barriers, as observed in mountainous terrains elsewhere (Alexander *et al.*, 2015; Mueller, Mahoney and Hughes, 2017). This implies that moisture from far sources contributes significantly to water inputs in the headwaters of the IB and GB via ARs. Another favorable passage for ARs would be from the southeast of IB (Figures 5.2 c, f, i, l, o). These observations suggest to a certain extent, that ARs' impacts on the annual and seasonal rainfall are region and season dependent and are critical 1) for water resource management, particularly in the forecast of ARs, and 2) in the designing of reservoirs capable of accommodating large inflows during AR events and storing stormwater for later uses. As ARs and floods are closely connected, ARs generate large runoffs and trigger floods, and as flood water cannot be stored entirely, they result in structural failure of reservoirs (Henn *et al.*, 2020) and a small net water gain for uses.

5.4.3. Impact of ARs on snowfall in IB and GB

The meltwaters from accumulated snowpack and glaciers sustain downstream streamflow in IB and GB during nonwinter seasons. We observe that snow accumulation is relatively lower in summers, especially in the IB, where it occurs only at higher altitudes compared to widespread snow accumulations in winter (Viste and Sorteberg, 2015). For this reason, we only selected the winter season for further in-depth analysis of AR impacts on snowfall. Snowfall of more than 200 mm w.e. (water equivalent) is noted along the northern IB (HK and WH) and a smaller region in north GB (western CH), that sharply reduces toward the northern reaches of IB (KA) southern parts of IB and GB (Figure 5.3a). The spatial distribution of snowfall is similar to rainfall patterns as in Figure 5.2d; however, the rainfall depths are slightly lower in comparison to snowfall. Snowfall of 200–400 mm w.e. is concentrated in the WH and HK at elevations of 3500–6000 m MSL The IB has extensive snow-covered areas compared to GB where snow cover is limited to regions above 1500 m MSL. The AR-related snowfall also shows similar spatial patterns but with slightly lower magnitudes (Figure 5.3b). ARs on average contribute 40% to winter snowfall over an extensive area in the mountains in both basins and ~50% in the northern reaches of IB (Figure 5.3c). This contribution is much higher than that obtained by Paltan et al. (2017) in their global study of AR impacts on hydrology including snowfall, which may be due to differences in AR identification algorithm and data used [i.e., WFDE5 (ERA5) versus WFDEI (ERA-Interim)]. The differences in spatial resolution showed that ERA5 (bias-corrected with GPCC) provided better precipitation estimates than ERA-Interim (bias-corrected with GPCC) (Cucchi, 2021). In the KA, ARs' contribution to winter snowfall varies from 40% in the central region to 50% in the eastern and western parts, suggesting ARs as the major driver of snowfall variability even at high altitudes, deep in the high-mountain ranges. In northern IB, winter precipitation is mostly attributed to WDs (Palazzi, von Hardenberg and Provenzale, 2013), but it is observed in this study that contributions to the total precipitation are also from ARs, which has not been studied earlier in detail.

In winter, the WDs travel eastward across semiarid to arid land before reaching the IB and northern GB with reduced atmospheric moisture while ARs appear to originate from the Arabian Sea and travel northeastward across southern IB and western GB [see Figure 4 in Nayak et al. (2021)], possibly with greater moisture content. Strong WDs in winter also favor moisture transport from the Arabian Sea (Dimri, 2006;

Madhura *et al.*, 2015; Riley *et al.*, 2021) into the KA, HK, and WH and leads to higher precipitation mostly in the form of snow at higher altitudes (see Figure 2A of (Azam *et al.*, 2021)). ARs may combine with WDs and intensify the impact on precipitation in these regions, though such relations are yet to be established in these regions. Baudouin et al. (2021) did note the influx of moisture advected from the northern Arabian Sea toward northern IB during WDs that increased the precipitable water on the windward side of the mountains, though the moisture flux from the Arabian Sea shown in their composite maps [in Figure 10a of (Baudouin, Herzog and Petrie, 2021)] could be moisture related to ARs. However, in other midlatitude regions, co-occurrences of extratropical cyclones (ECs, some WDs have similar dynamics to ECs) and ARs are often highlighted (Ralph, Neiman and Wick, 2004; Zhang, Ralph and Zheng, 2019). AR and snowfall links are also observed on the west coast of the USA, Sierra Nevada mountains (mean elevation of 3478 m) (Hu and Nolin, 2019), and the southern Andes Mountains (mean elevation of 4000 m) (Saavedra *et al.*, 2020). Curio and Scherer (2016) observed a strong correlation between IVT and winter precipitation in the KA, HK, and WH, including the northern regions of CH.

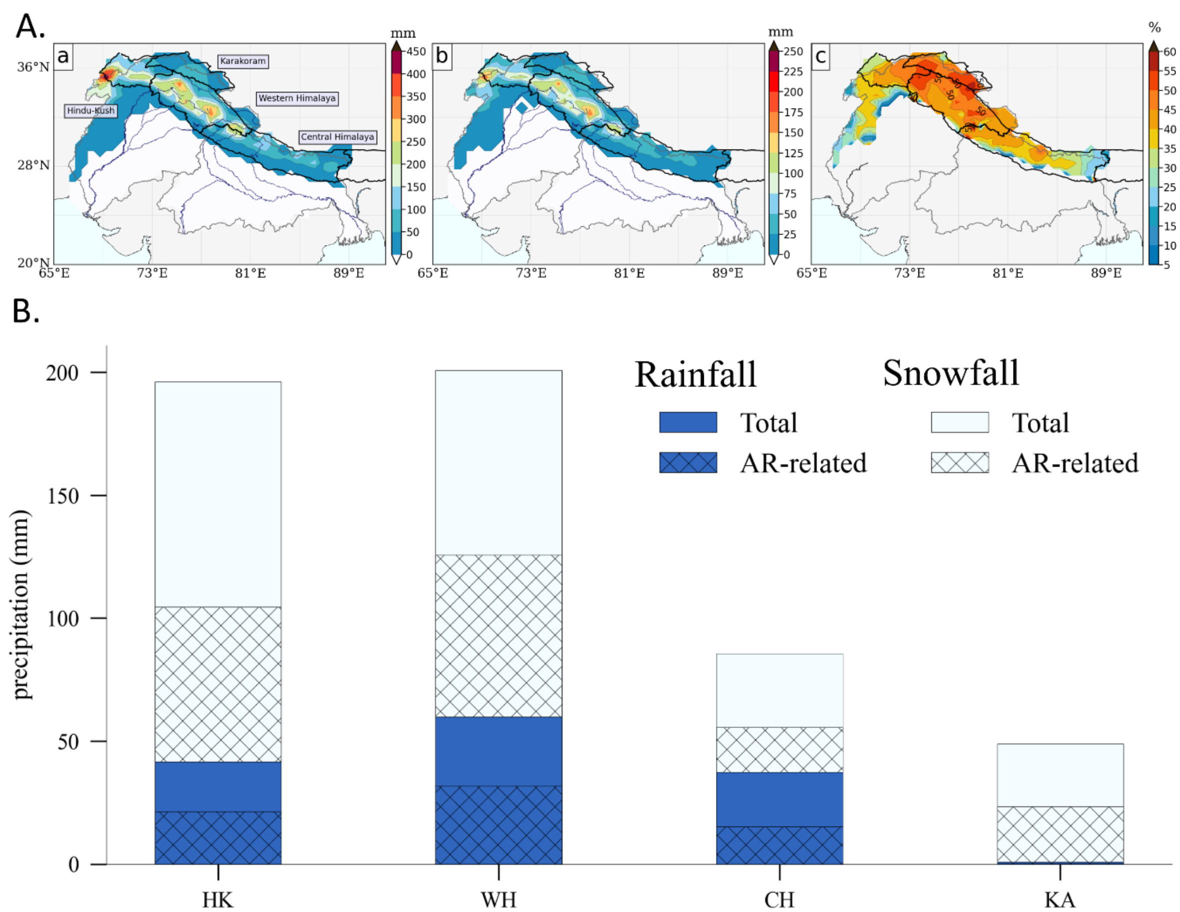

Figure 5.3: *(a) Average winter snowfall (mm w.e.), (b) AR-related average winter snowfall (mm), and (c) fractional contribution (%) over IB and GB. The black boundaries in the mountains represent the four mountain ranges considered here. (d) Average winter precipitation in HK, WH, CH, and KA; solid color*

represents the average winter rainfall (dark shades) and snowfall (light shades), and the solid color with hatches represents the annual average AR-related precipitation, respectively.

5.4.4. Impact of ARs on winter precipitation in the mountains of IB and GB

Winter precipitation is highest in WH, followed by HK, CH, and KA, roughly half of which is AR-related (Figure 5.3d). It is interesting to observe that the winter precipitation incisively follows the AR-related snowfall patterns, which highlights the role of ARs in defining precipitation variability. Nearly all the precipitation in KA in winter falls as snow with 75% interannual variability attributable to ARs (Figure 5.4d). ARs explain 57% and 63% of the winter snowfall and rainfall variability in HK, respectively, which is critical as HK receives most of its annual precipitation during winter (and also spring). In CH, ARs explain about 42% and 43% of the winter snowfall and rainfall variability, whereas in WH they explain 30% and 59% of snowfall and rainfall variability, respectively (Figures 5.4a–h). It can be argued that ARs may also impact the glaciers in HK, KA, WH, and CH by depositing large snow volumes during AR events. Further, a strong dependence of total precipitation on AR precipitation is observed in HK [regression slope of 1.24 for snowfall (1.2 for rainfall)] and KA [1.36 (1.2)], while comparatively milder dependencies are noticed in WH [0.56 (0.75)] and CH [0.87 (0.82)]. The above estimates underscore the previously ignored vital role of ARs in winter precipitation over the high-elevation mountain ranges of the Himalaya.

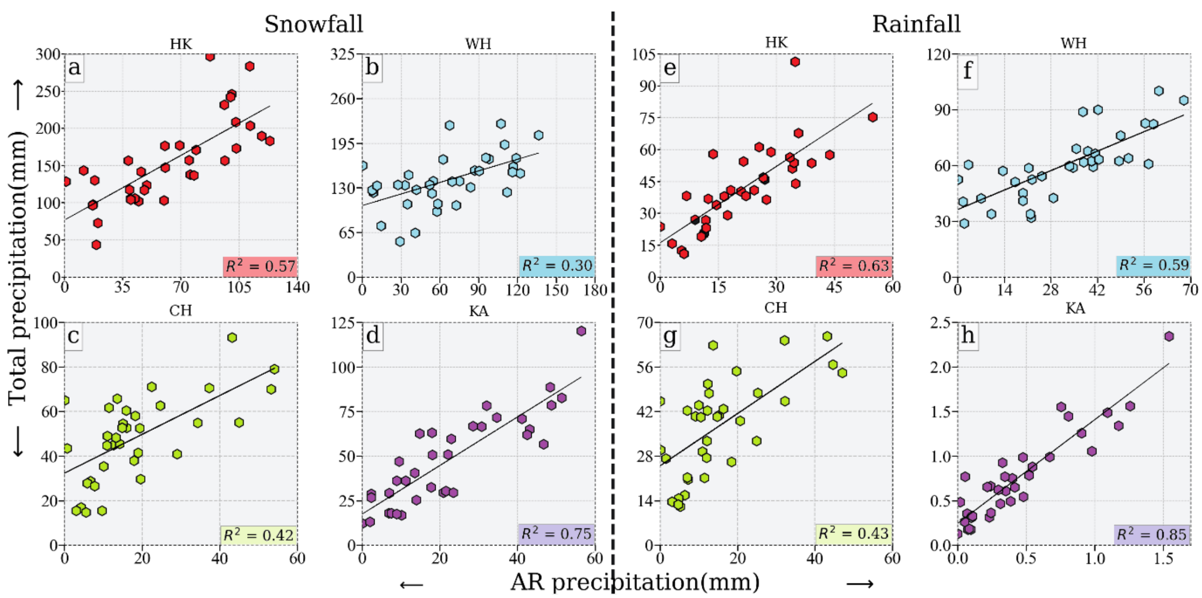

Figure 5.4: *Variability for average winter precipitation totals (y-axis) and AR-related precipitation (x-axis) for HK, WH, CH, and KA of (left) snowfall and (right) rainfall usingWFDE5 (all slopes are statistically significant at 5%).*

5.4.5. Seasonal rainfall extremes related to ARs

In Figure 5.5a, we find that 50%– 100% of winter rainfall extremes between 1982 and 2016 in the northern IB and GB (foothills of HK, WH, and CH) are AR related. The highest winter rainfall record happened often in the presence of ARs and these extremes may generate the largest streamflow records in these regions. In spring, 40%–60% of the rainfall extremes in northern IB (along the foothills of HK and WH) and between 10% and 60% in GB (CH and southeast GB) are related to ARs (Figure 5.5b). Consistent with Thapa et al. (2018), we observed higher fractions of rainfall extremes are AR related to non-monsoon (October–May), particularly in the winter season (DJF) over west Nepal. Smaller fractions of extremes in GB are related to ARs in summer and autumn, though extremes happen throughout the basin. In IB, 20%–50% of extremes are related to ARs in eastern parts, whereas in central and south IB, 20%–40% of extremes are related to ARs. Similar results are obtained using data from IMD, except that IMD showed more grids in WH and KA that have extremes related to ARs (Figures S5.8a, b). Furthermore, we also used a lower threshold of 2 mm for the daily maxima (Figure S5.5b), where we see large contributions of ARs (≥ 50%) to IB in winter and spring seasons and smaller contributions (≥ 25%) during summer and autumn.

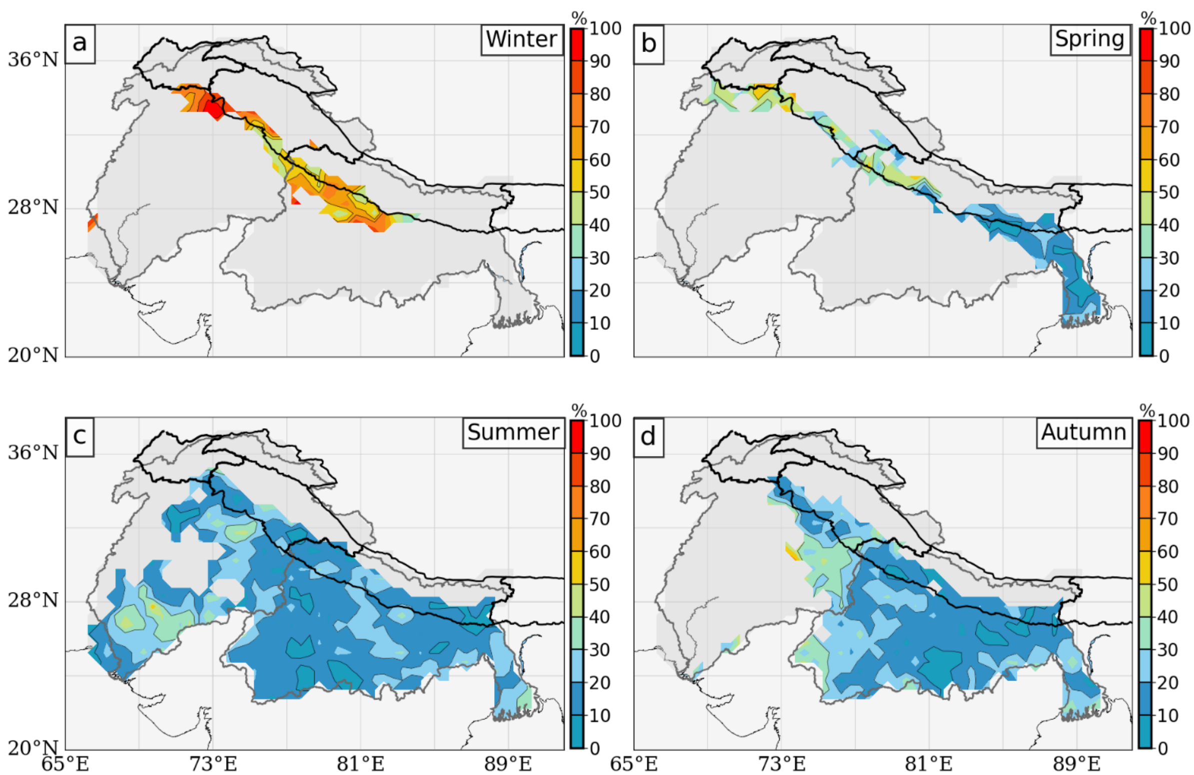

Figure 5.5: *Relative frequency of seasonal rainfall maxima related (%) to ARs for* 1982–2016 *using WFDE5 for (a) winter, (b) spring, (c) summer, and (d) autumn seasons. The grids shaded in dark gray have either seasonal maximum precipitation less than 40 mm or the number of seasonal maxima is less than 7.*

5.4.6. Floods associated with ARs

Several studies have shown that ARs produce extreme/ heavy precipitation that often leads to large-scale flooding (Leung and Qian, 2009; Lavers and Villarini, 2013b) in mountains (Neiman *et al.*, 2008; Thapa, Endreny and Ferguson, 2018) and have large societal impacts (Henn *et al.*, 2020) and economic losses. A total number of 189 flood events are observed during 1985–2015 in the IB (80) and GB (109) (Figure S5.9).

About 55% of the events in IB and 72.5% in GB (Figure 5.6) have occurred during the presence of ARs in the vicinity of the affected area. We find that many long-duration events were associated with AR clusters, which is the successive occurrence of multiple AR events over a region. To further understand the role of ARs in causing floods in Himalayan basins, we study the two most disastrous AR-related floods in IB and GB. The floods chosen are September 2014 Kashmir flood (in IB) and June 2013 Kedarnath flood (in GB). Previous studies have linked the 2013 and 2014 floods to the interaction between the cyclonic/frontal system of WDs and monsoonal flow that developed an intensified convective instability and resulted in extreme precipitation (Ray, Bhan and Bandopadhyay, 2015; Champati Ray *et al.*, 2016; Ranalkar *et al.*, 2016b; Yadav, Kumar and Lotus, 2017). On the contrary, Thapa et al. (2018) noted an AR during the 2013 flood. They stated the importance and utility of monitoring and forecasting AR storms for emergency preparedness. Along those lines, we illustrate and quantify the contribution of ARs to the accumulated precipitation and discharge during these events.

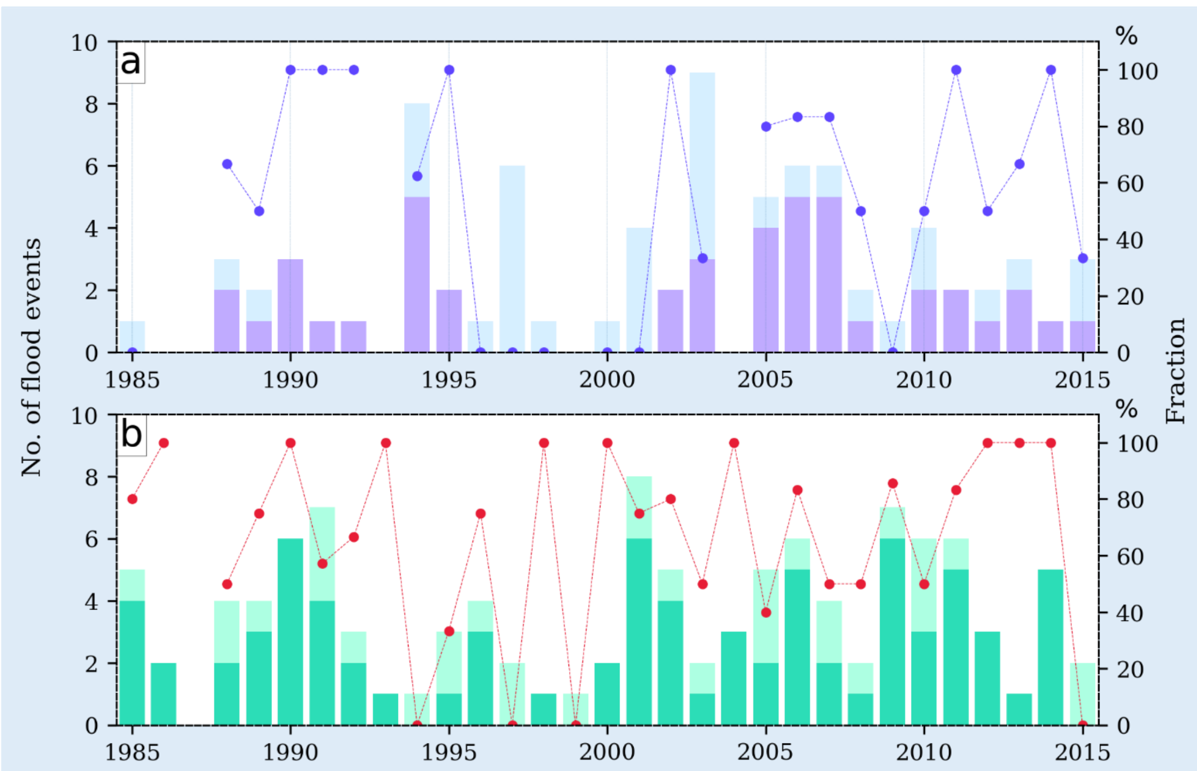

Figure 5.6: *Total and AR-related flood events (left y-axis) during* 1985–2015 *in (a) IB and (b) GB. Light gray bars show the total number of floods and dark gray bars show the number of flood events related to ARs. The fractions are shown by dotted line (right y-axis).*

ARs struck Jammu and Kashmir (WH) on 3rd Sept 2014 at 0600 UTC and Uttarakhand (CH) on 12th June 2013 at 0600 UTC (Figure 5.1). On 2nd–6th September 2014, the WH received precipitation between 350 and 650 mm, which corresponds to ~34%–40% of the total annual precipitation in the region (Figure 5.1c, Figure S5.1c). Consistent with other studies (Mishra, 2015; Ray, Bhan and Bandopadhyay, 2015;

Romshoo *et al.*, 2018), the Kashmir region received ≥ 400 mm of rainfall that generated a large flood flow in the two major rivers, Jhelum and Chenab. ARs were observed consistently during days of heavy precipitation and during the flood. The discharge at Rasul and Trimmu barrages attained peak inflow of $11088\ m^3/s$ and $16772\ m^3/s$ on 6th and 11th September 2014 (Figure 5.1e), respectively, which exceeded the corresponding very high flood levels by $4000\ m^3/s$. In June 2013, Uttarakhand received 300–650 mm of rainfall ($20\%-25\%$ of annual precipitation) between 12th and 18th June, and ≥ 650 mm of rainfall ($\sim 40\%-45\%$ of annual precipitation) was observed (Figure 5.1d, Figure S5.1d) near Haridwar. Moderate precipitation for the first 3 days saturated the soil layers, and the succeeding heavy precipitation on 16th–17th June generated substantial streamflow. The inflow in the Bhagirathi River (a tributary of the Ganga river) before 16th June was low, and the Tehri reservoir was almost at its dead storage. The inflow increased rapidly on 16th June and reached a peak discharge of $4220\ m^3/s$ on 17th June (peak hourly flow ≥ $7500\ m^3/s$; (Arora, Singh and Agrawal, 2018)), resulting in flooding (Figure 5.1f). During these dates, ARs were identified from 12th ─ 18th June, which contributed to the high streamflow observed in Tehri Dam during the flood.

These results highlight that ARs are important to hydrologic extremes over the Himalaya. Many areas are vulnerable to AR precipitation and associated impacts in different seasons, which underscores the need for forecasting of ARs. AR forecasts could help in improving seasonal and sub-seasonal forecasts of winter precipitation over the Himalaya. Numerical weather prediction models (NWPs) are adept at short-range forecasting of individual ARs and AR-related precipitation (Wick *et al.*, 2013; Hughes *et al.*, 2014; Nayak, Villarini and Lavers, 2014; Huang *et al.*, 2020). When paired with forecasted climate modes, the forecasting of AR frequency could be extended up to 9 months in advance (Baggett *et al.*, 2017; Tseng *et al.*, 2021). At present, NWPs are shown to produce reliable long-range AR forecasts with accurate probability of occurrence and their categories (Lavers *et al.*, 2020). In the Himalaya, however, there is no region-specific study dedicated to AR modeling/forecasting. Nevertheless, we suggest that future research will explore these areas of interest and include AR forecasting in existing NWPs in these regions. In addition to improving models' output through improved terrain data, observations, and precise initial conditions, the forecast can also be enhanced if physical processes are better described, and understanding of how IVT is resolved in models. Nonetheless, we believe that accurate forecasts of ARs may likely be a major breakthrough in hydrometeorological prediction over the Himalaya.

5.5. Conclusion

Precipitation in the Himalaya is mainly due to the orographic effect of very high mountain ranges that block and uplift the moisture fluxes approaching them. This study aims to quantify the relative contributions of ARs on regional precipitation, seasonal extremes, and AR-related floods in two major basins in the

Himalaya–IB and GB. ARs are unique synoptic features, responsible for 20%–30% of the total annual rainfall in IB and 5%–20% in GB, though the contributions are spatially heterogeneous. Seasonally, ARs contribute the largest fractions in winter, impacting large areas in IB and northwest GB, followed by autumn, spring, and summer. In three of the seasons (i.e., winter, spring, and autumn), the IB is more influenced by ARs than GB. In winter, the west and north of IB and northern GB receive up to 200 mm w.e. snowfall, of which 40%–50% is attributable to ARs. Since ARs contribute the highest (40%–80%) to rainfall in the winter season, we examined further the ARs' impact on winter precipitation in the mountain ranges of the Himalaya (as rainfall and snowfall totals are higher here compared to plains in the lower IB and GB). We observed that on average ARs contribute more than 50% of the annual winter rainfall and snowfall in HK, KA, WH, and CH, and ARs explained over 75%, 57%, 42%, and 30% of the variability in winter precipitation of KA, HK, CH, and WH, respectively. The streamflow in both IB and GB rely heavily on winter snowfall and ice cover available, and any fluctuation in annual snowfall will impact water availability for the billion inhabitants in the following season (Azam *et al.*, 2021). Other implications of snow cover extent in these mountains are their influence on the strength/delay of the ISM (Dash *et al.*, 2005; Mamgain, Dash and Sarthi, 2010). It is to be noted, however, that with limited observational stations in these regions, the snowfall estimated by reanalysis products is highly uncertain (Azam *et al.*, 2019).

A major fraction of extreme rainfall in different seasons (especially winter and spring) is associated with ARs over two Himalayan basins. These extremes have the potential to generate large floods that impact extensive areas and result in large social and economic consequences in these regions, especially for areas in the foothills of the mountains. However, not all ARs lead to floods. Our results revealed that a major fraction (56%–73%) of the floods in the Himalaya during 1985–2015 happened during the presence of ARs. In addition, the two largest floods in these basins further elucidate the importance of ARs on the hydrology and water resources in IB and GB basins.

These extreme events (precipitation and floods) are recurring natural disasters and understanding what generates them could help in improving the decision-making for management, forecasts, and mitigation. These results imply that ARs are key agents delivering water deep inland, more than thousands of kilometers from the Indian coasts, and are the potential mechanisms of flooding in the Himalayan basins. The seasonality of ARs combined with topographic barriers has an important implication on the region's water availability. Further exploration is needed to understand the impacts of ARs in these basins including ARs that bring warmer storms and lead to more rain instead of snow, and disasters related to avalanches and landslides in the mountains of IB and GB. Based on the importance of ARs to the Himalayan hydrology, it is imperative to channel research efforts into forecasting of ARs, for example through numerical and statistical approaches, for improving operational forecasts of precipitation and hydrologic extremes.

APPENXDIC-C: Supplementary Information

Details of ARs in mid-June 2013 and early Sept 2014

Two Category 5 ARs during mid-June 2013 and early Sept 2014 were observed in the northern India, Himalaya. The ARs struck Jammu & Kashmir on 3rd Sept 2014 and Uttarakhand on 12th June 2013, respectively. The AR in Sept 2014 lasted for 3 days from 3rd-5th Sept (Figures 5.1a and S5.1a, showed 3rd-Sept 2014, 18 UTC), and in 2013 the AR stalled for about 7 days from 12th-18th June and reached peak intensity on 16th and 17th June (Figure 5.1b, S5.1b; showed16 June, 18 UTC). The orographic lift of AR moisture resulted in heavy precipitation in the surrounding areas, which translated into the most disastrous floods in Northern India.

Figure S5.1: Illustrating the AR-link to high precipitation and flood events

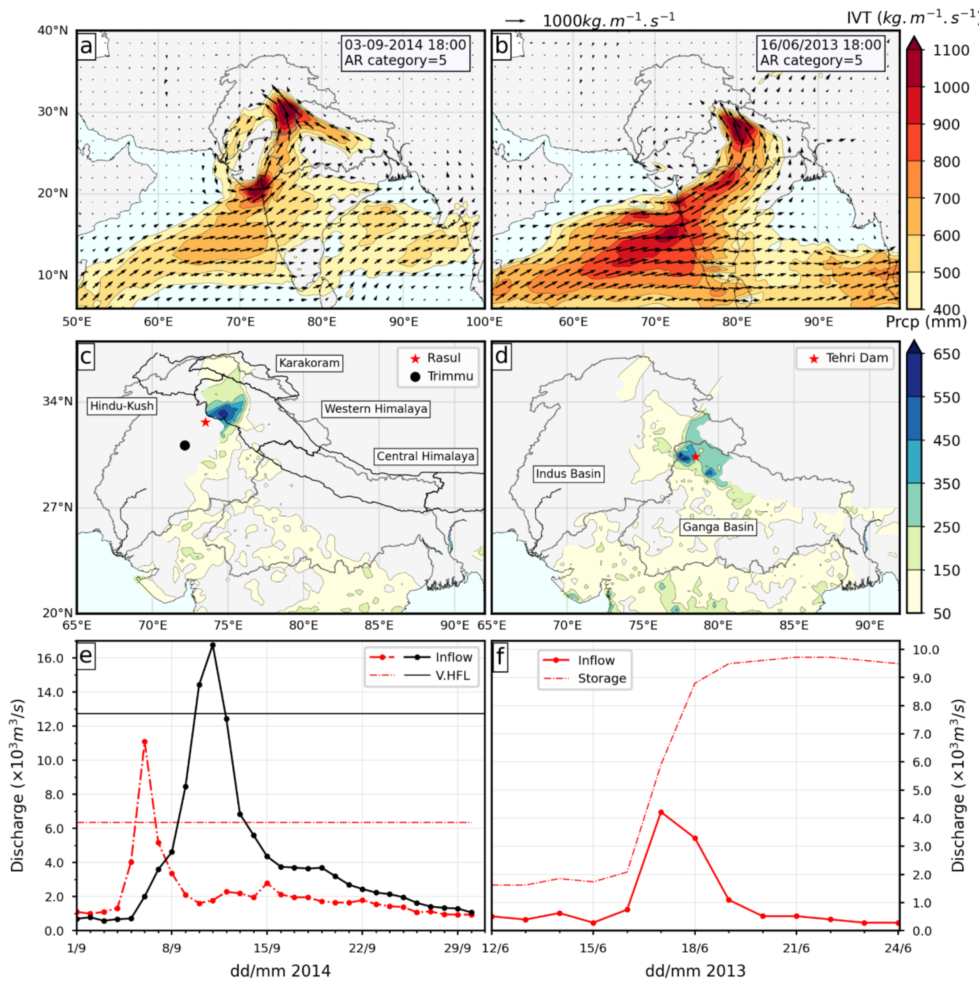

Figure S5.2: Similar to Figure 5.1, except for (c) and (d) in which IMD is used for precipitation. IVT ($kg.m^{-1}.s^{-1}$) on (a) 3rd Sept 2014 at 18 UTC and (b) 16th June 2013 at 18 UTC; (c) and (d) show the total accumulated precipitation (mm) during the events. The star and circle (solid) represent the discharge measuring stations in Jhelum River and Chenab River respectively in (c), and the star in (d) represents the location of the Tehri dam at Bhagirathi River. (e) and (f) show discharge at the gauge stations in (c) for September 2014, and storage in (d) for June 2013; In (e) the discharge and very high flood level are shown by *solid for at Rasul and by dashed lines for Trimmu in IB, and in (f) the discharges are shown by solid line and storage by dashed line at Tehri dam in GB.*

Text S5.1: Precipitation during the two AR events

IMD showed similar spatial patterns for rainfall as compared to WFDE5, except in the upper reaches of IB, and showed much higher rainfall accumulations near the gauge stations (Figure S5.1c). IMD showed a rainfall magnitude of 200 mm higher than that observed by WFDE5, which could be due to the lack of ground-based information used for bias correction and the low resolution of WFDE5.

From 2nd−6th Sept 2014, WH received precipitation greater than 450 mm precipitation (~32% of annual precipitation (Figure S5.1c)), nearly 550 mm in Kashmir generated surplus streamflow in Jhelum and Chenab Rivers. In June 2013, Uttarakhand received greater than 350 mm of precipitation (∼28% of annual precipitation) during 12th–18th June 2013.

Text S5.2: Summary of the Algorithm

1. At each grid, 6-hourly IVTs are computed in the study region for the period $1982 - 2018$.
2. IVT thresholds are computed for each calendar day as the local 85th percentile value of the IVT distribution for that calendar day at every grid.
3. To identify ARs that penetrate the Himalaya, a detection transect is then defined along the foothills of the Himalaya.
4. The transect is split into 5 bins (A to E) considering the large IVT variations along its length (due to latitude changes). Bin thresholds are then computed as the spatial average of grid thresholds within the bin.
5. At a timestep, the maximum IVT grid is identified on the transect and anchored as the first grid of the axis if its IVT surpasses the respective bin threshold (Steps 1 & 2).
6. Among three adjacent grids in the west of the first grid, the grid with maximum IVT is anchored as the second grid if it surpasses the grid's threshold.
7. Step 6 is repeated to find subsequent grids forming the axis until the maximum IVT of the adjacent grid is below the threshold.
8. Similarly, the grids forming the potential AR-axis are searched southward.
9. The axes obtained from step 8 are screened for the minimum length requirement of ARs, and the presence of cyclones (i.e., AR timesteps that match the cyclone timesteps).

10. Only persistent AR events that last longer than 18 hours are retained. An AR event is defined as a group of consecutive AR timesteps.

11. Lastly, the two sets of AR events are reviewed for unique events, i.e., if the events from the two sets have at least one timestep in common, the event with the largest average IVT is taken as the AR.

Figure S5.3: The 80th percentile precipitation using IMD

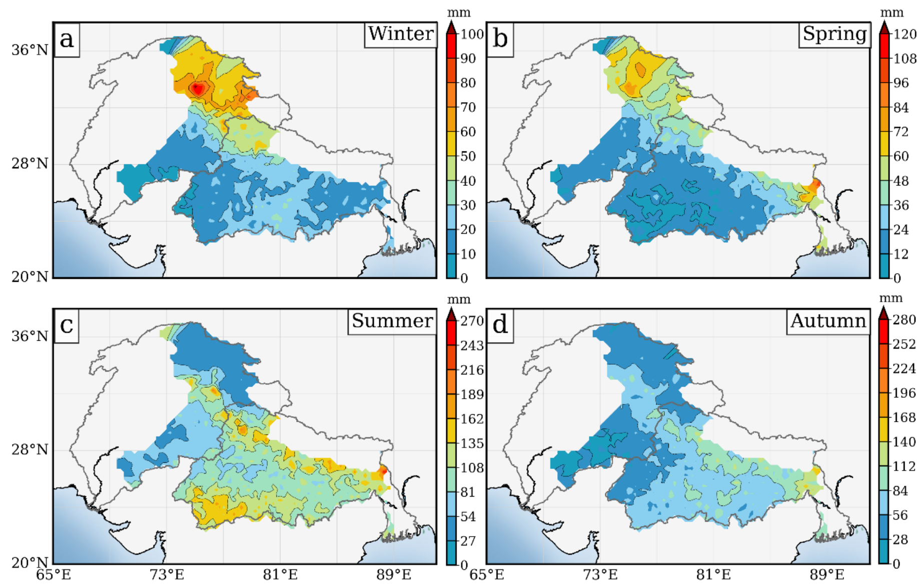

Figure S5.3: *The 80th percentile for (a) winter (b) spring (c) summer and (d) autumn seasons for Indian IB and GB, using IMD (1982 – 2018).*

Figure S5.4: Difference between IMD and WFDE5 80th percentile

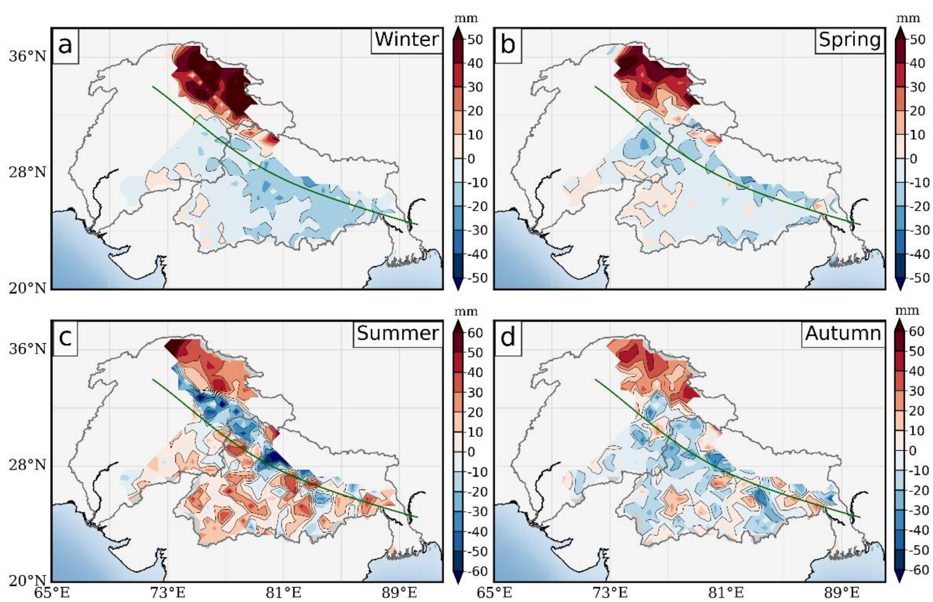

Figure S5.4: *Difference between IMD and WFDE5 80th percentile when the base period is same i.e., 1982-2016, and when the periods are different i.e., IMD (1982-2018) and WFDE5 (1982-2016) we observed no appreciable changes (Figure not shown). The differences were computed at* $0.5° \times 0.5$.

Figure S5.5: AR contribution to seasonal precipitation extreme using WFDE5

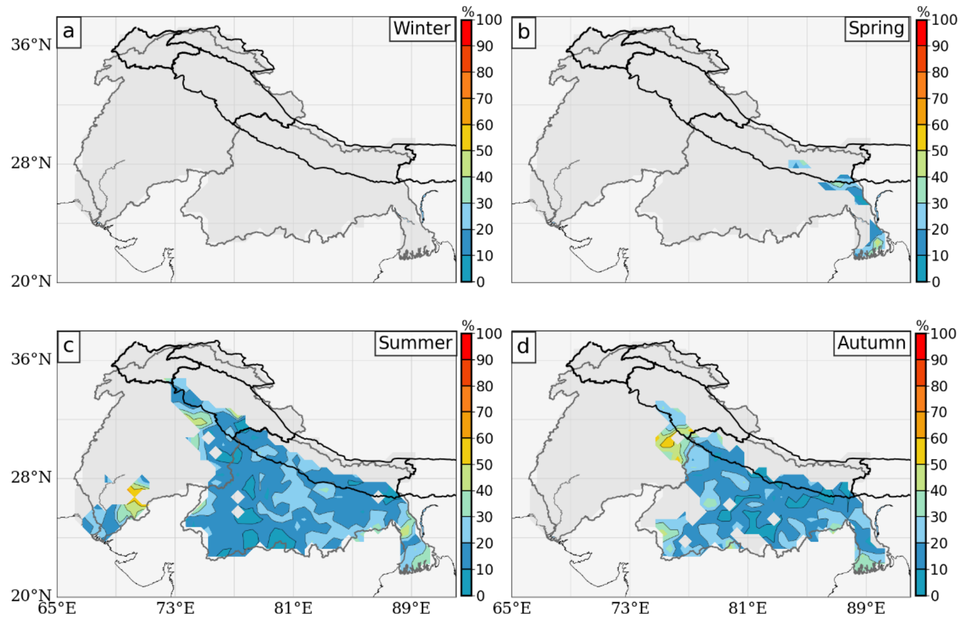

Figure S5.5a: *Same as Figure 5 but using WFDE5. The criteria for precipitation maxima are (a) above 60 mm for the daily precipitation maxima and (b) each grid cell should have at least 7 years of their seasonal maxima (greater than 60 mm). Grey color within the basins shows the grid cells that do not satisfy the criteria.*

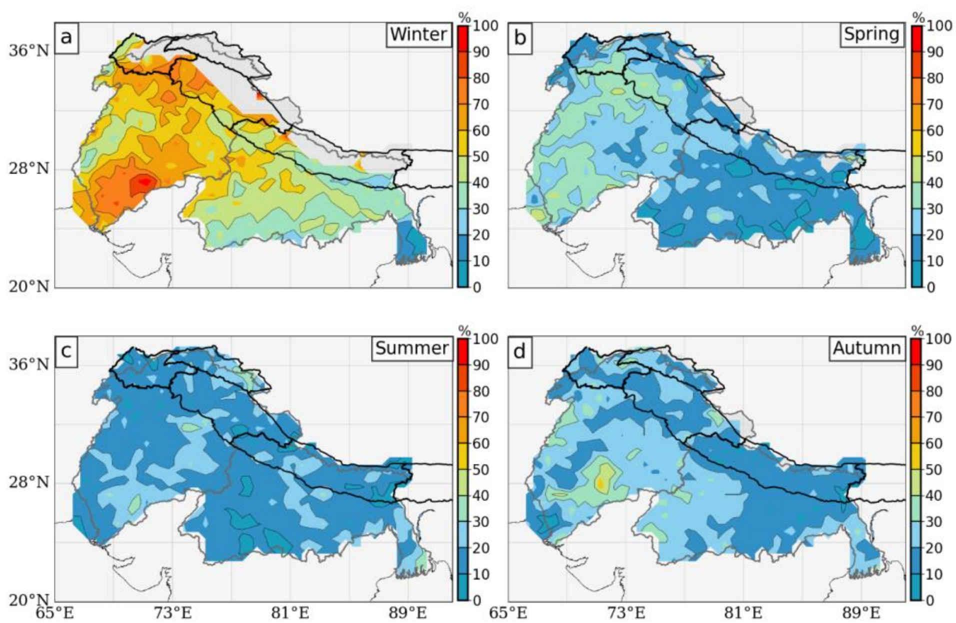

Figure S5.5b: *Relative frequency of seasonal rainfall maxima (in %) related to ARs for* 1982 − 2016 *using WFDE5. (a) for winter, (b) spring, (c) summer, and (d) autumn seasons. The grids shaded in dark gray have either seasonal maximum precipitation less than 2mm or the number of seasonal maxima is less than 7.*

Text S5.5: Sensitivity of AR contribution to thresholds

In order to assess the sensitivity of AR contributions to the threshold for daily maxima, we used a lower threshold of 2 mm (instead of 40 mm) (Figure S5.5b). The results highlight that ARs contributed mostly between $30 - 90\%$ (for comparison, the contribution is $50 - 100\%$ based on 40mm threshold; Figure 5.5) of the winter rainfall extremes in the IB and GB; up to 50% (up to 60%, Figure 5.5) of the extremes in spring are related to ARs, particularly in IB; and $20 - 50\%$ ($20 - 50\%$, Figure 5.5) of the extremes in summer and autumn are AR-related in both basins. Based on the two thresholds (2 mm and 40 mm), we find minor differences in the fractional AR contributions to extremes. Moreover, ARs contribute to "daily maxima" throughout the year; however, winter ARs have more contribution to the extreme precipitation highlighting that ARs are relevant to both small and large daily maxima at regional scale."

Figure S5.6: Average AR contribution to total and seasonal rainfall using IMD

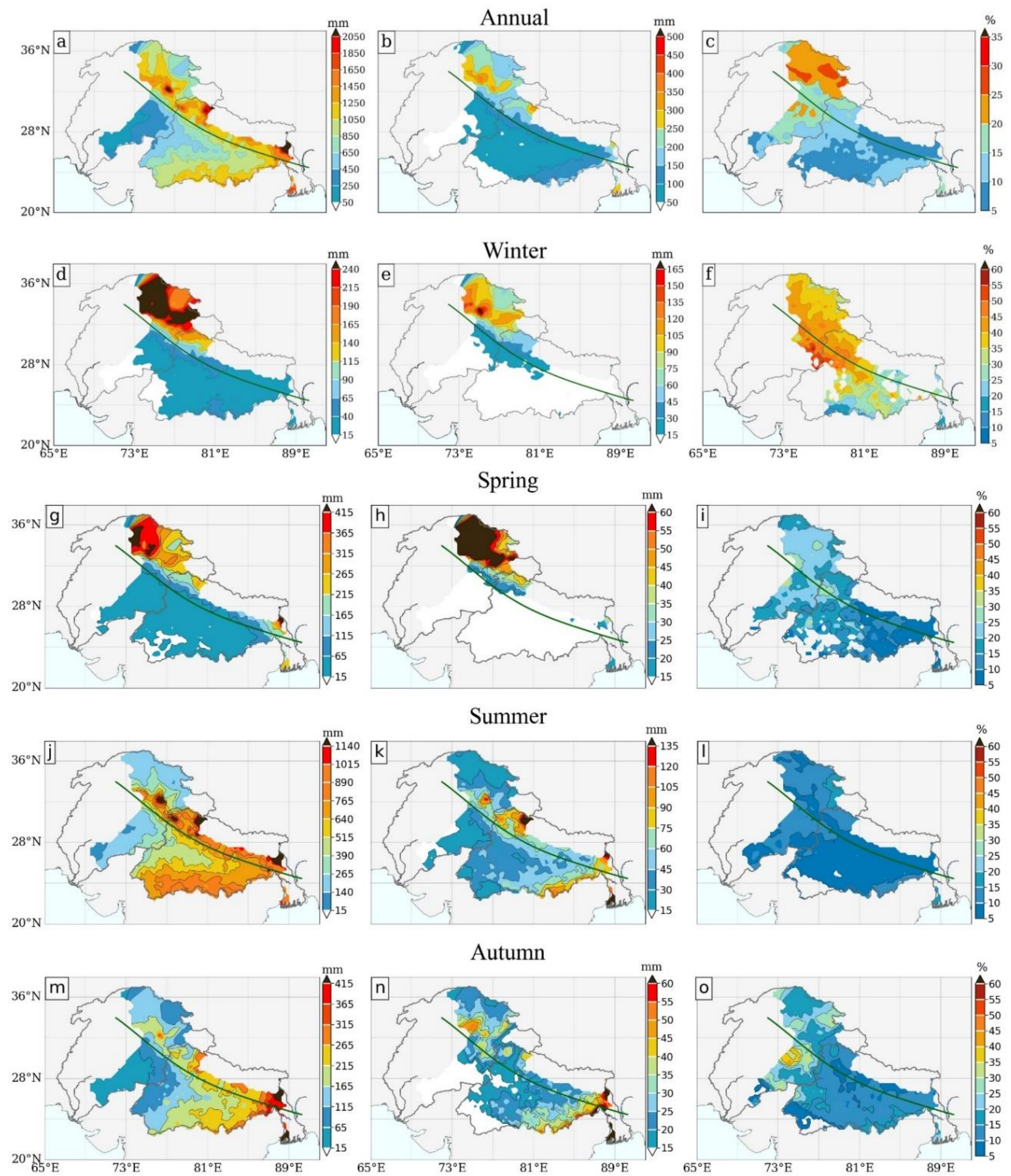

Figure S5.6: *Similar to Figure 5.2, but using rainfall data from IMD for the period 1982 – 2018 [Dates in AR Database are in UTC and IMD are in IST].*

Text S5.6: Average AR contribution to total and seasonal rainfall using IMD

Figure S5.6 shows the IMD annual average rainfall patterns resemble WFDE5 observations closely in magnitude over both basins except north IB, with precipitation highly underestimated by WFDE5. The maximum rainfall location matches well in both cases; however, there are large differences between the two in representing spatial patterns of rainfall for these basins, especially for the northern Indian IB. As described in the Data section, WDFE5 is a reanalysis data (i.e., it uses a combination of observations and model outputs) that may be associated with systematic model errors, and IMD is developed from gauge station observations which are interpolated into gridded data. However, it is to be noted that only a handful of stations are present in lower elevated areas of north India, and the observations from these gauge data are interpolated to extent up to the northern border of India (Rajeevan *et al.*, 2006; Pai and Bhan, 2014). Seasonally, the highest rainfall is observed in summer, followed by autumn and spring (Figures S5.6 g, j and m).

We observed that ARs contribute $20 - 35\%$ in northern IB, and $5 - 20\%$ in southern IB (for rainfall of $100 - 300$ mm/year. For GB, ARs contribute $5 - 15\%$ of annual rainfall in nearly the entire basin and $\sim 25\%$ is found for grid cells in the northern most reaches (Figure S5.6c). In winter, the average AR-related rainfall between $60 - 165$ mm/winter (Figure S5.6e) is observed in northern IB and northwest GB (Uttarakhand), predominantly over mountain regions. ARs contribute between $40 - 50\%$ to winter rainfall in northern IB (WH) and upper GB (west of CH), and $20 - 40\%$ in south GB (Figure S5.6f). These observations show similar relative contribution of ARs as observed using WFDE5, except for regions in the northmost IB. In summer, ARs contribute mainly 15% to the rainfall in IB though 10% and 20% are also observed in south and northern IB. In GB, ARs contribute between $10 - 15\%$ of the seasonal summer precipitation ($500 - 1125$ mm/summer) in the mountains and southern GB (Figures S5.6j, k and l). The spring rainfall patterns are similar to those observed using WFDE5 except for the high rainfall in Karakoram (KA), which is also observed for the summer and autumn. On average, ARs contribute $25 - 30\%$ of rainfall in spring to northern IB and northwest GB (Figures S5.6i). In autumn, ARs contributed $10 - 15\%$ in most parts of GB with some grid cells showing 20% in the west and southmost (for rainfall of greater than 870 mm/autumn). In IB, AR contributes from 5% in the south to 40% in the foothills and KA. Overall, the rainfall patterns and relative contribution using IMD and WFDE5 are similar over both basins except for north IB.

Figure S5.7: Average Seasonal contribution of ARs using WFDE5

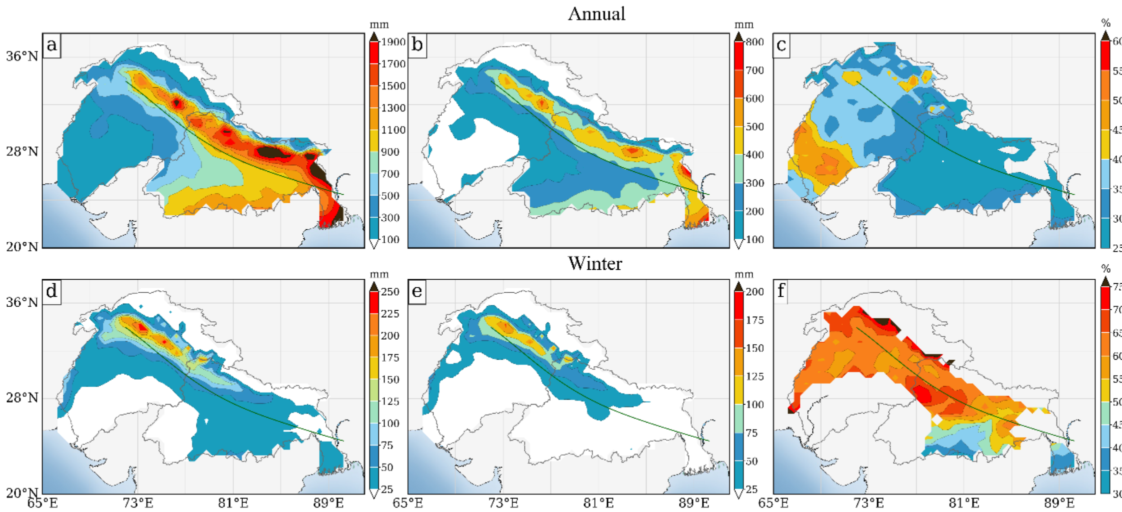

Figure S5.7a*: Similar to Figures 5.2 and S5.6. [Note: those grids that have annual average less than 100mm and winter average (other seasons) less than 25 mm are not shown in the fractional contribution (white color)].*

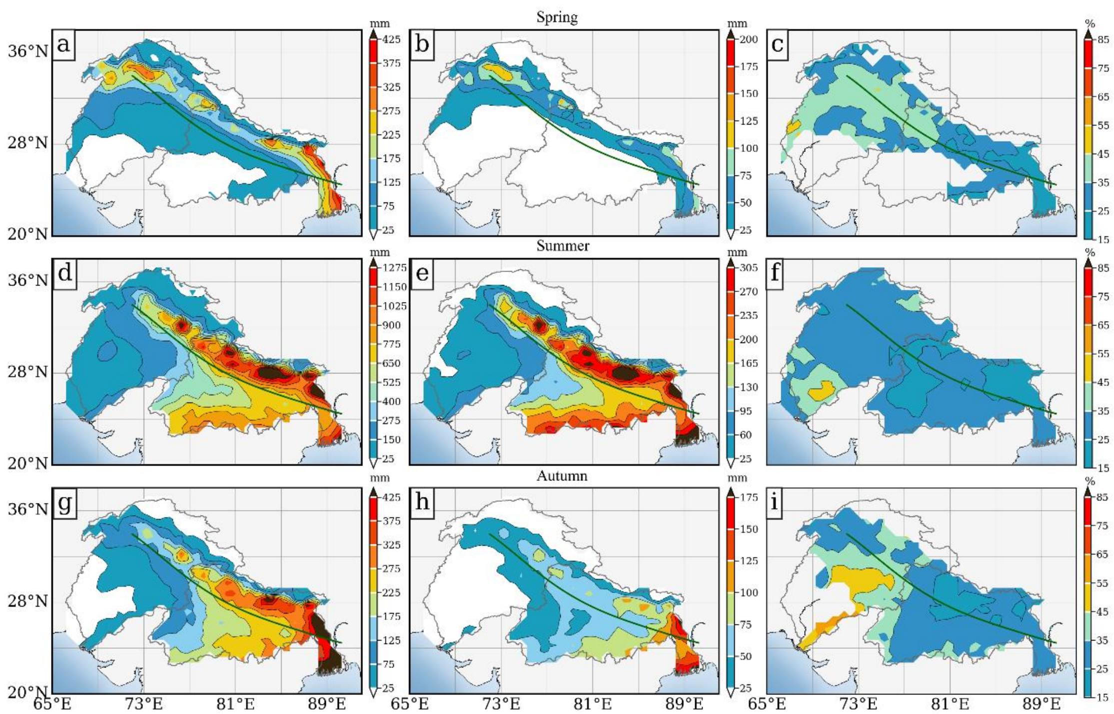

Figure S5.7b: *Similar to Figures 5.2 and S5.7a. [Note: those grids that have annual average less than 25 mm are not shown in the fractional contribution (white color)].*

Text S5.7a: Underestimation of AR fractional contributions

The AR-related rainfall defined in this study and the resulting AR fractional contributions may be underestimated because (1) the method followed here does not consider grids close to the region within 250 km from the AR axis whose precipitation may be related to ARs. This is for ARs with widths between 500 –

$1000\ km$ (i.e., greater than the “250 km” considered here), (2) in the mountains, grids within 350 km that do not have IVT above the threshold (or slightly lower than the threshold) at any AR time step may have also not been included, as AR IVT is strongly depleted evolving to precipitation. We present the fractional contributions of ARs to rainfall in the two basins (Figures S5.7a and S5.7b) if we considered that precipitation on an AR day in either basin is related to AR, considering that ARs are large-scale features and due to large moisture divergences upon striking the mountain barrier, they can lead to precipitation at distances far from their major axes. We also include one day before and one day after the AR event without double counting the days between consecutive AR events (similarly followed for AR-derived snowfall by Huning et al., (2019), AR impacts on precipitation by Eldardiry et al., (2019) and hydrology by Leung and Qian (2009) for western USA and Viale *et al.*, (2018) for southern South America). We observed that ARs contribute nearly 50% to the annual rainfall in the north IB and certain regions in lower IB (Figure S5.7c), and $25-35\%$ of the annual rainfall comes during ARs in GB, with higher fractions in the mountains (see Text S5.7b for more details).

Text S5.7b: Average Seasonal contribution of ARs using WFDE5

On an average, ARs contribute nearly 45% to the annual rainfall in the south IB and 40% in the northern IB and between $30-35\%$ of the annual rainfall in GB comes during ARs (Figure S5.7a (c)). ARs have the highest contribution to rainfall in winter season, with $70-75\%$ of the rainfall is related to ARs in IB, and northwest GB and $35-45\%$ in south GB (Figure S5.7a (f)). On an average, ARs contribute $35-45\%$ of rainfall in spring to upper IB and northwest GB (Figures S5.7b (c)). ARs contribute nearly 30% of the summer rainfall in the IB except in the south and in GB, ARs contribute $\sim 25-30\%$ of the seasonal summer rainfall (for rainfall between $625-1100$ mm/summer) in northern GB (Figures S5.7e and f). In autumn, ARs contributed $\sim 35\%$ in south GB and gradually the contribution decreases to 25% in north GB (CH), $25-50\%$ in the IB with higher fractions for precipitation below 125 mm/autumn. The relative contributions obtained using the method described in Text S5.7a are comparatively higher.

Figure S5.8: Seasonal precipitation extremes using IMD

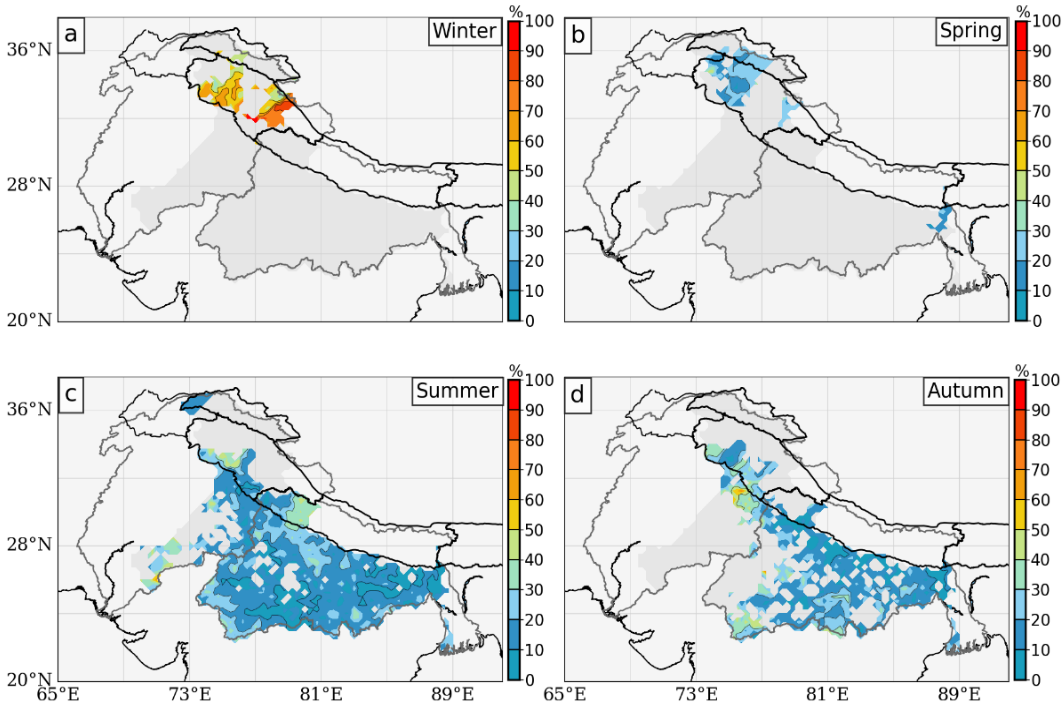

Figure S5.8a: *Similar to Figure 5 using IMD. Relative frequency of seasonal rainfall maxima related to ARs for* $1982 - 2018$ *(a) for winter, (b) spring (c) summer, and (d) autumn seasons. The grids shaded in grey have either seasonal maximum precipitation less than 60mm or the number of seasonal maxima is less than 7.*

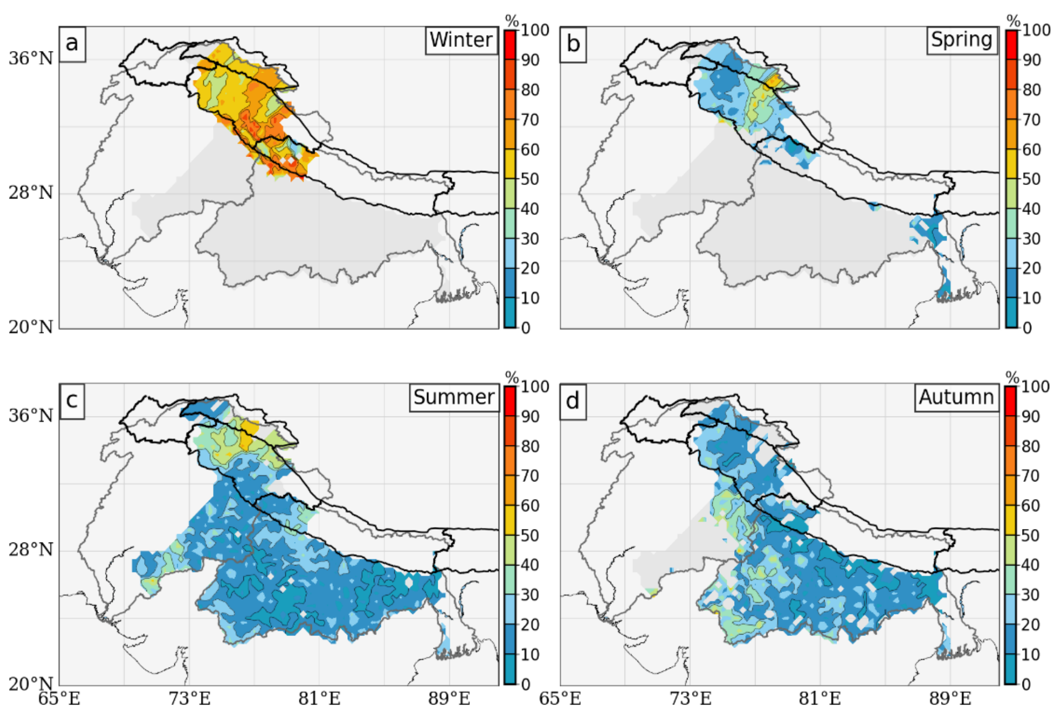

Figure S5.8b: *Similar to Figure 5 using IMD. The criteria for seasonal maximum rainfall include (1) daily rainfall amount greater than 40mm and (2) the number of seasonal maxima is should be 7 or more.*

Text S5.8: Seasonal precipitation extremes using IMD

In Figure S5.8a, over 50% of winter extremes are AR-related in the upper IB (WH and central KA). In GB, the winter maxima are very low (80th percentile varies between 20-50mm) to satisfy the conditions for extremes defined here. We observed similar results (over 50%) for spring extremes (Figure S5.8a (b)) and also noted $20-30\%$ of extremes in the east GB are AR-related. The gradual increase in contribution from west-east in the northern IB (WH and KA) corresponds to the gradual west-east increase in elevation where greater precipitation is extracted at higher altitudes (Neiman *et al.*, 2008). In east IB, some grids have $\sim 50\%$ of their spring extremes related to ARs, suggesting that intense ARs are capable to penetrate into the mountains. In summer, ARs are responsible for $50-70\%$ of extremes in upper IB (west of WH and central KA), and some regions in south IB, and less than 50% in the rest of IB (Figure S5.8a (c)). In GB, AR contributions to summer and autumn extremes are generally weak. Higher fractions are found along the southern periphery and in the mountains (northwest) In IB, summer and autumn AR-related extremes are higher than in GB and mostly along the foothills of the WH as precipitation is mainly concentrated here during these seasons.

Figure S5.9: Location of flood events in IB and GB

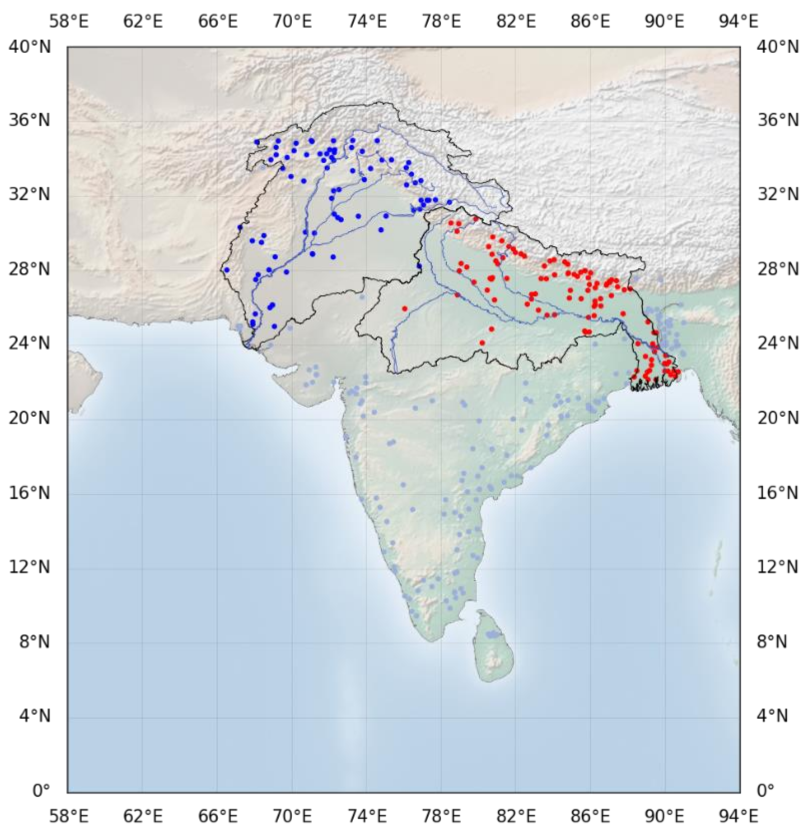

Figure S5.9: *The dots represent the locations of the flood events during the period* $1985-2018$ *in IB (in blue) and in GB (in red). The grey colored dots are for other parts of India outside the study region.*

Figure S5.10: Modified Lavers *et al.*, (2012) versus Guan and Waliser, (2019) AR detection algorithms

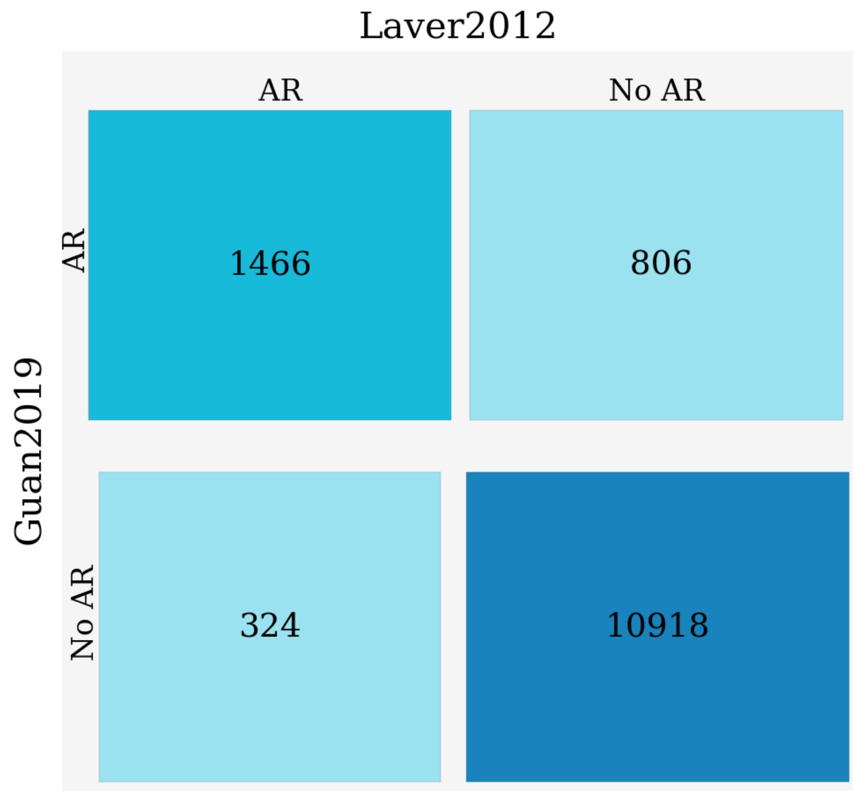

Figure S10a: *A contingency table showing the number of AR days detected by* Lavers *et al.*, (2012) *and* Guan and Waliser, (2019) *algorithms. The top left (ARs) and bottom right (no ARs) represents the days when both* Lavers *et al.*, (2012) *and* Guan and Waliser, (2019) *algorithms agree, the top right shows the number of AR days that only* Guan and Waliser, (2019) *algorithm identified, and similarly the bottom left shows the number of AR days that are detected only by the* Lavers *et al.*, (2012) *algorithm.*

Here, we considered an AR day if any of the time steps have an AR. We then compared the dates in the two sets, as shown in Figure S5.9, and we found that 82% of the ARs from Nayak et al. (2021) (using a modified Lavers *et al.*, (2012)) match the ARs from the Guan and Waliser, (2019) algorithm , “tARget”. Most of the AR events identified by “tARget” have short duration, existing less than a day, hence for the comparison we have included all the dates from GW19.

We have also shown the comparisons of the spatial patterns of average total and AR-related rainfall at annual and seasonal timescales below (Figure S5.9b, similar to Figure 5.2). We have followed the methods described in the main text to quantify AR-related rainfall for the ARs obtained from tARget.

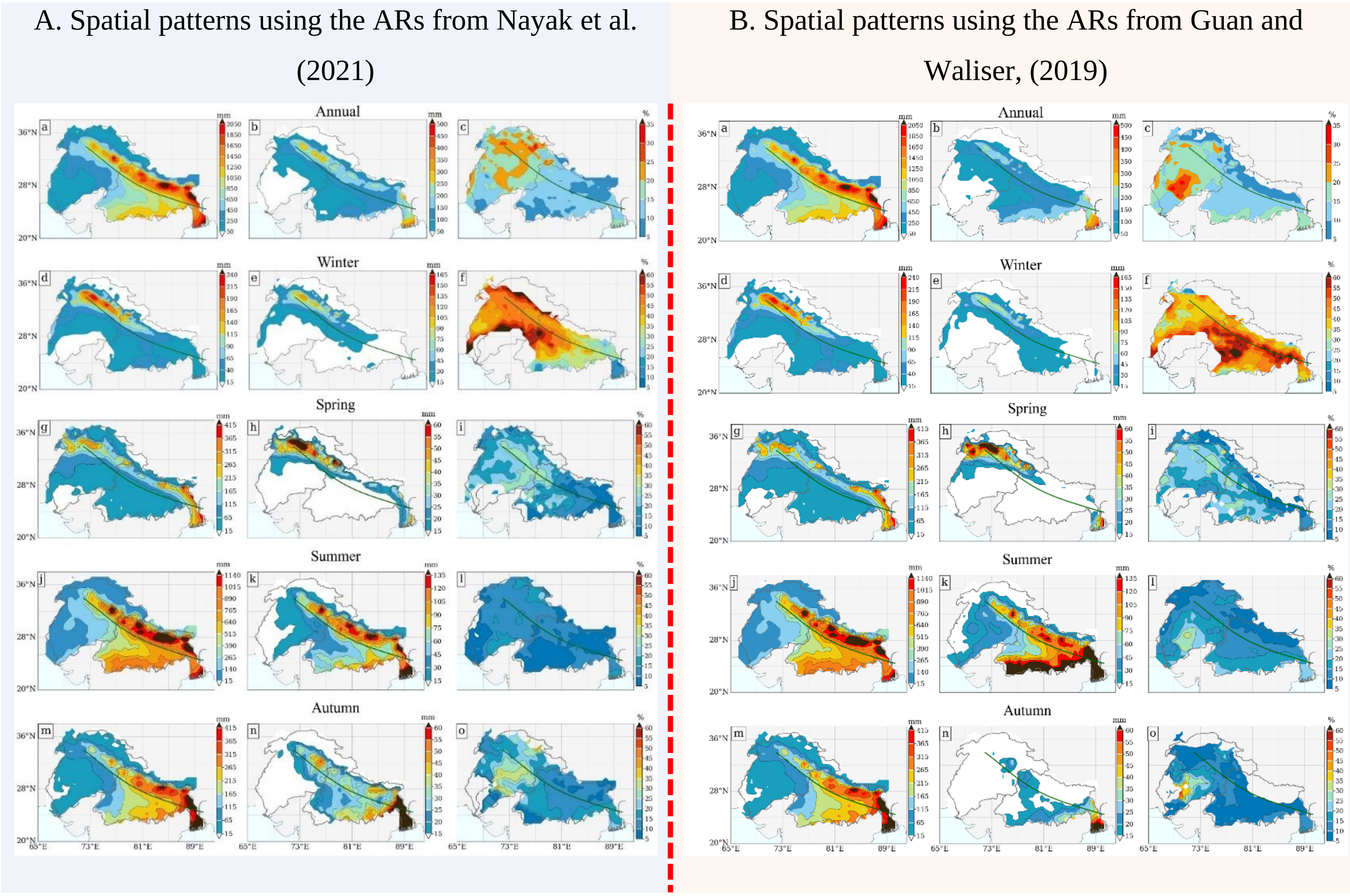

Figure S5.10b: *Comparison of spatial rainfall patterns of AR-related and percent contribution of ARs to total (average) rainfall using ARs from* Nayak et al. (2021) *(Panel A) and Guan and Waliser, (2019) (Panel B): In each panel the spatial distribution of annual (seasonal) average is shown in first column [(a), (d), (g), (j), (m), units are mm/year or mm/season]; AR-related rainfall in second column [(b), (e), (h), (k), (n), units are in mm/year or mm/season]; and fractional contributions are shown in the third column [(c),(f), (i), (l), (o), units are in %], over the period* 1982 – 2016 *using WFDE5 [Note: grid cells with annual (seasonal) average precipitation < 50 mm (<15) mm are not shown in the fractional contribution (white color)].*

In Figure S5.9b, the spatial distribution of AR-related rainfall from tARget (Guan and Waliser, 2019) ARs (Panel B) resembles the spatial distribution of AR-related rainfall estimated using Nayak et al. (2021) ARs (Panel A), though there are differences in the intensities in each season. Both algorithms showed an agreement on the percent contribution of ARs in Ganga Basin (GB), though a few more grids in the southeast showed slightly higher contribution when using the tARget algorithm. AR-related rainfall from both algorithms showed that the winter rainfall is mainly AR-rainfall [more than 60% comes from ARs, Panels A and B (f)]. In Panel B, a slightly higher AR contribution is observed in west IB and GB which is related to slightly more AR-related contributions in spring and summer [Panel B, (c), (i), and (l)]. Similarly, for the north and south of GB, there is an increased contribution from ARs in winter and summer [Panel B, (f) and (l)], though this increase may be related to AR-cyclones and ARs identified by tARget that intersect the transect at the southeast GB. In autumn, the contribution of AR-related rainfall is smaller [Panel B, (o)] due to the low number of ARs identified during this season, which is mainly related to the thresholds and AR criteria used in the algorithm.

The key reasons that contributed to the differences in ARs obtained from Nayak et al. (2021) and the tARget algorithm are as follows:

- tARget uses monthly thresholds that can vary from 85th to 95th, but not $\leq 100\ \mathrm{kg.m^{-1}.s^{-1}}$, while Nayak et al. (2021) uses daily 85th percentile values that can be $\leq 100\ \mathrm{kg.m^{-1}.s^{-1}}$in some season. Thus, tARget extracts more ARs in summer, but lesser ARs in non-monsoon, particularly over WH, KA, and HK.
- tARget produces many short-duration ARs ($<$ 18 hours), while ARs from Lavers *et al.*, (2012) approach and thus from (Nayak, Azam and Lyngwa, 2021) are all persistent ($\geq$ 18 hr).
- tARget retains timesteps when ARs and cyclones co-occur, which may affect the AR-impacts quantification. In contrast, Nayak et al. (2021) removed all AR timesteps that have cyclones.

Chapter 6

General Conclusions and Future Implications:

6.1. Conclusions

Atmospheric rivers (ARs)─filamentary forms of anomalous water vapor and winds that propagate coherently poleward within the lower troposphere─emerged as highly efficient means of transport of excess water vapor, heat, energy, and momentum nearly 30 years ago (Newell *et al.*, 1992). In mid-latitudes, ARs transport moisture from tropics-subtropics to the poles, being sustained through continuous moistening (evaporation, convergence from nearby sources, or distant contributions) along their journey (Payne *et al.*, 2020). Most intense and persistent ARs originate in the tropics-subtropics. The lack of regional investigations globally has led to ARs being considered primarily as extra-tropical and were only recently defined with broader scope by Ralph *et al.*, (2018) in GoM. The definition clarified the concept and term "river" in the scientific literature while keeping AR boundary criteria open for future research, benefitting the AR research community.

ARs are identified using IVT or/and IWV, with IVT preferred for its transport component, accurate representation of AR shapes across latitudes, and its closer link to precipitation. Appropriate thresholds (absolute, relative, or both) and criteria help identify ARs from the background IWV/IVT fields. The thresholds, methods, and dataset choice affect AR statistics (Shields *et al.*, 2018; Ralph, Wilson, *et al.*, 2019) and conclusions on their impacts. Nonetheless, certain key characteristics remain widely acceptable, including high IVT (2-3 deviations above the mean), length > 2,000 km, width <1,000 km, LWratio >2, poleward movement, and in mid-latitudes IWV $\geq$ 2 cm. Some algorithms show disagreement on less-intense ARs, especially in unexplored regions like the Himalayan region, yet some algorithms show their global presence. In mid-latitudes, ARs significantly influence precipitation (contribute ~60% of annual totals) and flooding (80% influence), while their absence escalates hydrological drought incidents by 90% (Paltan *et al.*, 2017). The ARs' characteristics vary by region and season, and when influenced by topography yield a diverse range of impacts on regional weather. Despite their infrequency and brief existence (Maclennan *et al.*, 2023), a two or three-day AR can have noticeable effects. Understanding their influence on hydrological variability is crucial for water resources and flood risk management, with relevance to both global climate and regional weather events.

Over the last decade, regional studies on tropical-subtropical ARs have emerged, revealing some distinctive characteristics compared to extra-tropical ARs (Park, Son and Kim, 2021). In India, AR studies have focused mainly on frequency, seasonality, and related extremes (Lakshmi and Satyanarayana, 2020). However, a comprehensive analysis of their nature and moisture sources remains lacking. Historically, heavy precipitation in northern Indian regions, including the southern slopes of the Himalaya, has often been attributed solely to tropical cyclones and the ISM. The Himalayan mountain ranges serve as important physical barriers to AR moisture transported, and regional investigations are required to accurately assess AR impacts, otherwise, their impacts over these regions may be underestimated. Therefore, understanding regional climatology and using suitable thresholds are crucial to identifying ARs in these regions and quantifying their hydro-climatological effects.

This thesis begins with an in-depth investigation of the August 2018 Kerala flood in relation to ARs. The event was so severe—with 500+ deaths, thirteen of fourteen districts inundated, and \$3.7 billion in flood damages—that it must have been driven by exceptional atmospheric conditions. During the first week of August, before ARs were present, rainfall were over 70 mm/day at multiple locations, which saturated the soil in most parts of the state of Kerala and elevated the flooding potential. When ARs (12th to 15th August) occurred during the second week, heavy precipitation received at many more stations primarily translated to direct runoff and generated large floods. IVT maps illustrated an intense (Category 5) elongated moisture transport form of west-to-northeast orientation, fitting the AR description Ralph *et al.*, (2018) over the area (13th–17th August). Synoptic overview revealed a polar westerly jet trough (extending equatorward to $35°-40°$N) induced low-pressure anomalies over India and intensified the low of the monsoon trough in Orissa and the Bay of Bengal. This drew moisture from the Arabian Sea and Indian Ocean to Kerala. The presence of the Western Ghats and the AR's perpendicular impact on the mountains intensified precipitation. Moisture-laden winds upon striking the Western Ghats resulted in deep convergence and eventual rainout. During 13th-15th August, there was a strong vertical uplift (>1 $Pa.s^{-1}$) of air on the windward side that indicated orographic, rather than convective, which is a typical feature of AR landfall in complex-coastal terrains. The backward Lagrangian trajectory analysis on 13th August showed that a large portion of moisture originated from the central-eastern Indian Ocean (60%) to Kerala and small amounts ($\sim 5\%$) from the Arabian Sea. These sources contributed to AR formation and subsequent rainfall in the windward region. This study provided insights into how pre-saturated soil and an AR event can result in devastating conditions in elevated and low-latitude regions.

The ARs that penetrated inland over India and stuck the south-facing Himalayan arc, impacting the Indus and Ganga Basins are studied. These ARs were identified by their central axis (regions of highest IVT, to focus on impactful ones) using a regional AR detection algorithm of Lavers *et al.*, (2012) and modified for the Himalaya. IVT thresholds revealed high seasonal variations across latitudes: in the extratropical Himalayan portion, the IVT 85th percentile threshold is very low, leading to the identification of many low-intensity ARs that are often overlooked with traditional thresholds ($100\ or\ 250 kg.m^{-1}.s^{-1}$) despite exceeding the local thresholds. In contrast, the tropical portion experiences higher IVT climatology, especially in summer. On average 24 ARs occur annually, peaking in winter (8/season), followed by summer (6/season), spring and autumn (5/season each). Most ARs are short-lived (<18 hours), but few exist for longer durations (>72 hours). Long-duration ARs (median of 30 hours) occur more in winter and autumn compared to spring and summer (median of 24 hours). The winter ARs in WH and CH mostly bring beneficial precipitations, while a few extreme ones in summer, and autumn can have devastating impacts. In CH and EH, ARs occur frequently in all seasons with the highest in summer and are primarily associated with high-impact precipitation events. The top AR events in IB and GB produced more than 150 mm/day of precipitation along their axes and at locations where they struck the mountains. In the headwaters, ARs released over 65 mm/day, while less than 50 mm/day were also observed in neighboring areas, thus highlighting the extensive precipitation impact of ARs. This thesis also focused on the processes contributing to moisture convergence and precipitation. The moisture budget analysis at one instant of time during the AR events revealed that high precipitation intensity near mountains and along the AR axis resulted from a combination of strong convergence, strong positive advection, and minimal evaporation. At these locations, there was also a small rate of change in the specific humidity (or atmospheric storage) that indicated the effective transformation of moisture flux into precipitation. The advection term was mainly found to control the atmospheric moisture storage. At two regions high IVT and intense precipitation, the vertical profile indicated that the troposphere was saturated throughout. Near mountains, low-level air is mildly unstable atmosphere (CAPE: $< 350\,J/kg$, CIN: $-0.6\ to\ -145\,J/kg$) but ascended due to orographic forcing and resulted precipitation, while near the AR axis, the unstable atmosphere (CAPE: $390\ to\ 875\,J/kg$, CIN: $-0.2\ to - 25\,J/kg$) was lifted due to air mass interaction, and generated precipitation. The right side of the axis remained nearly saturated due to warmer air temperatures and produced low precipitation despite high CAPE (with low CIN), which may be due to the absence of a triggering mechanism. Excess moisture leading to precipitation was traced to the northern and western Arabian Sea, the northern and eastern Bay of Bengal, and Middle Eastern Seas. It is concluded that the severity of AR precipitation depends on interaction with high mountains and precipitation-mechanisms, besides the intensity, duration, and orientation of winds.

Further, a detailed investigation of AR impacting the Himalayan hydrology of IB and GB is conducted. On average, ARs contribute up to 30% of the annual rainfall in IB, and up to 20% in GB, though the contributions vary spatially within the basins and tend to be highest near the mountains. Seasonally, ARs have the highest contribution ($> 60\%$) to winter precipitation, impacting large areas of IB and northwest GB ($50 - 60\%$). The higher contributions from ARs in the central IB and northwest GB during winter are likely due to just a few intense ARs that originated in the Arabian Sea and striking mostly the WH or western part of CH. In three of the seasons (winter, spring, and autumn), ARs influenced IB much more than GB, particularly in winter. Northern IB and northwest GB also received more than half of the winter snowfall during ARs. Further, it is found that ARs also contributed over half of the winter precipitation in the mountains (HK, KA, WH, and CH), and ARs explained over 75%, 57%, 42%, and 30% of the variability in winter precipitation of KA, HK, CH, and WH, respectively. This suggested ARs as the major driver of snowfall variability even at high altitudes, deep in the high-mountain ranges. In relation to extreme rainfall, the strongest links are in winter and spring, mostly at the foothills of the basins. The two cases of intense AR events contributed over 40% of the total annual precipitation at their respective locations. Each event raised the water levels from low flow to sudden very high flood levels/peak discharge and flooded Kashmir and Kedarnath areas. The two largest floods underscore ARs' significance in IB and GB. Notably, 56%–73% of the floods in the Himalaya during 1985–2015 coincided in space and time with ARs. These results imply that ARs are key agents delivering water deep inland, more than thousands of kilometers from the Indian coasts, and are the potential mechanisms of flooding in the Himalayan basins

These studies confirm the presence of ARs in Indian (tropical-subtropical latitudes), and the Himalayan (tropical-extratropical) regions. Their frequency varies by latitude, consistent with prior regional studies: the highest AR frequency (Himalayan ARs) in the tropics is in summer, as found by Kamae et al. (2021); Mahto et al. (2023), and in winter (followed by autumn) towards the extratropical portion, as found by Nayak and Villarini (2017) and others for ARs in extratropical regions. The identification of ARs in the Himalayan region, however, requires careful consideration due to their high-frequency variation and resulting impacts on precipitation and extremes. These findings emphasize the need to comprehend the hydrological modification caused by ARs. In this thesis, we have shown that ARs make a significant contribution to the annual (seasonal) precipitation, thereby influencing the hydrology of the two large basins in northern India. Himalayan mountain precipitation is heavily influenced by ARs, emphasizing their essential roles in regional water supply and sustainability of snowpack and glaciers there. Precipitation intensity during ARs varies due to various factors including precipitating mechanism and notably topography. Our investigation delves into understanding of mechanisms controlling atmospheric moisture, precipitation, and locating moisture sources for AR events, going beyond frequency and impact assessments. Despite concerns regarding attributing extremes to ARs in Asian Monsoon regions, our studies demonstrated that intense, impactful floods are indeed linked to ARs, establishing them as one of the causes of regional extremes. This thesis significantly contributes to the limited AR literature in this region.

6.2. Future Scope

The thesis has drawn several important conclusions from the objectives about ARs over India and the Himalaya, their implications on precipitation extremes, and climatological importance. This thesis also opened numerous avenues for future exploration that remain vital to gaining a deeper understanding of ARs in these regions. Some of the most important future perspectives are briefly discussed here:

- Distinguishing ARs and the ISM is an open challenge. Many ARs over the southern India resemble monsoon circulation and appear anomalously intense. Studying the similarities and differences between ARs and monsoon flow patterns would benefit the research community in attempting to predict and relate them to extreme events.
- Investigate the differences between ARs, WDs, and tropical cyclones over India and the Himalaya, and quantify how their relationship in impacting each other's strength, occurrences, and precipitation patterns.
- Estimate population exposure during AR events, identify hotspots, and the effectiveness of existing emergency plans.
- Quantify the contribution of ARs to water level rise in rivers or dams to manage excess water or store it for low-flow periods.
- Investigating exceptional flood events (like the Kerala 2018 Floods) with substantial precipitation intensity in relation to ARs, this can help establish the AR-extreme precipitation link over these regions that have not previously been considered. This will demonstrate their control on the tail distribution of extreme events. Quantify the contribution of ARs to water level rise in rivers or dams. Can the excess water be managed or stored for periods of low flows?
- Furthermore, extreme precipitation and floods are recurring phenomena, so it is imperative to channel research efforts into forecasting ARs over India and integrate them in existing Numerical Prediction Models. Understanding how IVT is resolved in models and describing physical processes better can improve accuracy, and may likely be a major breakthrough in hydrometeorological prediction over the Himalaya.
- Investigations on the impacts of AR winds on Himalayan glaciers. ARs may increase downwind leading to intense drier and warmer air impacting glaciers' surfaces.
- Further studies are needed to examine ARs' direct impacts on snowpack and glaciers since ARs also transport warm tropical moist air that can lead to either rainfall or snowfall, and impact snowmelt or snow accumulation. ARs can bring be associated with large-scale sensible heat that can impact the snowpack and increase discharge.
- We have lightly demonstrated that prior precipitation impacted soil moisture and generated large runoffs when AR precipitation occurred. However, further exploration can help understand how AR-

precipitation impacts the ground covered with different surfaces, and their timely response. The aspect of human impact can also be included to estimate the exposure of the population to extreme events.

REFERENCES

Aemisegger, F. and Papritz, L. (2018) 'A Climatology of strong large-scale ocean evaporation events. Part I: Identification, global distribution, and associated climate conditions', *Journal of Climate*, 31(18), pp. 7287–7312. Available at: https://doi.org/10.1175/JCLI-D-17-0591.1.

Albano, C.M., Dettinger, M.D. and Harpold, A.A. (2020) 'Patterns and drivers of Atmospheric River precipitation and hydrologic impacts across the Western United States', *Journal of Hydrometeorology*, 21(1), pp. 143–159. Available at: https://doi.org/10.1175/JHM-D-19-0119.1.

Albano, C.M., Dettinger, M.D. and Soulard, C.E. (2017) 'Influence of Atmospheric rivers on vegetation productivity and fire patterns in the southwestern U.S.', *Journal of Geophysical Research: Biogeosciences*, 122(2), pp. 308–323. Available at: https://doi.org/10.1002/2016JG003608.

Albergel, C. *et al.* (2018) 'ERA-5 and ERA-Interim driven ISBA land surface model simulations: which one performs better?', *Hydrology and Earth System Sciences*, 22(6), pp. 3515–3532. Available at: https://doi.org/10.5194/hess-22-3515-2018.

Alexander, M.A. *et al.* (2015) 'Moisture Pathways into the U.S. Intermountain West Associated with Heavy Winter Precipitation Events', *Journal of Hydrometeorology*, 16(3), pp. 1184–1206. Available at: https://doi.org/10.1175/JHM-D-14-0139.1.

Algarra, I. *et al.* (2020) 'Significant increase of global anomalous moisture uptake feeding landfalling Atmospheric rivers', *Nature Communications*, 11(1), p. 5082. Available at: https://doi.org/10.1038/s41467-020-18876-w.

Arora, H.L., Singh, A.K. and Agrawal, M. (2018) *Role of Tehri Dam in Prevention of Floods. THDC*, p. 3. Available at: https://thdc.co.in/content/role-tehri-dam-prevention-floodveling-and-centring.

Azam, M.F. *et al.* (2018) 'Review of the status and mass changes of Himalayan-Karakoram glaciers', *Journal of Glaciology*, 64(243), pp. 61–74. Available at: https://doi.org/10.1017/jog.2017.86.

Azam, M.F. *et al.* (2019) 'Snow and ice melt contributions in a highly glacierized catchment of Chhota Shigri Glacier (India) over the last five decades', *Journal of Hydrology*, 574, pp. 760–773. Available at: https://doi.org/10.1016/j.jhydrol.2019.04.075.

Azam, M.F. *et al.* (2021) 'Glaciohydrology of the Himalaya-Karakoram', *Science*, 373(6557), p. eabf3668. Available at: https://doi.org/10.1126/science.abf3668.

Baggett, C.F. *et al.* (2017) 'Advancing atmospheric river forecasts into subseasonal-to-seasonal time scales: Forecasting ARs at S2S Time Scales', *Geophysical Research Letters*, 44(14), pp. 7528–7536. Available at: https://doi.org/10.1002/2017GL074434.

Baisya, H. *et al.* (2018) 'Ramifications of atmospheric humidity on monsoon depressions over the Indian subcontinent', *Scientific Reports*, 8(1), p. 9927. Available at: https://doi.org/10.1038/s41598-018-28365-2.

Bao, J.-W. *et al.* (2006) 'Interpretation of enhanced integrated water vapor bands associated with extratropical cyclones: their formation and connection to tropical moisture', *Monthly Weather Review*, 134(4), pp. 1063–1080. Available at: https://doi.org/10.1175/MWR3123.1.

Barkiđija, S. and Fuchs, Z. (2013) 'Precipitation correlation between convective available potential energy, convective inhibition and saturation fraction in middle latitudes', *Atmospheric Research*, 124, pp. 170–180. Available at: https://doi.org/10.1016/j.atmosres.2012.12.010.

Barth, N.A. *et al.* (2017) 'Mixed populations and annual flood frequency estimates in the western United States: The role of Atmospheric Rivers', *Water Resources Research*, 53(1), pp. 257–269. Available at: https://doi.org/10.1002/2016WR019064.

Baudouin, J.P., Herzog, M. and Petrie, C.A. (2021) 'Synoptic processes of winter precipitation in the Upper Indus Basin', *Weather and Climate Dynamics*, 2(4), pp. 1187–1207. Available at: https://doi.org/10.5194/wcd-2-1187-2021.

Bernhardt, D. (2006) 'Glacier National Park Flooding November 2006', *NWS Western Region Tech. Attachment*, 8(23), p. 15.

Blamey, R.C. *et al.* (2018) 'The influence of Atmospheric rivers over the South Atlantic on winter rainfall in South Africa', *Journal of Hydrometeorology*, 19(1), pp. 127–142. Available at: https://doi.org/10.1175/JHM-D-17-0111.1.

Bolch, T. *et al.* (2012) 'The State and fate of Himalayan Glaciers', *Science*, 336(6079), pp. 310–314. Available at: https://doi.org/10.1126/science.1215828.

Bolch, T. *et al.* (2019) 'Status and Change of the Cryosphere in the Extended Hindu Kush Himalaya Region', in P. Wester et al. (eds) *The Hindu Kush Himalaya Assessment*. Cham: Springer International Publishing, pp. 209–255. Available at: https://doi.org/10.1007/978-3-319-92288-1_7.

Bolton (1980) 'The computation of equivalent potential temperature', *Monthly Weather Review*, 108(7), pp. 1046–1053. Available at: https://doi.org/10.1175/1520-0493(1980)108<1046:TCOEPT>2.0.CO;2.

Bookhagen, B. and Burbank, D.W. (2006) 'Topography, relief, and TRMM-derived rainfall variations along the Himalaya', *Geophysical Research Letters*, 33(8), p. L08405. Available at: https://doi.org/10.1029/2006GL026037.

Bookhagen, B. and Burbank, D.W. (2010) 'Toward a complete Himalayan hydrological budget: spatiotemporal distribution of snowmelt and rainfall and their impact on river discharge', *Journal of Geophysical Research*, 115(F3), p. F03019. Available at: https://doi.org/10.1029/2009JF001426.

Boschi, R. and Lucarini, V. (2019) 'Water pathways for the Hindu-Kush-Himalaya and an Analysis of three flood events', *Atmosphere*, 10(9), p. 489. Available at: https://doi.org/10.3390/atmos10090489.

Bowman, K.P. *et al.* (2013) 'Input data requirements for Lagrangian trajectory models', *Bulletin of the American Meteorological Society*, 94(7), pp. 1051–1058. Available at: https://doi.org/10.1175/BAMS-D-12-00076.1.

Bozkurt, D. *et al.* (2018) 'Foehn event triggered by an Atmospheric river underlies record-setting temperature along continental Antarctica', *Journal of Geophysical Research: Atmospheres*, 123(8), pp. 3871–3892. Available at: https://doi.org/10.1002/2017JD027796.

Bozkurt, D. *et al.* (2021) 'Influence of African Atmospheric rivers on precipitation and snowmelt in the near East's Highlands', *Journal of Geophysical Research: Atmospheres*, 126(4). Available at: https://doi.org/10.1029/2020JD033646.

Brands, S., Gutiérrez, J.M. and San-Martín, D. (2017) 'Twentieth-century Atmospheric River activity along the west coasts of Europe and North America: algorithm formulation, reanalysis uncertainty and links to atmospheric circulation patterns', *Climate Dynamics*, 48(9–10), pp. 2771–2795. Available at: https://doi.org/10.1007/s00382-016-3095-6.

Branstator, G. (1995) 'Organization of storm track anomalies by recurring low-frequency circulation anomalies', *Journal of the Atmospheric Sciences*, 52(2), pp. 207–226. Available at: https://doi.org/10.1175/1520-0469(1995)052<0207:OOSTAB>2.0.CO;2.

Browning, K.A. (1990) ‘Organization of clouds and precipitation in extratropical cyclones’, in *Extratropical Cyclones: The Erik Palmén Memorial Volume*. Boston, MA: American Meteorological Society, pp. 129–153. Available at: https://doi.org/10.1007/978-1-944970-33-8_8.

Brubaker, K.L., Entekhabi, D. and Eagleson, P.S. (1993) ‘Estimation of continental precipitation recycling’, *Journal of Climate*, 6(6), pp. 1077–1089. Available at: https://doi.org/10.1175/1520-0442(1993)006<1077:EOCPR>2.0.CO;2.

Cadet, D. and Reverdin, G. (1981) ‘Water vapour transport over the Indian Ocean during summer 1975’, *Tellus* [Preprint].

Cannon, F. *et al.* (2016) ‘Winter westerly disturbance dynamics and precipitation in the western Himalaya and Karakoram: a wave-tracking approach’, *Theoretical and Applied Climatology*, 125(1–2), pp. 27–44. Available at: https://doi.org/10.1007/s00704-015-1489-8.

Champati Ray, P.K. *et al.* (2016) ‘Kedarnath disaster 2013: causes and consequences using remote sensing inputs’, *Natural Hazards*, 81(1), pp. 227–243. Available at: https://doi.org/10.1007/s11069-015-2076-0.

Chen, X. *et al.* (2019) ‘Impact of Atmospheric Rivers on surface hydrological processes in Western U.S. watersheds’, *Journal of Geophysical Research: Atmospheres*, 124(16), pp. 8896–8916. Available at: https://doi.org/10.1029/2019JD030468.

Clemens, S.C. and Oglesby, R.J. (1992) ‘Interhemispheric moisture transport in the Indian Ocean summer monsoon: Data-model and model-model comparisons’, *Paleoceanography*, 7(5), pp. 633–643. Available at: https://doi.org/10.1029/92PA01752.

Cordeira, J.M., Ralph, F.M. and Moore, B.J. (2013) ‘The development and evolution of two Atmospheric Rivers in proximity to Western North Pacific tropical cyclones in October 2010’, *Monthly Weather Review*, 141(12), pp. 4234–4255. Available at: https://doi.org/10.1175/MWR-D-13-00019.1.

Corringham, T.W. *et al.* (2019) ‘Atmospheric Rivers drive flood damages in the western United States’, *Science Advances*, 5(12), p. eaax4631. Available at: https://doi.org/10.1126/sciadv.aax4631.

Couto, F.T., Salgado, R. and Costa, M.J. (2012) ‘Analysis of intense rainfall events on Madeira Island during the 2009/2010 winter’, *Natural Hazards and Earth System Sciences*, 12(7), pp. 2225–2240. Available at: https://doi.org/10.5194/nhess-12-2225-2012.

Cucchi, M. *et al.* (2020) ‘WFDE5: bias-adjusted ERA5 reanalysis data for impact studies’, *Earth System Science Data*, 12(3), pp. 2097–2120. Available at: https://doi.org/10.5194/essd-12-2097-2020.

Cucchi, M. (2021) *Near surface meteorological variables from 1979 to 2019 derived from bias-corrected reanalysis*, p. 14. Available at: https://datastore.copernicus-climate.eu/documents/derived-near-surface-meteorological-variables/C3S_Dataset-PUG_WFDE5_v2.0.pdf.

Curio, J. and Scherer, D. (2016) ‘Seasonality and spatial variability of dynamic precipitation controls on theTibetan Plateau’, *Earth System Dynamics*, 7(3), pp. 767–782. Available at: https://doi.org/10.5194/esd-7-767-2016.

Dacre, H.F. *et al.* (2015) ‘How do Atmospheric Rivers form?’, *Bulletin of the American Meteorological Society*, 96(8), pp. 1243–1255. Available at: https://doi.org/10.1175/BAMS-D-14-00031.1.

Dash, S.K. *et al.* (2005) ‘Response of the Indian summer monsoon circulation and rainfall to seasonal snow depth anomaly over Eurasia’, *Climate Dynamics*, 24(1), pp. 1–10. Available at: https://doi.org/10.1007/s00382-004-0448-3.

Derbyshire, S.H. *et al.* (2004) 'Sensitivity of moist convection to environmental humidity', *Quarterly Journal of the Royal Meteorological Society*, 130(604), pp. 3055–3079. Available at: https://doi.org/10.1256/qj.03.130.

Dettinger, M., Ralph, F. and Lavers, D. (2015) 'Setting the stage for a global science of Atmospheric rivers', *Eos*, 96. Available at: https://doi.org/10.1029/2015EO038675.

Dettinger, M.D. *et al.* (2011) 'Atmospheric Rivers, floods and the water resources of California', *Water*, 3(2), pp. 445–478. Available at: https://doi.org/10.3390/w3020445.

Dettinger, M.D. (2011) 'Climate change, Atmospheric rivers, and floods in California - A multimodel analysis of storm frequency and magnitude changes.', *JAWRA Journal of the American Water Resources Association*, 47(3), pp. 514–523. Available at: https://doi.org/10.1111/j.1752-1688.2011.00546.x.

Dettinger, M.D. (2013) 'Atmospheric rivers as drought busters on the U.S. West Coast', *Journal of Hydrometeorology*, 14(6), pp. 1721–1732. Available at: https://doi.org/10.1175/JHM-D-13-02.1.

Dettinger, M.D. and Cayan, D. (2014) 'Drought and the California Delta—A matter of extremes', *San Francisco Estuary and Watershed Science*, 12(2). Available at: https://doi.org/10.15447/sfews.2014v12iss2art4.

Dey, D. and Döös, K. (2021) 'Tracing the origin of the south asian summer monsoon precipitation and its variability using a novel lagrangian framework', *Journal of Climate*, 34(21), pp. 8655–8668. Available at: https://doi.org/10.1175/JCLI-D-20-0967.1.

Dimri, A.P. (2006) 'Surface and upper air fields during extreme winter precipitation over the Western Himalayas', *Pure and Applied Geophysics*, 163(8), pp. 1679–1698. Available at: https://doi.org/10.1007/s00024-006-0092-4.

Dimri, A.P. *et al.* (2015) 'Western Disturbances: A review', *Reviews of Geophysics*, 53(2), pp. 225–246. Available at: https://doi.org/10.1002/2014RG000460.

Dixon, P.G. (2008) 'Effects of precipitable water and CAPE on precipitation in Southern Arizona', *Journal of the Arizona-Nevada Academy of Science*, 40(1), pp. 66–73. Available at: https://doi.org/10.2181/1533-6085(2008)40[66:EOPWAC]2.0.CO;2.

Doiteau, B. *et al.* (2021) 'Atmospheric rivers and associated precipitation over France and Western Europe: 1980–2020 climatology and case study', *Atmosphere*, 12(8), p. 1075. Available at: https://doi.org/10.3390/atmos12081075.

Dominguez, F. *et al.* (2006) 'Impact of atmospheric moisture storage on precipitation recycling', *Journal of Climate*, 19(8), pp. 1513–1530. Available at: https://doi.org/10.1175/JCLI3691.1.

Dong, W. *et al.* (2019) 'Precipitable water and CAPE dependence of rainfall intensities in China', *Climate Dynamics*, 52(5–6), pp. 3357–3368. Available at: https://doi.org/10.1007/s00382-018-4327-8.

Draxler, R.R. and Hess, G.D. (1997) *Description of the HYSPLIT_4 modelling system*, p. 24.

Draxler, R.R. and Hess, G.D. (1998) 'An overview of the HYSPLIT_4 Modelling system for trajectories, dispersion, and deposition', *Aust.ralian Meteorological Magazine*, (47), pp. 295–308.

Draxler, R.R. and Stunder, B.J.B. (1988) 'Modeling the CAPTEX Vertical Tracer Concentration Profiles', *Journal of Applied Meteorology*, 27(5), pp. 617–625. Available at: https://doi.org/10.1175/1520-0450(1988)027<0617:MTCVTC>2.0.CO;2.

Durán-Quesada, A.M. *et al.* (2010) 'Moisture sources for central America: identification of moisture sources using a Lagrangian analysis technique', *Journal of Geophysical Research*, 115(D5), p. D05103. Available at: https://doi.org/10.1029/2009JD012455.

Eiras-Barca, J. *et al.* (2021) 'European west coast Atmospheric rivers: A scale to characterize strength and impacts', *Weather and Climate Extremes*, 31, p. 100305. Available at: https://doi.org/10.1016/j.wace.2021.100305.

Eldardiry, H. *et al.* (2019) 'Atmospheric River–induced precipitation and snowpack during the western United States cold season', *Journal of Hydrometeorology*, 20(4), pp. 613–630. Available at: https://doi.org/10.1175/JHM-D-18-0228.1.

Farinotti, D. *et al.* (2019) 'A consensus estimate for the ice thickness distribution of all glaciers on Earth', *Nature Geoscience*, 12(3), pp. 168–173. Available at: https://doi.org/10.1038/s41561-019-0300-3.

Farr, T.G. *et al.* (2007) 'The Shuttle Radar Topography Mission', *Reviews of Geophysics*, 45(2), p. RG2004. Available at: https://doi.org/10.1029/2005RG000183.

Findlater, J. (1969) 'A major low-level air current near the Indian Ocean during the northern summer', *Quarterly Journal of the Royal Meteorological Society*, 95(404), pp. 362–380. Available at: https://doi.org/10.1002/qj.49709540409.

Fischer, A.S. *et al.* (2002) 'Mesoscale eddies, coastal upwelling, and the upper-ocean heat budget in the Arabian Sea', *Deep Sea Research Part II: Topical Studies in Oceanography*, 49(12), pp. 2231–2264. Available at: https://doi.org/10.1016/S0967-0645(02)00036-X.

Fish, M.A., Wilson, A.M. and Ralph, F.M. (2019) 'Atmospheric River Families: Definition and associated synoptic conditions', *Journal of Hydrometeorology*, 20(10), pp. 2091–2108. Available at: https://doi.org/10.1175/JHM-D-18-0217.1.

Florsheim, J.L. and Dettinger, M.D. (2015) 'Promoting Atmospheric-river and snowmelt-fueled biogeomorphic processes by restoring river-floodplain connectivity in California's Central Valley', in P.F. Hudson and H. Middelkoop (eds) *Geomorphic Approaches to Integrated Floodplain Management of Lowland Fluvial Systems in North America and Europe*. New York, NY: Springer New York, pp. 119–141.

Fowler, H.J. and Archer, D.R. (2006) 'Conflicting signals of climatic change in the upper Indus Basin', *Journal of Climate*, 19(17), pp. 4276–4293. Available at: https://doi.org/10.1175/JCLI3860.1.

Fremme, A. and Sodemann, H. (2019) 'The role of land and ocean evaporation on the variability of precipitation in the Yangtze River valley', *Hydrology and Earth System Sciences*, 23(6), pp. 2525–2540. Available at: https://doi.org/10.5194/hess-23-2525-2019.

Fujita, T.T. (1970) 'Proposed characterization of tornadoes and hurricanes by area and intensity'. Available at: http://hdl.handle.net/10605/261875.

Gershunov, A. *et al.* (2017) 'Assessing the climate-scale variability of Atmospheric rivers affecting western North America', *Geophysical Research Letters*, 44(15), pp. 7900–7908. Available at: https://doi.org/10.1002/2017GL074175.

Gimeno, L. *et al.* (2014) 'Atmospheric Rivers: a mini-review', *Frontiers in Earth Science*, 2. Available at: https://doi.org/10.3389/feart.2014.00002.

Gimeno, L. *et al.* (2016) 'Major mechanisms of Atmospheric moisture transport and their role in extreme precipitation events', *Annual Review of Environment and Resources*, 41(1), pp. 117–141. Available at: https://doi.org/10.1146/annurev-environ-110615-085558.

Gimeno, L. *et al.* (2021) ‘Atmospheric river, a term encompassing different meteorological patterns’, *WIREs Water*, 8(6). Available at: https://doi.org/10.1002/wat2.1558.

Gorodetskaya, I.V. *et al.* (2014) ‘The role of Atmospheric rivers in anomalous snow accumulation in East Antarctica’, *Geophysical Research Letters*, 41(17), pp. 6199–6206. Available at: https://doi.org/10.1002/2014GL060881.

Guan, B. *et al.* (2010) ‘Extreme snowfall events linked to Atmospheric rivers and surface air temperature via satellite measurements’, *Geophysical Research Letters*, 37(20). Available at: https://doi.org/10.1029/2010GL044696.

Guan, B. *et al.* (2013) ‘The 2010/2011 snow season in California’s Sierra Nevada: Role of atmospheric rivers and modes of large-scale variability: Atmospheric Rivers and modes of large-scale variability’, *Water Resources Research*, 49(10), pp. 6731–6743. Available at: https://doi.org/10.1002/wrcr.20537.

Guan, B. *et al.* (2016) ‘Hydrometeorological characteristics of rain-on-snow events associated with Atmospheric rivers’, *Geophysical Research Letters*, 43(6), pp. 2964–2973. Available at: https://doi.org/10.1002/2016GL067978.

Guan, B. and Waliser, D.E. (2015) ‘Detection of Atmospheric Rivers: evaluation and application of an algorithm for global studies’, *Journal of Geophysical Research: Atmospheres*, 120(24), pp. 12514–12535. Available at: https://doi.org/10.1002/2015JD024257.

Guan, B. and Waliser, D.E. (2017) ‘Atmospheric Rivers in 20 year weather and climate simulations: A multimodel, global evaluation’, *Journal of Geophysical Research: Atmospheres*, 122(11), pp. 5556–5581. Available at: https://doi.org/10.1002/2016JD026174.

Guan, B. and Waliser, D.E. (2019) ‘Tracking Atmospheric Rivers globally: spatial distributions and temporal evolution of life cycle characteristics’, *Journal of Geophysical Research: Atmospheres*, 124(23), pp. 12523–12552. Available at: https://doi.org/10.1029/2019JD031205.

Guan, B., Waliser, D.E. and Ralph, F.M. (2018) ‘An intercomparison between reanalysis and dropsonde observations of the total water vapor transport in individual Atmospheric rivers’, *Journal of Hydrometeorology*, 19(2), pp. 321–337. Available at: https://doi.org/10.1175/JHM-D-17-0114.1.

Guan, B., Waliser, D.E. and Ralph, F.M. (2020) ‘A multimodel evaluation of the water vapor budget in atmospheric rivers’, *Annals of the New York Academy of Sciences*, 1472(1), pp. 139–154. Available at: https://doi.org/10.1111/nyas.14368.

Guan, B., Waliser, D.E. and Ralph, F.M. (2023) ‘Global application of the Atmospheric River scale’, *Journal of Geophysical Research: Atmospheres*, 128(3), p. e2022JD037180. Available at: https://doi.org/10.1029/2022JD037180.

Guirguis, K. *et al.* (2019) ‘Atmospheric rivers impacting Northern California and their modulation by a variable climate’, *Climate Dynamics*, 52(11), pp. 6569–6583. Available at: https://doi.org/10.1007/s00382-018-4532-5.

Guo, X. *et al.* (2021) ‘Atmospheric rivers over the Indo-Pacific and its associations with boreal summer intraseasonal oscillation’, *Journal of Climate*, pp. 1–46. Available at: https://doi.org/10.1175/JCLI-D-21-0290.1.

Guo, Y. *et al.* (2020) ‘Statistical Relationship between Atmospheric rivers and extratropical cyclones and anticyclones’, *Journal of Climate*, 33(18), pp. 7817–7834. Available at: https://doi.org/10.1175/JCLI-D-19-0126.1.

Gupta, S.K. *et al.* (2005) ‘Groundwater δ18O and δD from central Indian Peninsula: influence of the Arabian Sea and the Bay of Bengal branches of the summer monsoon’, *Journal of Hydrology*, 303(1–4), pp. 38–55. Available at: https://doi.org/10.1016/j.jhydrol.2004.08.016.

Hatchett, B.J. *et al.* (2017) 'Avalanche fatalities during Atmospheric river events in the Western United States', *Journal of Hydrometeorology*, 18(5), pp. 1359–1374. Available at: https://doi.org/10.1175/JHM-D-16-0219.1.

Hayes, J.L. (2011) *Record Floods of Greater Nashville: Including Flooding in Middle Tennessee (TN) and Western Kentucky (KY), May 1-4- 2010: Service Assessment*. DIANE Publishing.

Held, I.M. (1975) 'Momentum transport by quasi-geostrophic eddies', *Journal of the Atmospheric Sciences*, 32(7), pp. 1494–1497. Available at: https://doi.org/10.1175/1520-0469(1975)032<1494:MTBQGE>2.0.CO;2.

Henn, B. *et al.* (2020) 'Extreme runoff generation from Atmospheric River driven snowmelt during the 2017 Oroville Dam spillways incident', *Geophysical Research Letters*, 47(14). Available at: https://doi.org/10.1029/2020GL088189.

Hersbach, H. *et al.* (2019) 'Global reanalysis: goodbye ERA-Interim, hello ERA5'. Available at: https://doi.org/10.21957/VF291HEHD7.

Hersbach, H., Bell, B., Berrisford, P., Hirahara, S., Horányi, A., Muñoz-Sabater, J., Nicolas, J., Peubey, C., Radu, R., Schepers, D., Simmons, A., Soci, C., *et al.* (2020) 'The ERA5 global reanalysis', *Quarterly Journal of the Royal Meteorological Society*, 146(730), pp. 1999–2049. Available at: https://doi.org/10.1002/qj.3803.

Hersbach, H., Bell, B., Berrisford, P., Hirahara, S., Horányi, A., Muñoz-Sabater, J., Nicolas, J., Peubey, C., Radu, R., Schepers, D., Simmons, A., Soci, Cornel, *et al.* (2020) 'The ERA5 global reanalysis', *Quarterly Journal of the Royal Meteorological Society*, 146(730), pp. 1999–2049. Available at: https://doi.org/10.1002/qj.3803.

Hewitt, K. (2005) 'The Karakoram anomaly? Glacier expansion and the "elevation effect," Karakoram Himalaya', *Mountain Research and Development*, 25(4), pp. 332–340. Available at: https://doi.org/10.1659/0276-4741(2005)025[0332:TKAGEA]2.0.CO;2.

Hochman, A. *et al.* (2023) 'The sources of extreme precipitation predictability; the case of the "Wet" Red Sea Trough', *Weather and Climate Extremes*, 40, p. 100564. Available at: https://doi.org/10.1016/j.wace.2023.100564.

Hoffmann, L. *et al.* (2019) 'From ERA-Interim to ERA5: the considerable impact of ECMWF's next-generation reanalysis on Lagrangian transport simulations', *Atmospheric Chemistry and Physics* [Preprint].

Horan, M.F. *et al.* (2023) 'Moisture sources for precipitation variability over the Arabian Peninsula', *Climate Dynamics*, 61(9–10), pp. 4793–4807. Available at: https://doi.org/10.1007/s00382-023-06762-2.

Hoskins, B.J., James, I.N. and White, G.H. (1983) 'The shape, propagation and mean-flow interaction of large-scale weather systems', *Journal of the Atmospheric Sciences*, 40(7), pp. 1595–1612. Available at: https://doi.org/10.1175/1520-0469(1983)040<1595:TSPAMF>2.0.CO;2.

Hu, H. and Dominguez, F. (2019) 'Understanding the role of tropical moisture in Atmospheric rivers', *Journal of Geophysical Research: Atmospheres*, 124(24), pp. 13826–13842. Available at: https://doi.org/10.1029/2019JD030867.

Hu, J.M. and Nolin, A.W. (2019) 'Snowpack contributions and temperature characterization of landfalling Atmospheric rivers in the western cordillera of the United States', *Geophysical Research Letters*, 46(12), pp. 6663–6672. Available at: https://doi.org/10.1029/2019GL083564.

Huang, X. *et al.* (2020) 'Simulating and evaluating Atmospheric river-induced precipitation extremes along the U.S. Pacific Coast: case studies from 1980–2017', *Journal of Geophysical Research: Atmospheres*, 125(4). Available at: https://doi.org/10.1029/2019JD031554.

Hughes, M. *et al.* (2014) 'The landfall and inland penetration of a flood-producing Atmospheric River in Arizona. Part II: sensitivity of modeled precipitation to terrain height and Atmospheric River orientation', *Journal of Hydrometeorology*, 15(5), pp. 1954–1974. Available at: https://doi.org/10.1175/JHM-D-13-0176.1.

Huning, L.S. *et al.* (2019) 'Sensitivity of seasonal snowfall attribution to Atmospheric Rivers and their reanalysis-based detection', *Geophysical Research Letters*, 46(2), pp. 794–803. Available at: https://doi.org/10.1029/2018GL080783.

Hunt, K.M.R., Turner, A.G. and Shaffrey, L.C. (2018) 'Extreme daily rainfall in pakistan and north India: scale interactions, mechanisms, and precursors', *Monthly Weather Review*, 146(4), pp. 1005–1022. Available at: https://doi.org/10.1175/MWR-D-17-0258.1.

Ionita, M., Nagavciuc, V. and Guan, B. (2020) 'Rivers in the sky, flooding on the ground: the role of atmospheric rivers in inland flooding in central Europe', *Hydrology and Earth System Sciences*, 24(11), pp. 5125–5147. Available at: https://doi.org/10.5194/hess-24-5125-2020.

Jackson, M. *et al.* (2023) 'Chapter 2: Consequences of climate change for the cryosphere in the Hindu Kush Himalaya', in *Water, ice, society, and ecosystems in the Hindu Kush Himalaya: An outlook*. International Centre for Integrated Mountain Development (ICIMOD), pp. 17–71. Available at: https://doi.org/10.53055/ICIMOD.1030.

Jaswal, A.K., Narkhede, N.M. and Shaji, R. (2014) 'Atmospheric data collection, processing and database management in India Meteorological Department', *Proceedings of the Indian National Science Academy*, 80(3), p. 697. Available at: https://doi.org/10.16943/ptinsa/2014/v80i3/55144.

Jiang, T. and Deng, Y. (2011) 'Downstream modulation of North Pacific atmospheric river activity by East Asian cold surges.', *Geophysical Research Letters*, 38(20), p. n/a-n/a. Available at: https://doi.org/10.1029/2011GL049462.

Joseph, P.V. and Simon, A. (2005) 'Weakening trend of the southwest monsoon current through peninsular India from 1950 to the present', *Current Science*, 89(4), pp. 687–694.

Kamae, Y. *et al.* (2017) 'Atmospheric rivers over the Northwestern Pacific: Climatology and interannual variability', *Journal of Climate*, 30(15), pp. 5605–5619. Available at: https://doi.org/10.1175/JCLI-D-16-0875.1.

Kamae, Y. *et al.* (2021) 'Atmospheric rivers bring more frequent and intense extreme rainfall events over East Asia under global warming', *Geophysical Research Letters*, 48(24). Available at: https://doi.org/10.1029/2021GL096030.

Keune, J., Schumacher, D.L. and Miralles, D.G. (2022) 'A unified framework to estimate the origins of atmospheric moisture and heat using Lagrangian models', *Geoscientific Model Development*, 15(5), pp. 1875–1898. Available at: https://doi.org/10.5194/gmd-15-1875-2022.

Khouakhi, A. *et al.* (2022) 'Atmospheric rivers and associated extreme rainfall over Morocco', *International Journal of Climatology*, 42(15), pp. 7766–7778. Available at: https://doi.org/10.1002/joc.7676.

Khouakhi, A. and Villarini, G. (2016) 'On the relationship between Atmospheric rivers and high sea water levels along the U.S. West Coast', *Geophysical Research Letters*, 43(16), pp. 8815–8822. Available at: https://doi.org/10.1002/2016GL070086.

Kirkpatrick, C., McCaul, E.W. and Cohen, C. (2011) 'Sensitivities of simulated convective storms to environmental CAPE', *Monthly Weather Review*, 139(11), pp. 3514–3532. Available at: https://doi.org/10.1175/2011MWR3631.1.

Knippertz, P. and Wernli, H. (2010) 'A lagrangian climatology of tropical moisture exports to the northern hemispheric extratropics', *Journal of Climate*, 23(4), pp. 987–1003. Available at: https://doi.org/10.1175/2009JCLI3333.1.

Komatsu, K.K. *et al.* (2018) ‘Poleward upgliding Siberian Atmospheric rivers over sea ice heat up Arctic upper air’, *Scientific Reports*, 8(1), p. 2872. Available at: https://doi.org/10.1038/s41598-018-21159-6.

Konrad, C.P. and Dettinger, M.D. (2017) ‘Flood runoff in relation to water vapor transport by Atmospheric rivers over the western United States, 1949–2015’, *Geophysical Research Letters*, 44(22), p. 11,456-11,462. Available at: https://doi.org/10.1002/2017GL075399.

Kotal, S.D., Roy, S.S. and Bhowmik, S.K.R. (2014) ‘Catastrophic heavy rainfall episode over Uttarakhand during 16–18 June 2013 – observational aspects’, *Current Science*, 107(2).

Krishnamurti, T.N. and Ramanathan, Y. (1982) ‘Sensitivity of the monsoon onset to differential heating’, *Journal of the Atmospheric Sciences*, 39(6), pp. 1290–1306. Available at: https://doi.org/10.1175/1520-0469(1982)039<1290:SOTMOT>2.0.CO;2.

Kropač, E. *et al.* (2021) ‘A detailed, multi-scale assessment of an Atmospheric river event and its impact on extreme glacier melt in the Southern Alps of New Zealand’, *Journal of Geophysical Research: Atmospheres*, 126(9). Available at: https://doi.org/10.1029/2020JD034217.

Lakshmi, D.D. and Satyanarayana, A.N.V. (2019) ‘Influence of Atmospheric Rivers in the occurrence of devastating flood associated with extreme precipitation events over Chennai using different reanalysis data sets’, *Atmospheric Research*, 215, pp. 12–36. Available at: https://doi.org/10.1016/j.atmosres.2018.08.016.

Lakshmi, D.D. and Satyanarayana, A.N.V. (2020) ‘Climatology of landfalling Atmospheric Rivers and associated heavy precipitation over the Indian coastal regions’, *International Journal of Climatology*, 40(13), pp. 5616–5633. Available at: https://doi.org/10.1002/joc.6540.

Lakshmi, D.D., Satyanarayana, A.N.V. and Chakraborty, A. (2019) ‘Assessment of heavy precipitation events associated with floods due to strong moisture transport during summer monsoon over India’, *Journal of Atmospheric and Solar-Terrestrial Physics*, 189, pp. 123–140. Available at: https://doi.org/10.1016/j.jastp.2019.04.013.

Lamjiri, M. *et al.* (2018) ‘Hourly analyses of the large storms and Atmospheric rivers that provide most of california’s precipitation in only 10 to 100 hours per year’, *San Francisco Estuary and Watershed Science*, 16(4), p. art1. Available at: https://doi.org/10.15447/sfews.2018v16iss4art1.

Lamjiri, M.A. *et al.* (2017) ‘Hourly storm characteristics along the U.S. West Coast: role of Atmospheric Rivers in extreme precipitation: storm characteristics in U.S. West Coast’, *Geophysical Research Letters*, 44(13), pp. 7020–7028. Available at: https://doi.org/10.1002/2017GL074193.

Lang, T.J. and Barros, A.P. (2004) ‘Winter storms in the Central Himalayas’, *Journal of the Meteorological Society of Japan. Ser. II*, 82(3), pp. 829–844. Available at: https://doi.org/10.2151/jmsj.2004.829.

Lavers, D.A. *et al.* (2012) ‘The detection of Atmospheric Rivers in atmospheric reanalyses and their links to British winter floods and the large-scale climatic circulation’, *Journal of Geophysical Research: Atmospheres*, 117(D20). Available at: https://doi.org/10.1029/2012JD018027.

Lavers, D.A. *et al.* (2020) ‘Improved forecasts of Atmospheric rivers through systematic reconnaissance, better modelling, and insights on conversion of rain to flooding’, *Communications Earth & Environment*, 1(1), p. 39. Available at: https://doi.org/10.1038/s43247-020-00042-1.

Lavers, D.A. and Villarini, G. (2013a) ‘Atmospheric Rivers and flooding over the Central United States’, *Journal of Climate*, 26(20), pp. 7829–7836. Available at: https://doi.org/10.1175/JCLI-D-13-00212.1.

Lavers, D.A. and Villarini, G. (2013b) ‘The nexus between Atmospheric Rivers and extreme precipitation across Europe: ARs and extreme Eurpopean precipitation’, *Geophysical Research Letters*, 40(12), pp. 3259–3264. Available at: https://doi.org/10.1002/grl.50636.

Lavers, D.A. and Villarini, G. (2015a) ‘The contribution of Atmospheric Rivers to precipitation in Europe and the United States’, *Journal of Hydrology*, 522, pp. 382–390. Available at: https://doi.org/10.1016/j.jhydrol.2014.12.010.

Lavers, D.A. and Villarini, G. (2015b) ‘The relationship between daily European precipitation and measures of Atmospheric water vapour transport’, *International Journal of Climatology*, 35(8), pp. 2187–2192. Available at: https://doi.org/10.1002/joc.4119.

Lepore, C., Veneziano, D. and Molini, A. (2015) ‘Temperature and CAPE dependence of rainfall extremes in the eastern United States’, *Geophysical Research Letters*, 42(1), pp. 74–83. Available at: https://doi.org/10.1002/2014GL062247.

Leung, L.R. and Qian, Y. (2009) ‘Atmospheric Rivers induced heavy precipitation and flooding in the western U.S. simulated by the WRF regional climate model.’, *Geophysical Research Letters*, 36(3). Available at: https://doi.org/10.1029/2008GL036445.

Li, B. *et al.* (2022) ‘Increase in intraseasonal rainfall driven by the Arabian Sea warming in recent decades’, *Geophysical Research Letters*, 49(20). Available at: https://doi.org/10.1029/2022GL100536.

Liang, J. and Yong, Y. (2020) ‘Climatology of Atmospheric rivers in the Asian monsoon region’, *International Journal of Climatology*, 41(S1), pp. E801–E818. Available at: https://doi.org/10.1002/joc.6729.

Liang, K. *et al.* (2023) ‘The role of Atmospheric rivers in Antarctic sea ice variations’, *Geophysical Research Letters*, 50(8), p. e2022GL102588. Available at: https://doi.org/10.1029/2022GL102588.

Little, K. *et al.* (2019) ‘The role of Atmospheric Rivers for extreme ablation and snowfall events in the Southern Alps of New Zealand’, *Geophysical Research Letters*, 46(5), pp. 2761–2771. Available at: https://doi.org/10.1029/2018GL081669.

Lora, J.M., Shields, C.A. and Rutz, J.J. (2020) ‘Consensus and disagreement in Atmospheric river detection: ARTMIP global catalogues’, *Geophysical Research Letters*, 47(20). Available at: https://doi.org/10.1029/2020GL089302.

Lorenz, D.J. and Hartmann, D.L. (2001) ‘Eddy–zonal flow feedback in the southern hemisphere’, *Journal of the Atmospheric Sciences*, 58(21), pp. 3312–3327. Available at: https://doi.org/10.1175/1520-0469(2001)058<3312:EZFFIT>2.0.CO;2.

Lyngwa, R.V. and Nayak, M.A. (2021) ‘Atmospheric River linked to extreme rainfall events over Kerala in August 2018’, *Atmospheric Research*, 253, p. 105488. Available at: https://doi.org/10.1016/j.atmosres.2021.105488.

Maclennan, M.L. *et al.* (2022) ‘Contribution of Atmospheric rivers to Antarctic precipitation’, *Geophysical Research Letters*, 49(18). Available at: https://doi.org/10.1029/2022GL100585.

Maclennan, M.L. *et al.* (2023) ‘Climatology and surface impacts of atmospheric rivers on West Antarctica’, *The Cryosphere*, 17(2), pp. 865–881. Available at: https://doi.org/10.5194/tc-17-865-2023.

Madhura, R.K. *et al.* (2015) ‘Changes in western disturbances over the Western Himalayas in a warming environment’, *Climate Dynamics*, 44(3–4), pp. 1157–1168. Available at: https://doi.org/10.1007/s00382-014-2166-9.

Mahesh, A. *et al.* (2023) *Identifying Atmospheric rivers and their poleward latent Heattransport with generalizable neural networks: ARCNNv1*. preprint. Atmospheric sciences. Available at: https://doi.org/10.5194/egusphere-2023-763.

Mahoney, K. *et al.* (2016) 'Understanding the role of Atmospheric rivers in heavy precipitation in the southeast United States', *Monthly Weather Review*, 144(4), pp. 1617–1632. Available at: https://doi.org/10.1175/MWR-D-15-0279.1.

Mahto, S.S. *et al.* (2023) 'Atmospheric rivers that make landfall in India are associated with flooding', *Communications Earth & Environment*, 4(1), p. 120. Available at: https://doi.org/10.1038/s43247-023-00775-9.

Mamgain, A., Dash, S.K. and Sarthi, P.P. (2010) 'Characteristics of Eurasian snow depth with respect to Indian summer monsoon rainfall', *Meteorology and Atmospheric Physics*, 110(1–2), pp. 71–83. Available at: https://doi.org/10.1007/s00703-010-0100-1.

Mattingly, K.S., Mote, T.L. and Fettweis, X. (2018) 'Atmospheric River impacts on Greenland Ice sheet surface mass balance', *Journal of Geophysical Research: Atmospheres*, 123(16), pp. 8538–8560. Available at: https://doi.org/10.1029/2018JD028714.

Michaelis, A.C. *et al.* (2022) 'Atmospheric river precipitation enhanced by climate change: A case study of the storm that contributed to California's Oroville Dam Crisis', *Earth's Future*, 10(3). Available at: https://doi.org/10.1029/2021EF002537.

Minallah, S. and Steiner, A.L. (2021) 'Role of the atmospheric moisture budget in defining the precipitation seasonality of the Great Lakes Region', *Journal of Climate*, 34(2), pp. 643–657. Available at: https://doi.org/10.1175/JCLI-D-19-0952.1.

Mishra, A.K. (2015) 'A study on the occurrence of flood events over Jammu and Kashmir during September 2014 using satellite remote sensing', *Natural Hazards*, 78(2), pp. 1463–1467. Available at: https://doi.org/10.1007/s11069-015-1768-9.

Mishra, V. and Shah, H.L. (2018) 'Hydroclimatological Perspective of the Kerala Flood of 2018', *Journal of the Geological Society of India*, 92(5), pp. 645–650. Available at: https://doi.org/10.1007/s12594-018-1079-3.

Mo, R. *et al.* (2019) 'Impacts of Hydrometeor Drift on orographic precipitation: two case Studies of landfalling Atmospheric rivers in British Columbia, Canada', *Weather and Forecasting*, 34(5), pp. 1211–1237. Available at: https://doi.org/10.1175/WAF-D-18-0176.1.

Moore, B.J. *et al.* (2012) 'Physical processes associated with heavy flooding rainfall in Nashville, Tennessee, and vicinity during 1–2 May 2010: The role of an Atmospheric river and mesoscale convective systems', *Monthly Weather Review*, 140(2), pp. 358–378. Available at: https://doi.org/10.1175/MWR-D-11-00126.1.

Mueller, M.J., Mahoney, K.M. and Hughes, M. (2017) 'High-resolution model-based investigation of moisture transport into the Pacific Northwest during a strong Atmospheric River event', *Monthly Weather Review*, 145(9), pp. 3861–3879. Available at: https://doi.org/10.1175/MWR-D-16-0466.1.

Mundhenk, B.D., Barnes, E.A. and Maloney, E.D. (2016) 'All-season climatology and variability of Atmospheric River frequencies over the North Pacific', *Journal of Climate*, 29(13), pp. 4885–4903. Available at: https://doi.org/10.1175/JCLI-D-15-0655.1.

Najibi, N. and Devineni, N. (2018) 'Recent trends in the frequency and duration of global floods', *Earth System Dynamics*, 9(2), pp. 757–783. Available at: https://doi.org/10.5194/esd-9-757-2018.

Nanditha, J.S. *et al.* (2023) 'The Pakistan Flood of August 2022: Causes and Implications', *Earth's Future*, 11(3), p. e2022EF003230. Available at: https://doi.org/10.1029/2022EF003230.

Nash, D. *et al.* (2018) 'The role of Atmospheric rivers in extratropical and polar hydroclimate', *Journal of Geophysical Research: Atmospheres*, 123(13), pp. 6804–6821. Available at: https://doi.org/10.1029/2017JD028130.

Nash, D. *et al.* (2021) 'Winter and spring Atmospheric Rivers in High Mountain Asia: climatology, dynamics, and variability', *Climate Dynamics* [Preprint]. Available at: https://doi.org/10.1007/s00382-021-06008-z.

Nash, D. and Carvalho, L.M.V. (2020) 'Brief communication: an electrifying Atmospheric River – understanding the thunderstorm event in Santa Barbara County during March 2019', *Natural Hazards and Earth System Sciences*, 20(7), pp. 1931–1940. Available at: https://doi.org/10.5194/nhess-20-1931-2020.

Nayak, M.A., Azam, M.F. and Lyngwa, R.V. (2021) 'ERA5-based database of Atmospheric Rivers over Himalayas', *Earth System Science Data Discussions*, pp. 1–35. Available at: https://doi.org/10.5194/essd-2020-397.

Nayak, M.A. and Villarini, G. (2017) 'A long-term perspective of the hydroclimatological impacts of Atmospheric Rivers over the central United States', *Water Resources Research*, 53(2), pp. 1144–1166. Available at: https://doi.org/10.1002/2016WR019033.

Nayak, M.A. and Villarini, G. (2018) 'Remote sensing-based characterization of rainfall during Atmospheric rivers over the central United States', *Journal of Hydrology*, 556, pp. 1038–1049. Available at: https://doi.org/10.1016/j.jhydrol.2016.09.039.

Nayak, M.A., Villarini, G. and Bradley, A.A. (2016) 'Atmospheric rivers and rainfall during NASA's Iowa Flood Studies (IFloodS) Campaign', *Journal of Hydrometeorology*, 17(1), pp. 257–271. Available at: https://doi.org/10.1175/JHM-D-14-0185.1.

Nayak, M.A., Villarini, G. and Lavers, D.A. (2014) 'On the skill of numerical weather prediction models to forecast Atmospheric rivers over the central United States', *Geophysical Research Letters*, 41(12), pp. 4354–4362. Available at: https://doi.org/10.1002/2014GL060299.

Neff, W. *et al.* (2014) 'Continental heat anomalies and the extreme melting of the Greenland ice surface in 2012 and 1889: Melting of Greenland in 1889 and 2012', *Journal of Geophysical Research: Atmospheres*, 119(11), pp. 6520–6536. Available at: https://doi.org/10.1002/2014JD021470.

Neiman, P.J. *et al.* (2002) 'The statistical relationship between upslope flow and rainfall in California's coastal mountains: observations during CALJET', *Monthly Weather Review*, 130, p. 25. Available at: https://doi.org/10.1175/1520-0493(2002)130<1468:TSRBUF>2.0.CO;2.

Neiman, P.J. *et al.* (2008) 'Meteorological characteristics and overland precipitation impacts of Atmospheric Rivers affecting the west coast of North America based on eight years of SSM/I satellite observations', *Journal of Hydrometeorology*, 9(1), pp. 22–47. Available at: https://doi.org/10.1175/2007JHM855.1.

Neiman, P.J. *et al.* (2009) 'A water vapour flux tool for precipitation forecasting', *Proceedings of the Institution of Civil Engineers - Water Management*, 162(2), pp. 83–94. Available at: https://doi.org/10.1680/wama.2009.162.2.83.

Neiman, P.J. *et al.* (2011) 'Flooding in Western Washington: The connection to Atmospheric rivers', *Journal of Hydrometeorology*, 12(6), pp. 1337–1358. Available at: https://doi.org/10.1175/2011JHM1358.1.

Neiman, P.J. *et al.* (2013) 'The landfall and inland penetration of a flood-producing Atmospheric River in Arizona. Part I: observed synoptic-scale, orographic, and hydrometeorological characteristics', *Journal of Hydrometeorology*, 14(2), pp. 460–484. Available at: https://doi.org/10.1175/JHM-D-12-0101.1.

Newell, R.E. *et al.* (1992) 'Tropospheric rivers? - A pilot study', *Geophysical Research Letters*, 19(24), pp. 2401–2404. Available at: https://doi.org/10.1029/92GL02916.

Newell, R.E. and Zhu, Y. (1994) 'Tropospheric rivers: A one-year record and a possible application to ice core data', *Geophysical Research Letters*, 21(2), pp. 113–116. Available at: https://doi.org/10.1029/93GL03113.

Nie, Y. and Sun, J. (2022) 'Moisture sources and transport for extreme precipitation over Henan in July 2021', *Geophysical Research Letters*, 49(4). Available at: https://doi.org/10.1029/2021GL097446.

Nieto, R. *et al.* (2019) 'Contribution of the main moisture sources to precipitation during extreme peak precipitation months', *Advances in Water Resources*, 131, p. 103385. Available at: https://doi.org/10.1016/j.advwatres.2019.103385.

Norris, J.R. *et al.* (2020) 'The observed water vapor budget in an Atmospheric river over the northeast Pacific', *Journal of Hydrometeorology*, 21(11), pp. 2655–2673. Available at: https://doi.org/10.1175/JHM-D-20-0048.1.

Nuimura, T. *et al.* (2015) 'The GAMDAM glacier inventory: a quality-controlled inventory of Asian glaciers', *The Cryosphere*, 9(3), pp. 849–864. Available at: https://doi.org/10.5194/tc-9-849-2015.

Numaguti, A. (1999) 'Origin and recycling processes of precipitating water over the Eurasian continent: Experiments using an atmospheric general circulation model', *Journal of Geophysical Research: Atmospheres*, 104(D2), pp. 1957–1972. Available at: https://doi.org/10.1029/1998JD200026.

O'Brien, T.A. *et al.* (2022) 'Increases in future AR count and size: Overview of the ARTMIP Tier 2 CMIP5/6 experiment', *Journal of Geophysical Research: Atmospheres*, 127(6), p. e2021JD036013. Available at: https://doi.org/10.1029/2021JD036013.

O'Rourke, A.K. and Vallis, G.K. (2016) 'Meridional rossby wave generation and propagation in the maintenance of the wintertime tropospheric double jet', *Journal of the Atmospheric Sciences*, 73(5), pp. 2179–2201. Available at: https://doi.org/10.1175/JAS-D-15-0197.1.

Pai, D. *et al.* (2014) 'Development of a new high spatial resolution (0.25° × 0.25°) long period (1901-2010) daily gridded rainfall data set over India and its comparison with existing data sets over the region', *Mausam*, 65(1), pp. 1–18. Available at: https://doi.org/10.54302/mausam.v65i1.851.

Pai, D.S. and Bhan, S.C. (2014) *Monsoon Report 2014. ESSO Document No.: ESSO/IMD/Synoptic Met./01(2015)/17,*. India Meteorological Department, p. 219. Available at: https://www.tropmet.res.in/~kolli/MOL/Monsoon/year2014/Monsoon-2014-NEW.pdf.

Palazzi, E., von Hardenberg, J. and Provenzale, A. (2013) 'Precipitation in the Hindu-Kush Karakoram Himalaya: Observations and future scenarios', *Journal of Geophysical Research: Atmospheres*, 118(1), pp. 85–100. Available at: https://doi.org/10.1029/2012JD018697.

Paltan, H. *et al.* (2017) 'Global floods and water availability driven by Atmospheric Rivers.', *Geophysical Research Letters*, 44(20), p. 10,387-10,395. Available at: https://doi.org/10.1002/2017GL074882.

Pan, M. and Lu, M. (2019) 'A novel Atmospheric River identification algorithm', *Water Resources Research*, 55(7), pp. 6069–6087. Available at: https://doi.org/10.1029/2018WR024407.

Pan, M. and Lu, M. (2020) 'East Asia Atmospheric River catalog: annual cycle, transition Mechanism, and Precipitation', *Geophysical Research Letters*, 47(15). Available at: https://doi.org/10.1029/2020GL089477.

Park, C., Son, S.W. and Kim, H. (2021) 'Distinct Features of Atmospheric Rivers in the Early Versus Late East Asian Summer Monsoon and Their Impacts on Monsoon Rainfall', *Journal of Geophysical Research: Atmospheres*, 126(7). Available at: https://doi.org/10.1029/2020JD033537.

Parthasarthy, B. and Mooley, D.A. (1978) 'Some Features of a long homogeneous series of Indian summer monsoon rainfall', *Monthly Weather Review*, 106(6), pp. 771–781. Available at: https://doi.org/10.1175/1520-0493(1978)106<0771:SFOALH>2.0.CO;2.

Pathak, A. *et al.* (2017) 'Role of oceanic and land moisture sources and transport in the seasonal and interannual variability of summer monsoon in India', *Journal of Climate*, 30(5), pp. 1839–1859. Available at: https://doi.org/10.1175/JCLI-D-16-0156.1.

Payne, A.E. *et al.* (2020) 'Responses and impacts of atmospheric rivers to climate change', *Nature Reviews Earth & Environment*, 1(3), pp. 143–157. Available at: https://doi.org/10.1038/s43017-020-0030-5.

Payne, A.E. and Magnusdottir, G. (2014) 'Dynamics of landfalling Atmospheric rivers over the North Pacific in 30 Years of MERRA Reanalysis', *Journal of Climate*, 27(18), pp. 7133–7150. Available at: https://doi.org/10.1175/JCLI-D-14-00034.1.

Payne, A.E. and Magnusdottir, G. (2016) 'Persistent landfalling Atmospheric Rivers over the west coast of North America', *Journal of Geophysical Research: Atmospheres*, 121(22). Available at: https://doi.org/10.1002/2016JD025549.

Peixóto, J.P. and Oort, A.H. (1983) 'The atmospheric branch of the hydrological cycle and climate. Variations in the global water budget', pp. 5–65.

Peixoto, J.P. and Oort, A.H. (1992) *Physics of Climate*. 1st edn. American Institute of Physics Melville, NY. Available at: https://link.springer.com/book/9780883187128 (Accessed: 29 May 2023).

Persing, J. and Montgomery, M.T. (2005) 'Is environmental CAPE important in the determination of maximum possible Hurricane intensity?', *Journal of the Atmospheric Sciences*, 62(2), pp. 542–550. Available at: https://doi.org/10.1175/JAS-3370.1.

Petterssen, S. (1940) *Weather Analysis And Forecasting*. McGraw-Hill Book Company Inc. Available at: http://archive.org/details/in.ernet.dli.2015.25456 (Accessed: 23 June 2023).

Prince, H.D. *et al.* (2021) 'A climatology of Atmospheric rivers in New Zealand', *Journal of Climate*, 34(11), pp. 4383–4402. Available at: https://doi.org/10.1175/JCLI-D-20-0664.1.

Rajeevan, M. *et al.* (2006) 'High resolution daily gridded rainfall data for the Indian region: Analysis of break and active monsoon spells', *Current Science*, 91(3), pp. 296–306.

Ralph, F.M. *et al.* (2006) 'Flooding on California's Russian River: Role of Atmospheric rivers', *Geophysical Research Letters*, 33(13), p. L13801. Available at: https://doi.org/10.1029/2006GL026689.

Ralph, F.M. *et al.* (2013) 'Observed Impacts of Duration and Seasonality of Atmospheric-River Landfalls on Soil Moisture and Runoff in Coastal Northern California', *Journal of Hydrometeorology*, 14(2), pp. 443–459. Available at: https://doi.org/10.1175/JHM-D-12-076.1.

Ralph, F.M. *et al.* (2017) 'Dropsonde observations of total integrated water vapor transport within North Pacific Atmospheric rivers', *Journal of Hydrometeorology*, 18(9), pp. 2577–2596. Available at: https://doi.org/10.1175/JHM-D-17-0036.1.

Ralph, F.M. *et al.* (2018) 'Defining "Atmospheric River": How the Glossary of Meteorology helped resolve a debate', *Bulletin of the American Meteorological Society*, 99(4), pp. 837–839. Available at: https://doi.org/10.1175/BAMS-D-17-0157.1.

Ralph, F.M., Rutz, J.J., *et al.* (2019) 'A scale to characterize the strength and impacts of Atmospheric Rivers', *Bulletin of the American Meteorological Society*, 100(2), pp. 269–289. Available at: https://doi.org/10.1175/BAMS-D-18-0023.1.

Ralph, F.M., Wilson, A.M., *et al.* (2019) 'ARTMIP-early start comparison of atmospheric river detection tools: how many atmospheric rivers hit northern California's Russian River watershed?', *Climate Dynamics*, 52(7–8), pp. 4973–4994. Available at: https://doi.org/10.1007/s00382-018-4427-5.

Ralph, F.M. and Dettinger, M.D. (2011) 'Storms, floods, and the science of Atmospheric Rivers', *Eos, Transactions American Geophysical Union*, 92(32), pp. 265–266. Available at: https://doi.org/10.1029/2011EO320001.

Ralph, F.M. and Dettinger, M.D. (2012) 'Historical and national perspectives on extreme west coast precipitation associated with Atmospheric Rivers during december 2010', *Bulletin of the American Meteorological Society*, 93(6), pp. 783–790. Available at: https://doi.org/10.1175/BAMS-D-11-00188.1.

Ralph, F.M., Neiman, P.J. and Rotunno, R. (2005) 'Dropsonde observations in Low-Level Jets over the Northeastern Pacific Ocean from CALJET-1998 and PACJET-2001: Mean vertical-profile and Atmospheric-river characteristics', *Monthly Weather Review*, 133(4), pp. 889–910. Available at: https://doi.org/10.1175/MWR2896.1.

Ralph, F.M., Neiman, P.J. and Wick, G.A. (2004) 'Satellite and CALJET aircraft observations of Atmospheric Rivers over the eastern north Pacific Ocean during the winter of 1997/98', *Monthly Weather Review*, 132(7), pp. 1721–1745. Available at: https://doi.org/10.1175/1520-0493(2004)132<1721:SACAOO>2.0.CO;2.

Ramos, A.M. *et al.* (2015) 'Daily precipitation extreme events in the Iberian Peninsula and its sssociation with Atmospheric rivers', *Journal of Hydrometeorology*, 16(2), pp. 579–597. Available at: https://doi.org/10.1175/JHM-D-14-0103.1.

Ramos, A.M. *et al.* (2018) 'Extreme precipitation events in summer in the Iberian Peninsula and Its relationship with Atmospheric rivers', *Frontiers in Earth Science*, 6, p. 110. Available at: https://doi.org/10.3389/feart.2018.00110.

Ramos, A.M. *et al.* (2019) 'From Amazonia to southern Africa: atmospheric moisture transport through low-level jets and atmospheric rivers: Moisture transport across the South Atlantic Ocean', *Annals of the New York Academy of Sciences*, 1436(1), pp. 217–230. Available at: https://doi.org/10.1111/nyas.13960.

Rana, P. (2015) *How Chennai Floods Stack Up Against Other Natural Disasters in 2015 - WSJ*, *The Wall Street Journal*. Available at: https://www.wsj.com/articles/BL-IRTB-31036 (Accessed: 18 September 2023).

Ranalkar, M.R. *et al.* (2016a) 'Dynamical features of incessant heavy rainfall event of June 2013 over Uttarakhand, India', *Natural Hazards*, 80(3), pp. 1579–1601. Available at: https://doi.org/10.1007/s11069-015-2040-z.

Ranalkar, M.R. *et al.* (2016b) 'Dynamical features of incessant heavy rainfall event of June 2013 over Uttarakhand, India', *Natural Hazards*, 80(3), pp. 1579–1601. Available at: https://doi.org/10.1007/s11069-015-2040-z.

Rao, P.C., Shinde, A.S. and Jaswal, A.K. (2016) 'Intense precipitation causing floods over Himalayan Region of Northern India – A case study on role of Atmospheric rivers', *The Journal of Indian Geophysical Union*, 20(2), p. 10.

Ray, K., Bhan, S. and Bandopadhyay, B.K. (2015) 'The catastrophe over Jammu and Kashmir in September 2014: a meteorological observational analysis', *Current science*, accepted.

Raymond, D.J., Sessions, S.L. and Fuchs, Ž. (2007) 'A theory for the spinup of tropical depressions', *Quarterly Journal of the Royal Meteorological Society*, 133(628), pp. 1743–1754. Available at: https://doi.org/10.1002/qj.125.

Reid, K.J. *et al.* (2021) 'Extreme rainfall in New Zealand and its association with Atmospheric rivers', *Environmental Research Letters*, 16(4), p. 044012. Available at: https://doi.org/10.1088/1748-9326/abeae0.

Riley, C. *et al.* (2021) 'Characteristics of historical precipitation in high mountain Asia based on a 15-year high resolution dynamical downscaling', *Atmosphere*, 12(3), p. 355. Available at: https://doi.org/10.3390/atmos12030355.

Rolph, G., Stein, A. and Stunder, B. (2017) 'Real-time environmental applications and display system: READY', *Environmental Modelling & Software*, 95, pp. 210–228. Available at: https://doi.org/10.1016/j.envsoft.2017.06.025.

Romshoo, S.A. *et al.* (2018) 'Climatic, geomorphic and anthropogenic drivers of the 2014 extreme flooding in the Jhelum basin of Kashmir, India', *Geomatics, Natural Hazards and Risk*, 9(1), pp. 224–248. Available at: https://doi.org/10.1080/19475705.2017.1417332.

Roxy, M.K. *et al.* (2017) 'A threefold rise in widespread extreme rain events over central India', *Nature Communications*, 8(1), p. 708.

Rutz, J.J. *et al.* (2019) 'The Atmospheric River Tracking Method Intercomparison Project (ARTMIP): Quantifying uncertainties in Atmospheric river climatology', *Journal of Geophysical Research: Atmospheres*, 124(24), pp. 13777–13802. Available at: https://doi.org/10.1029/2019JD030936.

Rutz, J.J., Steenburgh, W.J. and Ralph, F.M. (2014) 'Climatological characteristics of Atmospheric Rivers and their inland penetration over the Western United States', *Monthly Weather Review*, 142(2), pp. 905–921. Available at: https://doi.org/10.1175/MWR-D-13-00168.1.

Saavedra, F. *et al.* (2020) 'Atmospheric rivers contribution to the snow accumulation over the Southern Andes (26.5° S–37.5° S)', *Frontiers in Earth Science*, 8, p. 261. Available at: https://doi.org/10.3389/feart.2020.00261.

Sarkar, S., Kuttippurath, J. and Patel, V.K. (2023) 'Long-term changes in precipitable water vapour over India derived from satellite and reanalysis data for the past four decades (1980–2020)', *Environmental Science: Atmospheres*, 3(4), pp. 749–759. Available at: https://doi.org/10.1039/D2EA00139J.

Sattar, A.M. and Cheung, K.K.W. (2019) 'Comparison between the active tropical cyclone seasons over the Arabian Sea and Bay of Bengal', *International Journal of Climatology*, 39(14), pp. 5486–5502. Available at: https://doi.org/10.1002/joc.6167.

Seager, R. *et al.* (2003) 'Why is There an evaporation minimum at the equator?', *Journal of Climate*, 16(22), pp. 3793–3802. Available at: https://doi.org/10.1175/1520-0442(2003)016<3793:WITAEM>2.0.CO;2.

Seager, R. *et al.* (2007) 'Model projections of an imminent transition to a more arid climate in Southwestern North America', *Science*, 316(5828), pp. 1181–1184. Available at: https://doi.org/10.1126/science.1139601.

Seager, R. and Henderson, N. (2013) 'Diagnostic computation of moisture budgets in the ERA-Interim reanalysis with reference to analysis of CMIP-archived atmospheric model data', *Journal of Climate*, 26(20), pp. 7876–7901. Available at: https://doi.org/10.1175/JCLI-D-13-00018.1.

Seager, R., Naik, N. and Vecchi, G.A. (2010) 'Thermodynamic and Dynamic Mechanisms for Large-Scale Changes in the Hydrological Cycle in Response to Global Warming*', *Journal of Climate*, 23(17), pp. 4651–4668. Available at: https://doi.org/10.1175/2010JCLI3655.1.

Seager, R. and Vecchi, G.A. (2010) ‘Greenhouse warming and the 21st century hydroclimate of southwestern North America’, *Proceedings of the National Academy of Sciences*, 107(50), pp. 21277–21282. Available at: https://doi.org/10.1073/pnas.0910856107.

Sellars, S. *et al.* (2013) ‘Computational earth science: Big data transformed into insight’, *Eos, Transactions American Geophysical Union*, 94(32), pp. 277–278. Available at: https://doi.org/10.1002/2013EO320001.

Sellars, S.L. *et al.* (2017) ‘Genesis, pathways, and terminations of intense global water vapor transport in association with large-scale climate patterns’, *Geophysical Research Letters*, 44(24), pp. 12–465. Available at: https://doi.org/10.1002/2017GL075495.

Sellars, S.L., Gao, X. and Sorooshian, S. (2015) ‘An object-oriented approach to investigate impacts of climate oscillations on precipitation: A western United States case study’, *Journal of Hydrometeorology*, 16(2), pp. 830–842. Available at: https://doi.org/10.1175/JHM-D-14-0101.1.

Sharifi, E., Steinacker, R. and Saghafian, B. (2016) ‘Assessment of GPM-IMERG and Other Precipitation Products against Gauge Data under Different Topographic and Climatic Conditions in Iran: Preliminary Results’, *Remote Sensing*, 8(2), p. 135. Available at: https://doi.org/10.3390/rs8020135.

Shearer, E.J. *et al.* (2020) ‘Examination of global midlatitude Atmospheric River lifecycles using an object-oriented methodology’, *Journal of Geophysical Research: Atmospheres*, 125(22). Available at: https://doi.org/10.1029/2020JD033425.

Shepard, D. (1968) ‘A two-dimensional interpolation function for irregularly-spaced data’, in *Proceedings of the 1968 23rd ACM national conference on -. the 1968 23rd ACM national conference*, ACM Press, pp. 517–524. Available at: https://doi.org/10.1145/800186.810616.

Shields, C.A. *et al.* (2018) ‘Atmospheric River Tracking Method Intercomparison Project (ARTMIP): project goals and experimental design’, *Geoscientific Model Development*, 11(6), pp. 2455–2474. Available at: https://doi.org/10.5194/gmd-11-2455-2018.

Shields, C.A. *et al.* (2019) ‘Meridional heat transport during Atmospheric Rivers in high-resolution CESM climate projections’, *Geophysical Research Letters*, 46(24), pp. 14702–14712. Available at: https://doi.org/10.1029/2019GL085565.

Shu, J., Shamseldin, A.Y. and Weller, E. (2021) ‘The impact of Atmospheric Rivers on rainfall in New Zealand’, *Scientific Reports*, 11(1), p. 5869. Available at: https://doi.org/10.1038/s41598-021-85297-0.

Sil, S. *et al.* (2021) ‘Shifting seasonality of cyclones and western boundary current interactions in Bay of Bengal as observed during Amphan and Fani’, *Scientific Reports*, 11(1), p. 22052. Available at: https://doi.org/10.1038/s41598-021-01607-6.

Skinner, C.B. *et al.* (2023) ‘Atmospheric river contributions to ice sheet hydroclimate at the last glacial maximum’, *Geophysical Research Letters*, 50(1), p. e2022GL101750. Available at: https://doi.org/10.1029/2022GL101750.

Smith, B.L. *et al.* (2010) ‘Water vapor fluxes and orographic precipitation over Northern California associated with a landfalling Atmospheric river’, *Monthly Weather Review*, 138(1), pp. 74–100. Available at: https://doi.org/10.1175/2009MWR2939.1.

Sodemann, H., Schwierz, C. and Wernli, H. (2008a) ‘Interannual variability of Greenland winter precipitation sources: Lagrangian moisture diagnostic and North Atlantic Oscillation influence’, *Journal of Geophysical Research: Atmospheres*, 113(D3), p. 2007JD008503. Available at: https://doi.org/10.1029/2007JD008503.

Sodemann, H., Schwierz, C. and Wernli, H. (2008b) ‘Interannual variability of Greenland winter precipitation sources: Lagrangian moisture diagnostic and North Atlantic Oscillation influence’, *Journal of Geophysical Research*, 113(D3), p. D03107.

Sodemann, H. and Stohl, A. (2013) ‘Moisture origin and meridional transport in Atmospheric Rivers and their association with multiple cyclones*’, *Monthly Weather Review*, 141(8), pp. 2850–2868. Available at: https://doi.org/10.1175/MWR-D-12-00256.1.

Starr, V.P. and Peixoto, J.P. (1958) ‘On the global balance of water vapor and the hydrology of deserts’, *Tellus*, 10(2), pp. 188–194. Available at: https://doi.org/10.1111/j.2153-3490.1958.tb02004.x.

Starr, V.P., Peixoto, J.P. and Livadas, G.C. (1958) ‘On the meridional flux of water vapor in the northern hemisphere’, *Geofisica Pura e Applicata*, 39(1), pp. 174–185. Available at: https://doi.org/10.1007/BF02001143.

Stein, A.F. *et al.* (2015) ‘NOAA’s HYSPLIT Atmospheric Transport and Dispersion Modeling System’, *Bulletin of the American Meteorological Society*, 96(12), pp. 2059–2077. Available at: https://doi.org/10.1175/BAMS-D-14-00110.1.

Stohl, A. (1998) ‘Computation, accuracy and applications of trajectories—A review and bibliography’, *Atmospheric Environment*, 32(6), pp. 947–966. Available at: https://doi.org/10.1016/S1352-2310(97)00457-3.

Stohl, A. and James, P. (2004) ‘A lagrangian analysis of the atmospheric branch of the global water cycle. Part I: method description, validation, and demonstration for the August 2002 flooding in Central Europe’, *Journal of Hydrometeorology*, 5(4), pp. 656–678.

Stohl, A. and Seibert, P. (1998) ‘Accuracy of trajectories as determined from the conservation of meteorological tracers’, *Quarterly Journal of the Royal Meteorological Society*, 124(549), pp. 1465–1484. Available at: https://doi.org/10.1002/qj.49712454907.

Suthinkumar, P.S., Varikoden, H. and Babu, C.A. (2023) ‘Changes in extreme rainfall events in the recent decades and their linkage with atmospheric moisture transport’, *Global and Planetary Change*, 221, p. 104047. Available at: https://doi.org/10.1016/j.gloplacha.2023.104047.

Tan, Y. *et al.* (2020) ‘The role of circulation and its changes in present and future Atmospheric rivers over Western North America’, *Journal of Climate*, 33(4), pp. 1261–1281. Available at: https://doi.org/10.1175/JCLI-D-19-0134.1.

Tan, Y. *et al.* (2022) ‘Moisture budget analysis of extreme precipitation associated with different types of atmospheric rivers over western North America’, *Climate Dynamics*, 58(3–4), pp. 793–809. Available at: https://doi.org/10.1007/s00382-021-05933-3.

Thapa, K., Endreny, T.A. and Ferguson, C.R. (2018) ‘Atmospheric Rivers carry nonmonsoon extreme precipitation into Nepal’, *Journal of Geophysical Research: Atmospheres*, 123(11), pp. 5901–5912. Available at: https://doi.org/10.1029/2017JD027626.

Trenberth, K.E. (1991) ‘Climate diagnostics from global analyses: conservation of mass in ECMWF analyses’, *Journal of Climate*, 4(7), pp. 707–722. Available at: https://doi.org/10.1175/1520-0442(1991)004<0707:CDFGAC>2.0.CO;2.

Trenberth, K.E. (1998) ‘Atmospheric moisture residence times and cycling: Implications for rainfall rates and climate change.’, *Climatic Change*, 39(4), pp. 667–694. Available at: https://doi.org/10.1023/A:1005319109110.

Trenberth, K.E. (1999) ‘Atmospheric moisture recycling: role of advection and local evaporation’, *Journal of Climate*, 12(5), pp. 1368–1381. Available at: https://doi.org/10.1175/1520-0442(1999)012<1368:AMRROA>2.0.CO;2.

Trenberth, K.E. and Guillemot, C.J. (1995) ‘Evaluation of the global atmospheric moisture budget as seen from analyses’, *Journal of Climate*, 8(9), pp. 2255–2272. Available at: https://doi.org/10.1175/1520-0442(1995)008<2255:EOTGAM>2.0.CO;2.

Tseng, K.C. *et al.* (2021) ‘Are multiseasonal forecasts of Atmospheric rivers possible?’, *Geophysical Research Letters*, 48(17). Available at: https://doi.org/10.1029/2021GL094000.

Viale, M. *et al.* (2018) ‘Impacts of Atmospheric Rivers on precipitation in Southern South America’, *Journal of Hydrometeorology*, 19(10), pp. 1671–1687. Available at: https://doi.org/10.1175/JHM-D-18-0006.1.

Viste, E. and Sorteberg, A. (2015) ‘Snowfall in the Himalayas: an uncertain future from a little-known past’, *The Cryosphere*, 9(3), pp. 1147–1167. Available at: https://doi.org/10.5194/tc-9-1147-2015.

Vittal, H. *et al.* (2016) ‘Revisiting the dependence of precipitation extremes on temperature with the observed long-term dataset over India.’, p. 1228.

Waliser, D. and Guan, B. (2017) ‘Extreme winds and precipitation during landfall of Atmospheric Rivers’, *Nature Geoscience*, 10(3), pp. 179–183. Available at: https://doi.org/10.1038/ngeo2894.

Wallace, John M, Wallace, John Michael and Hobbs, P.V. (2006) *Atmospheric Science: an Introductory Survey.* Burlington: Elsevier Science.

Wang, T., Wei, K. and Ma, J. (2021) ‘Atmospheric Rivers and Mei-yu Rainfall in China: A case study of summer 2020’, *Advances in Atmospheric Sciences*, 38(12), pp. 2137–2152. Available at: https://doi.org/10.1007/s00376-021-1096-9.

Wei, J. *et al.* (2012) ‘Water vapor sources for Yangtze River Valley rainfall: Climatology, variability, and implications for rainfall forecasting’, *Journal of Geophysical Research: Atmospheres*, 117(D5), p. n/a-n/a. Available at: https://doi.org/10.1029/2011JD016902.

Wheeler, M.C. and Hendon, H.H. (2004) ‘An all-season real-time multivariate MJO Index: Development of an index for monitoring and prediction’, *Monthly Weather Review*, 132(8), pp. 1917–1932. Available at: https://doi.org/10.1175/1520-0493(2004)132<1917:AARMMI>2.0.CO;2.

Wick, G.A. *et al.* (2013) ‘Evaluation of forecasts of the water vapor signature of Atmospheric rivers in 0perational Numerical Weather Prediction Models’, *Weather and Forecasting*, 28(6), pp. 1337–1352. Available at: https://doi.org/10.1175/WAF-D-13-00025.1.

Wick, G.A., Neiman, P.J. and Ralph, F.M. (2013) ‘Description and validation of an automated objective technique for identification and characterization of the integrated water vapor signature of Atmospheric Rivers’, *IEEE Transactions on Geoscience and Remote Sensing*, 51(4), pp. 2166–2176. Available at: https://doi.org/10.1109/TGRS.2012.2211024.

Wille, J.D. *et al.* (2019) ‘West Antarctic surface melt triggered by Atmospheric Rivers’, *Nature Geoscience*, 12(11), pp. 911–916. Available at: https://doi.org/10.1038/s41561-019-0460-1.

Wille, J.D. *et al.* (2021) ‘Antarctic Atmospheric river climatology and precipitation impacts’, *Journal of Geophysical Research: Atmospheres*, 126(8), p. e2020JD033788. Available at: https://doi.org/10.1029/2020JD033788.

Woollings, T. *et al.* (2008) ‘A new rossby wave–breaking interpretation of the North Atlantic Oscillation’, *Journal of the Atmospheric Sciences*, 65(2), pp. 609–626. Available at: https://doi.org/10.1175/2007JAS2347.1.

Xiong, Y. and Ren, X. (2021) ‘Influences of Atmospheric rivers on North Pacific winter precipitation: climatology and dependence on ENSO condition’, *Journal of Climate*, 34(1), pp. 277–292. Available at: https://doi.org/10.1175/JCLI-D-20-0301.1.

Xu, J. *et al.* (2009) 'The melting Himalayas: cascading effects of climate change on water, biodiversity, and livelihoods', *Conservation Biology*, 23(3), pp. 520–530. Available at: https://doi.org/10.1111/j.1523-1739.2009.01237.x.

Yadav, B.P., Kumar, N. and Lotus, S. (2017) 'Synoptic & climatological aspects of extreme rainfall over western Himalayas towards end of 2014 southwest monsoon season', *Mausam*, 68, pp. 597–606.

Yang, Y. *et al.* (2018) 'Atmospheric Rivers over the Bay of Bengal lead to northern Indian extreme rainfall', *International Journal of Climatology*, 38(2), pp. 1010–1021. Available at: https://doi.org/10.1002/joc.5229.

Yang, Z. *et al.* (2023) 'Moisture Sources of Precipitation in the Great Lakes Region: Climatology and Recent Changes', *Geophysical Research Letters*, 50(5), p. e2022GL100682. Available at: https://doi.org/10.1029/2022GL100682.

You, C., Tjernström, M. and Devasthale, A. (2021) 'Eulerian and Lagrangian views of warm and moist air intrusions into summer Arctic', *Atmospheric Research*, 256, p. 105586. Available at: https://doi.org/10.1016/j.atmosres.2021.105586.

Young, A.M., Skelly, K.T. and Cordeira, J.M. (2017) 'High-impact hydrologic events and Atmospheric Rivers in California: an investigation using the NCEI storm events database', *Geophysical Research Letters*, 44(7), pp. 3393–3401. Available at: https://doi.org/10.1002/2017GL073077.

Yu, J.-Y. and Hartmann, D.L. (1993) 'Zonal flow vacillation and eddy forcing in a simple GCM of the atmosphere', *Journal of the Atmospheric Sciences*, 50(19), pp. 3244–3259. Available at: https://doi.org/10.1175/1520-0469(1993)050<3244:ZFVAEF>2.0.CO;2.

Zangvil, A. *et al.* (2010) 'Comparative study of atmospheric water vapor budget associated with precipitation in Central US and eastern Mediterranean', *Advances in Geosciences*, 23, pp. 3–9. Available at: https://doi.org/10.5194/adgeo-23-3-2010.

Zhang, J. *et al.* (2022) 'The warming of the Arabian Sea induced a northward summer monsoon over the Tibetan Plateau', *Journal of Climate*, 35(23), pp. 7541–7554. Available at: https://doi.org/10.1175/JCLI-D-22-0273.1.

Zhang, P. *et al.* (2023) 'More frequent Atmospheric rivers slow the seasonal recovery of Arctic sea ice', *Nature Climate Change*, 13(3), pp. 266–273. Available at: https://doi.org/10.1038/s41558-023-01599-3.

Zhang, Z., Ralph, F.M. and Zheng, M. (2019) 'The relationship between extratropical cyclone strength and Atmospheric River intensity and position', *Geophysical Research Letters*, 46(3), pp. 1814–1823. Available at: https://doi.org/10.1029/2018GL079071.

Zhou, T.J. (2005) 'Atmospheric water vapor transport associated with typical anomalous summer rainfall patterns in China', *Journal of Geophysical Research*, 110(D8), p. D08104. Available at: https://doi.org/10.1029/2004JD005413.

Zhou, Y. *et al.* (2022) 'Characteristics and variability of winter northern pacific Atmospheric river flavors', *Journal of Geophysical Research: Atmospheres*, 127(23). Available at: https://doi.org/10.1029/2022JD037105.

Zhou, Y. and Kim, H. (2019) 'Impact of distinct origin locations on the life cycles of landfalling Atmospheric rivers over the U.S. west coast', *Journal of Geophysical Research: Atmospheres*, 124(22), pp. 11897–11909. Available at: https://doi.org/10.1029/2019JD031218.

Zhou, Y., Kim, H. and Guan, B. (2018) 'Life cycle of Atmospheric Rivers: identification and climatological characteristics', *Journal of Geophysical Research: Atmospheres*, 123(22). Available at: https://doi.org/10.1029/2018JD029180.

Zhu, Y. and Newell, R.E. (1994) ‘Atmospheric rivers and bombs’, *Geophysical Research Letters*, 21(18), pp. 1999–2002. Available at: https://doi.org/10.1029/94GL01710.

Zhu, Y. and Newell, R.E. (1998) ‘A proposed algorithm for moisture fluxes from Atmospheric Rivers’, *Monthly Weather Review*, 126(3), pp. 725–735. Available at: https://doi.org/10.1175/1520-0493(1998)126<0725:APAFMF>2.0.CO;2.